Dissertation

Submitted to the
Combined Faculty of Natural Sciences and Mathematics
Heidelberg University, Germany
for the degree of
Doctor of Natural Sciences (Dr. rer. nat.)

Presented by

Camilo del Río, M. Sc.

Oral examination: November 6th, 2019

Spatiotemporal characteristics of coastal fog in the Atacama Desert

A remote sensing based analysis of the past, present and future distribution and variability of low clouds under climate change in a hyper-arid region of northern Chile

Evaluators: Prof. Dr. Alexander Siegmund

Prof. Dr. Jörg Bendix

Acknowledgements

Thanks to ERANet-LAC, a bi-regional cooperation between the European Union and Latin America and the Caribbean on Research and Innovation, for partially funding this work through CONICYT project #ELAC2015/T01-0872.

Personally, there are many people I would like to thank for continually supporting me through the dissertation process. First, to my supervisor Prof. Dr. Alexander Siegmund, thank you for the constant support, constructive discussions and suggestions, and especially for the reliable professional and friendly relationship. I extend the latter to his family (Alexandra, Charlotte, Helena, Mathilde and Benjamin), who received me several times in a very kind and welcoming manner in their home at Gaiberg during my stays in Germany. Secondly, I want to thank Prof. Dr. Jörg Bendix for agreeing to be my second evaluator. Thanks also to Prof. Dr. Marcus Koch and Prof Dr. Hans Gebhardt for agreeing to be part of my committee.

Thanks also to former and present members of the ʳgeo-team of the Department of Geography, Heidelberg University of Education, especially to Dr. Nils Wolf, Dipl.-Ing. Hans-Peter Mayer, Dipl.-Geoökol. Daniel Volz, Dr. Svenja Brockmüller, Dr. Signe Mikulane and Brigitte Beck-Ritzert. Special thanks to the Center of Excellence in Research and Teaching of the University of Heidelberg in Santiago de Chile, the Heidelberg Center for Latin America, who financially supported my time in Heidelberg. I would like to personally thank the Executive Director, Dr. Walter Eckel, and Academic Coordinator, Dr. Johanna Höhl, for supporting and encouraging me from the very beginning of my doctorate.

Thank you very much to the Dean of the Faculty of History, Geography and Political Sciences of the Pontificia Universidad Católica de Chile (UC), Prof. Dr. Patricio Bernedo, and to the Director of the UC Institute of Geography, Prof. Dr. Federico Arenas for your constant support. Additionally, I would like to thank my colleagues and friends, Prof. Pablo Osses (Director of the Atacama UC research station - Alto Patache) and Prof. Dr. Juan Luis García (Director of the UC Center Desierto de Atacama), for sharing their valuable scientific experience and knowledge during the development of this thesis.

To the numerous individuals who supported my research, be it by processing satellite images, sorting data series, supporting field work, searching for funds, editing or

proofreading translations or with a good conversation, helping with ideas or solutions to improve this research, to all of them, many thanks: Constanza Vargas, Daniela Rivera, Sujey González, María-Elisa Valdés, Nicolás Zanetta, Kathya Rodríguez, Juan Pablo Zaldívar, Sofía Ramírez, Prof. Dr. Rodrigo Escobar, Prof. Dr. Cristián Tejos, Prof. Dr. Fabrice Lambert, Felipe Lobos, Prof. Dr. Johannes Rehner, Juan Pablo Astaburuaga and Prof. Pilar Cereceda.

Finally, I thank my parents, Germán and Patricia, for their unconditional support in all my projects. To Paloma, Baltazar, Guadalupe and Simón, for accompanying me in this stage of my journey, this research is dedicated to them.

Abstract

The Atacama Desert is well known for its arid and hyper-arid conditions; nevertheless, in the coastal Atacama, where the extended low stratocumulus clouds cover over the southeast Pacific Ocean meets the Coastal Cordillera it produces a highly dynamic advective marine fog. This fog is a major feature of the local climate, which provides humidity and freshwater to this hyper-arid environment. Along the fog belt, fragile and highly endemic ecosystems have developed various strategies for adaptation that take advantage of fog water inputs, and therefore are sensitive indicators of change in fog and low clouds. At the same time, the fog belt covers an area with high potential for fog water collection, which could be used for a number of purposes, including human consumption and low-scale economic activities. However, currently there is little known about the dynamics between fog and climate in the coastal Atacama. For example, we still lack a basic understanding of the long-term spatiotemporal dynamics of this extensive coastal fog, how climate change has affected it in the recent past, is affecting it at present and how it will change in the near future. These are important questions, as understanding cloud variability over the coastal Atacama will provide insights into the regional, tropical Pacific atmospheric-oceanic system, and therefore the long-term climate controls on coastal biodiversity in the Atacama, as well as the potential of fog water as an alternative fresh water resource.

In this research is presented an integrated approach of scales of analysis, based on time series analysis of satellite data collected between 1995 and 2017 and a local network of instruments that measure atmospheric variables, including a new ground oriented fog observation system (GOFOS) created for this project. Based on detailed knowledge of the seasonal and daily cycles of the fog and low clouds, as well its spatial distribution, frequency presence, inter-annual variability, trends and vertical dynamics allow to enhance understanding of the fog climate and the factors involved in its spatiotemporal changes. Results show that for the month of September there was a weak positive trend in fog presence over the ocean and onshore areas (below 1.000 m a.s.l.) during the study period; however, those areas close to the coast with elevations above 1.000 m a.s.l. showed a weak negative trend in fog presence, demonstrating a decrease in the altitude of the thermal inversion layer over the years. At the same time, the El Niño Oceanic Oscillation (ENSO) apparently exerts significant influence on the inter-annual variability in fog and low clouds in the coastal Atacama, as there is a possible causal-link between ENSO anomalies in the

Niño 3.4 region and fog and low cloud frequency presence (FFP). ENSO phases (+/-) generate opposing seasonal fog conditions: i) ENSO (+) produces an increase in FFP during summer, and a decrease in winter; ii) ENSO (-) produces a decrease in FFP during summer, and an increase in winter. Furthermore, linear regression indicates that ENSO anomalies explain ~50% of the variance in inter-annual FFP over the ocean and near shore areas during summer. In the winter/early spring, regression indicates that ENSO anomalies explain a ~47% of FFP variation over the ocean and ~66% in onshore areas. At the same time, results indicate that during the winter/early spring, FFP trends are apparently under a Pacific decadal signal (La Niña-like), whose influence can only be confirmed with a dataset that covers a longer time span. Results also demonstrate that the annual daily cycle shows a strong inverse correlation between FFP and the altitude of the thermal inversion layer, with lower (higher) altitudes related with higher (lower) FFPs, and this pattern holds from sunset to sunrise (from early morning to the afternoon). Finally, spatiotemporal identification and characterization of fog and low clouds along the coast of Atacama, allows to precisely determine the areas with higher or lower fog presence, as well as the seasonal and daily trends (horizontal and vertical) in fog presence. Understanding spatiotemporal changes in fog and low clouds may allow to link these changes with recent geographic changes in fog-dependent ecosystems, allowing for a better understanding of the existing connection between the atmosphere and biosphere, which is vital to comprehend both past and future climatic changes. Such understanding of fog patterns will also allow the identification of sites with greater potential for fog water collection, and to forecast changes in fog patterns that will affect fog harvesting in the future, in a region where growing demand for water resources requires alternative and sustainable sources.

Zusammenfassung (Abstract in German language)

Die Atacama-Wüste ist bekannt für ihre trockenen und hyperariden Bedingungen, jedoch in der Küsten-Atacama, wenn die ausgedehnte Stratocumulus-Niederwolke über dem südöstlichen Pazifik auf die Küstenkordillere trifft und einen hochdynamischen, advektiven Meeresnebel erzeugt, der ein wesentliches Merkmal des lokalen Klimas ist, das die hyperaride Umgebung mit Feuchtigkeit und Süßwasser versorgt. Entlang des Nebelbandes haben zerbrechliche und sehr endemische Ökosysteme verschiedene Anpassungsstrategien entwickelt, um die Vorteile der Nebelwassereinträge zu nutzen, und sind daher empfindliche Indikatoren für Veränderungen in der Nebelwolke. Gleichzeitig deckt das Nebelband ein Gebiet mit einem hohen Potenzial für die Sammlung von Nebelwasser für vielfältige Einsatzmöglichkeiten ab, wie z.B. den menschlichen Verzehr und wirtschaftliche Aktivitäten in geringem Umfang. Allerdings fehlt derzeit ein allgemeines Verständnis der Dynamik des Nebelklimas an der Küste Atacamas. So fehlt beispielsweise noch ein grundlegendes Verständnis für die langfristige raumzeitliche Dynamik dieser ausgedehnten Küstenwolke, wie sich der Klimawandel in der jüngsten Vergangenheit ausgewirkt hat, ihn derzeit beeinflusst und wie er sich in naher Zukunft verändern wird. Diese sind wichtig, da das Verständnis der Wolkenvariabilität über der Küste Atacama Einblicke in das regionale tropische pazifische Atmosphären-Ozeansystem und damit in die langfristigen Klimakontrollen der Küstenbiodiversität Atacama sowie in das Potenzial von Nebelwasser als alternative Ressource gibt. Basierend auf der Zeitreihenanalyse von Satellitendaten zwischen 1995 und 2017 und einem lokalen Netzwerk von Instrumenten zur Messung atmosphärischer Variablen, zu denen ein neues bodenorientiertes Nebelbeobachtungssystem (GOFOS) gehört, das für diese Forschung entwickelt wurde, wird hier ein integrativer Ansatz von Analyseskalen, ein verbessertes Verständnis des Nebelklimas und der beteiligten Faktoren auf seine raumzeitlichen Veränderungen gezeigt, basierend auf einer detaillierten Kenntnis des saisonalen und täglichen Zyklus des Nebels mit niedriger Wolke, sowie seiner räumlichen Verteilung, Frequenzpräsenz, interjährigen Variabilität, Trends und vertikalen Dynamik. Es wird festgestellt, dass die September-Trends innerhalb des Untersuchungszeitraums einen schwachen positiven Trend über dem Ozean und Onshore-Gebiete unter 1.000 m über dem Meeresspiegel zeigen, im Gegenteil, die küstennahen Gebiete über 1.000 m über dem Meeresspiegel zeigen einen schwachen negativen Trend, was einen Rückgang der Höhe der thermischen Inversionsschicht im Laufe der Jahre zeigt. Gleichzeitig übt die ENSO offenbar einen signifikanten Einfluss auf

die zwischenjährliche Variabilität der nebelarmen Wolke in der Küstenregion von Atacama aus, da ein möglicher Kausalzusammenhang zwischen ENSO-Anomalien in der Zone 3,4 und dem Vorhandensein der nebligen niederen Wolkenfrequenz (FFP) besteht. Die ENSO-Phase (+/-) erzeugt entgegengesetzte saisonale Nebelbedingungen; ENSO (+) erzeugt einen Anstieg des FFP im Sommer und einen Rückgang im Winter; ENSO (-) erzeugt einen Rückgang des FFP im Sommer und einen Anstieg im Winter. Darüber hinaus zeigt eine lineare Regression, dass ENSO-Anomalien, erklären ~50% der Varianz in der zwischenjährlichen FFP über dem Meer und Nearshore-Gebieten im Sommer. Im Falle des winterfrühen Frühlings deutet die Regression darauf hin, dass ENSO-Anomalien in den ozeanischen und an Land liegenden Gebieten einen Wert von ~47 % bzw. ~66 % erklären. Gleichzeitig wurde festgestellt, dass sich die FFP-Trends im frühen Winter-Frühling offenbar unter einem pazifischen Dekadalsignal (La Niña-ähnlich) befinden, dessen Einfluss nur mit einem längeren Datensatz bestätigt werden kann. Die Ergebnisse zeigen auch, dass der jährliche Tageszyklus eine starke umgekehrte Korrelation zwischen dem FFP und der thermischen Inversionsschichthöhe zeigt, wobei eine niedrigere (höhere) Höhe der thermischen Inversionsschicht mit einem höheren (niedrigeren) FFP verbunden ist, der von Sonnenuntergang bis Sonnenaufgang (vom frühen Morgen bis zum Nachmittag) auftritt. Schließlich ist die Identifizierung und Charakterisierung in räumlicher und zeitlicher Hinsicht der Low-Cloud-Nebel an der Küste von Atacama, ermöglicht es, mit Präzision zu bestimmen, die Bereiche mit mehr oder weniger Präsenz, sowie ihre Saisonalität und tägliche Zyklen (horizontal und vertikal). Dieses Ergebnis ist von Bedeutung, da die räumlich-zeitlichen Veränderungen der Nebelbewölkung es ermöglichen, sie mit den jüngsten räumlichen Veränderungen in den nebelabhängigen Ökosystemen zu verknüpfen, um den bestehenden Zusammenhang zwischen Atmosphäre und Biosphäre besser zu verstehen, der für die Kenntnis vergangener und zukünftiger Klimaänderungen entscheidend sein kann. Ebenso sollen Standorte mit größeren Eignungen für die Sammlung von Nebelwasser sowie für die zukünftige Nebelernte in einer Region ermittelt werden, in der der wachsende Bedarf an Wasserressourcen alternative und nachhaltige Quellen erfordert

Table of Contents

List of abbreviations

CB: Cloud base

CD: Cloud depth

CT: Cloud top

DGA: Dirección General de Aguas (General Direction of Water)

DMC: Dirección Meteorológica de Chile (Meteorological Direction of Chile)

ENSO: El Niño Oceanic Oscillation

FFP: Fog frequency presence

FLC: Fog and Low Clouds (FLCs)

GOES: Geostationary Operational Environmental Satellite

GOFOS: Ground-based Optical Fog Observation System

IPO: Interdecadal Pacific Oscillation

LTS: Low tropospheric stability

LWC: liquid water content

m a.s.l.: Meters above Sea Level

MBL: Marine boundary layer

MODIS: Moderate Resolution Imaging Spectroradiometer

ND: No data

NOAA: National Oceanic and Atmospheric Administration

ONI: Oceanic Niño Index

PDO: Pacific Decadal Oscillation

PUC: Pontificia Universidad Católica de Chile

Sc: Stratocumulus

SD: Standard Deviation

SEP: Southeast Pacific

SEPA: Southeast Pacific anticyclone

SFC: Standard Fog Collector

SST: Sea surface temperature

WCT: Weather and Climate Toolkit

θ: Potential temperature

q: Specific humidity

List of Figures

List of Tables

1 Introduction

Located along the western territories of the Andes Cordillera, from southern Perú to northern Chile, is one of the oldest and driest deserts on Earth: The Atacama Desert (Clarke, 2006:108; Hartley et al., 2005:422). This desert is well known for its arid and hyper-arid conditions. Its extreme climate has existed for at least 10 million years (Armijo et al., 2015:25; Jordan et al., 2014:1038). Within the Atacama there exists an ecosystem that is highly specialized/adapted to survive in conditions of scarce water availability (Latorre et al., 2011). This desert is also home to various human societies, with a long history of occupying and interacting with this exceptionally arid environment (Calogero et al., 2017:29; Latorre et al., 2013:20; Escobar & García, 2017:13; McRostie et al., 2017:7).

At present, the extreme aridity and nearly non-existent precipitation in the Atacama (e.g., in Iquique - 20°32' S, 70°10' W – average annual rainfall is 0.6 mm, DMC, 2017), means water resources are limited and expensive to access (Oyarzún & Oyarzún, 2011:266), making water a major social and economic issue in the region (Alonso, 2001). Additionally, over the next 15 years the Chilean General Water Direction (DGA, 2017:19) has projected the following increases in demand for water in the region: an 80% increase from the mining industry, a 14% increase for the sanitation sector, and a 100% from non-mining industries. This increased demand will most likely be met through desalinization of seawater, which poses high environmental and economic costs that have yet to be fully assessed, or through the use of groundwater resources; however, in the case of groundwater, the extraction rate is higher than the natural recharge rate (Rojas & Dassargues, 2007:547; CIDERH, 2013). Currently, the intensive use of existing water sources, coupled with climatic variations in recent decades, are putting at risk diverse fragile ecosystems, rich in biodiversity and endemism, primarily due to variations in their water inputs, which may be leading them to a state of extreme vulnerability (Schulz et al., 2011b; Muñoz-Schick et al. 2001; Pinto 2006; Romero et al., 2012). Moreover, a very small portion of the Atacama Desert is protected by the state of Chile (Pauchard & Villarroel, 2002:323), with no protected areas along the coast north of latitude ~26° S.

Conversely, one of the main components of the climate in the southeast Pacific (SEP) Ocean is stratocumulus (Sc) clouds, which cover a wide area of this subtropical region. Here, on the one hand there exists cold sea surface temperatures (SST), enhanced by the Humboldt

current and upwelling of cold waters, and on the other hand, a dry and warm air aloft, generating a persistent thermal inversion layer capping the marine moisture, which under certain atmospheric well-mixed conditions condense into small droplets and form a cloud, developing a widespread low-cloud deck (Cereceda et al., 2002; Garreaud et al, 2008a; Lobos et al., 2018). When this extensive Sc cloud deck meets the coastal Cordillera of coastal Atacama, it produces a highly dynamic advective marine fog, locally referred to as *Camanchaca*. This fog is a major feature of the local climate that provides humidity and freshwater to the hyper-arid environment. Therefore, there is an expansive one along the coastal Atacama where the consistent presence of fog presents a potential alternative water source to its regular atmospheric water income, in the form of fog water (Cereceda et al., 2008a:314; Larraín et al., 2002:277; del Río et al., 2018:127). The fog and low clouds (FLCs) extend from the base of the thermal inversion layer (the top of the cloud deck), which fluctuates both daily and seasonally, spanning an altitudinal range that regularly moves from 1.200 m to 500 or 600 m a.s.l., the lowest altitude covered by the cloud base (Cereceda et al., 2008b:320; Garreaud et al., 2008a:5). At a local scale, topographic features such as hillslope, aspect, altitude and ground morphology control fog presence, distribution and liquid water content within the Coastal Cordillera (Osses et al., 1998; Cereceda et al., 2002; Osses et al., 2007). The FLCs cover the Coastal Cordillera for about 25 km inland, and even occasionally penetrates topographic corridors for up to 50 km reaching the Atacama steppe (called the *Pampa*) (Farías et al., 2005:57). Thus, this fog belt over the coastal Atacama represents an area with high potential for fog water collection; in turn, this water has a diversity of potential uses, such as: human consumption and low-scale economic activities. Thus, a better understanding of the spatiotemporal variability of this fog belt is necessary in order to assess the feasibility and sustainability of water collection over time.

Nonetheless, despite clear links between regional Sc cloud cover, SSTs, the strength and position of the subtropical Anticyclone and the Atacama fog bank and its water content (Garreaud et al., 2008a), current knowledge on the dynamics of fog climate in the coastal Atacama is still lacking. For example, still lack a basic understanding of the long-term spatiotemporal dynamics of this extensive coastal cloud deck, how climate change is affecting it today and how it will change in the near future. Since understanding of cloud variability over the coastal Atacama provides insight into the regional tropical Pacific atmospheric-ocean system, and therefore the potential of fog water as an alternative

resource, as well as the long-term climate controls on the Atacama coastal biodiversity (Garreaud et al. 2008a), these are vital questions to understand.

At the same time, it is known that the inter-annual variability of the SEP climate is primarily controlled by the El Niño Southern Oscillation (ENSO), which is linked to SST and intensity changes in anticyclone air-subsidence (Ortlieb et al., 1995), which in turn seems to exert a direct influence on FLC frequency presence (del Río et al., 2018; Garreaud et al., 2008). Furthermore, over the last decades in the SEP, an intensification of the anticyclone, associated with the regional prevalence of the negative phase of ENSO (La Niña) (Muñoz et al., 2016; Schulz et al., 2011a) has been observed, during this phase air mass subsidence is stronger causing the thermal inversion layer to occur at lower altitudes, and at the same time, there are colder than usual sea surface and air temperatures. This phenomenon may be generating spatial variations in fog distribution, a factor that has not been previously considered in the study of fog climate, fog water content or the potential to collect fog water.

The complex oceanic-atmospheric and land interaction that give life to the dynamic coastal FLCs and the related fog phenomena along the coastal Atacama Desert beside with its tendencies and variability in the recent past, open a series of questions, including: what will be in the impact of changing climate conditions, which are increased due to the fact that climate model projections for the coastal Atacama do not reflect the recent cooling (Falvey & Garreaud, 2009:2), on factors that influence cloud cover? And will climate change lead to greater uncertainty in cloud cover in the Atacama? A time series analysis of the spatial and temporal variability of the presence of FLCs under different ENSO scenarios, and thereby different oceanic-atmospheric conditions, allows us to assess the factors involved in the spatiotemporal variability of FLCs, and thus provide a first approximation of what may be expected in the future given the manifestation of a particular ENSO phase. Whether global warming or natural oceanic-atmospheric interactions within the SEP, such as ENSO or the cyclic Pacific decadal oscillation (PDO), are the responsible for changes in the formation, tendencies and spatiotemporal variability of FLCs over the last decade is still an open question. Thus, there is a need to analyze FLC cover carefully from the regional to the local scale, including a spatiotemporal dimension.

Hence, the main scientific questions guiding this research are as follows: What are the frequency presence trends of fog and low clouds? Is the spatiotemporal distribution of fog

and low clouds changing? Does inter-annual variability in ENSO affect Atacama fog presence? Does the presence of fog and low clouds offshore and along the coast have the same spatiotemporal response to sea surface temperatures anomalies? Is there any relationship between the quantity of fog and low clouds and the altitude of the thermal inversion layer? At the local scale, what are the basic atmospheric conditions necessary for fog presence? Does the daily presence of fog and low clouds and its seasonal and daily cycles relate to the thickness of the cloud? Does fog decrease at higher altitudes during the last decades?

The overall goal of this research is to determine and characterize the past, present and future spatiotemporal variability of coastal fog and low clouds, under climate change conditions, from 1995 – 2017 along the coast of the Atacama Desert. To address the various research questions, two interrelated scales have been approached, regional and local. The research has five strongly interconnected goals, differentiated by scale. Goals for the regional-scale analysis are: (1) to characterize and analyze the spatiotemporal distribution of fog and low clouds within the study period, determining their tendencies and variability; (2) to assess and analyze the role of SST along the Atacama coast on the presence of coastal fog and low clouds; and (3) to evaluate the relationship between inter-annual variability in FLCs and ENSO anomalies. Goals for the local-scale analysis are: (4) to describe and contrast the fog cycle and spatial parameters of its altitude and thickness with local atmospheric variables and indices; (5) to assess if spatiotemporal variability in fog is closely related to the regional oceanic-atmospheric realm or is more closely linked to local factors, such as temperature, humidity, wind and topography.

Thus, the present research hopes to contribute to an enhanced understanding of the horizontal and vertical spatiotemporal distribution and variability of FLCs in coastal Atacama, as well as ocean-atmosphere-land interactions involved in FLC presence. It is hoped that the findings on the behavior of FLCs in the recent past can be used to model and predict FLC presence for the present and future given predicted changes in climate in region. Understanding where fog will for, and in what quantities, for the present and future is key to assess the feasibility of harnessing fog as an alternative water supply in an extremely fragile environment with an increasing population that is searching for sustainable alternatives to their current water resources.

To accomplish these goals, multi-scale geographic and statistical analyses were applied, including the use of satellite remote sensing techniques and *in situ* observations and measurements. Here first it is compare over 20 years of continuous satellite data on FLCs and SSTs. Both datasets are contrasted with local and regional atmospheric and oceanographic variables and indices in order to assess the main factors influencing in the inter-annual dynamics of FLCs in northern coastal Chile. Second, local measurements from the Iquique airport are contrasted with an instrumental network, which includes high quality weather stations and a new developed method for fog monitoring (Ground-based Optical Fog Observation System: GOFOS; a system of LED solar lights and time-lapse cameras), installed in the Coastal Cordillera. Local analysis allows us to understand the spatiotemporal variability of FLCs, as well as the basic atmospheric conditions within the marine boundary layer (MBL) necessary for the presence of FLCs. Finally, an integrated scale-analysis was conducted for a specific period of time (February and September 2017), in order to better understand the factors influencing FLC spatiotemporal variability at both a regional and local scale.

2 State of the Art

A complete bibliographic review was carried out. The topics reviewed are presented in the same order as the research goals, moving from a regional to a local scale. Here is presented a synthesis of stratocumulus clouds and the oceanic-atmospheric interactions involved in their formation and variability. Next, it is presented a summary of coastal FLCs, their cycles and variability, and finally, a specific review of fog research in Chile with an emphasis on the fog climatology of the coastal Atacama Desert.

2.1 The stratocumulus cloud

The stratocumulus (Sc) cloud is the most common cloud type on Earth; these clouds exist primarily above the oceans, with a base height that does not exceed 2.000 m a.s.l. They are compact clouds of water with gray to whitish tonality, whose cloudy banks always present shadows and dark parts; they are composed of small water droplets and rarely produce precipitation (AMS, 2018). They are defined as a low-cloud system whose main dynamism is due to convective instability as a result of radiative cooling. Their layered form is composed of an aggregation of individual convections that together form the stratus (Wood, 2012: 2374). Fig. 1 shows the main dynamism and processes typical of an Sc cloud capped by a thermal inversion layer. Formation of Sc clouds primarily occurs when there is stability in the lower troposphere, which is linked to strong subsidence; therefore, their formation is controlled by large-scale meteorological elements. In other words, their formation and presence are closely related to the general circulation of the atmosphere (Albrecht et al., 1988; Klein and Hartmann, 1993; Wood 2012).

Stable lower-tropospheric conditions imply a sharp thermal difference between the top of the cloud and the layer immediately above; these differences can be as strong as 10 to 20 K (Roach et al., 1982). Long-wave cooling in the upper portion of the cloud is the main driver of turbulence within the MBL; such turbulence is necessary to achieve a well-mixed regime condition favoring cloud formation (Bretherton and Wyant, 1997; Duynkerke et al., 1995; Wood, 2012). Surface buoyancy fluxes are another driver that increase convection within the MBL, but their influence is significantly reduced (Duynkerke et al., 1995). Klein and Hartmann (1993) demonstrated, using linear regressions, that 61% of variances low-cloud cover can be explained by low-tropospheric stability (LTS) and 39% can be explained by the

variations in surface air temperatures, which are associated with the SSTs; thus, they concluded that variations in low-cloud cover are more closely related to variations in LTS than variations in SST. Similar results were obtained by Seethala et al (2015), who used a multi regression approach to show that SSTs have the smallest independent effect on predicted cloud trends in relation to thermal inversion force indicators.

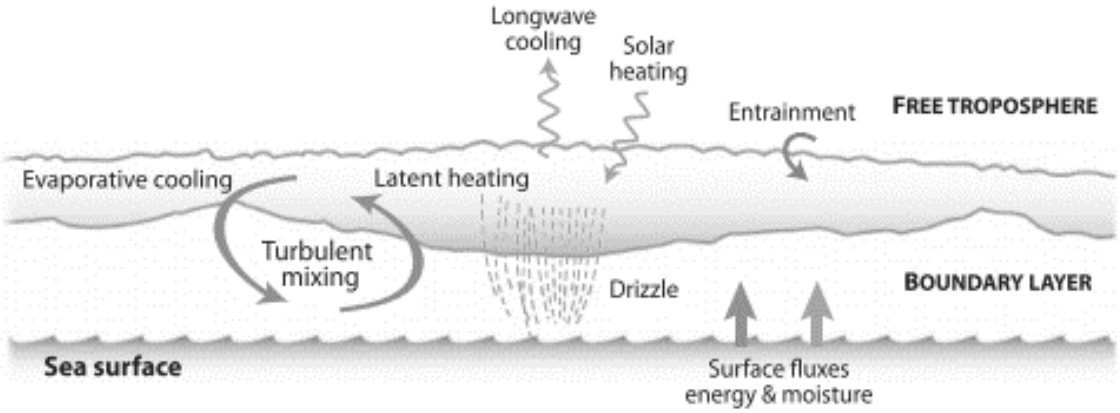

Figure 1: Schema of the main processes present in the marine boundary layer in presence of a stratocumulus cloud (Source: Wood 2012: 2375).

Conversely, in the case of a weak thermal inversion layer (reduced LTS), the marine layer tends to be deeper, producing a decoupling and stratification within the MBL, which in turn allows dry air to enter from the free troposphere, thus drying the marine layer (Bretherton and Wyant., 1997; Bretherton et al., 2010). It has been well described that the main factors necessary for the presence of Sc are subsidence and LTS. In areas with greater subsidence there is a greater presence of Sc, and when there is lesser subsidence there is less Sc cover. Subsidence is closely linked to LTS, and therefore the strength of the thermal inversion layer; thus, greater stability and increased strength of the thermal inversion are related to greater presence of Sc, whereas less stability and less strength of the thermal inversion is related to a lower presence of Sc. In addition, SST is also related to subsidence and LTS, in that cooler SSTs show a relation with higher subsidence and higher LTS, and vice-versa with warmer SST (Bretherton and Wyant 1997). Consequently, cooler SSTs are related to higher Sc presence and warmer SSTs are related to lower Sc presence (Norris and Leovy 1994). Sc cover over the oceans occurs primarily along the eastern boundary of the subtropical regions, since these areas combine both cold SSTs and the subsidence of air linked to high pressure, forming a thermic inversion layer that captures a cold and humid MBL.

On the other hand, Sc clouds capped by the thermal inversion layer occur under a well-mixed regime, which present a vertical structure within the MBL, where the temperature follows the moist adiabatic within the cloud layer, and a near–dry adiabatic lapse rate below cloud. At the same time, the equivalent potential temperature and the total water mixture ratio are practically constant with height (Stull, 1988). In addition, the liquid water content within the Sc cloud increases in a nearly linear relationship with altitude, and is a little lower than the adiabatic value. In turn, the droplet concentration varies minimally with height. In this sense, the deeper the MBL, the larger the drop (Duynkerke et al., 1995; Wood, 2012). The schematic vertical profiles are illustrated in Fig. 2.

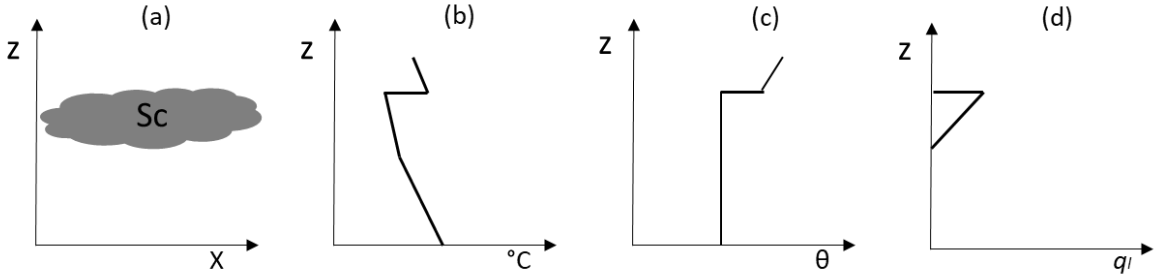

Figure 2: Schematic vertical profiles of a Sc cloud capped by a thermal inversion layer, a) Sc location, b) temperature, c) potential temperature, and d) liquid water mixing ratios (Source: Adapted from Stull 1988).

2.1.1 Stratocumulus cloud variability

Sc clouds located over the oceans have a well-known and pronounced seasonal cycle, which is highly determined by LTS (Klein & Hartmann, 1993). Seasonality is determined by an annual shift in large-scale air subsidence, and in turn, in related changes in SSTs, which contribute to LTS. In the subtropical zones, the large Sc clouds of the southern hemisphere have a wider oscillation compared to those of the northern hemisphere, as they peak earlier in the season and have a larger extent, up to a few hundred kilometers in favor of the wind (Wood, 2012). The asymmetry between the hemispheres is related to greater orographic forcing as a result of the high altitudes present in the continents (Richter & Mechoso, 2006). On a daily scale, Sc clouds also show a pronounced cycle, given the influence of solar radiation on their formation process. During the day there is higher cloud fragmentation due to the absorption of solar radiation, which warms the cloud and partially compensates for long-wave cooling, therefore partially weakening turbulence within the MBL. On the other

hand, the maximum Sc presence usually occurs at dawn, when long-wave thermal cooling is at its extreme and acts as a turbulence enhancer (Klein & Hartmann, 1993; Wood 2012). In addition, Rozendaal et al (1995), found that the largest daily oscillations in both hemispheres occur in summer, which is linked higher winds which favor a deeper MBL. While there have been few studies on an inter-annual scale, variation in Sc clouds (Wood, 2012) is closely related to the LTS (Klein and Hartmann, 1993), just as in the other time scales. On the other hand, since the LTS is connected with SSTs, inter-annual variations in SST are inversely correlated with Sc presence (Park & Leovy, 2004). Klein et al (1995), demonstrated this inverse connection for the northeast Pacific during summertime, which is particularly true in the areas of transition from Sc to cumulus, which mainly occur in offshore areas (Norris & Leovy 1994). In this sense, at inter-annual temporal scales, the El Niño Southern Oscillation (ENSO) is known to exert control on the Pacific climate, and is linked with an intensification in air-subsidence and changes in SSTs; therefore, anomalies in SST linked to ENSO affect inter-annual differences in Sc cover. In addition, Park & Leovy (2004), suggest that they are also linked to mid latitude storm-track teleconnections that affect the advection of temperature.

2.1.2 The southeast Pacific stratocumulus cloud

In the Southeast Pacific (SEP) Ocean, the Humboldt current and upwelling along the western coast of South America cool SSTs. Additionally, the Hadley circulation creates large-scale quasi-permanent subsidence and in connection with southeast Pacific anticyclone (SEPA) generate a stable thermal inversion layer, capping the moisture within the MBL and forming a regular Sc cloud deck with an extent of more than 2.000 km, stretching from southern Equator to central Chile (25°-30°S) (Bretherton et al. 2010; Klein & Hartmann, 1993) (see Fig. 3). Due to its relevance in the global radiation balance and its influence on the global climate, understanding this cloud deck has been the aim of several investigations (Randall et al., 1984; Hartmann et al., 1992; Rozendaal et al.,1995; Wood, 2012). The SEP Sc deck has high seasonal variation in its latitude, reaching its northernmost extent in the austral winter, off the coast of Peru, and its southernmost extent in the austral summer, off the northern coast of Chile (20°-25° S) (Painemal & Zuidema, 2009). The Sc frequency is slightly lower when it moves to the southern latitudes during the austral summer (Garreaud et al., 2007).

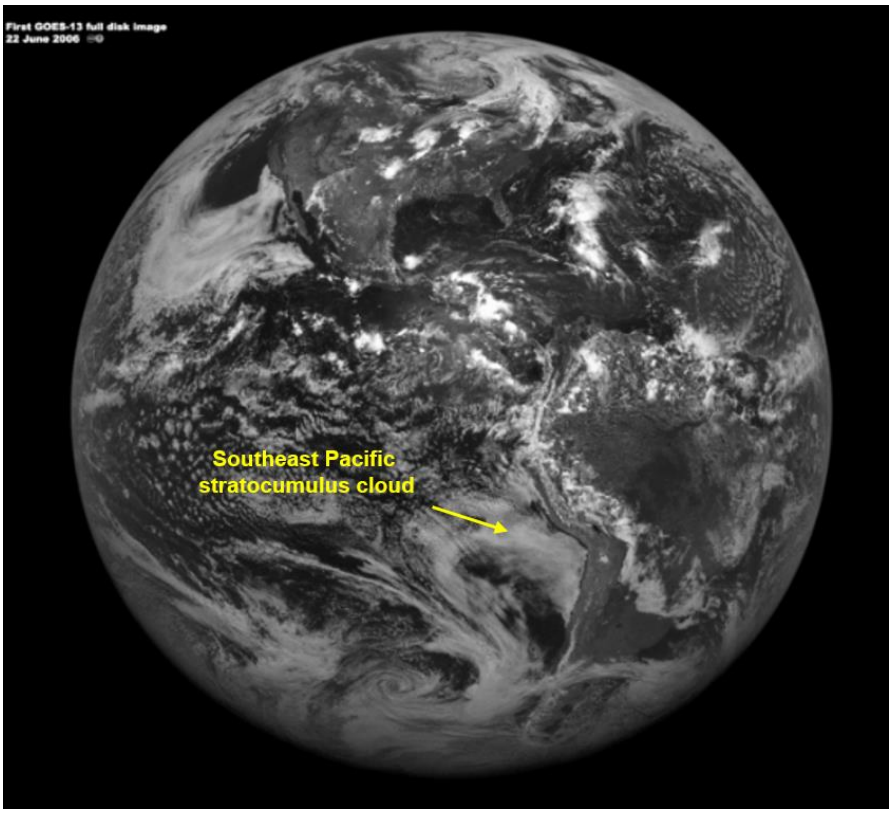

Figure 3: GOES-13 daily image over the eastern part of the Pacific basin (GOES: geostationary satellite; Source: NOAA, www.class.ngdc.noaa.gov).

In the last few decades many notable projects have been conducted aimed at understanding the SEP Sc cloud, due to a lack of information on its structure and microphysics in relation to other Sc clouds. The East Pacific Investigation of Climate (EPIC), carried out a research cruise from coast to open sea in 2001, followed by others in 2003 and 2004, complemented by satellite observations and buoy datasets (Serpetzoglou et al., 2008). An international research program, the VAMOS Ocean-Cloud-Atmosphere-Land Study Regional Experiment (VOCALS-REx), has been the largest project focused on a better understanding of ocean-atmosphere-land interactions within the SEP (Garreaud et al., 2011). Ship and aircraft campaigns in southern Peru and northern Chile, from coast to open sea (~1.500 km offshore), characterized the structure and the physical process within the first 3.000 m of the atmosphere and therefore the MBL and the free troposphere above it. In October 2008, their work along the parallel 20° S (latitude of Iquique) characterized the depth of the MBL, demonstrating an increase from coast to open sea, from the 1.000 m a.s.l. in the coastal area to about 1.200 meters a few kilometers offshore, followed by an increase, with minor variations, to a depth that can exceed the 1.600 m a.s.l. in the open sea (Bretherton et al., 2010). In the same transect, from coast to open sea, in the coastal areas the troposphere

stability is greater, but high daily influences from land-ocean thermodynamic fluxes make it more variable (Rutllant et al., 2003); then in the nearshore areas the thermal inversion is strong and the MBL is usually shows well mixed conditions. Towards offshore, the inversion layer is less strong and the MBL tends to get deeper, in this condition it is typical that the vertical structure of the MBL shows stratification (Seethala et al., 2015), resulting in a decoupling between 500 m and 1.000 m, separating the moisture source from the condensation zone. In addition, the weakening of the thermal inversion generates the entry of dry air from the free troposphere, drying the MBL, thus higher cloud fragmentation leads to no Sc cloud formation (Bretherton et al., 2010). Droplet concentration is higher near the coast (250 cm^{-3}) and decreases offshore (100 cm^{-3}). Thus drizzle is rare on the coast, and its frequency increases over the open sea; however, it rarely reaches the surface, as it evaporates beforehand (Serpetzoglou et al., 2008; Bretherton et al., 2010).

2.2 Coastal fog and low clouds in the Atacama Desert

2.2.1 Fog and fog types

Fog can be defined either by its geographical or physical attributes. The geographical definition of fog, is that it reduces visibility under 1 km (Roach, 1994); such reduced visibility occurs due to the location of FLSs, that is when a cloud comes in contact with the Earth's surface (Bendix et al., 2005). The second definition, related to the physical attributes of fog, is "water droplets suspended in the atmosphere in the vicinity the Earth's surface that affect visibility" (AMS, 2018). Here, despite, the fact that visibility and location are also part of the definition, they are not the primary criteria for defining fog, but rather a consequence (Cermark, 2007). Therefore, fog differs from clouds only in that fog is in contact with the Earth's surface, while clouds exist above the surface (AMS, 2018). Water droplets of fog are characterized by their small size, with a possible radius of 1 – 40 µm, but more typically between 10 – 20 µm (Roach, 1994).

Extensive low Sc clouds over southeastern boundary of the SEP are horizontally transported by prevailing winds from the south – southwest (S-SW) towards the coast of the Atacama Desert. When they reach the coast, low Sc clouds first covers the thin coastal plain and then meet a prominent coastal mountain range, where a dense fog belt forms, called advective

marine fog (see Fig. 4), the most common type of fog in the coastal Atacama (Cereceda et al., 2002).

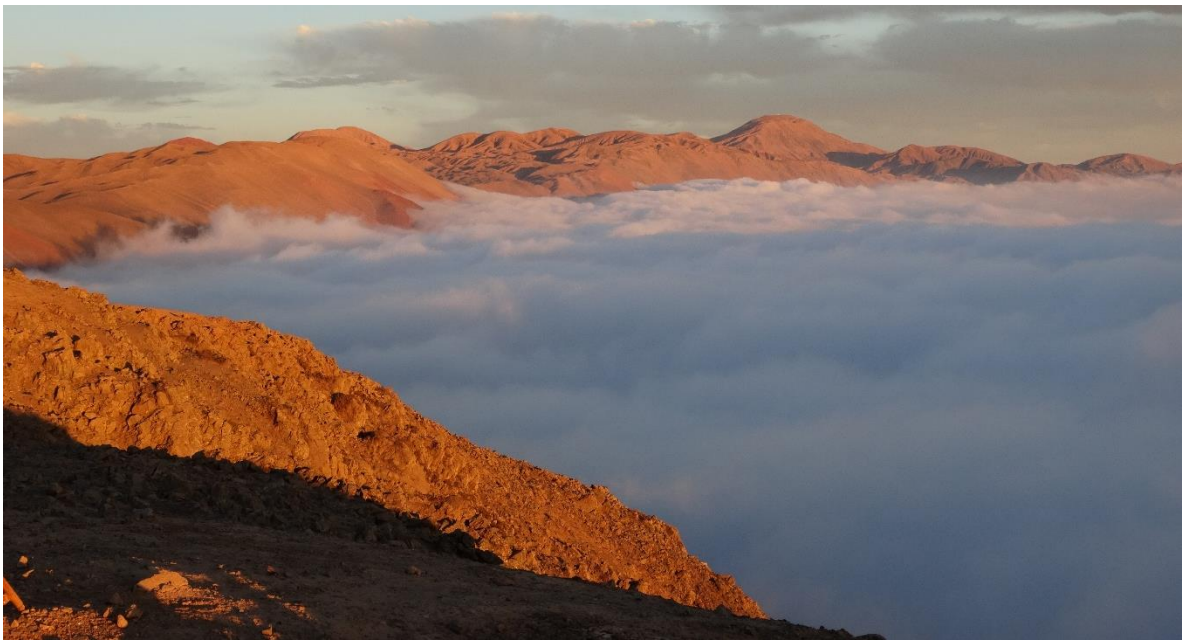

Figure 4: Advective marine fog meets the prominent Coastal Cordillera at sunset in the Atacama Desert (~20° S) (August 2016).

Orographic fog, produced by the cooling and condensation of air masses that rise abruptly in elevation due to relief of the landscape (see Fig. 5), is is also common over the coastal cliffs in the Atacama. Formation of orographic fog primarily occurs areas where the coastline and the coastal cliffs have a southwest orientation, opposite the predominant wind direction. These areas are also characterized by rich fog ecosystems, called fog oases; examples of these oases include: Alto Patache, Punta Gruesa and Punta Chipana, among others (Cereceda et al., 2002). A third type of fog, radiation fog, is produced ~25 – 50 km inland from the coast. Radiation fog primarily forms at dawn due to the contact of the cold soil of the Pampas with humidity coming mainly from the ocean that enters through inland corridors (Cereceda et al., 2008a).

Figure 5: Orographic fog over Alto Patache (~20° S) (Source: Larraín, H.; http://eco-antropologia.blogspot.com).

2.2.2 Fog's Seasonal and daily cycles

Seasonal fog cycles are determined by regional factors, such as annual shifts in SEPA and changes in SSTs. On the other hand, daily fog cycles are primarily determined by local factors, such as ocean-land flows of their thermal interactions. In terms of seasonal cycles, during winter and spring, colder SSTs and warmer air above the thermal inversion layer generate a stronger temperature inversion, resulting in better conditions for cloud development. During summer and early autumn, a higher and weaker thermal inversion layer allows thermal interactions between the MBL and the dry air above (Garreaud et al., 2007; Cereceda et al., 2008a). The daily cycle is strongly influenced by local onshore – offshore air exchanges, with cloud cover peaking during the night, sunset and early morning due to low atmospheric temperatures, whereas mid-day solar radiation dissipates the fog bank (Rutllant et al., 2003; Garreaud and Muñoz, 2004; Cereceda et al., 2008a; Muñoz et al., 2011).

Based on data from geostationary satellite (GOES) images taken in the 2001 and 2002, Farías et al (2005) described the spatial distribution of FLCs in coastal Atacama for both summer and winter months, identifying for the first time areas with the greatest frequency of FLC presence, as well as the corridors through which fog moves inland, such corridors are

typically valleys of low altitude. The authors also characterized the daily fog cycle of the 3 different types of fog defined above. Fog was characterized based on the frequency and presence (%) of each fog type during the period from June 2001 to May 2002 (see Fig. 6).

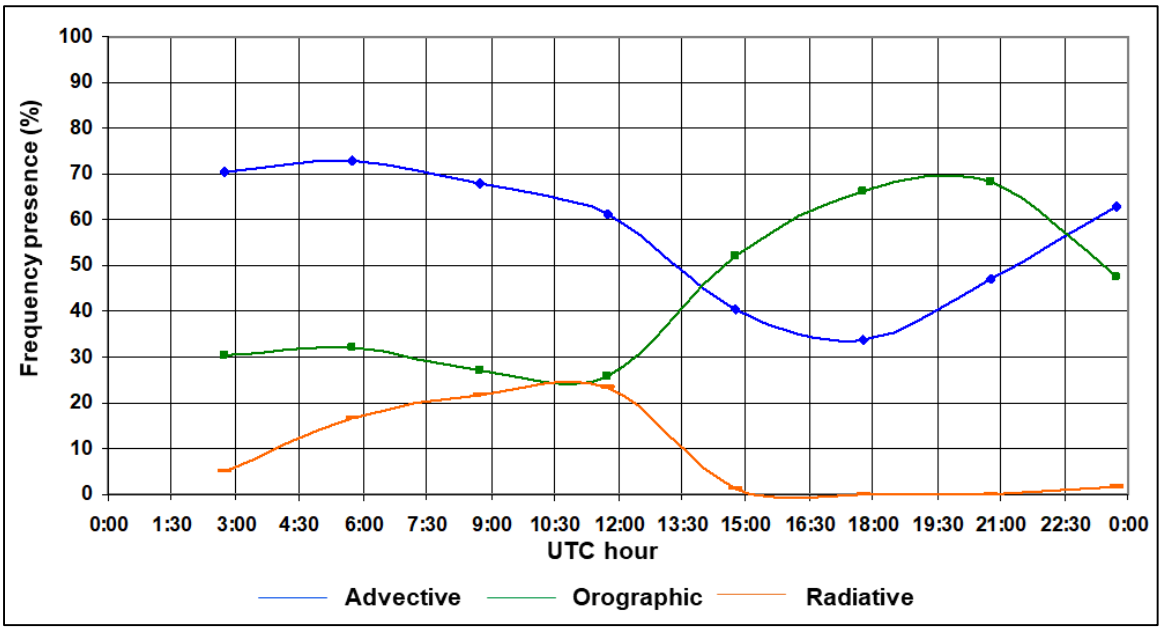

Figure 6: Types of fog and their average daily cycle along the coast of the Atacama Desert for the period from June 2001 to May 2002 (Source: Farías, 2006:9).

At the local scale, topographic features control fog distribution, such as hillslope, aspect, altitude and ground morphology (Marzol, 2002; Marzol & Sánchez, 2008; Osses et al., 2007). These variables have been studied primarily with the aim of determining the spatial distribution of fog for the purpose of exploiting it as a water resource.

2.2.3 Inter-annual and inter-decadal variations in fog

Is well known that at inter-annual and inter-decadal time scales the ENSO, the PDO (Mantua et al., 1997) and the Interdecadal Pacific Oscillation (IPO) (Power et al., 1999) exert control on the SEP climate, specifically they affect the intensity of anticyclone air-subsidence and changes in SSTs (Garreaud et al., 2008b; Muñoz et al., 2016; Schulz et al., 2011a). In the case of ENSO, while El Niño years bring precipitation, La Niña years enhance arid conditions in the Atacama (Ortlieb, 1995). The implications of ENSO on the presence of Sc clouds and fog are not completely clear. For instance, del Río et al (2018) showed higher fog presence and fog water yields during summer for extreme El Niño years in the hyper-arid region (~20°

S); however, the opposite occurred in the semiarid region (~30° S), with higher fog presence during spring in La Niña years (Garreaud et al., 2008a). On the other hand, links between ENSO and variability in fog presence have primarily been studied on the basis of their relationship with fog ecosystems. Beresford-Jones et al (2015) combined vegetation and archeological surveys with reconstructions of SST for southern Peru and found millennial periods (between 8000 - 4500 BP) of abundant *lomas* vegetation and marine ecosystems that they relate with ENSO-linked colder SST. In the same manner, Latorre et al (2011) demonstrated sub-millennial variability in *Tillandsia landbeckii* ecosystem is linked to local environmental shifts (e.g., advective fog ENSO variations), based on radiocarbon and stable isotopes. This latter work underlines the sensitivity of fog ecosystems to climate variability and their relevance as bio-indicators of past and present changes in FLCs. Manrique et al (2010) discussed the effects of ENSO on fog oases of coastal Peru and Chile over the last few decades; they found contradictory results in terms of the ENSO phase effects, as the higher amount of fog and its potential water input during La Niña years could have a counterpart with rains or drizzle associated to El Niño years.

On an inter-decadal timescale, there has been an intensification of La Niña years (negative PDO phase) over the last decades. This has resulted in conditions associated with cooler sea-surface and air temperatures within the MBL and intensification of the SEPA (Muñoz et al., 2016), thus generating atmospheric stability and stratification of air masses, creating a thermal inversion layer that is difficult to brake. These conditions are presumably more favorable to fog formation along the northern coast of Chile. Based on contrasting meteorological observations (including precipitation, temperature and cloud cover) with the IPO index, Schulz et al. (2011a, 2011b) assume an intensification of aridity and a probable impoverishment of the fog ecosystems since the mid-20th century. Although this trend could be related to inter-annual and inter-decadal variability in climate (Montecinos et al. 2000, Montecinos & Aceituno, 2003; Rutllant et al. 2003; Parker et al. 2007), for instance, linked to reorganization in ENSO oceanographic-atmospheric circulation, Schulz's (2011b) conclusion agrees well with the idea that *Tillandsia spp.* are sensitive to regional climate changes at various time scales.

Also linked to the negative PDO and its corresponding SEPA intensification, is higher subsidence of warm air, which has over the last decade produced a continuous negative trend in the altitude of the thermal inversion layer; altitude has been decreasing by an order

of 100 m per decade, resulting in decreased depth of the MBL (Muñoz et al., 2016). This could be generating variations in cloud thickness, which has not been duly studied. Lack of knowledge on the cloud thickness is even greater for related fog clouds, where there is a complete absence of sensors along the Coastal Cordillera and limited knowledge as to the role that local factors, such as wind speed and topography, play. As cloud depth is intimately linked to the ground area covered by the fog, its temporal variation reveals that there are areas that will in the future be regularly outside of the fog belt and other new areas that will be hit by the cloud.

The influence of the PDO on fog has been studied in other arid subtropical areas, including California, where Witiw & LaDochy (2008) and LaDochy & Witiw (2012) discuss the possible causes of a reduction in the presence of dense fog. The authors found a strong relation between fog and PDO phases and incorporated the influence urban heat effects on fog dissipation.

For the coastal Atacama, over the last decade various authors have analyzed the recent climatology and trends in the presence of FLCs using observations and measurements taken at airports located along the narrow coastal plain. For Iquique Muñoz et al (2016) showed there were no changes in low cloud cover during summer over the last 30 years; however, for winter and early spring FLCs showed a slight increase over this period. These trends are in accordance with Seethala et al (2015), who showed an increase in the annual average trend of low clouds in the SEP for the period 1984-2009 based on various satellite global model approximations. Despite this concordant results, this latter study should be interpreted with caution, as it focused mainly on low clouds over the oceans at a large scale, and does not necessarily capture the coastal-land influences. Conversely, Schulz et al (2011a) and Quintana & Berrios (2007), also using measurements taken at the Iquique airport, show negative trends in cloud cover; however, they applied different methodological approaches, with Schulz et al focused on particular hours of the day, and they used different definitions for low clouds. Nevertheless, these studied cover a longer period of time, including the 1970's, when there was a significant increase in low clouds, associated with a warm IPO phase, producing an expected decrease thereafter. However, there is coincidence that during the last 20 years the cold decadal phase of the Pacific (PDO and IPO) has predominated, which has generated a decrease in the thermal inversion layer

altitude, which has been estimated at about 100 m decade^{-1} for the period 1995-2010 according to Muñoz et al (2016).

2.2.4 Fog research in Chile

Fog research in Chile has a long history, with particular focus on its use as an alternative water resource in areas of desertic climates (Schemenauer & Cereceda, 1994; Cereceda & Schemenauer, 1997). Fog studies in the northern arid part of Chile have their origins in the 1980's and 1990's, mostly lead by the Pontificia Universidad Católica de Chile (PUC) and foreign partners. Since then, an increasing number of research projects have aimed to determine the geographic distribution of coastal fog (Farías et al., 2005; del Río et al., 2018), its potential as a water source (Larraín et al. 2002; Cereceda et al, 1999, 2008a), its relation with fog-dependent ecosystems (Garreaud et al., 2008a; Westbelt et al. 2009; Latorre et al., 2011; Pinto et al., 2006), and present-time physical attributes, such as climatology, water-content and cloud physics (Rutllant et al., 2003; Cereceda et al., 2008b; Muñoz et al., 2011; 2016; Lobos et al., 2018), among others.

In the field of fog water as an alternative water resource, various applied projects have been developed in northern Chile. For example, in the semiarid region of Coquimbo (~30°S) the El Tofo initiative was carried out to provide potable water to the fishing town of Chungungo. This project was sponsored by the International Development Research Center of Canada in the 1990's. More recently, the Peñablanca project, also in a semiarid region, conducted research to improve the efficacy of large (40 m^2) fog collectors in fighting desertification in the coastal dryland areas and in providing water to small farmers. In the arid Atacama Region (~26°S), the Falda Verde project was developed to reforest in the desert. In the hiper-arid region of Tarapacá (~20°S), the first Atacama Desert fog research station was launched in 1997 with the goal of studying the fog climate belt, fog-water resources, fog ecosystems and solar energy. The Fog Oasis Alto Patache station is located on a 1.114 hectares of public land 70 km south of the city of Iquique. This station is managed, under concession, by PUC. This station has been the center of fog research for in Chile for more than 20 years, resulting in a high impact on science, technology, education and conservation. Currently, the station contains a complete meteorological monitoring station, solar energy sensors and a number of fog collectors (both standard sized and large). Since 1997, monthly systematic measurements of fog water volume have been recorded. This

unique record is of significant scientific importance, as this time-span includes a range of ENSO (El Niño Southern Oscillation) variations that allows us for first time to conduct an integrated study of the coastal Atacama fog geo-ecosystem, considering the ocean (ENSO), the atmosphere (Sc) and its ecology (del Río et al., 2018).

3 Research concept and hypotheses

3.1 The research concept

The research has both a conceptual and methodological approach to the fog climate, which seeks to produce an enhanced understanding of the spatiotemporal distribution of fog and low clouds at a regional and local scale. At a regional scale, satellite data was processed in order to obtain estimates of FLC cover and SSTs, which are contrasted with different oceanic indices of SST anomalies. At a local scale, existing atmospheric datasets collected at the Iquique airport, together with two new weather stations, which collect and measure fog water using a Standard Fog Collector (SFC) as well as a new developed system for fog monitoring (GOFOS), which was developed within and for this study, were contrasted to characterize the temporal distribution of FLCs and to assess the atmospheric conditions needed for their presence and variability. In this manner, integration of the various variables analyzed here represent a novel method that interconnects the presence and variability of FLCs with regional and local geographic, oceanic and atmospheric variables, thus creating a model of coastal fog and its dynamics and sensitivity to recent past, present and future climate changes (see Fig. 7).

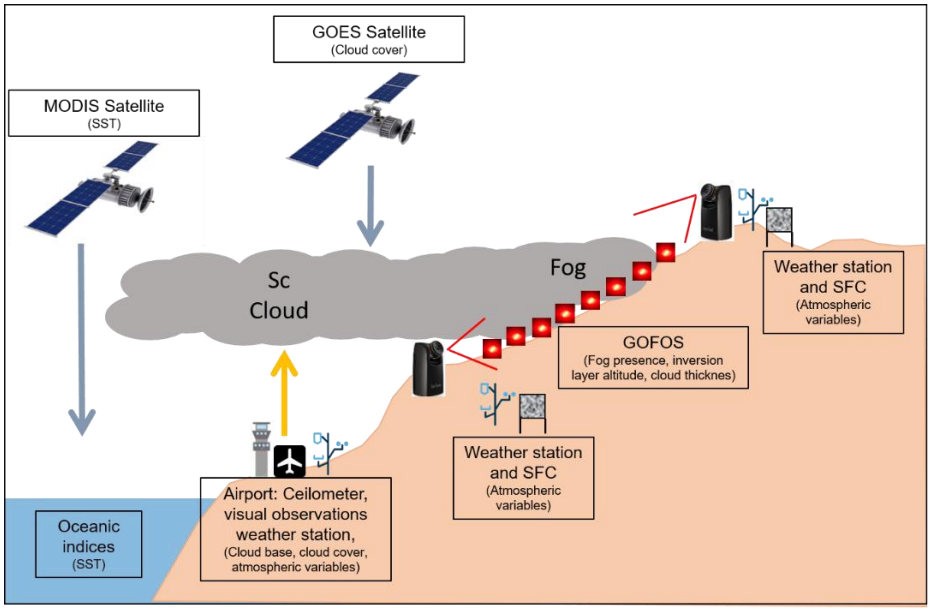

Figure 7: The multi-scale data sources and measurement systems for fog monitoring.

The methodological approach is organized according to the scale of analysis. Here it is presented and specified the different sources and datasets used, the respective workflow, processes and steps that were carried out in order to obtain the results for each stated objective. Fig. 8 shows the overall workflow of the research concept approach.

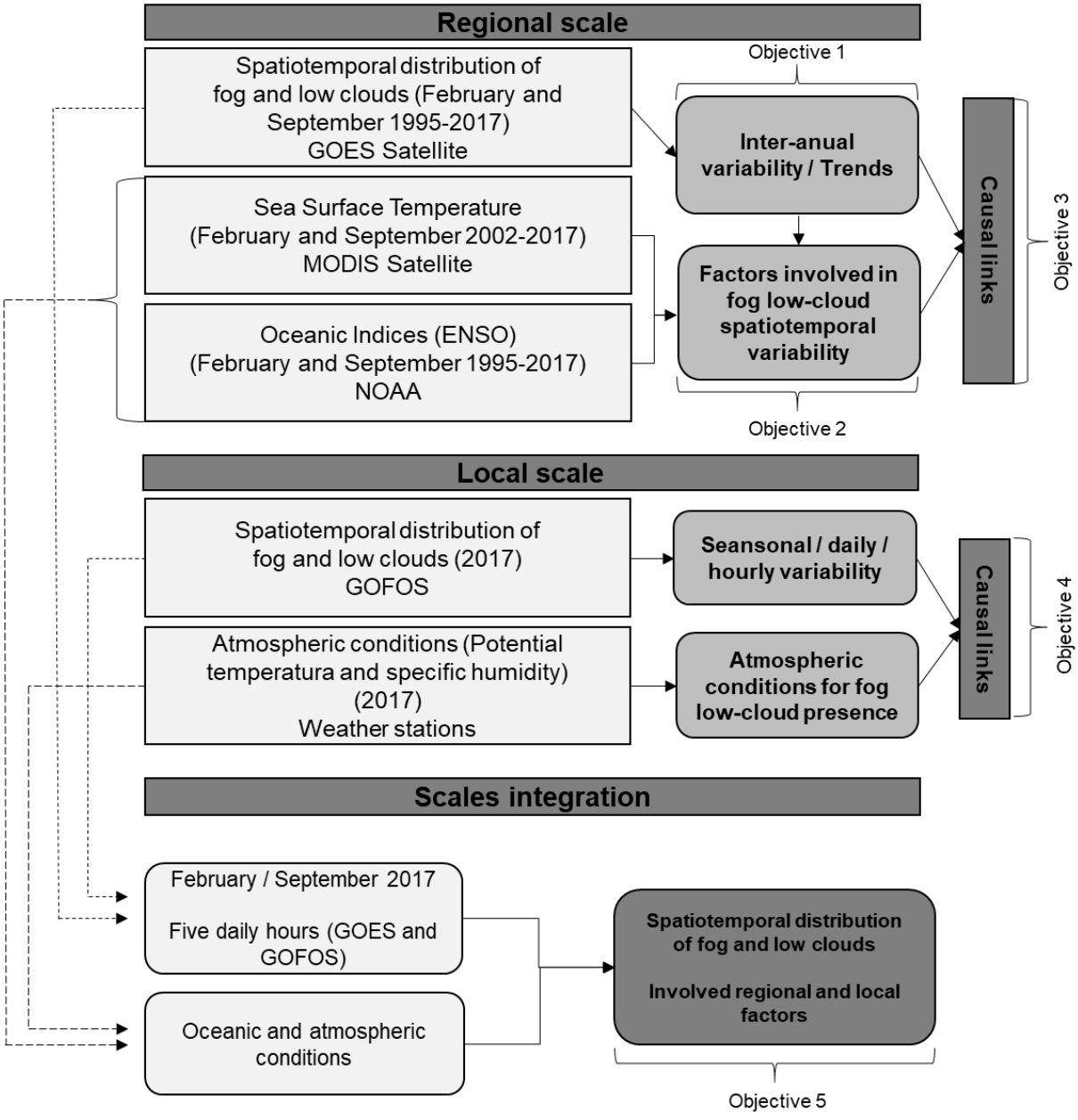

Figure 8: Integrative multi-scale research concept approach.

3.2 Hypotheses

Based on the state of the art and in concordance with the research concept and its scales of analysis, two hypotheses arise.

I. Over the last decades in the Southeast Pacific Ocean, an intensification of the anticyclone has been observed, associated with the prevalence of the regional El Niño southern oscillation (ENSO) negative phase (La Niña), which is associated with stable conditions within the low-troposphere, due to higher air mass subsidence, a strengthening of the thermal inversion layer and colder than normal sea surface temperature (SST). This phenomenon is changing the presence, distribution and variability of fog and low clouds (FLCs) in the coastal Atacama. If correct, it is expected that, given the prevailing oceanic-atmospheric conditions for the period 1995-2017, there should be positive (negative) trends in the presence of FLCs at lower (higher) altitudes in the coastal Atacama. In the same way, inter-annual variability will present a higher (lower) presence of low clouds during La Niña-like (El Niño-like) years.

II. In accordance with the annual shift in the Southeast Pacific anticyclone and the resulting increase in air subsidence in winter and decrease in summer for latitude 20°S, the altitude of the thermal inversion layer varies seasonally; however, its daily cycle is highly influenced by the ocean-land fluxes. In addition, the deep marine boundary layer is linked to a stratified regime, where the humidity at the ocean's surface fails to rise and condense forming the FLCs. Conversely, a shallower marine boundary layer is linked to a well-mixed regime, where turbulence allows humidity to homogeneously cover the boundary layer, favoring the formation of the FLCs. If correct, it is expected that seasonally and daily, a thermal inversion layer at higher (lower) altitudes will be related to lower (higher) fog frequencies, and in turn to clouds that have a greater (lesser) thickness, and the cloud base will be at a higher (lower) altitude

4 Study area. The coastal Atacama Desert

The present investigation focuses on the region from 19°S to 21°50´ S and from 71°W to 69°W, which corresponds in Chile administratively to the region of Tarapacá, and is representative of the hyper-arid section of the Atacama Desert in northern Chile. This area extends to around 90 km offshore and 100 km onshore (see Fig. 9).

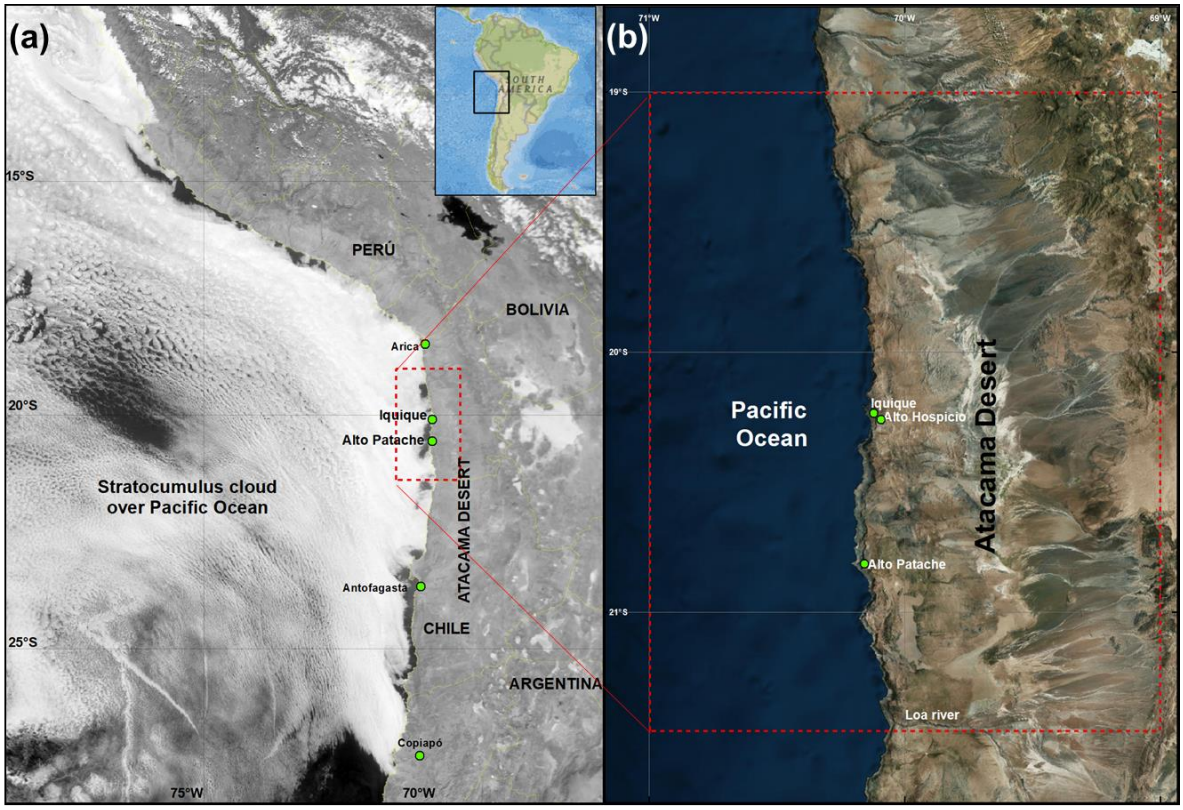

Figure 9: Geographical context of the Atacama Desert in relation to South America and northern Chile. (a) The stratocumulus deck over the Pacific Ocean and the coastal Atacama Desert, (b) The study area. Red dashed rectangle corresponds to the area analyzed by satellite to estimate the frequency of fog and low cloud.

The Atacama Desert is part of a belt of deserts located in subtropical regions of both hemispheres. It stands out among other deserts in the belt for being a macro region where aridity and hyper-aridity predominate. The particular conditions present in the Atacama correspond to a unique combination of climatic and geographical factors, determined by the quasi-permanent presence of the Southeast Pacific Anticyclone (SEPA) and its related air warming by subsidence, proper of the subtropical regions; the cold SSTs, which contribute to the development of a strong thermal inversion layer and the consequential impossibility

of convection of air masses and potential precipitation; and finally, the presence of a Coastal Cordillera that inhibits the inland penetration of oceanic moisture and the presence of the Andes Cordillera that acts as a natural barrier limiting the entry of moisture from the Amazon basin (Falvey & Garreaud, 2009; Schulz et al. 2011a).

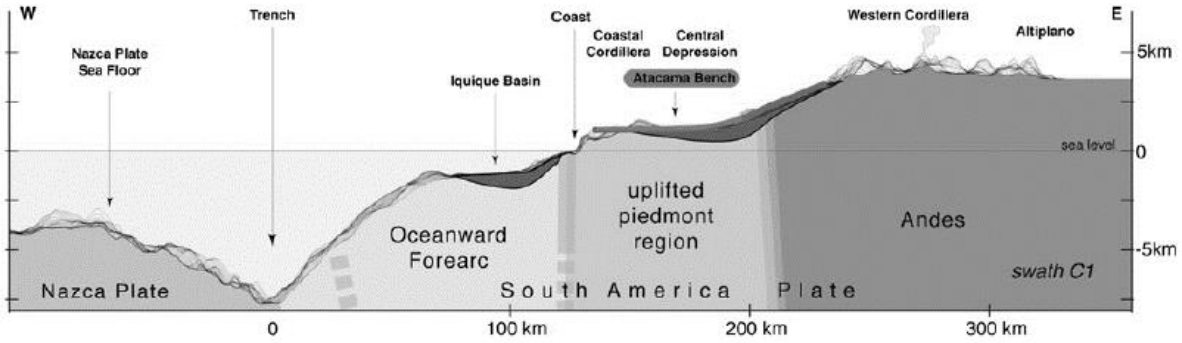

Figure 10: Topographic profile and basic geology of northern Chile (Source: Armijo et al., 2015:11).

Fig. 10 shows a topographic profile of northern Chile for the latitude ~20°S. The orographic patterns of the Tarapacá region allow the identification of five more or less homogeneous longitudinal stripes that segment the territory and originate differentiated landscapes. From west to east these are: the coastal plains, limited to the east by the coastal cliff; the Coastal Cordillera; the desertic pampa (the Atacama bench); the andean foothills; and the Western Andes Cordillera and altiplano (Cereceda & Errázuriz, 2015). Only the first two are of major relevance for the preset research, so they will be reviewed in greater detail. In this zone, coastal plains are coastal rocky or sedimentation zones of limited width (Cereceda & Errázuriz, 2015). To the south of the city of Iquique (20°31´S) these are presented as beaches and coastal terraces up to 3 km wide, while between the north of the city and the town of Pisagua (19°25´S) the beaches disappear, the sea instead coming into contact with the coastal cliff. This coastal cliff is a definitive and continuous feature of the coastal relief of the region, reaching altitudes above 1.000 m and slopes of 80°. In this sense, it constitutes a barrier that abruptly interrupts the area of direct marine influence. The Coastal Cordillera, for its part, acts in the same way, intercepting the masses of humid air coming from the ocean. In the region, this mountain range is presented as a series of island hills overhanging the pampas at altitudes ranging from 1.000 to 1.700 m a.s.l. (Cereceda & Errázuriz, 2015). The Coastal Cordillera has an average width of 50 km and is strongly faulted, so it presents interior depressions without drainage in which salt flats have developed (e.g. Salar grande and Soronal). In the two units described there are almost no streams or rivers that interrupt

their continuity, as most of the Andes Cordillera tributaries flow into the endorreic basin of the pampa del Tamarugal. The only exceptions are the Loa River along the southern limit of the Tarapacá region, and the Camarones stream, near the northern limit.

The Atacama Desert is one of the driest regions of the planet, containing some of the most extreme arid ecosystems (Weischet, 1975). Plant organisms existing under these environmental conditions have developed highly specialized adaption strategies, mainly concerning the limited availability of fresh-water. Along the Coastal Cordillera are located fog-dependent ecosystems; these ecosystems are located precisely where the prominent coastal topography of the Atacama Desert intercepts Sc cloud coverage (Cereceda et al. 2008a). A major component of these coastal fog-oases are plant species from the genus *Tillandsia spp.*, (see Fig. 11) a well-adapted, rootless desert plant species forming discrete vegetation patches on the coastal relief of the Atacama coast (Masuzawa, 1985; Rundel & Dillon, 1998; Muñoz-Schick, 2001; Pinto el al., 2006).

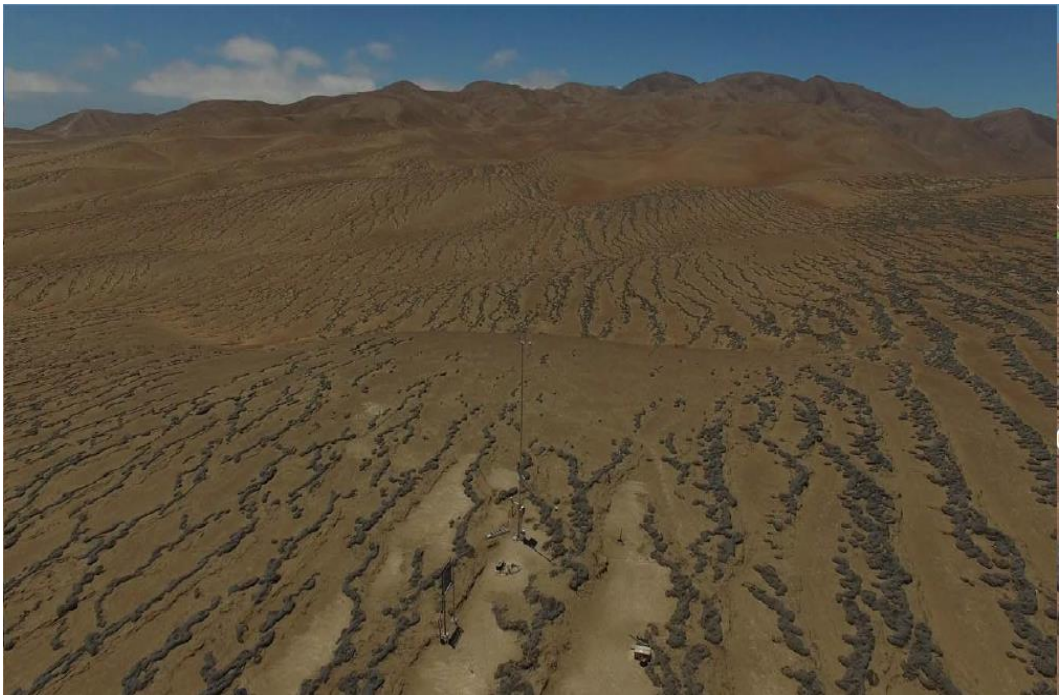

Figure 11: *Tillandsia spp.* distributed in bands running opposite to the wind direction. Cerro Oyarbide, Costal Cordillera (~20°S) (Source: Siegmund A., drone capture, November 2016).

Tillandsia ecosystems primarily develop when coastal fog allows plant growth due to surface condensation or dew, light drizzle and interception of fog water. As *Tillandsia spp.* are entirely dependent on fog moisture, their spatial distribution is constrained to areas covered

by coastal fog of sufficient frequency, duration and intensity (Hesse, 2012). Therefore, their biogeographic location follows a distinct pattern of distribution associated to the existence of major fog- respectively cloud-corridors along the coastal area (Cereceda et al. 1999). In addition, the fog ecosystems of the coastal Atacama Desert are sensitive indicators of climate change within a hyper-arid environment, due to their direct association with mid-to-long term variation in nearby oceanographic and atmospheric elements (Latorre et al., 2011). Despite their potential as a key biosensor of climate variability along the coastal Atacama, there remain major knowledge gaps with regard to the biogeographic distribution of *Tillandsia spp.* ecosystems and how these respond to climate change. For instance, geologic and geochemical data show significant variations in *Tillandsia landbeckii* ecosystems to regional climate anomalies (e.g., affected by fog intensity, cloud thickness and elevation), revealing its aptitude as an environmental proxy along the coastal Atacama.

In relation to human populations, the desertic climate of the Tarapacá region is a condition that has historically influenced its processes of land occupation. In this sense, the population has settled mainly on the coasts and, to a lesser extent, along the valleys that cross the pampa or in the high altiplano. Only mining activity has motivated settlement in the arid parts of the pampas or the foothills, with varying intensity depending on the period. According to the National Statistics Institute (INE, 2017), 90% of the total regional population (330.000 inhabitants) lives in the coastal areas, concentrated in Iquique and Alto Hospicio, which together form an important conurbation of nearly 300.000 habitants. Of the coastal population, 98,1% live in the urban conurbation and the remaining population of the coastal areas is distributed along the coast in small towns and fishing villages (INE, 2017). These fishing villages, (e.g. Los Verdes, Chanavayita, Río Seco, San Marcos) have variable populations, reaching 50 to 1.200 inhabitants, and in some cases have neither electricity nor basic sewage treatment. Furthermore, water is delivered by trucks, which only visit villages three times per month. Although the local government provides this water free of cost, it is dependent on truck drivers, truck maintenance, road conditions, etc., inevitably leading to interruptions in service and quality. Results from a survey conducted in these coastal communities found that water consumption per person/day varied from 11 to 22 liters, averaging 15 L/person/day (unpublished data). This is 15% of what an average Chilean consumes per day, based on the Chilean Supervision of Health Services.

Northern Chile, and in particular the Tarapacá region, has a concentrated and undiversified economy, where the main productive activities are mining, trade, tourism, services and construction, among them generating 75% of the regional GDP (INE, 2017). However, the mining industry is the most important activity in the region, accounting for almost 40% of regional GDP. The main mining operations are focused on metallic mining of copper, gold and silver, and in the present century, a growing non-metallic mining industry, such as lithium, sodium chloride and iodine. As is the case in many of the northern hyper-arid territories of northern Chile, where mining is the main economic activity, there is enormous social inequality, and Tarapacá region is an example of this. On the one hand, the city of Iquique is a prosperous port city that emerged due to historical mining activities, and on the other hand, the nearby Alto Hospicio has some of the lowest social indexes in Chile, with minimum levels of health, education and security (Observatorio social, 2014). Together with the smaller inland localities within the Tarapacá Region (e.g., Pica, Mamiña), both the urban and rural populations that have settled in the Atacama Desert confront a growing pressure on their most limited resource, water, due to increased water demand from copper mining and associated large-scale activities (DGA, 2017).

5 Methodology: An integrative multi-scale approach for fog monitoring

This chapter details the data series that were produced and used in this research, the information collected and the processing applied to the data according to the scale structure of the research.

5.1 The regional scale

The regional scale is defined here as the totality of the study area (showed in Fig. 9); thus the variables at this scale are those that affect the entire study area as well as those that are representative of the conditions in the SEP. The atmospheric and oceanic variables analyzed are stratocumulus cloud coverage, fog and low cloud coverage, and the SST.

5.1.1 The fog and low cloud satellite identification and characterization

Geostationary Operational Environmental Satellite (GOES) satellite data was used to identify and characterize the spatiotemporal coverage of the fog and low cloud, as well its variability and tendencies. The GOES Imager is a five-channel radiometer, whose spectral and spatial characteristics are detailed in Table 1 (e.g. GOES 13 Imager).

Spectral band	Wavelength (>µm)	Spatial resolution
1	0,55 – 0,75	1km
2	3,80 – 4,00	4km
3	5,77 – 7,33	8km
4	10,20 – 11,20	4km
6	12,96 – 13,72	4km

Table 1: Spectral and spatial resolution of GOES 13 Imager sensor (Source: https://goes.gsfc.nasa.gov/text/goestechnotes.html#technical).

For the area between 19°S – 21°50´S and 71°W – 69°W (see Fig. 9), almost 6.000 GOES images were processed and analyzed to determine the spatiotemporal percentage of fog and low cloud frequency presence (FFP) during September (1995 to 2017) and February (1997 to 2017). These months were chosen as they correspond to the maximum (September) and minimum (February) periods of fog water yields (L per m^{-2} and $month^{-1}$),

based on data collected from 1997-present by an SFC in the costal Atacama (Schemenauer and Cereceda, 1994), specifically in Alto Patache, located on the summit of the Coastal Cordillera (850 m a.s.l.) about 3.5 km lineal distance from the coastline (Larrain et al., 2002; Cereceda et al., 2008a; del Río et al., 2018). The presence of advective fog reaches its maximum at night and its minimum at noon, at dawn and sunset there is an inflection in the amount of fog present; given this daily cycle (Farías et al., 2005), five images per day were selected for analysis, captured at 03:39, 07:39, 10:39; 15:39 and 21:39 UTC (00:39, 04:39, 07:39, 12:39 and 19:39 local time). For ease of understanding, local time will be used from now on.

GOES satellite images were downloaded for free from the National Oceanic and Atmospheric Administration (NOAA) web server. The format of the images was transformed (.tiff), then the area of interest was selected, geometrically corrected and calibrated using NOAA's Weather and Climate Toolkit (WCT). As the full data set of desired images for the years and specific times under study was not available, a search buffer of ±60 minutes was applied. The primarily temporal scale of analysis is monthly, thus in order to have sufficient representation, a minimum of 15 images was required. At the same time, the presence of extensive high cloud coverage interferes with the identification of low clouds. For this reason, images with high cloud coverage in the study area of greater than 20% were removed from analysis. Table 2 shows the number of images processed for each month.

	February (local time)					September (local time)				
	0:39	4:39	7:39	12:39	19:39	0:39	4:39	7:39	12:39	19:39
1995	<15	<15	<15	<15	<15	25	20	<15	17	21
1996	<15	<15	<15	<15	<15	27	18	<15	26	26
1997	25	23	23	27	26	15	15	<15	16	16
1998	28	26	27	28	28	28	29	30	30	29
1999	28	28	27	28	28	30	30	28	30	27
2000	22	22	24	29	29	29	29	26	29	30
2001	28	28	27	28	26	29	30	28	30	29
2002	28	28	28	28	28	30	30	30	30	29
2003	28	28	28	28	28	30	30	30	30	26
2004	29	29	29	28	29	30	29	30	30	30
2005	28	28	27	28	28	30	30	<15	29	29
2006	28	27	28	28	28	28	30	30	30	27
2007	28	28	28	28	28	30	30	30	29	28
2008	29	29	25	29	29	29	30	30	26	25
2009	28	28	28	28	28	30	30	30	30	29
2010	28	28	28	28	28	30	30	30	30	29
2011	28	28	28	28	28	29	30	30	30	24
2012	29	29	29	29	29	29	30	30	29	29
2013	28	28	28	28	28	26	26	28	30	25
2014	28	28	26	28	28	27	29	28	29	27
2015	28	28	26	28	28	29	30	30	30	30
2016	29	29	26	29	28	29	30	30	30	29
2017	27	27	27	26	26	20	25	25	23	21
Average	27.7	27.5	27	28.1	27.9	27.8	27.8	29.2	28	26.7

Table 2: Number of satellite images processed for the study period. Months with < 15 images were not included in analysis.

Nighttime identification of FLCs was performed in three steps using the *Trimble eCognition* (*Developer Rulesets*) software. First, a primary identification step was performed followed by two tests to determine if the pixels preliminarily identified as low clouds were actually low clouds, or whether they corresponded to high clouds or to desert soil. Results were then contrasted with ground truth measurements for final validation (see Fig. 12). Primary identification was based on a widely used metric, the difference between short (3,8 µm) and long (10,9 µm) thermal infrared wavelengths (Eyre et al. 1984; Ellrod, 1995; Lee et al. 1997; Anthis and Cracknell 1999; Bendix 2002; Underwood et al. 2004; del Río et al., 2018). To the thermal difference result, a threshold of -2 was set (adapted from Lee et al., 1997), where lower values were classified as low cloud and higher values as cloud free. Then, the pixels classified as low cloud were tested using two filters: the first, distinguishes and classifies whether the cloud top temperature, estimated by the bright temperature at 10,9 µm wavelength, is above or below 273°K threshold (Torregrosa et al., 2015). Pixels under the temperature threshold were classified as high clouds and those above the threshold as low clouds. Second, a segmentation analysis, based on the thermal band difference, clustering neighboring pixels into a minimum of 10 km^2, was conducted. Then, within each cluster, those clouds within one standard deviation (SD) were classifying as low clouds, based on the homogeneity of the cloud deck, while those clusters with a SD greater than one were classified as no clouds, as it is assumed that they correspond to dessert soil, salt flats or local radiative fog produced inland (Pampa), which is not part of this research. In the last step, pixels identified as low clouds for the year 2016, were contrasted and validated by GOFOS (see section 5.2.1), which represents a ground truth technique that allow for the empirical observation of the presence or absence of coastal fog. Comparisons with satellite data showed >96% agreement with processed images (see section 8.1 for details).

For analysis of daytime cloud cover, it was used the *Macro Modeler* module of the *Terrset* software; two processes were conducted, based on changes in detection techniques and thermal temperatures (Jedlovec and Laws, 2003; Torregrosa et al., 2015). First, using the visible range, a clear sky image (100% absence of clouds) from within the study period was selected for February and September at each time point under analysis. Then, a difference was applied between every available visible image to the corresponding clear sky image (either February or September at the same time point), allowing the identification of areas with or without cloud presence. To the visible image difference result, a threshold of -5 was

set (the threshold varied ±1 for the various hours and months, depending on visual analysis of the results), where lower values were classified as low clouds and higher values as cloud free. The second step was to discriminate between high or low clouds, based on whether they were above or below the 273°K threshold using the bright temperature at 10,9 µm wavelength, (Torregrosa et al., 2015). Just as in the case of nighttime identification of low cloud cover, the pixels finally identified as low clouds (for the year 2016) were validated against the ground truth technique based on GOFOS (see section 5.2.1). Comparisons with satellite data showed >89 % agreement with processed images (see section 8.1 for details).

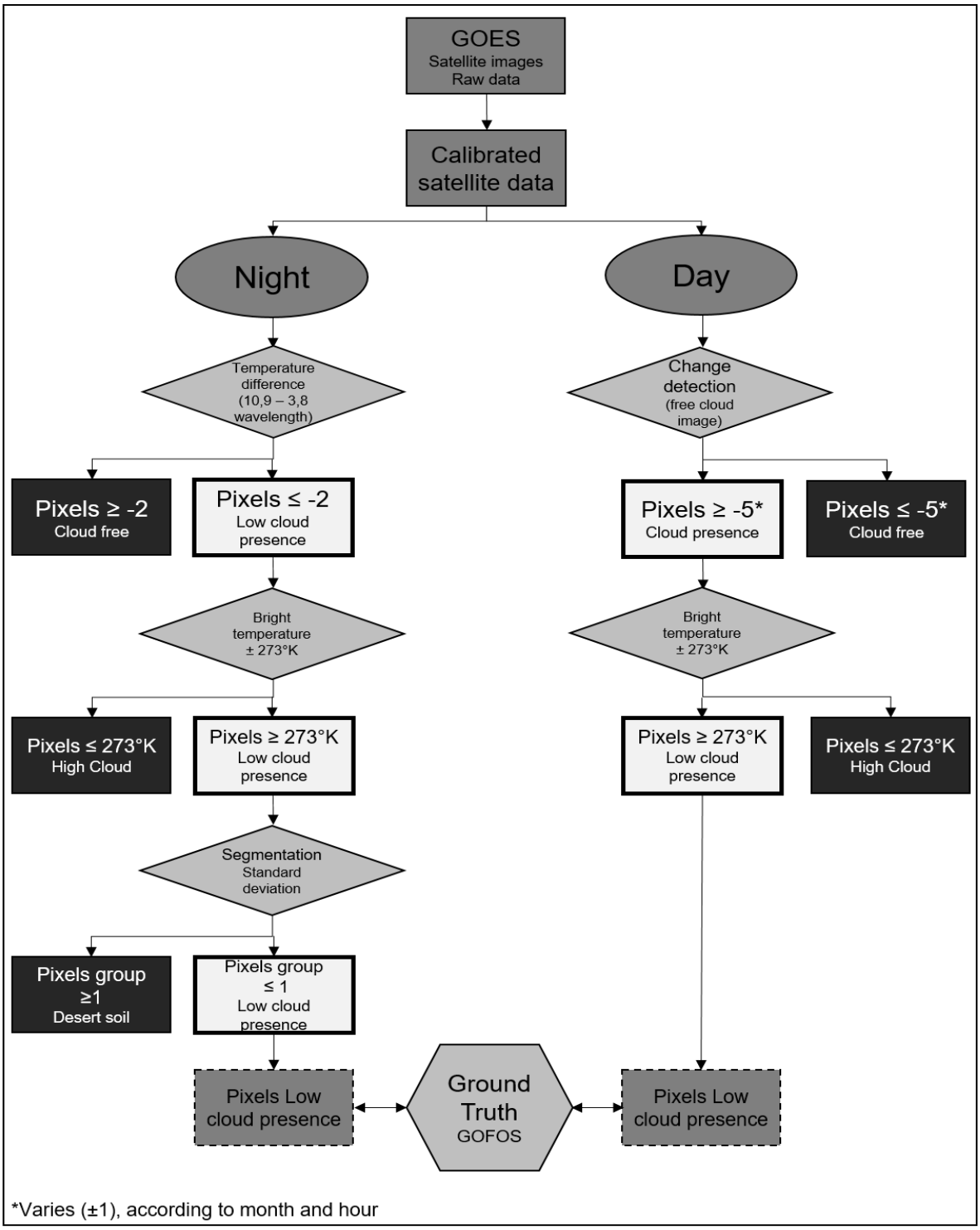

Figure 12: General overview of the workflow for nighttime and daytime low cloud identification using satellite images.

The process of analyzing satellite images in order to describe the spatiotemporal distribution, trends and variability in low-cloud cover is composed of three different

approaches: (a) Pixel by pixel, (b) Sample areas based on systematic locations, and (c) Cluster areas based on fog and low cloud frequency presence.

a. Pixel by pixel. Making use of the spatial continuity of satellite data, arithmetical and statistical analysis were realized in order to obtain the following data, among others:
    - Hourly means (5 selected hours)
    - Monthly means
    - Annual means
    - Monthly study period means
    - Study period trends
    - Annual ENSO means
    - Annual anomalies

    To estimate tendencies, a median trend analysis was applied; this is a robust non-parametric trend operator that is highly recommended for evaluating the rate of change in short or noisy series (Hoaglin et al., 2000). The median trend is calculated by determining the slope between every pairwise combination and then finding the median value. All median trends are presented with a significance image, that expresses the probability that the observed trend could occur by chance.

b. Sample areas based on: (A) Systematic locations and (B) Ocean-land and altitudinal criteria. (A) To obtain a latitudinal and longitudinal FLC presence description, systematic sample areas were created and used to extract satellite FLC frequency presence data. The sample areas, of ~35 km^2, present a latitudinal distance between them of approximately 21 km (see Fig. 13A). From West to East they are located at 65 km offshore, 20 km offshore, 5 km offshore, over the coastline, 5 km inland, 15 km inland and 25 km inland. The longitudinal distribution was chosen due to our interest in understanding and comparing offshore areas with inland areas with lower and higher land influence (Garreaud et al. 2007, estimated that land influences reach around the 30 km offshore), with shoreline areas (coastal fringe conditions) and with onshore areas (from lower to higher topographic influences). Additionally, for specific analysis, sample areas located over 1.000 m a.s.l. and over 1.200 m a.s.l. were selected in order to explore in a more detailed way the topographic influence on fog distribution. (B) To contrast the ocean-land FFP differences, and at the same time the variances produced

inland by altitude, 4 macro units were created to describe and characterize trends and inter-annual variability, as well as to obtain datasets for correlation analysis. The units addressed all the pixel present in: i) the ocean; ii) from the coastline to 1.000 m a.s.l, the typical altitude of the thermal inversion layer in September; iii) from 1.000 to 1.200 m a.s.l., the typical altitude of the thermal inversion layer in February; and iv) from 1.200 to 1.500 m a.s.l., the maximum altitude of advective FLC within the study period.

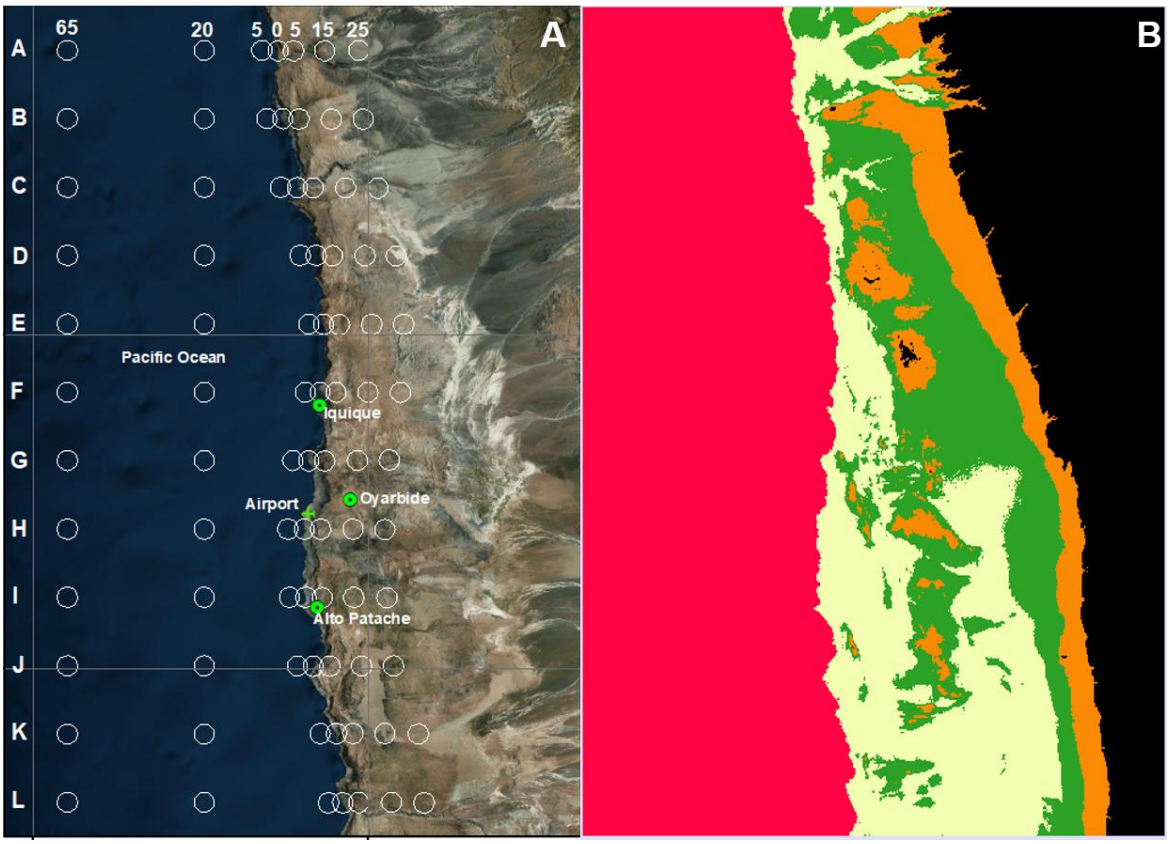

Figure 13: Sample areas for fog and low cloud analysis; A) systematic latitudinal and longitudinal areas, B) Ocean-land and altitudinal criteria areas.

c. Cluster areas based on fog and low cloud presence. To identify the areas where the presence of FLC present similar spatiotemporal behavior, a chain-cluster analysis was applied (Jensen, 2005). The clustering process was conducted using a two-step algorithm. The first step reads the dataset and sequentially builds clusters; the dataset is read from the first row to the last row and image pixels are processed in a rightward fashion. In the second step, depending on the minimum distance to the mean classification, each pixel is classified as belonging to one of the clusters. These clusters

are also used to relate the FLC presence with oceanic indices, in order to assess the potential influence of the oceanic SST on specific FLC areas with similar behavior.

5.1.2 Characterization of sea surface temperature (SST)

The characterization of the SST along the offshore Atacama was performed based on data from the satellite Aqua, which carries on board the sensor Moderate Resolution Imaging Spectroradiometer (MODIS) administrated by NASA. The ocean area analyzed here is the same as considered in the satellite-based identification of low-cloud cover (see Fig. 9 and Table 3). The Aqua MODIS long-wave SST product (Level 1) uses bands 31 and 32, which have a wavelength of 11µm and 12µm, respectively and present a spatial resolution of 1x1 km. The algorithm used to obtain the brightness temperature is derived from the observed radiances by inversion of the radiance versus blackbody temperature relationship (NASA, 2014). In order to process the images, a series of steps were carried out using a specialized software called SeaDAS, originally developed by NASA for ocean color analysis. It was analyzed the time period from 2002 to 2017 (2002 is the first year for which data is available) for the months of February and September, which are the same months analyzed for the FLC identification. Depending on the availability, one or two daily images in between 18.00 and 20.00 UTM hours were processed to generate monthly averages of SST for each year. The resulting brightness temperature data are from the first 50 cm of depth, which is the maximum distance reached by satellite measurement. In order to contrast and explore relations between SST and FLC presence, datasets with SST averages were obtained from the complete ocean area, as well from 3 longitudinal samples, areas 30 km wide (see Fig. 14). Finally, statistical analysis was carried out for data on offshore Atacama SSTs and the FLC frequency presence in order to explore the relation and potential causal links between both variables. The analysis was performed contrasting the monthly inter-annual variability.

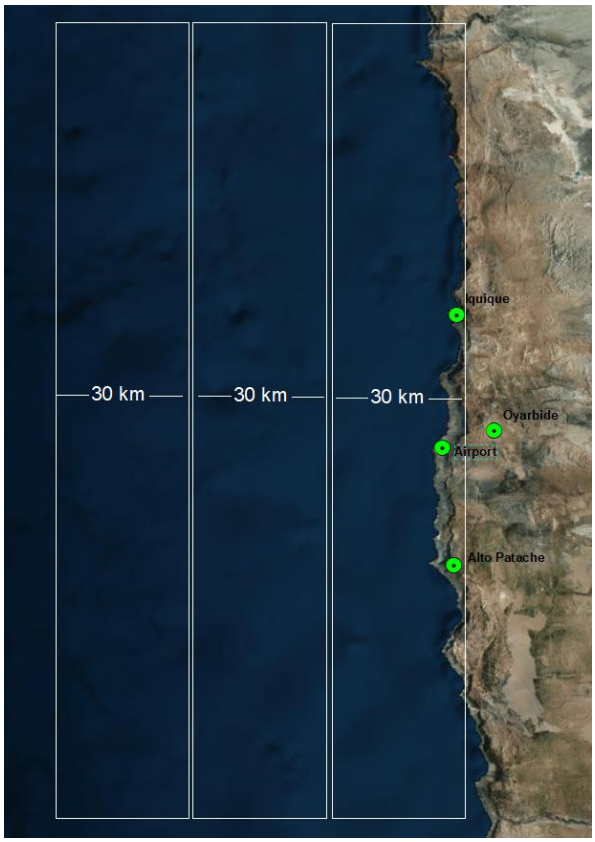

Figure 14: Sample areas for sea surface temperature analysis.

5.1.3 Oceanic indices

In addition to SSTs characterized for the offshore Atacama in section 5.1.2, additional indices of oceanic SST used herein include: (i) the SST 3,4 (monthly SST area average), (ii) the Oceanic Niño Index (ONI) (a 3-month running mean of SST anomalies in zone 3,4), (iii) the SST 1+2 (monthly SST zone average), and (iv) the Interdecadal Pacific Oscillation (IPO) (mean difference in SST anomalies between the central equatorial Pacific and the the Northwest and Southwest Pacific). All indices were obtained from the National Oceanic and Atmospheric Administration (NOAA) webpage (http://origin.cpc.ncep.noaa.gov/products/analysis_monitoring/ensostuff/ONI_v5.php).

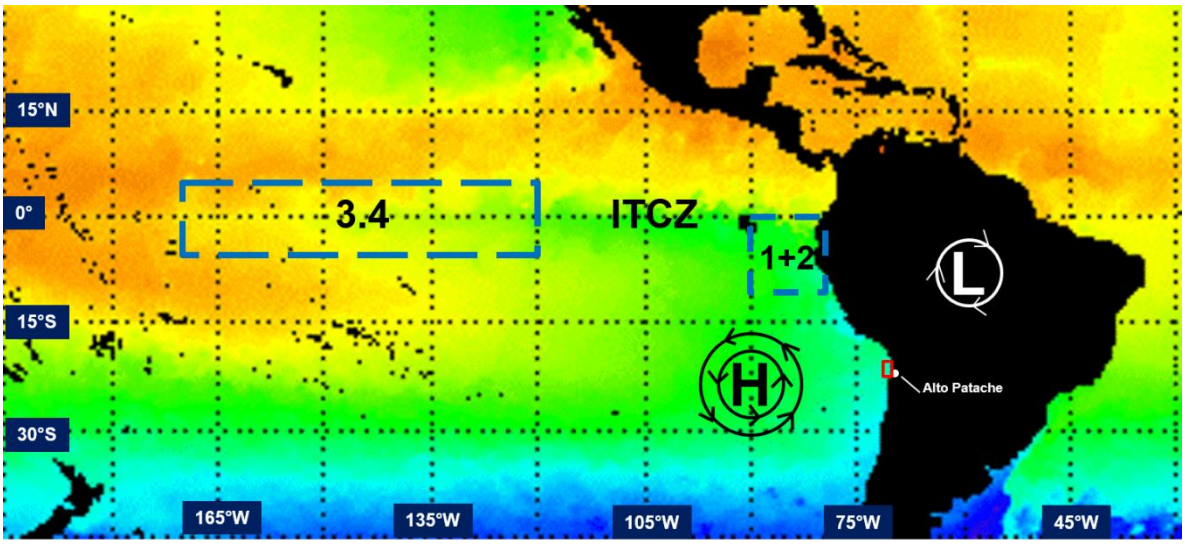

Figure 15: Atmospheric and oceanographic multi-scale indices analyzed in this study. The dashed blue boxes represent regional data, including the ENSO 3,4 and 1 + 2 SST zones. The red box shows the local-scale study area offshore of the Atacama, corresponding to the analyzed SST by MODIS satellite. (Source: Adapted from del Río et al., 2018:129).

Figure 15 shows the locations of the analyzed indicators and their respective characteristics are described in Table 3. The ENSO SST indices are analyzed from a spatiotemporal perspective to assess potential influences of SST anomalies on the FLC variability (e.g., ENSO 3.4 SST with FLC presence). The study period (1995-2017) covers a number of ENSO years, including some very strong El Niño years (1997-1998, 2010 and 2015), as well as some strong La Niña years (e.g. 1999-2000, 2008 and 2011). Therefore, a first step to correlate the satellite FLC monthly presence frequency estimated for February and September by the various methodological approaches (pixel by pixel, ocean-land and altitude sample areas and cluster areas) with the SST indices. To assess the potential causal links, various linear regressions were carried out to define which predictive variable (analyzed SST) is influencing FLC spatiotemporal variability.

Indicator	Coordinates (point or area)	Source	Available Data	Data Used	Original measurement interval	Measurement interval analyzed
SST Tarapacá	19° S - 21°30' S; 72 °- 70° W	MODIS Aqua	2002 - Present	2002 - 2017	Daily	Monthly
SST ENSO 1+2	0° - 10° S; 90 °- 80° W	NOAA/ National Weather Service	1950 - Present	2002 - 2017	Monthly	Monthly
SST ENSO 3.4 / ONI	5° N - 5° S; 120° W - 170° W	NOAA/ National Weather Service	1950 - Present	2002 - 2017	Monthly	Monthly

Table 3: Analyzed multi-scale SST.

5.2 The local scale

Estimations of the local scale cloud cover are based on a network of instruments installed in the coastal Atacama to accurately measure local-scale the vertical spatiotemporal FLC variability and the atmospheric variables influencing low-cloud cover. At a local scale were analyzed variables that are obtained in situ, in this case atmospheric and visual measurements taken from the Iquique airport, named Diego Aracena Airport (20°32´S – 70°10´W; 50 m a.s.l., ~3 km from the Coastal Cordillera), and from various sensors installed along the Coastal Cordillera. The specific location of the instruments is shown in Fig. 16.

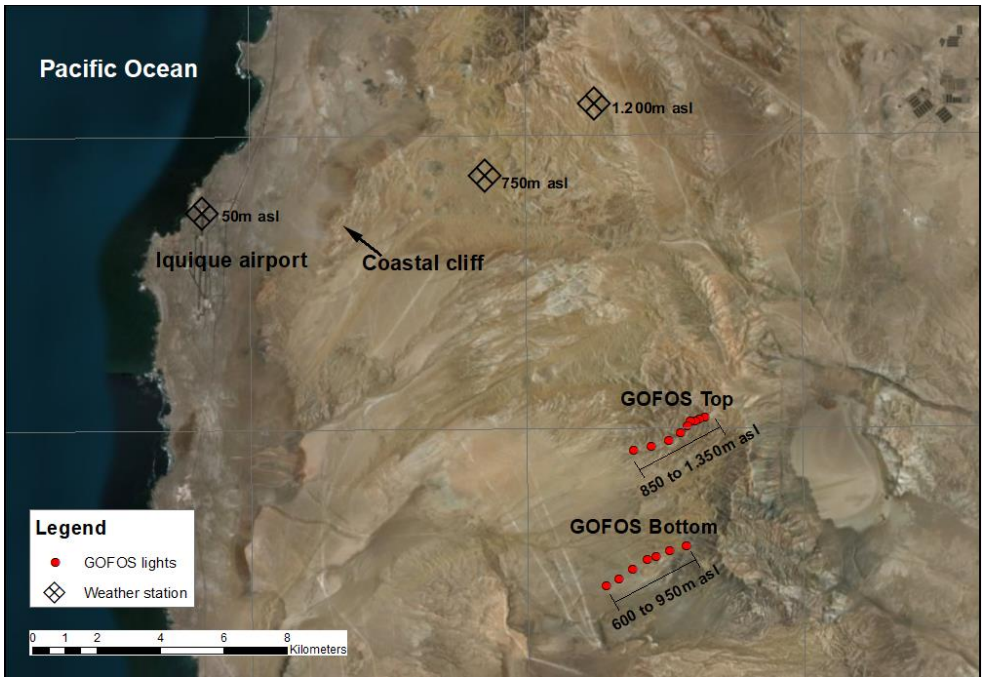

Figure 16: Instrument location within the Coastal Cordillera.

5.2.2 GOFOS: a new fog monitoring system

Local fog and low cloud spatiotemporal variability on the coast of the Atacama Desert is measured by the Ground-based Optical Fog Observation System (GOFOS), which was developed together with the Department of Geography Research Group for Earth Observation (ʳgeo) at Heidelberg University of Education as part of this study. GOFOS is a system composed of two optical time-lapse cameras that capture images every 10 minutes, and a series of autonomous lights (solar energy) automatically activated when the sun sets. The cameras observe a section of the western slopes of the Coastal Cordillera (see Fig. 16), where the lights are located in an altitudinal profile, with coverage spanning the entire range of regular fog presence. As the advective fog has a greater presence during the night (Cereceda et al., 2008a), observation of the different lights or indicates: (1) fog and low cloud presence, (2) the altitude of thermal inversion, and (3) the thickness of the fog and low cloud. During daytime the position of the lights is known (regardless of whether they are on or not), so the identification and characterization of the fog and low cloud is also possible. The cameras (Brinno proTLC) are installed on a plastic tripod and are connected to a 10W solar panel for continuous energy supply (see Fig. 17a). The lights are attached to galvanized iron, and made up of to 44 LEDs, lighting in a red mode, supplied by a 6W solar panel (see Fig. 17b).

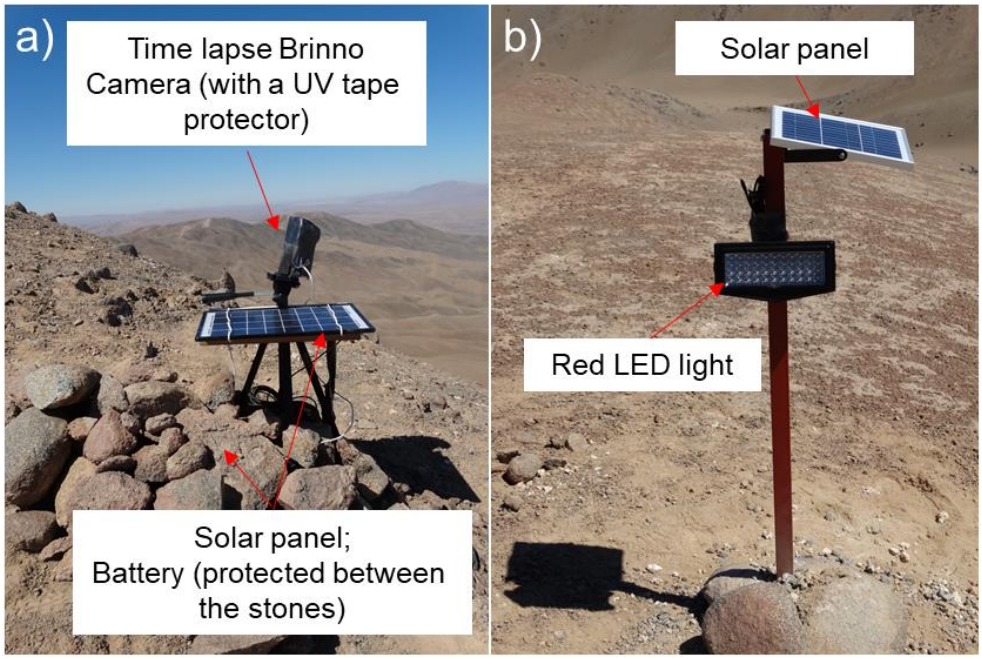

Figure 17: Ground-based Optical Fog Observation System (GOFOS), a) Time lapse camera; b) Autonomous LED lights.

The first camera (GOFOS Top, see Fig. 18a), installed on August 2016, at 1.350 m a.s.l., which is regularly over the thermal inversion layer, has a vision framework from East to West that allows it to observe from the West slopes of the Cordillera to the Ocean (see Fig. 18a). Along the slope, nine lights are located every 50 vertical meters, from 1.250 m to 850 m a.s.l.. The second camera (GOFOS Bottom, see Fig. 18b), installed in mid-January 2017 at 600 m a.s.l., observes from West to East a slope with a second profile of lights (also equidistant every 50 m altitude), that goes from 650 m to 900 m a.s.l. Both cameras and light systems, worked correctly until January 2018, when they were moved to another position to continue with the same measurements in areas with the presence of specific fog ecosystems.

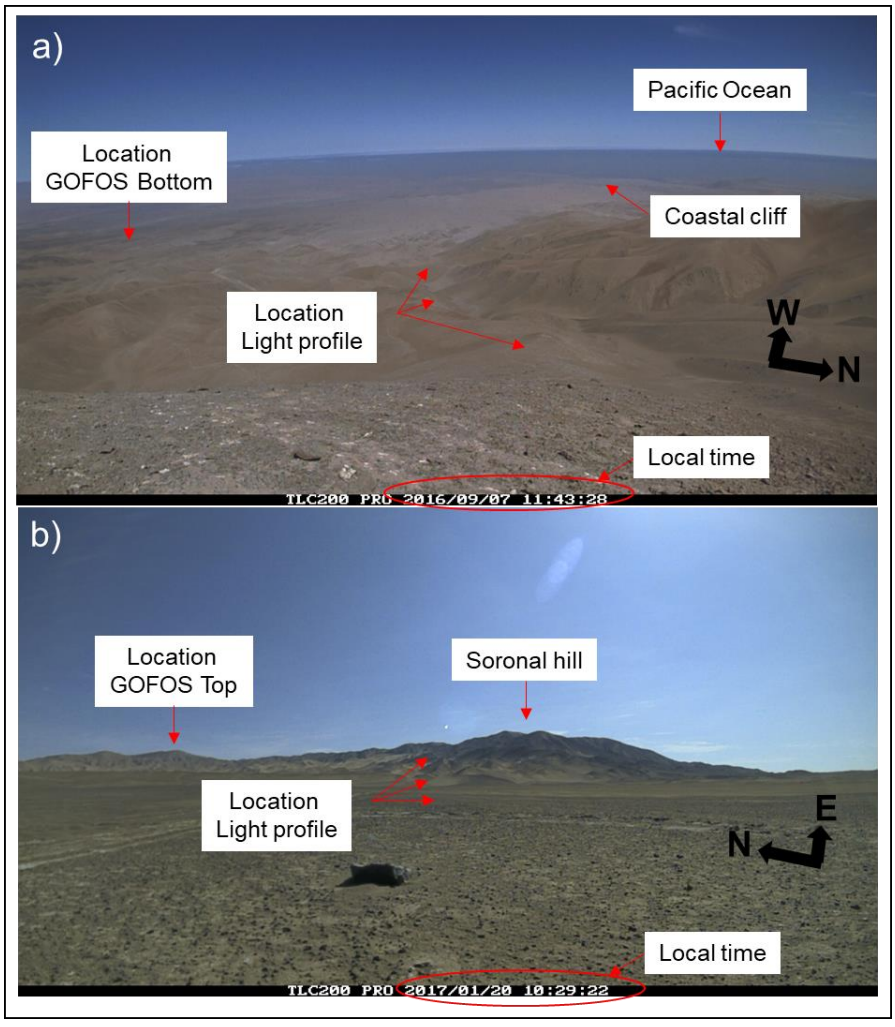

Figure 18: GOFOS framework vision over the coastal Atacama, a) GOFOS Top, b) GOFOS Bottom.

Dataset creation consisted of two processes, differentiated for night and day. For the night, first it was necessary to manually generate a binary base by visual observation of images every ten minutes extracted from the recorded videos: (1) indicates fog presence, when the light is not visible (see Fig. 19b and Fig. 19d); and (0) indicates fog absence, when the lights are visible (see Fig. 19a and Fig. 19c). Over 800 different cases of FLC presence or absence were analyzed in order to train a specific software, developed by electric engineers at Pontificia Universidad Católica de Chile, that bases its operation on the use of convolutional neural networks, which after training allows the software to automatically classify the remaining images (nearly 32.000 images). The software (written in Phyton language), is configured so that in case of doubt (due to limits of the cloud with a light or dimmed lights), the user can manually classify images (see Fig. 20). The results (1 and 0) were systematized automatically into an Excel file.

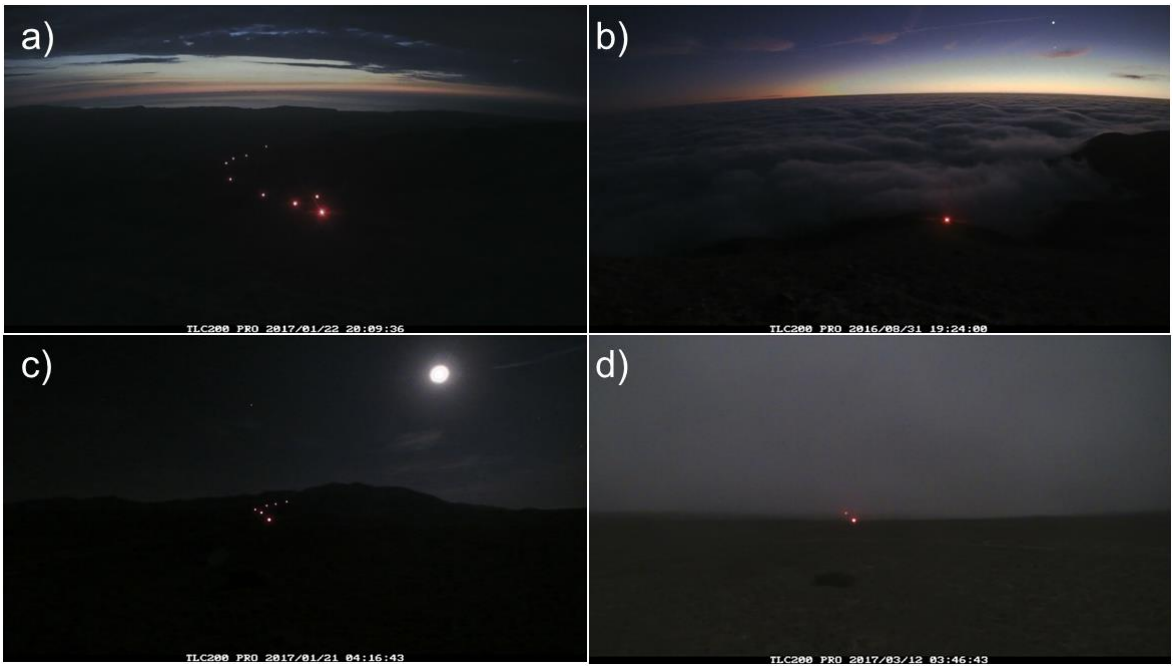

Figure 19: GOFOS Top, a) Nine observed lights showing absence of fog and low cloud; b) Only one light observed, showing fog presence and that the base of the thermal inversion layer is at 1.200 m a.s.l. GOFOS Bottom, c) Six observed lights showing absence of fog and low cloud on a moonlit night; d) Two lights observed, showing fog presence and that the cloud base is at 700 m a.s.l.

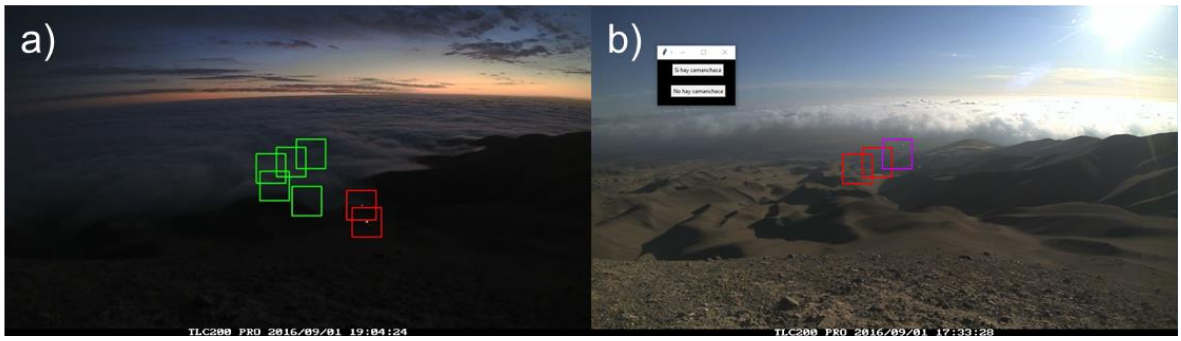

Figure 20: Example of the software created for fog cloud classification, a) automatic classification, green squares mean fog presence and red fog absence; b) Purple square means the definition of fog presence or absence must be performed manually by the user, which is configured in the upper-left window (yes/no *Camanchaca*).

For daytime (see Fig. 21), the entire classification was performed manually; nearly 30.000 images were analyzed with a transparent mica sheet placed over the computer screen highlighting the location of the light. This allowed the creation of the daily datasets with ones (1) and zeros (0) in an Excel file.

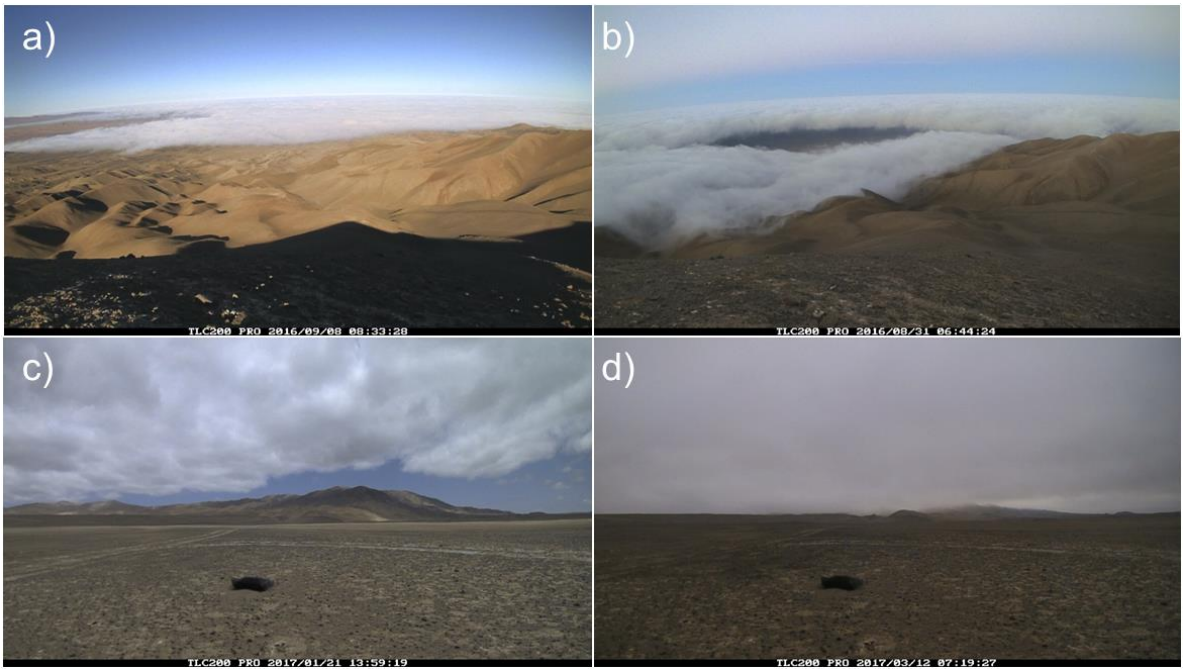

Figure 21: GOFOS Top, a) Daytime image with low cloud entering inland; b) Daytime fog presence, covering lights. GOFOS Bottom, c) Daytime image with low cloud entering inland; d) Daytime fog presence, covering lights.

The GOFOS dataset allowed for a complete description of the spatiotemporal distribution of the FLC, determining its hourly, daily, monthly and seasonal variability in terms of presence

(absence), thermal inversion layer altitude and cloud thickness. The GOFOS results on FLC presence and cloud base were contrasted with airport observations (visual oktas and ceilometers measurements). It should be noted that minor differences in the FLC presence estimations by the GOFOS top and bottom instruments might occur, principally due to the fact that low-clouds present at a higher altitude could cover the bottom camera and transect lights. However, as the measurements from the top camera cover a wider range, the observations from GOFOS top are considered to be the correct ones.

GOFOS measurements were also used to validate the GOES satellite identification of the FLC as described in section 8.1. The validation consisted of comparing and contrasting all available satellite images at the different time points, for September 2016 and GOFOS observations for the same period. Each GOES raster binary result (presence or absence of FLC) was extended using the free software Google Earth, in this manner you can visualize the spatial distribution of the estimated FLC cover over base imagery of the coastal Atacama. Additionally, integrated into the Google Earth view was a layer with GOFOS locations (lights and camera). Finally, GOES results (presence/absence and altitude) were contrasted with GOFOS observations (presence/absence and altitude), obtaining a ground truth validation for the satellite model.

5.2.3 Atmospheric measurements: both existing and new

The systematic long-term measurements taken at the Iquique Airport, 50 m a.s.l., (see Fig. 16) come from two sources. The first is a dataset of atmospheric variables recorded every ten minutes (air temperature, precipitation, air pressure and relative humidity, among others) by a weather station. The second source is hourly visual observations taken by the Dirección Meteorológica de Chile (DMC; Meteorological Direction of Chile). Observations consisted of watching and recording sky conditions in *oktas* cloud cover data; values range from 0 to 8, with 0 indicating no cloud cover and 8 indicating 100% cloud cover. From 1981 until July 2017, the visual observations taken by DMC also estimated the altitude of the cloud base, based on the known altitudes of the coastal cliff next to the airport, giving a higher reliability to the measurements. Nevertheless, starting in August 2017, the cloud base altitude measurements were taken using a ceilometer, an active laser sensor with an accuracy of ±5 m. In addition to the airport weather station, two new Thies Clima weather stations, also collecting data every ten minutes, were installed in November 2016 and October 2017, at

an altitude of 1.200 m a.s.l and 750 m a.s.l, respectively. These locations correspond to the regular range of FLC presence, in the Coastal Cordillera and are positioned in a direct altitudinal profile from the airport, following the primary wind direction (see Fig. 16).

Both visible *oktas* cloud cover and the cloud base altitude datasets were used to analyze and compare with the FLC local spatiotemporal variability measured by the fog monitoring system GOFOS. This allowed us to observe the spatial differences between the coast and the Coastal Cordillera. Atmospheric variables from the weather stations were used to characterize the vertical structure of the atmosphere within the MBL, as well to estimate the MBL regime and its spatiotemporal variability.

5.2.4 The marine boundary layer (MBL) regimes

Based on the measurements every 10 minutes, a hourly mean was calculated for the variables of air pressure, relative humidity and air temperature, in order to estimate the potential temperature (θ) and the specific humidity (*q*). Both indices were proposed as indicators of the predominant regime within the MBL, be it well-mixed or stratified (Lobos et al., 2018). The formulas for θ and *q* are as follow:

Potential temperature (θ):

$$\theta = T\left(\frac{P0}{P}\right)^{R/cp}$$

where:

θ: Potential temperature
T: Absolute temperature in °K
P0: Reference pressure (at 50 m a.s.l.) (Pascals)
P: Pressure observed at the stations (Pascals)
R/cp: Gas constant and specific heat capacity at a constant pressure= 0.286

Specific humidity (*q*):

q = (rh1*qs) [g/kg]

Where:

es: e0*exp((b*(tk-t1))/(tk-t2))
qs: (0.622*es)/(p/10)
rh1: rh/100

Constants:
Rcp: 0.286 r/cp = 287/1004 [Joule K^{-1} kg^{-1}/Joule K^{-1} kg^{-1}]
e0: 611 [Pa] (saturation pressure)
b: 17,2694 dimensionless
t1: 273,16 [K]
t2: 35,86 [K]

Assuming vertical distribution of the two weather stations, and based on air pressure measured at the airport (50 m a.s.l), the θ and *q* were calculated to determine the changes in an air parcel forced to descend to 50 m a.s.l.. In this manner, the experimented changes or similarities with the air parcel at 1.200 m a.s.l. allow us to define the MBL is in a well-mixed or stratified atmosphere. It is assumed that a well-mixed MBL is an indicator of conditions favorable for fog and low cloud formation and that a stratified MBL is not favorable to low-cloud formation. To determine the MBL regime, measurements were contrasted using an adaption of the thresholds established by Lobos et al (2018). The GOFOS measurements, in which the presence of fog is recorded, are compared with the ABL regimes, which estimate the fog presence-dissipation through a well-mixed/stratified regime. It was necessary to apply a filter based on the GOFOS definition of the base altitude of the thermal inversion layer, selecting those measurements where the inversion layer was greater than or equal to 1.200 m a.s.l. (the location of the weather station), because if the altitude of the inversion layer is below this point, the weather station at 1.200 m a.s.l. is in a free troposphere condition and consequentially would erroneously define the indicators as a stratified MBL. Therefore, the total number of MBL regime estimations that permitted temporal characterization of its vertical structure conditions was reduced to the number of measurements from GOFOS with the exposed thermal inversion altitude.

The classification of the MBL as well-mixed or stratified was based on the following thresholds for θ and *q*:

For a well-mixed regime:

- Moisture: $\frac{\delta q}{\delta t}$ (1.219 m – 40 m) ≤ 1,88 gr kg^{-1}
- Potential temperature: $\frac{\delta \theta}{\delta t}$ (1.219 m – 40 m) ≤ 3,65 K

For a stratified regime:

- Moisture: $\frac{\delta q}{\delta t}$ (1.219 m – 40 m) ≥ 1,88 gr kg^{-1}
- Potential temperature: $\frac{\delta \theta}{\delta t}$ (1.219 m – 40 m) ≥ 3,65 K

5.3 The integrated-scale analysis

Integration of the regional scale (GOES satellite data) with the local scale (GOFOS), was carried out for the time period of time over which information was available from both sources, February and September 2017. A comparative analysis was carried out on the results on fog presence between both methodologies, at an hourly, daily and monthly scale. Here the satellite result validation, presented previously, is included. The results are contrasted from a spatial perspective, both horizontal and vertical, according to the location of the sensors that provided local measurements. Finally, the results at a local scale are contextualized according to the phase and magnitude of ENSO anomalies in 2017 and general oceanic-atmospheric conditions.

Finally, the integration of scales allows for a general review and interpretation of the results of the research, and at the same time highlights the contributions and new information regarding the understanding of the foggy climate on the coast of Atacama.

6 Regional Scale Results and Discussion

This chapter provides a description and characterization of the spatial-temporal variations of the FLCs and SSTs, and then in the discussion section, an analysis and argument as to the potential factors that influence their variability and trends, thus encompassing the specific objectives 1, 2 and 3, of the present research (Fig. 22).

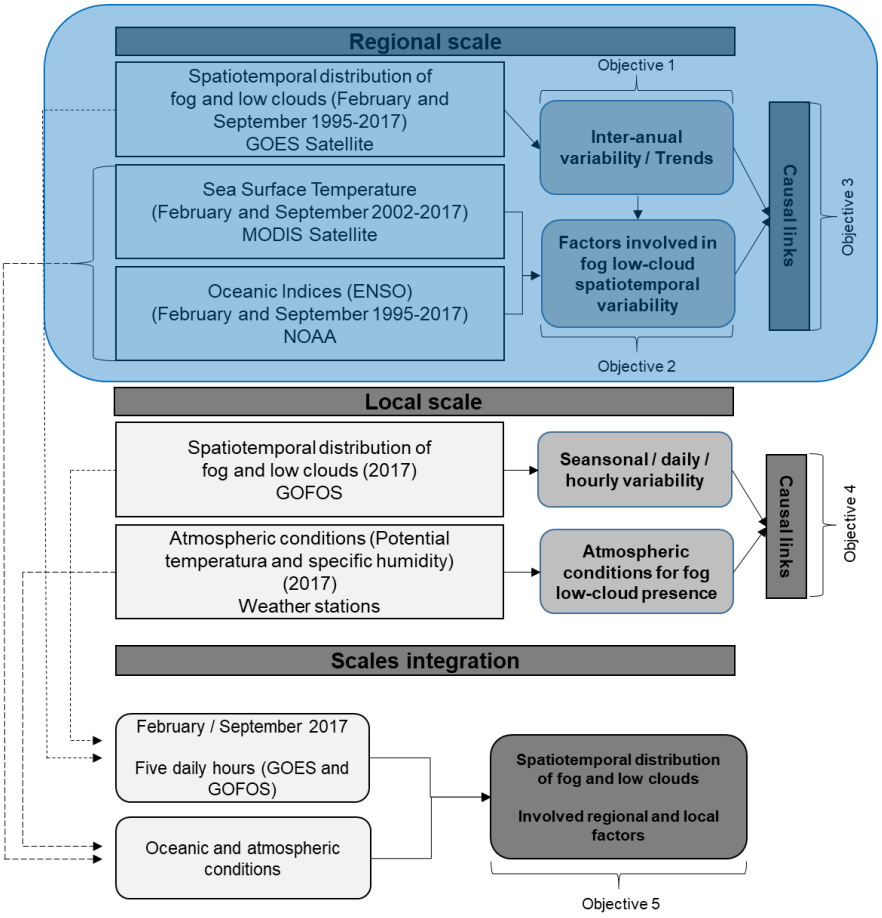

Figure 22: Regional scale within the study design for spatiotemporal characterization and analysis of fog and low cloud cover and sea surface temperatures, based on satellite datasets and oceanic indices.

6.1 Long-term fog and low cloud spatiotemporal distribution

Processed GOES satellite images for February and September, the month's representative of the minimum and maximum of fog and low cloud frequency presence (FFP) respectively,

for the period 1995 – 2017, allow us to estimate the annual mean spatial distribution of FFP (see Fig. 23).

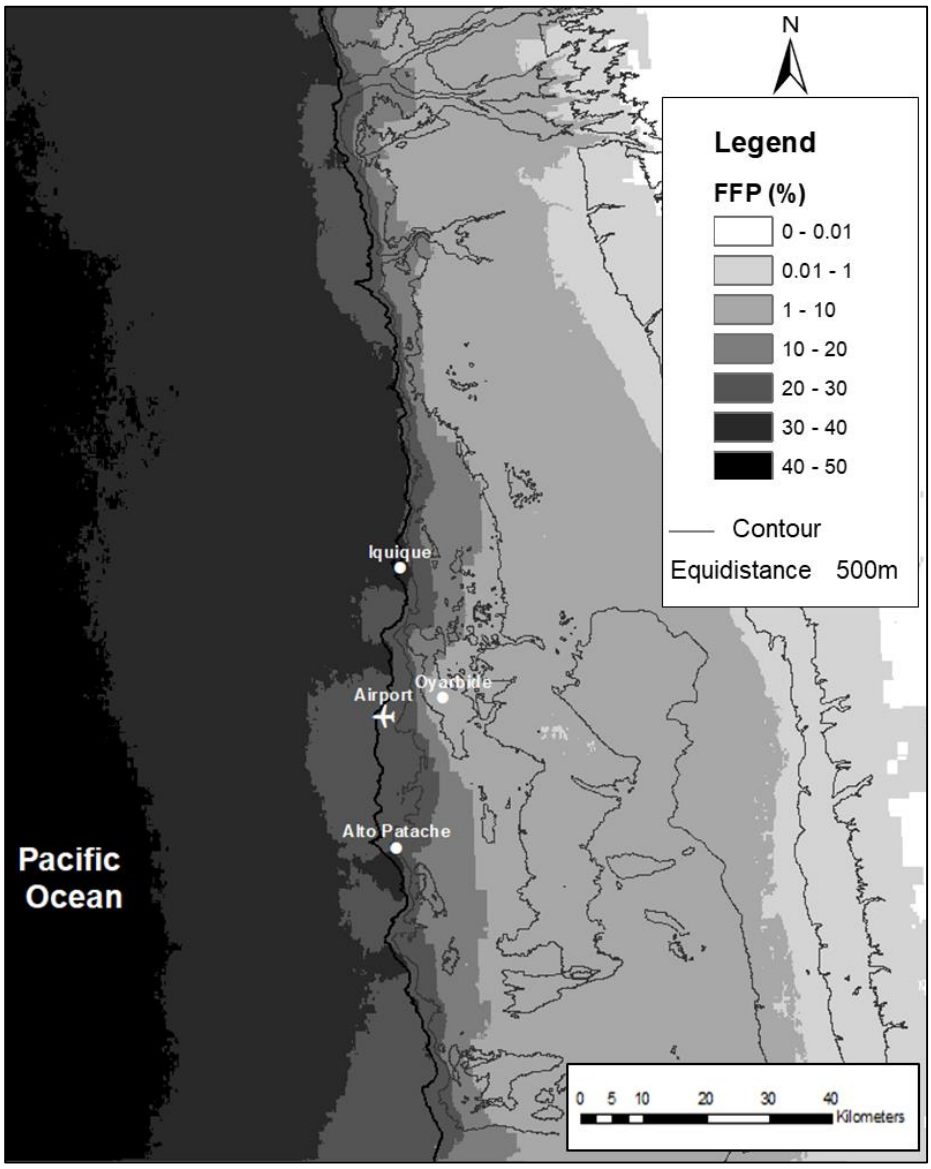

Figure 23: Average annual fog and low cloud frequency presence (FFP) for the study period (1995 - 2017).

Existing seasonal differences in FFP and distribution between February and September, representative of summer and winter-early spring respectively, is shown in Fig. 24. FFP is considerably higher during September, when the average FFP in offshore areas undergoes a transition from 80% to 50%, as you move closer to the coast, with clear north-south meridional bands that run parallel to the coastline (see Fig. 24B), corroborating Sc cloud

deck advection toward the coast and at the same time the influence of land on the distribution of coastal FLC.

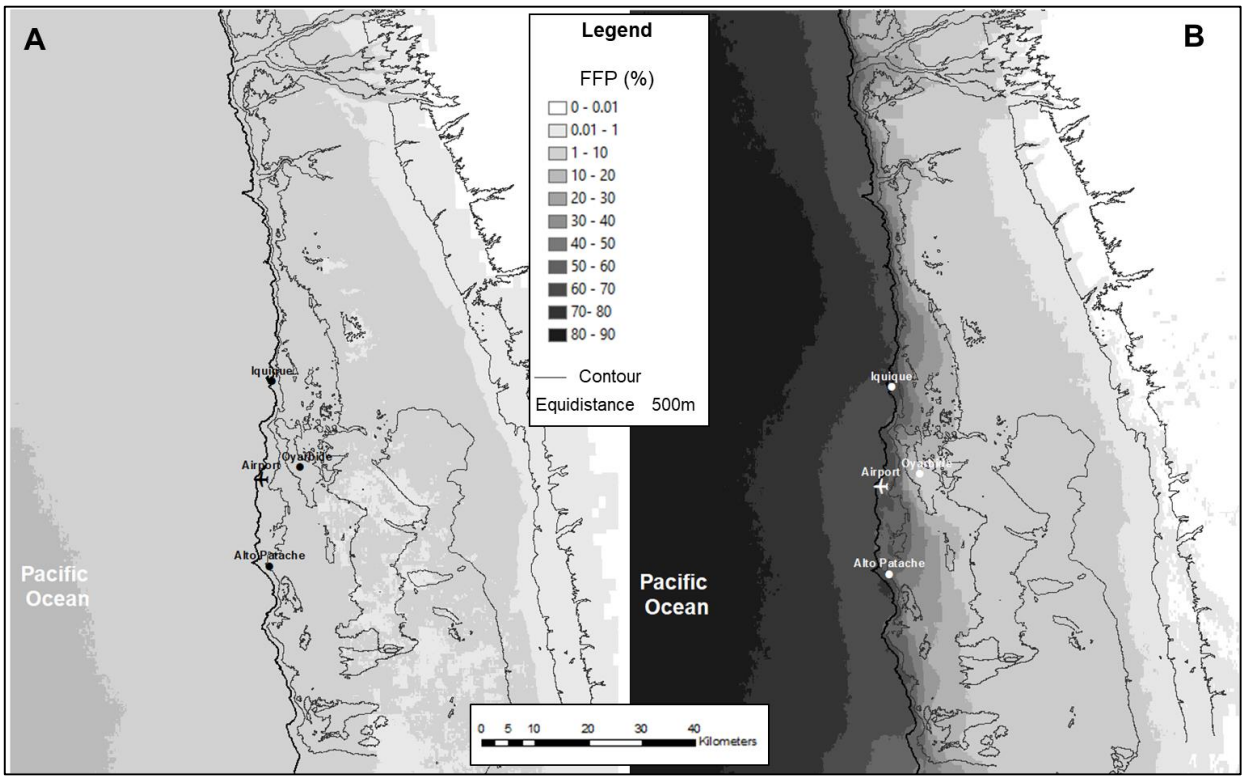

Figure 24: Fog and low cloud frequency presence (FFP) as a percent during the study period (1995 - 2017) for the months of (A) February, and (B) September.

In between the coastline and the first ~15 km onshore, which can be considered representative of the advective FLC belt, there is an average FFP of 50 to 20%, again showing a north-south meridional band pattern, in this case with higher spatial variability; this is a product topographic influence and a barrier effect on the FLC. The contours in Fig. 24B, denote the limit of inland FLC distribution, including areas with lower altitudes that act as topographic corridors for fog penetration. In inland areas, greater than ~15 km east of the shoreline, the presence of FLC decreases considerably, with an FFP of less than 20% over the Pampa and reaching zero FFP at the beginning of the Andes foothills, at altitudes over 1.500 to 2.000 m a.s.l. It is worth pointing out higher FFPs occur in areas where the coastline presents a southwest aspect and there exists elevated relief close to the coast (e.g. Alto Patache).

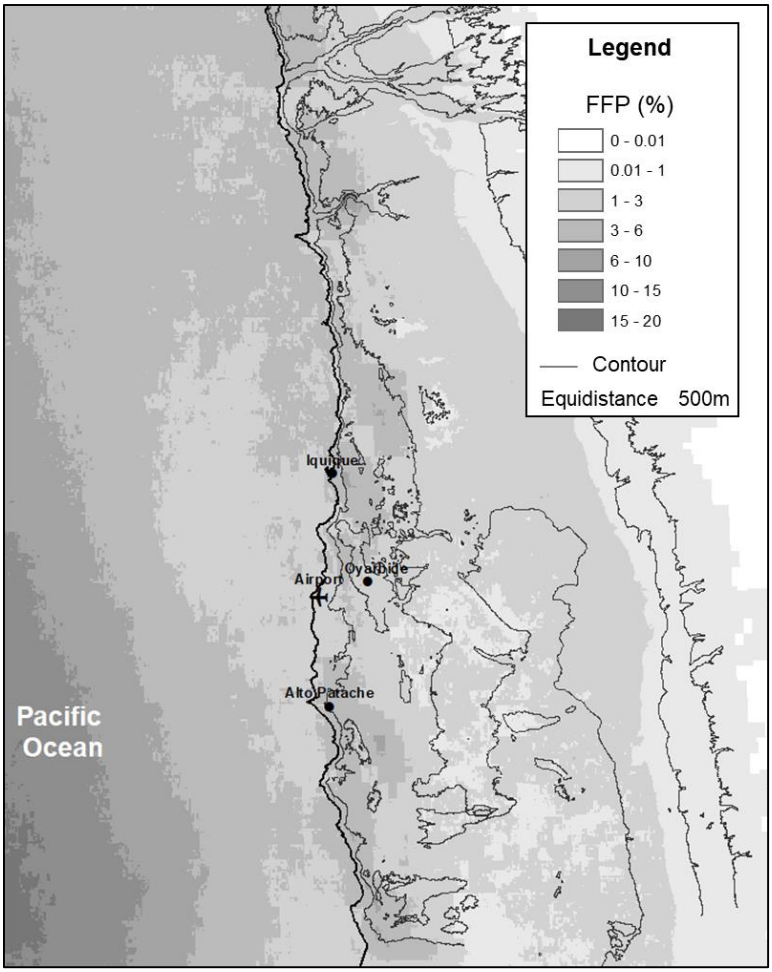

Figure 25: Fog and low cloud frequency presence (FFP) in percentages for February over the study period (1995 - 2017).

On the other hand, during February, the maximum FFP over the study area reached 10 to 20% in offshore zones; this maximum occurred at distance of ~50 km from the coastline, focused in the southern zone of the study area (see Fig. 24A). The areas close to the coastline, both offshore and onshore, present average FFPs between 1 and 10%, with practically no FFP beyond ~15 km inland (FFPs between 0 and 1%). Nevertheless, if the FFP classification ranges are reduced, it is observed similar north-south meridional bands patterns, similar to those observed in September (see Fig. 25), as well as higher cloud fragmentation in offshore areas near the coast and the influence of topography in onshore fog and low cloud distribution.

Satellite results reveal the expected seasonal differences in FPP, and also expose a decrease in the presence of Sc cloud over the ocean as you move closer to the coast. Additionally, they show that FLC cover decreases as you move from the coastline inland,

denoting the influence of fluxes in ocean-land thermodynamics and cloud dissipation due to surface heating.

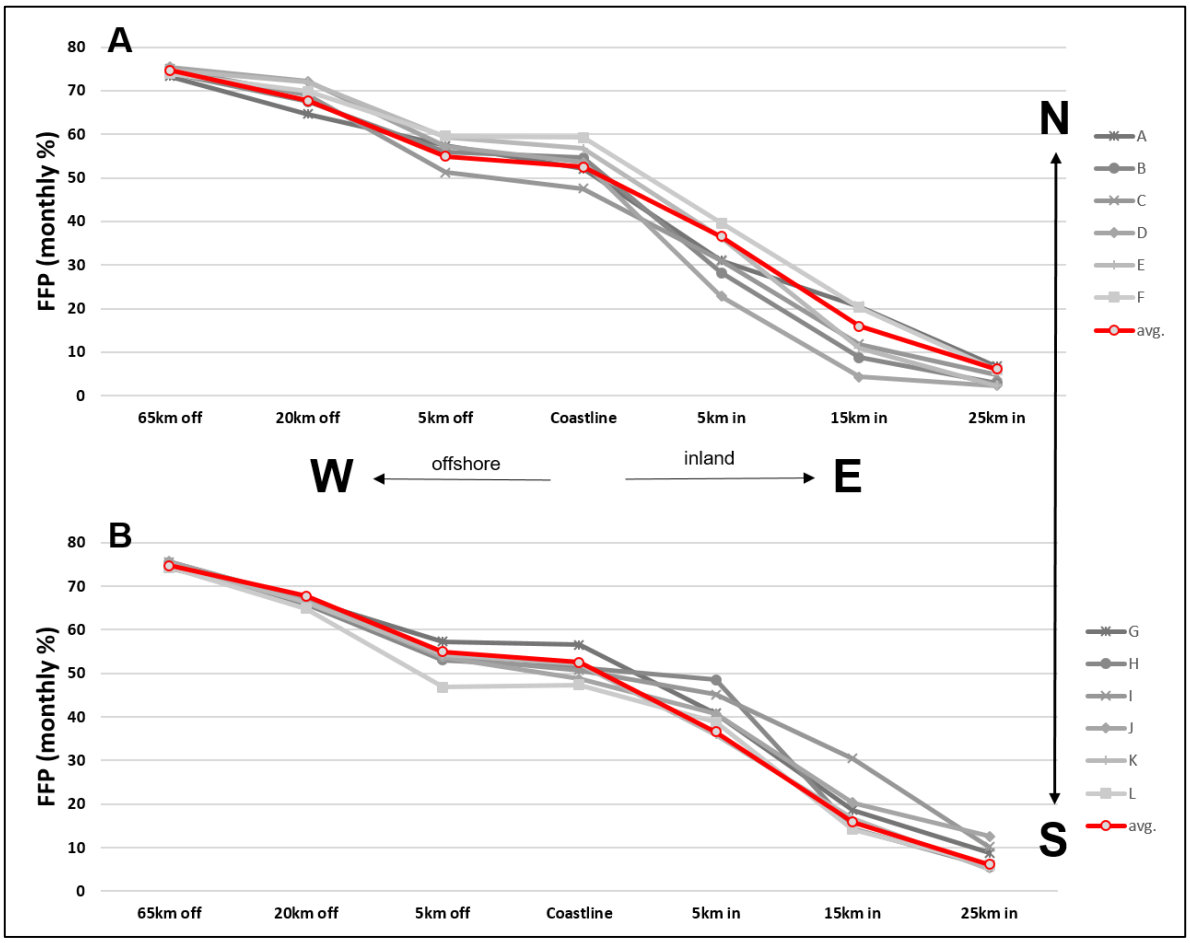

Figure 26: A west to east profile of FFP during the month of September at the systematic sampling areas. A) the northern section of the study area. B) the southern section of the study area. The red line is an average of the entire sample area (A to L profiles).

Figures 26 & 27 shows a west to east profile of FFP within the study period for the months of September and February, respectively. These profiles show the latitudinal variability along the sampled areas (~21 km). During September FPP variability increases near the coastline and especially in areas of the Coastal Cordillera (5-15 km inland), where the topography and the daily ocean-land fluxes influence the spatial distribution and presence of the FLC. The average FFP and associated SD in inland sampling areas is as follows: at 5 km: 37 ± 7%, at 15 km: 16 ± 7%, and at 25 km: 6 ± 3%. The three inland areas present higher FFPs in the southern zone of the study area. The average FFP and related SD at the coastline and 5km offshore is very similar, ~54 ± 4%, with no significant latitudinal differences. FFP

variability decreases as you move away from the coastline (68 ± 2% at 20 km offshore and 75 ± 1% at 65 km offshore), revealing a regular and stable presence of Sc clouds at the sampling areas located furthest offshore.

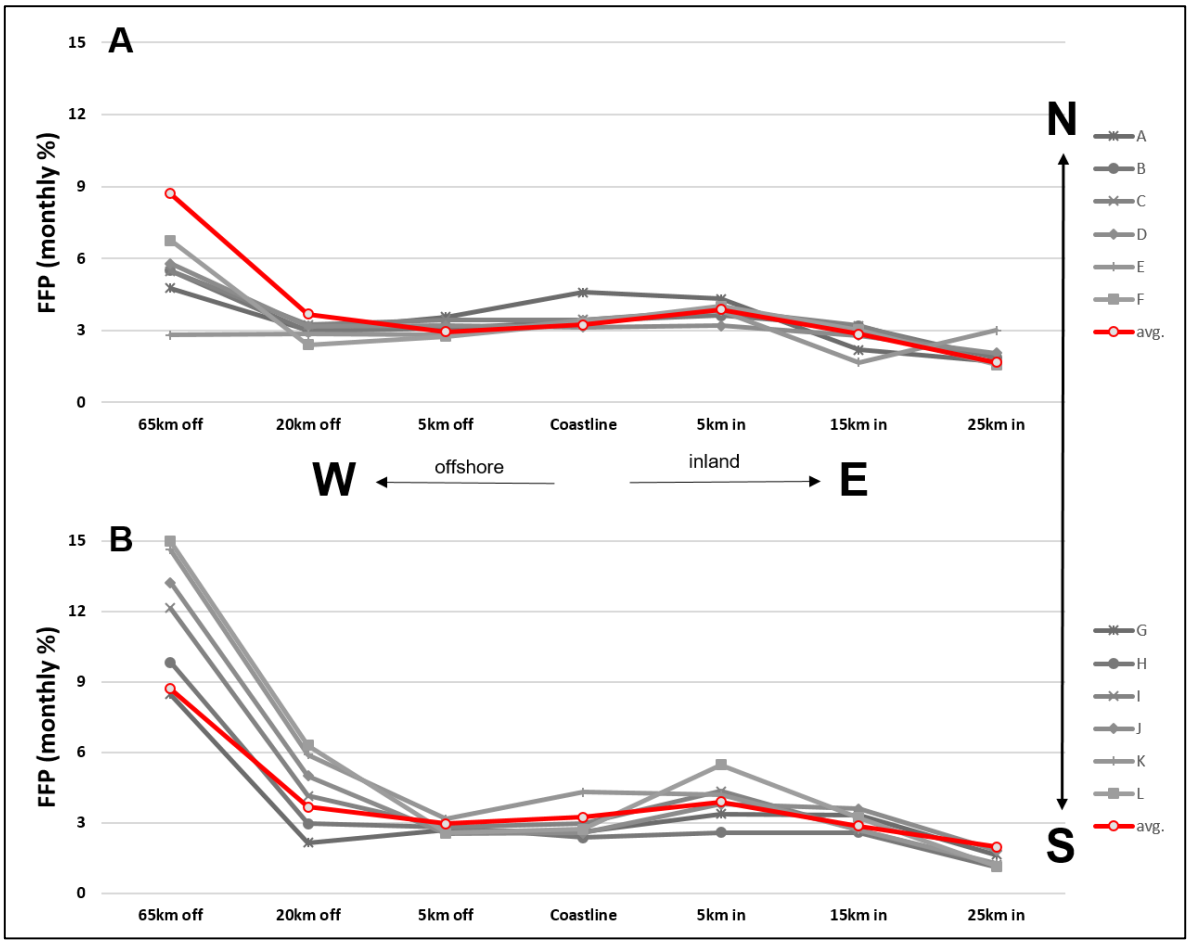

Figure 27: A west to east profile of FFP during the month of February at the systematic sampling areas. A) the northern section of the study area. B) the southern section of the study area. The red line is an average of the entire sample area (A to L profiles).

On the other hand, the significantly lower FFPs observed in February, as compared to September, make it difficult to compare dispersion between both these two time periods. Nonetheless, February presents higher latitudinal variability in the zone 65 km offshore (average FFP and SD: 9 ± 4%), with higher FFPs in the southern section of the study area; this pattern is also observed, but to a lesser degree at 20 km offshore (4 ± 1,3%). The other sampling sites near the coastline, both offshore and inland site, present low FFPs, with a mean and SD of ~3 ± 0,5%.

Average FFPs at the 5 time points analyze for September and February show seasonal differences. During September, while the 5 time points present a discernable north-south meridional bands distribution, there are also significant quantitative and spatial differences, as well as a higher cloud fragmentation in certain offshore areas (see Fig. 28), which is not observed clearly when looking at the average for the entire period (Fig. 24B). At dawn and dusk, higher FFPs occur over both the ocean and coastal areas. From midnight to early morning, there is a successive progression in Sc cloud formation and advection toward the coast, which is finally trapped by the Coastal Cordillera, confirming the higher presence of fog during the night and early morning. At dawn, principally in the southern part of the study area, fog penetrates inland through topographic corridors, covering a wide area of the Pampa. Contrary, at noon and at sunset, there is a lower FLC presence, with lower FFPs over the ocean and coastal areas. At noon, surface heating dissipates cloud presence, decreasing FFP significantly in the coastal offshore areas. An interesting pattern of distribution can be observed at sunset, when a thin band of higher FFPs occurs between the coastline and the coastal cliffs, which are enhanced in the coastal zones with a south, southwest orientation. At the same time, in the coastal offshore areas, zones with lower FFPs can be observed along the northern side of prominent peninsulas that face regular southerly winds; this is the case in the areas of Alto Patache and Pisagua.

Fig. 29 describes and quantifies FFPs at the sampled areas at the 5 time points, allowing us to describe the daily cycle present in different zones. Fig. 29A shows that in the westward offshore area the maximum FFP occurs at dawn, while in the near coast and onshore areas the maximum FPPs occur during the night, specifically around midnight. The minimum FFP in all areas occurs at noon. Fig. 29B shows the daily maximum and minimum FFPs according to the analyzed zone. Over the ocean, at 65 km offshore, maximum FFPs occur at dawn (07:39 local) and at night (00:39 and 04:39), when a clear Sc cloud deck is present with an average FFP of 82 and 75%, respectively. Minimum FFPs in this zone, while still relatively high (over 70%), occur at sunset (19:39) and midday (12:39). At 20 km offshore, the highest presence also occurs dawn and during the night, with average FFPs of over 80 and 75%, respectively. The minimum occurs at sunset, with a significant drop in presence to an average of 50%. Towards the coast the FFP decreases; at 5km offshore and over the coastline, the mean is practically the same, with slightly higher presence during night than at dawn (~70% and 65%). However, higher fragmentation of the Sc cloud can be observed throughout the night in the northern section of the study area, a pattern that is not observed

at dawn. The minimum in this area occurs at noon, with a FFP of less than 40%. In the inland areas, there is a prominent decrease in FFP at all hours

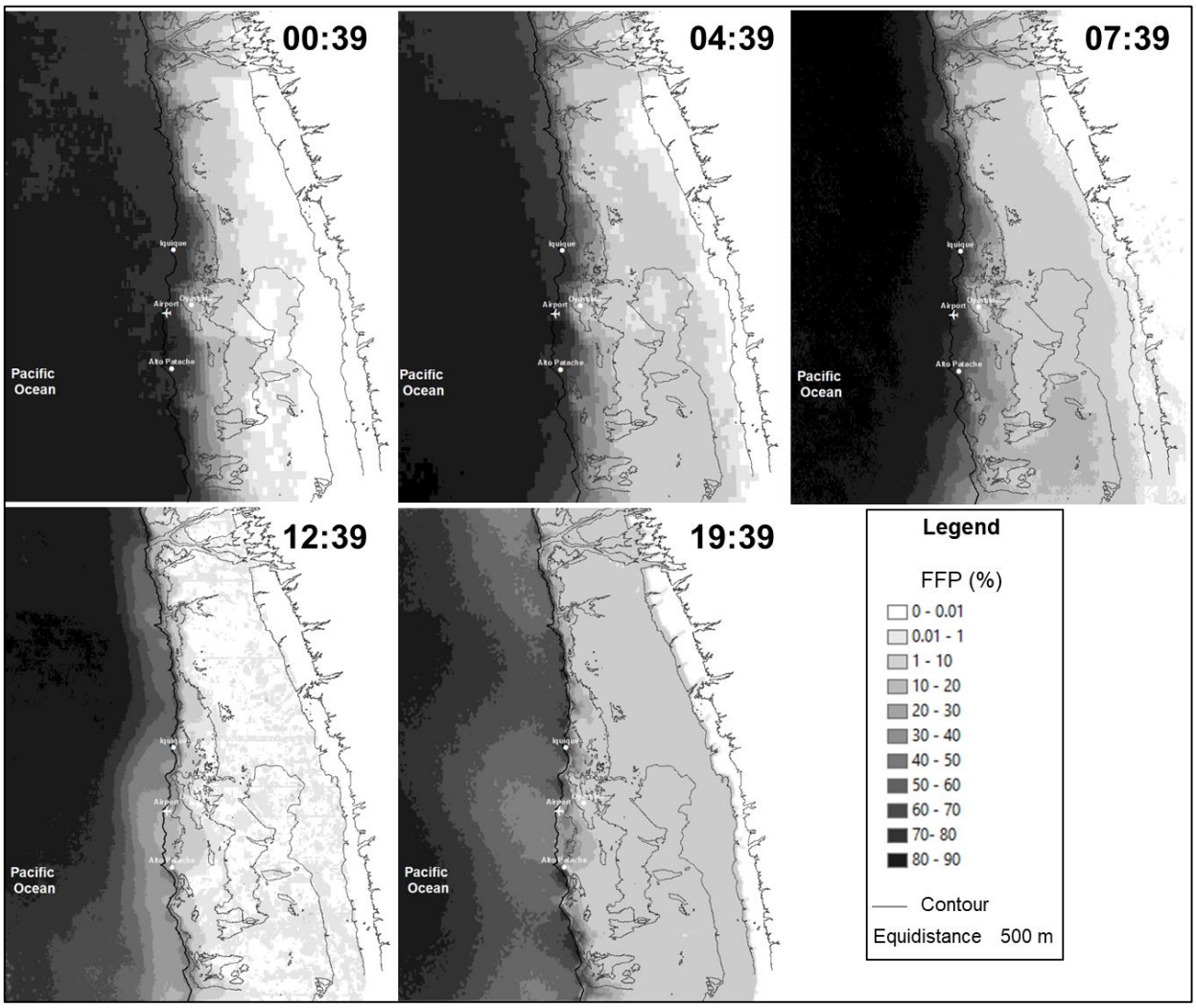

Figure 28: September FFP means within the study period (1995-2017) at the 5 time points analyzed (local time).

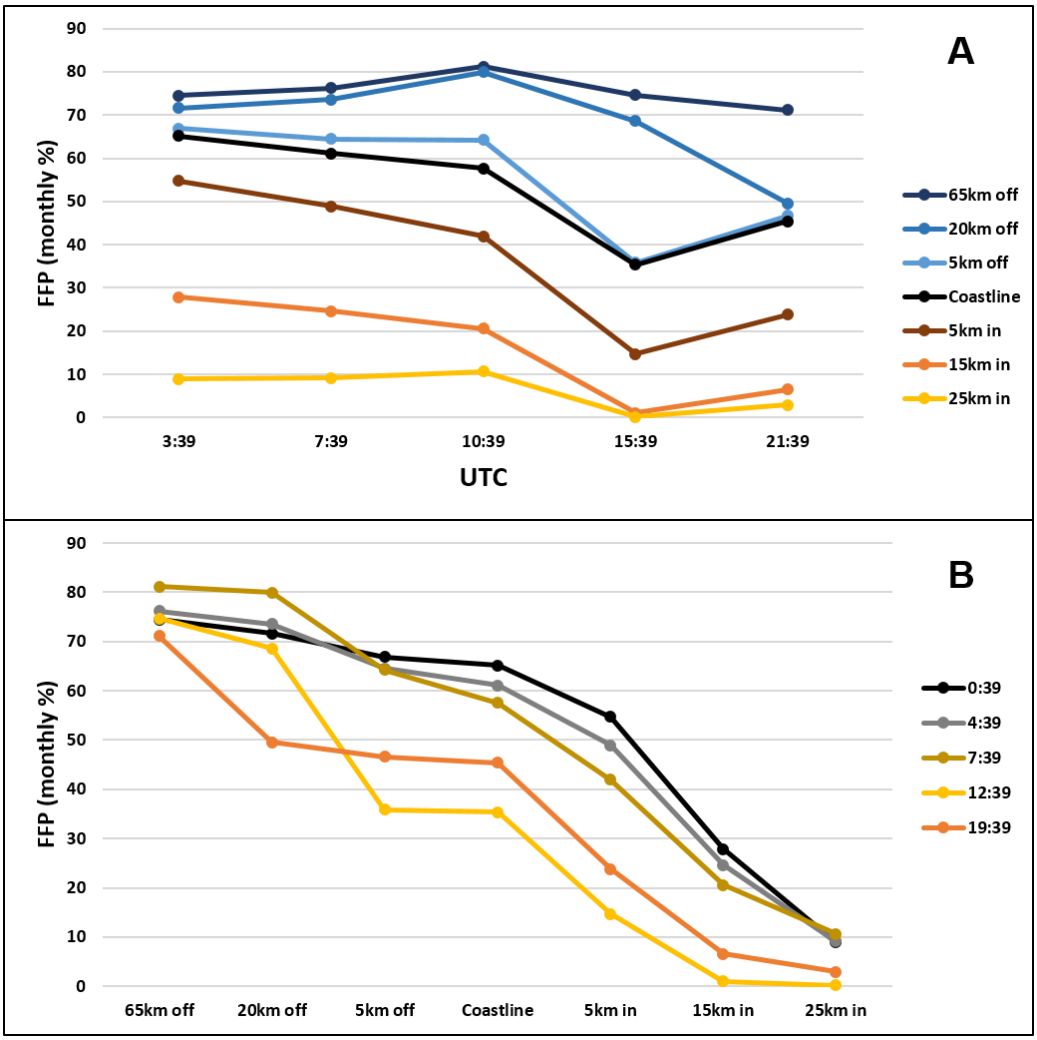

Figure 29: Daily FFP cycles at the different analyzed zones for the month of September.

FFPs in February also vary by time of day (see Fig. 30. Note that the classification ranges are significantly lower than September). The higher cloud fragmentation that occurs during February is notable. This fragmentation is observed independent of the zone and time of day; however, you can barely distinguish the north-south meridional band pattern. No zones present an FFP of more than 10%, with the exception of the offshore areas farthest from the coast. Maximum FFPs are observed at dawn and dusk. Interestingly, the areas with higher onshore FPPs are located over the Coastal Cordillera and are disconnected from the Sc cloud deck, therefore, there is a wide coastal offshore area with low FFPs (1-3%). At night there are very similar FFPs in the offshore and inland areas, and like September, you can observe progressive development and advection of the Sc cloud deck toward the coast from the southwest from midnight to early morning. Minimum FFPs are observed at midday, with

almost no (0,01 – 1%) inland cloud presence, despite higher presence (1-3%) in specific areas of the northern section; this pattern is replicated in the coastal offshore areas.

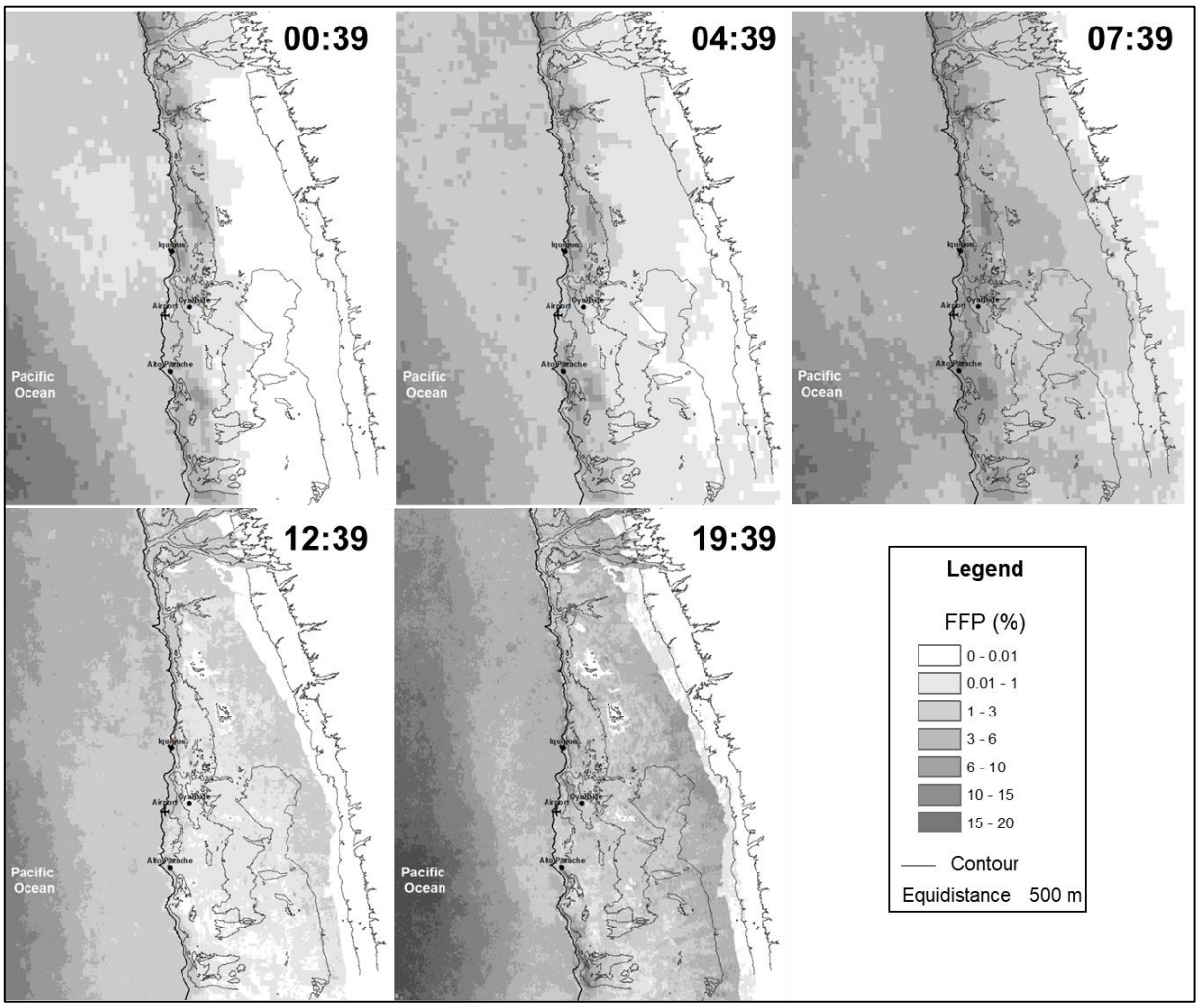

Figure 30: February FFP means within the study period (1995-2017) at the 5 time points analyzed (local time).

Fig. 31 describes and quantifies FFPs at the sampled areas at the 5 time points, allowing us to describe the daily cycle present in different zones for the month of February. The daily cycle presents maximum FFPs at dawn in all the locations, with the exception of the areas 65 km offshore, where FFPs are considerably higher at sunset (see Fig. 31A). Minimum FFPs vary slightly depending on whether looking at offshore (midnight) or inland (noon) areas. In any case, as the FFP values are very low, the variations are not significant (~ 2-3%). Fig. 31B shows the daily maximum and minimum variations in FFP according to the analyzed zone. At night and early morning presents magnitudes vary, with maximum FFPs

in the offshore area and decreasing toward the coast (minimum at 5 km offshore), then increasing to 5km onshore, when they begin to decrease again as you move inland. On the other hand, at midday and sunset, maximum FFPs occur in the 65 km offshore areas, then decrease significantly toward 20 km offshore, and then decrease gradually until 25 km inland.

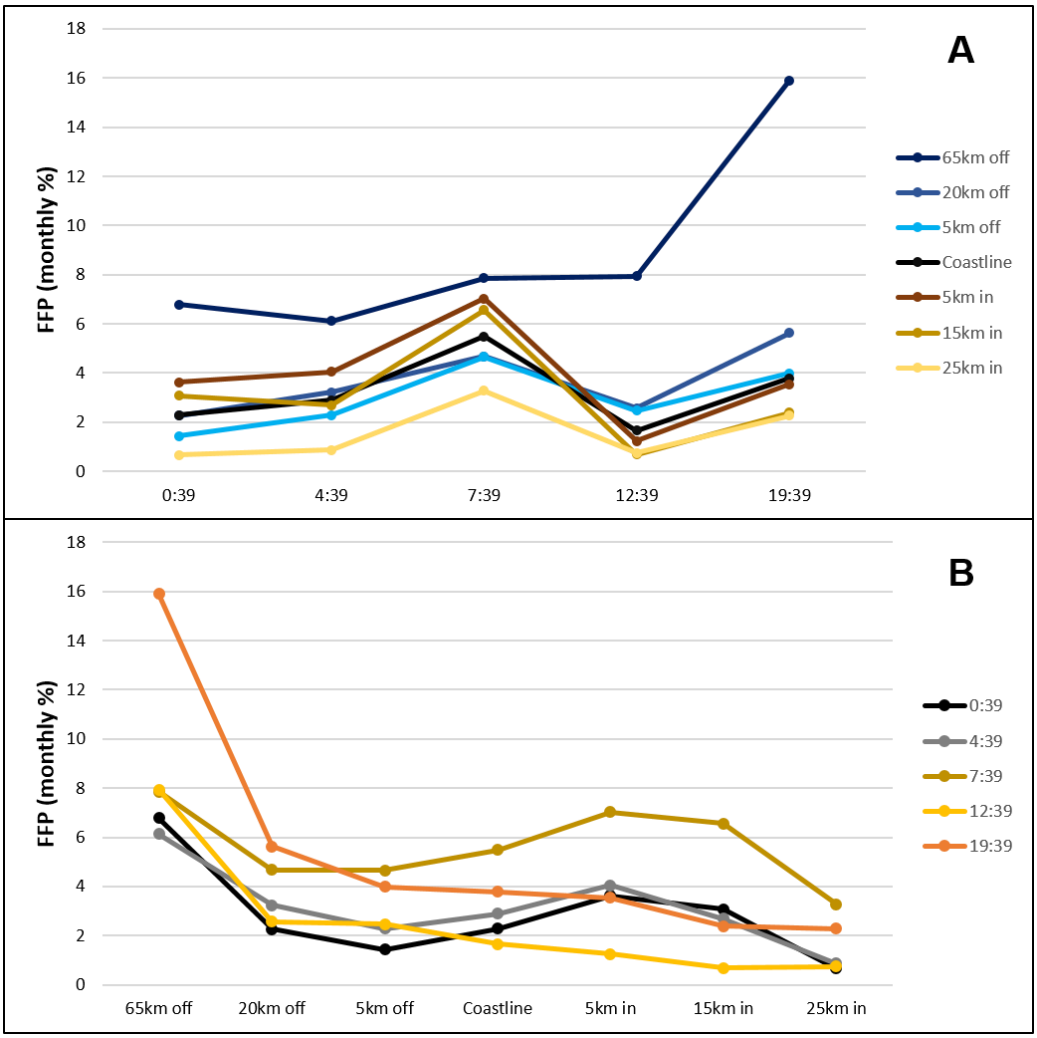

Figure 31: Daily FFP cycles at the different analyzed zones for the month of February.

Based on satellite results a cluster analysis was generated in order to determine homogeneous areas that present similar spatiotemporal behavior in FFP values. Given the advective condition of the phenomenon under study, the presence of the Coastal Cordillera and the presented offshore-onshore FFP distribution and variability, five clusters were defined. Fig. 32 shows the clusters for September, presented for individual time points and the daily mean. Following, as expected, similar patterns of distribution as the FFP maps (see

Fig. 28), the cluster analysis set for nighttime (00:39 and 04:39) presents one main cluster for the ocean (N°1), which reaches the coast in specific areas (e.g. Alto Patache and Iquique), and presents an average FFP of 73%. Then two clusters for the areas closer to the coast, which oscillate between offshore and onshore (N° 2 and 3), present an FFP mean of 64 and 59%, respectively. Cluster N°4, located ~15 km onshore along the coast, shows a significant decrease in FFP (~18%). The last cluster, N°5, covers the inland areas greater than 15-20 km from the coast, and presents an FFP of less than 1%. For the clusters formed at dawn, there is one cluster over the ocean (N°1) with a nearly regular distance from the coast of 15 km, with an FFP mean of 81%. Cluster N°2, is located along the coast offshore and has an FFP of 68%. Cluster N°3 primarily covers the nearshore inland areas, with a mean FFP of 42%. Cluster N°4 highlights FLC corridors inland (FFP = 15%), and a final cluster (N°5) comprises the rest of the inland areas (FFP = 3%). At noon, four clusters form over the ocean, one in the northern offshore section (N°1) with a FFP mean of 77%. Cluster N°2 covers the southern offshore section (FFP = 69%), and a third cluster (N°3) formed over the ocean along the coast, only reaching the coastline slightly in the northern part (FFP = 52%). Cluster N°4 covers the first 1-5 km onshore and an area of 10-15 km offshore in the southern section, and presents an FFP of 28%. Cluster N°5 incorporates almost all of the inland area, with an FFP of less than 1%. At sunset, three cluster formed over the ocean; cluster N°3 near the coast, in three different oval areas (FFP = 44%), then cluster N°2 surrounds cluster N°3 (FFP = 56%), with another cluster offshore to the west (N°1; FFP = 69%); cluster N°4 primarily comprises coastal and local onshore areas (FFP = 26%), and cluster N°5, covers all inland areas (FFP = 2%). Finally, the daily average, presents a strong north-south band pattern, with three clusters over the ocean: 1) concentrated in the southwest (N°1) with the highest FFP (74%); 2) spans north to south, but concentrated primarily in the northern section (FFP = 71%); and 3) covers the first ~20 km offshore and some specific onshore areas, primarily under 1.000 m a.s.l, with an FFP of 58%. Cluster N°4 covers inland areas from the coastline to ~20 km onshore (FFP = 22%), and cluster N°5 represents a wide inland area with a consistently low presence of FLC (FFP = 2%).

In the case of February, lower FFP and higher cloud fragmentation produced clusters that exhibit less compact cluster areas; additionally, the north-south band pattern is less defined that in the September clusters. At midnight, the cluster N°1 is present in the southwest offshore area (see Fig. 33) with an average FFP of 12%. Cluster N° 2 and 3 surround the first cluster over the ocean and also cover limited onshore areas (FFP = 7 and 3%,

respectively). Cluster N°4 covers a wide area over the ocean and specific areas near shore, with a mean FFP of 1,5%. The last cluster primarily covers the inland areas farther than 15-20 km from the coast (FFP = >1%). At 04:39 and 07:39, clusters show high fragmentation, with cluster N°1 in the southern offshore area (FFP ~10%). Then clusters N°2 and 3 are divided over the ocean and coastal areas (FFP = 5 and 3%, respectively). Cluster N°4 is distributed over inland areas (FFP = 2%). Cluster N°5 is in the eastern areas with an FFP of less than 1%.

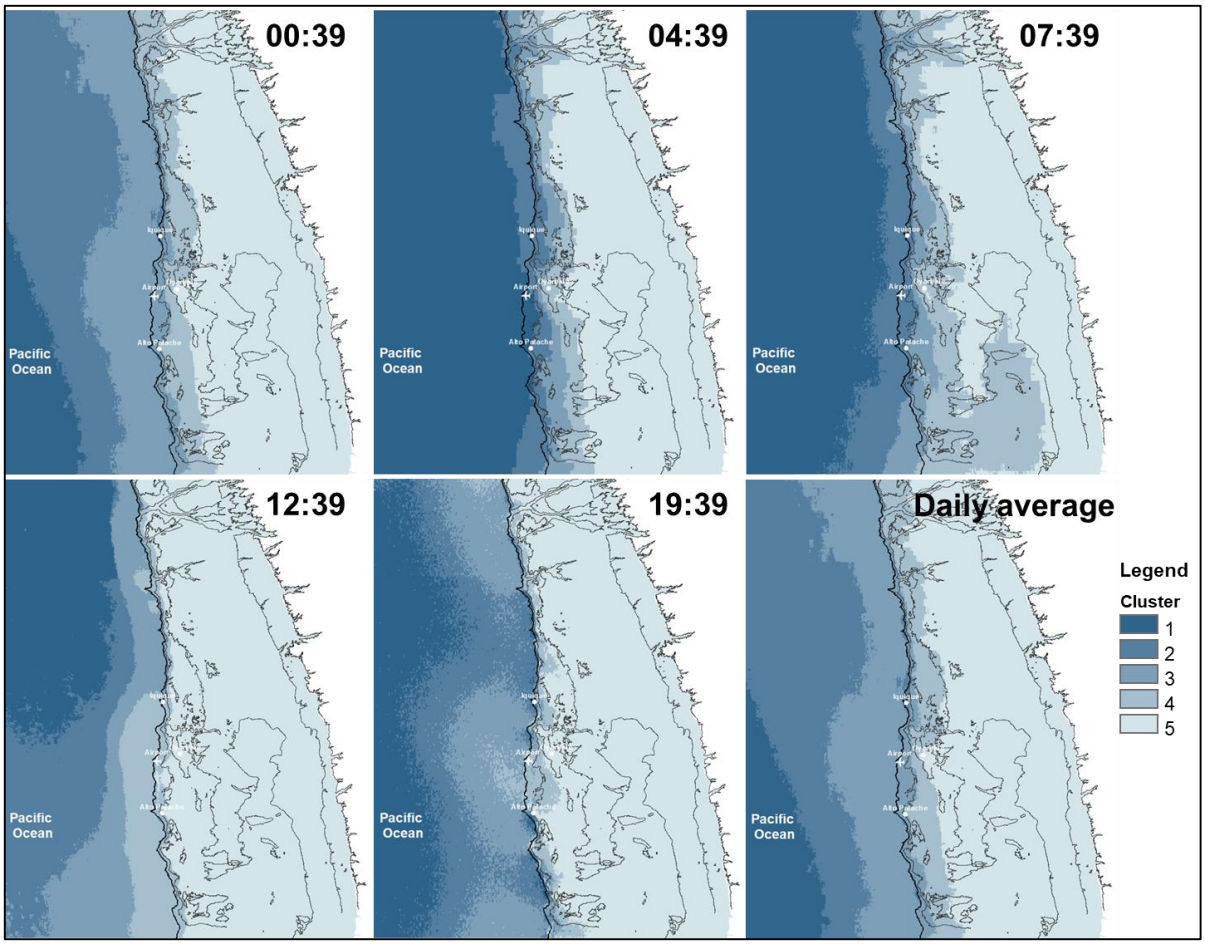

Figure 32: Cluster areas of fog and low cloud frequency presence for September.

At noon, the three clusters over the ocean (N°1, 2 and 3) show a north-south pattern and present FFPs of 9, 5 and 2%, respectively. Clusters N°4 and 5 in the inland areas present FFPs of less than 1%. At sunset, clusters N°1 and 2, located in the western offshore areas present FFPs of 19 and 11%, respectively. Cluster N°3 covers the nearshore area, with an FFP of 5%. Cluster N°4 is primarily over inland areas, but also covers limited offshore areas (FFP = 4%). Cluster N°5 is dominantly over the inland areas with an FFP of less than 1%.

Finally, when looking at the daily average, we see the most defined north-south and ocean-land trends in the clusters. Cluster N°1 and 2 are over the ocean and present FFPs of over 12 and 6%, respectively. Cluster N°3 occurs over a wide offshore area and the first ~10 km inland, with an FFP of 3%. Clusters N°4 and 5 occur in the inland areas with FFPs of around 1%.

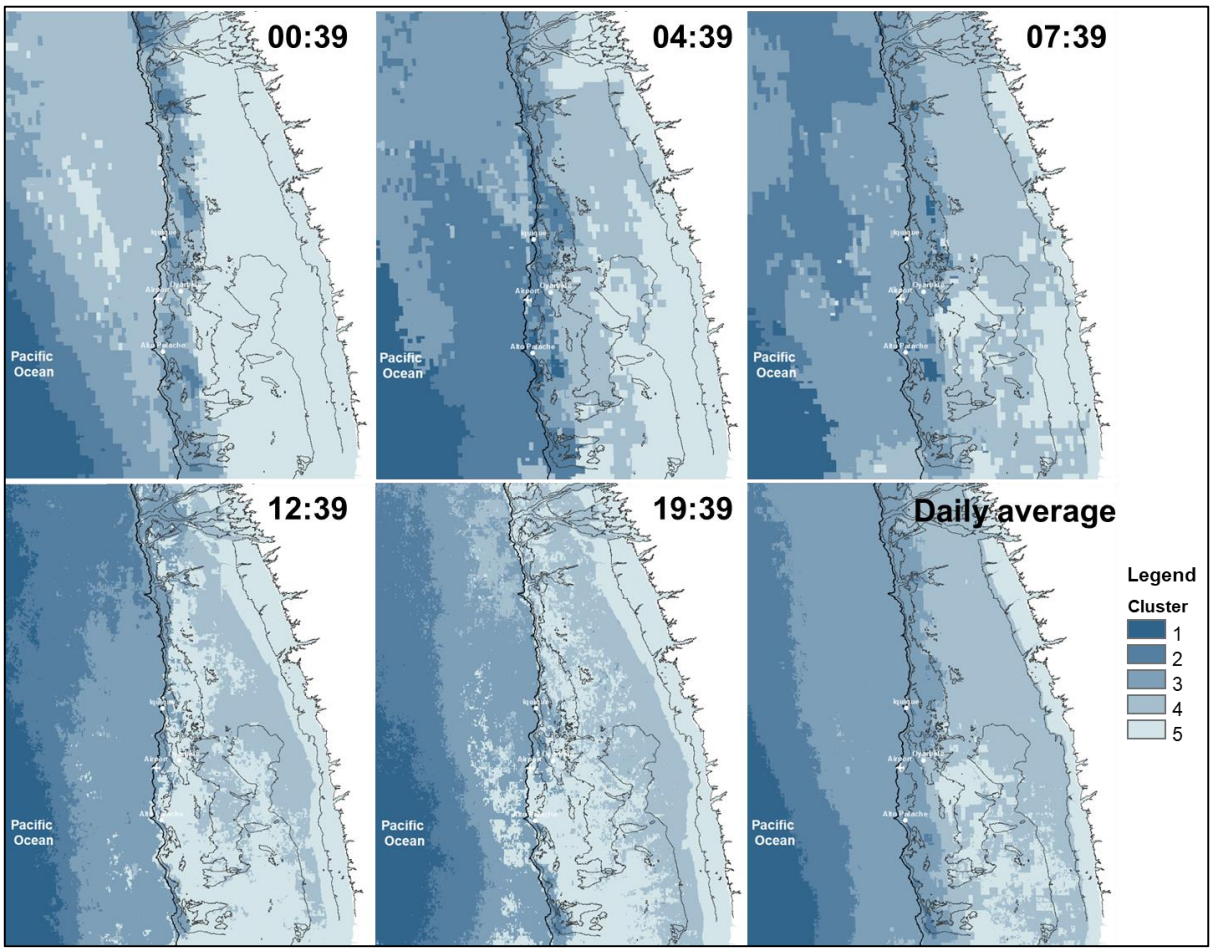

Figure 33: Cluster areas of fog and low cloud frequency presence for February.

6.2 Inter-annual variability and trends in fog and low cloud presence

Satellite identification of FLCs for September and February within the study period (1995-2017), allows us to determine tendencies in FFP and its inter-annual variation. When analyzing FFP trends by month, for the five sampled time points, and as a daily average, noteworthy spatial and statistical significances can be seen. Based on the cluster area using daily averages for September (see Fig. 32), it is possible to observe a trend in differences

between the ocean, near the coast (both onshore and offshore) and inland areas. The median trend slope (*m*) and its statistical significance (*p* value) are presented in Table 4.

	Cluster 1		Cluster 2		Cluster 3		Cluster 4		Cluster 5	
Time of day	*m*	*p*	*m*	*p*	*m*	*p*	*m*	*p*	*m*	*p*
0:39	0,012	0,000	0,001	0,000	0,010	0,001	0,000	*non*	-0,001	*non*
4:39	0,009	0,001	0,009	*non*	0,010	*non*	-0,001	*non*	0,000	*non*
7:39	0,010	0,005	0,006	*non*	0,005	*non*	0,007	*non*	0,003	*non*
12:39	0,006	*non*	0,007	*non*	0,006	*non*	0,000	*non*	-0,001	*non*
19:39	0,008	*non*	0,007	*non*	0,004	*non*	0,000	*non*	0,001	*non*
Daily avg.	0,010	0,000	0,009	0,000	0,008	0,002	0,001	*non*	0,001	*non*

Table 4: September fog and low cloud slope (*m*) and significance (*p* value) for analyzed hours, based on cluster areas for the daily average.

The daily average in September over the ocean area (clusters 5 and 4) shows a weak, but statistically significant, positive trend (*m* = ~0,01); this same trend is also present in cluster 3, which primarily covers the near coast, offshore and also some onshore areas, revealing, an increase in the average FFP of ~20% for the study period. For the onshore areas near the coast, as well as the inland areas (cluster 2 and 1), the trend was nearly neutral (*m* = 0,001), however not statistically significant, which is expected due to the continuous very low FFPs in this area. Analyzing the individual time points, a weak positive trend is present over the ocean at night (00:39 and 04:39) and at dawn (07:39), but is only statistical significant for clusters 5 in the three time points, and for clusters 3 and 4 at 00:39. Over the ocean at noon and sunset, despite a weak positive trend (*m* = ~0,007), the clusters are not significant. In the onshore areas (clusters 2 and 1), the consistently low fog presence, due to the dissipating land heat effect at all times analyzed, present trends that are around 0 (positive or negative), with the exception of dawn, when there is a weak but not significant positive trend (*m* = ~0,007).

Considering the statistical significant of the clusters, the spatial distribution of the FFP estimated from median trend slopes using a pixel-by-pixel method is shown in Fig. 34. In the figure is possible to observe the differences between the ocean and near shore and inland areas; additionally, specific spatial variations within the analysis area, which are primarily influenced by the altitude and orientation of the Coastal Cordillera, can be observed. The weak positive trends mainly occur over the ocean at various hours, but with higher notoriety

at 00:39 and 04:39, which is consequently reflected in the daily mean. At dawn, specific onshore zones near the coast demonstrate higher trends (m = 0,026 – 0,032), however there is no clear geographical pattern. At noon and sunset, in practically all onshore areas the trends are 0, as expected given the very low or nonexistent FFP. On the other hand, for onshore areas at night and dawn the trend magnitude and sign is closely related to the altitude. Fig. 34 shows that over onshore areas between the coastline and ~1.000 m a.s.l. a weak-positive slope prevails, and above this altitude (1.000 m a.s.l) limited areas present a weak-negative trend (e.g. over Oyarbide), evidence of the relationship between FFP trends and the thermal inversion layer altitude and topography.

For February, low FFPs and less regular cloud deck formation are expressed through higher low cloud fragmentation, which manifests as a practically null FFP trend over the study period with no statistical significance in any of the studied zones (ocean, near shore or inland, based on the same cluster areas used for September) for the analyzed hours. In any case, and considering they are not statistical significant, Fig.35 shows the few areas where there is a very low trend (slopes between -0,003 and 0,006). Focusing mainly on the daily mean map, a null trend over the ocean can be observed, with the exception of the southwestern part of the study area, where negative but fragmented trends are present. In the near coast onshore area, there are limited sectors with a very weak positive; this mirrors findings for the early morning, with no clear geographical patterns. Finally, inland areas above 1.200 m a.s.l. present a desegregated, very weak negative trend.

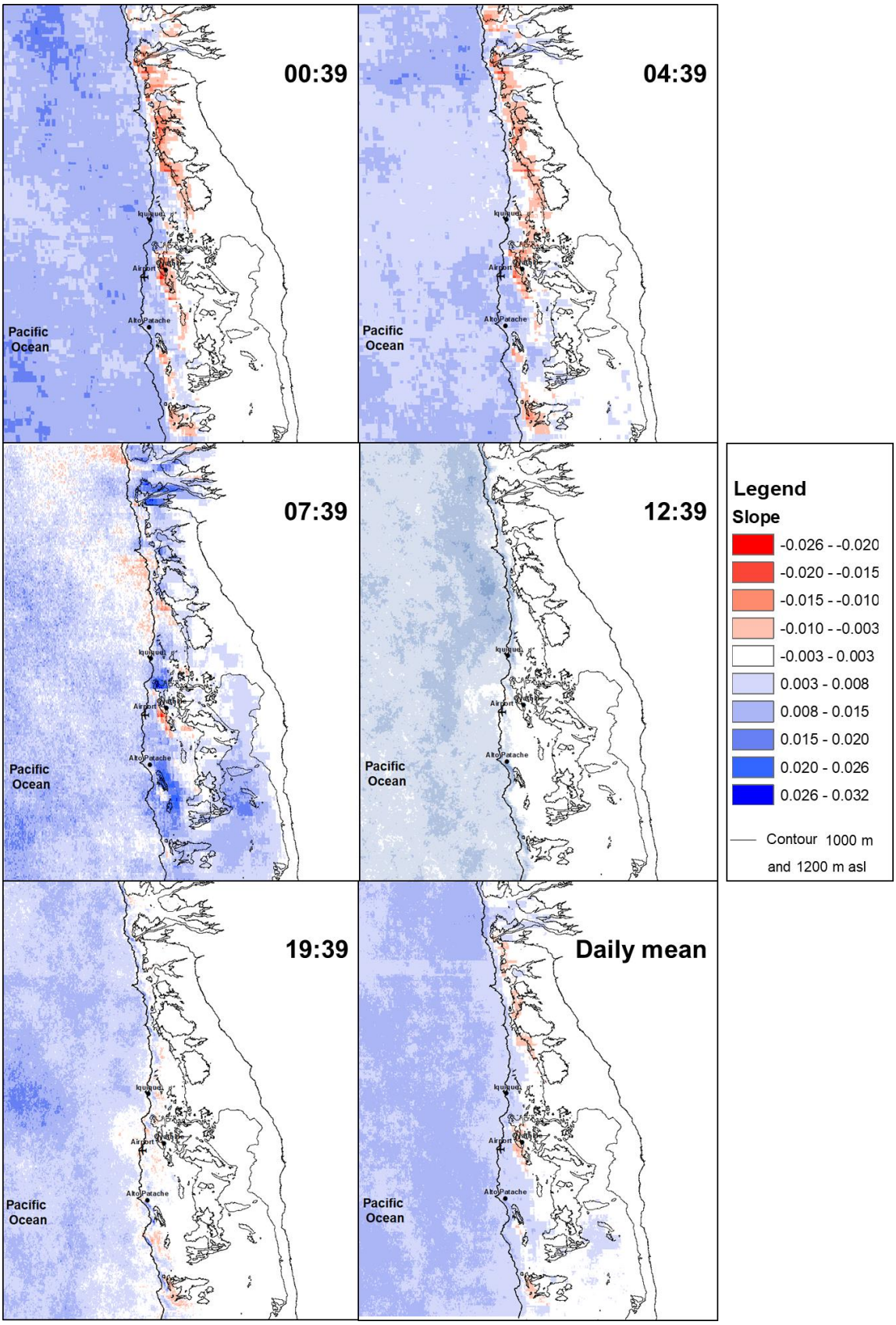

Figure 34: Hourly fog and low clouds trend slope for September (1995 – 2017).

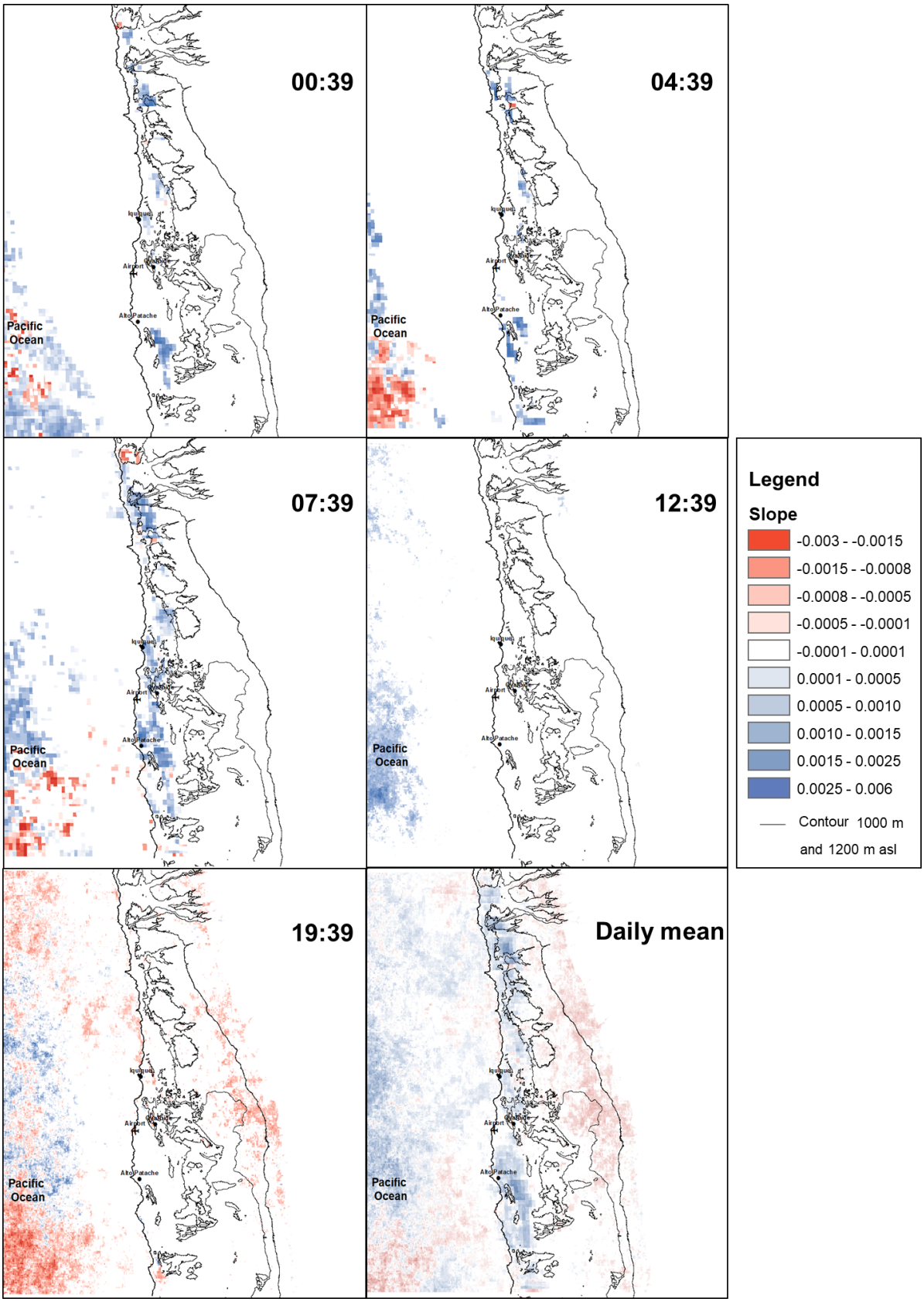

Figure 35: Hourly fog and low cloud trend slope for February (1997 – 2017).

Analysis of the hourly and daily means of the systematically sampled areas allowed us to describe inter-annual variability in the different zones. During September, inter-annual variability (SD) in the daily mean is lower in offshore areas (65 km and 20 km offshore), areas with higher FFP percentages. Variability then increases toward the coast, with higher variability 5 km offshore than over the coastline and 5km onshore, where it increases again at 15 and 25 km inland. The inter-annual variability, shows that the areas 65 km offshore have a mean FFP of 75% (SD = 9,5), with extremes that goes from a unique minimum of 45% in the year 1997, which is within a period of 6 years (1995–2000) with the lowest FFP values for the study period (see Fig. 36). On the other hand, the maximum was 87% in 2011; nevertheless, several years had values over 80% (e.g. 2003, 2004, 2007, 2008, 2009, 2012, 2013, 2015 and 2016). At 20 km offshore the average FFP was 68% (SD = 10), with a minimum in the year 1997 of less than 40%; the annual minimum FFP was under 60% from 1995 to 1998. The maximum occurred in 2011, the only year FFPs reached over 80%; the next highest FFP was 78%, which occurred in 2007 and 2012. At 5 km offshore the mean FFP was 55% (SD = 9.5); the minimum, of less than 30%, also occurred in 1997, and the only years with a minimum of less than 50% were during the first 6 years of the study (1995–2000). The maximum at 5 km offshore occurred in 2007 and is the only year with more than 70% FFP. The coastline had a mean of 52% (SD = 8,4); this area shows similar patterns to the offshore areas, with minimums occurring during the first 6 years of the study period, reaching its lowest value of ~30% in 1997. The maximum occurred in 2007 (67% of FFP); there were 3 other 3 years with FFPs of over 60%, 2009, 2012 and 2013. At 5 km inland the average FFP was 36% (SD = 5,5), with the minimum of less than 28% occurring in 2005. In 1997 the FFP was nearly as low. Maximum FFPs occurred in the years 2012 and 2013 (46 and 44%, respectively). At 15 km inland, the mean was 16% (SD = 3,2), and the minimum occurred in 2005, with an FFP of less than 10%. Maximum FFPs occurred in the years 2001 (23%) and 2012 (21%). Finally, the areas 25 km inland had a mean FFP of 6,2% of FFP (SD = 2,1), and the minimum of around 3% occurred during the years 2005 and 2011; maximum FFPs of about 10% of occurred in the years 2001 and 2012. The inter-annual variability of the 5 time points in September, show, as expected, similar patterns to the daily mean, with lower variation over the ocean and near shore areas, and higher variation in the inland areas (see Fig. 37). Despite variations in FFPs at the sampled time points, variability was higher at noon and sunset for all samples areas, particularly from 5 km offshore toward the inland. Conversely, lower variability was observed at dawn and at night. Variability at dawn is likely

influenced by the fact that there are no measurements for the year 1997 at 07:39, the time point typically with the lowest FFP.

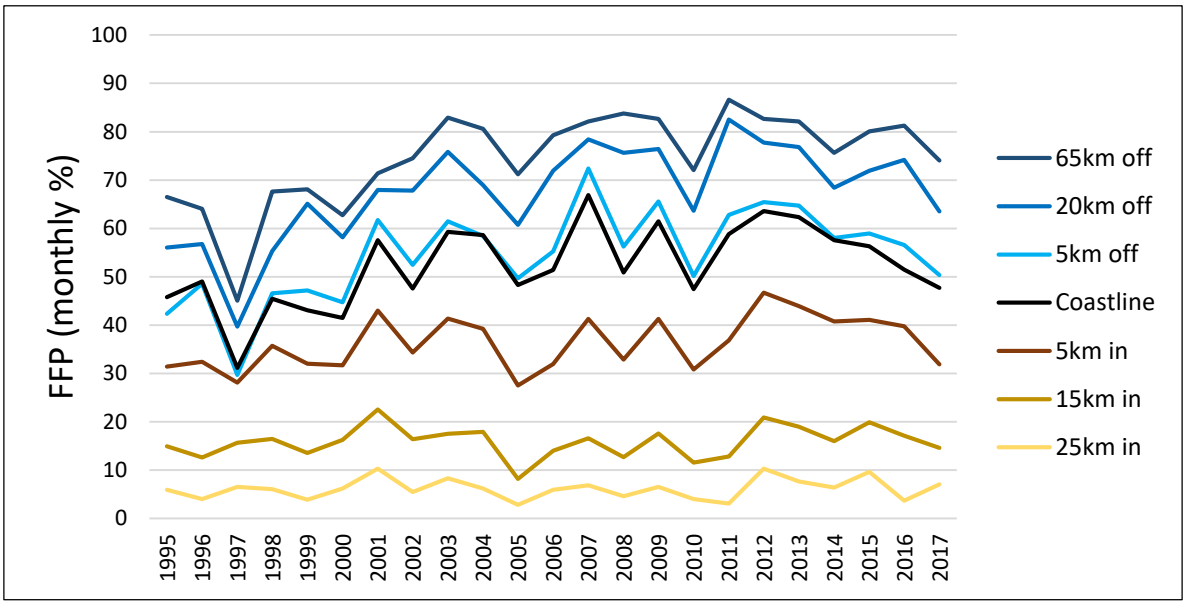

Figure 36: Daily mean fog and low cloud frequency presence and its inter-annual variability for the month of September.

The 6-year period from 1995-2000 had the lowest FFPs for all daily time points over the ocean and near shore areas, including the extreme minimum for the year 1997. The only exception occurred at sunset, where the 1997 minimum is only observed at 65 km offshore. In addition, other notable minimums can also be observed at noon in 2016 and at sunset in 2010. At the same time, over the ocean and near shore areas, all time points have maximum FFPs that occur in the same years or within the period 2007 – 2012. Again exceptions occur at noon and at sunset, which in present maximums in 2011 and 2013, respectively. Interestingly, all time points show a decreasing tendency in FFP during the final years of the study period; thus the ocean and near shore areas, in spite of their inter-annual variability, present transition from a first period of lower FLC presence (1995-2000), to maximum FLC presence (2007-2012), followed by another period of low FLC presence (2013-2017). The onshore areas, specifically 15 and 25 km inland, show higher inter-annual variability; nevertheless, they do not always present correspond with oceanic variability or with minimum or maximum FFP years. An exception occurs at dawn and dusk, when inland areas closely follow inter-annual variations in the near shore. To analyze the inter-annual relationship between ocean-land FFPs, statistical correlations (r) were carried out for the

daily mean and for the different daily time points. Table 5 shows the daily mean correlations, with significant relationships marked in light grey.

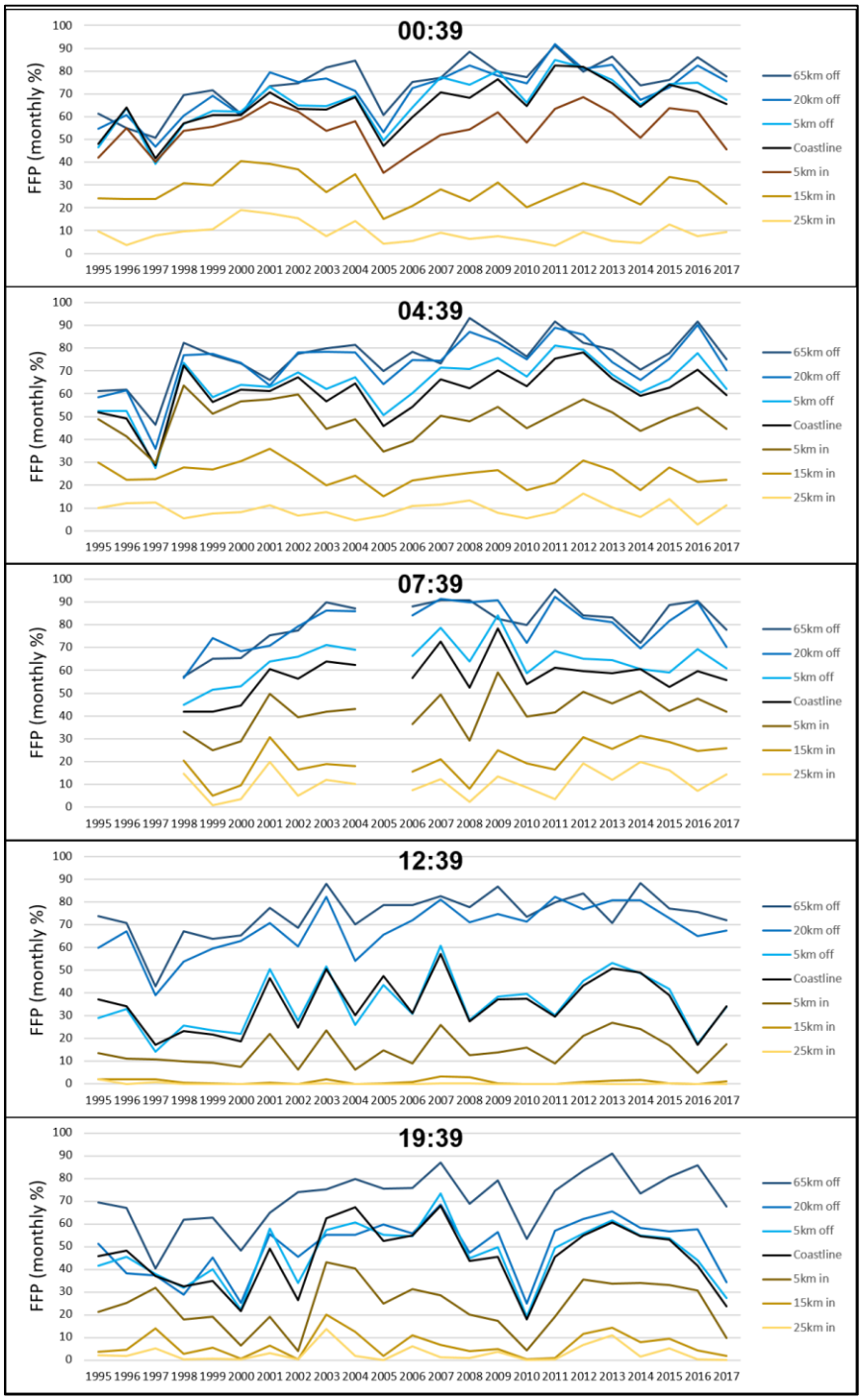

Figure 37: Mean fog and low cloud frequency presence and its inter-annual variability for September at daily time points.

Inter-annual variability in the sampled areas shows a close relationship in between offshore areas (e.g. between 65 and 5 km offshore r = +0,88). The offshore areas continue to be correlated with the coastline, and even with the areas 5km onshore (see Table 5). The significant relation of the near shore (5 km) and coastline areas with areas further inland only extends until 15 km inland, but not to 25 km inland.

		65km off	20km off	5km off	Coastline	5km in	15km in	25km in
65km off	Pearson correlation	1	,963**	,887**	,845**	,632**	0.202	0.120
	Sig. (bilateral)		0.000	0.000	0.000	0.001	0.355	0.586
	N		23	23	23	23	23	23
20km off	Pearson correlation		1	,924**	,860**	,686**	0.271	0.163
	Sig. (bilateral)			0.000	0.000	0.000	0.211	0.457
	N			23	23	23	23	23
5km off	Pearson correlation			1	,973**	,815**	,418*	0.345
	Sig. (bilateral)				0.000	0.000	0.047	0.107
	N				23	23	23	23
Coastline	Pearson correlation				1	,845**	,445*	0.399
	Sig. (bilateral)					0.000	0.033	0.059
	N					23	23	23
5km in	Pearson correlation					1	,805**	,654**
	Sig. (bilateral)						0.000	0.001
	N						23	23
15km in	Pearson correlation						1	,863**
	Sig. (bilateral)							0.000
	N							23
25km in	Pearson correlation							1
	Sig. (bilateral)							
	N							

**. The correlation is significant at the level 0,01 (two-sided).
*. The correlation is significant at the level 0,05 (two-sided).

Table 5: Correlation analysis between daily mean FFPs for sampled areas for the month of September

The ocean-land relationship varies slightly for the sampled time points in comparison to the daily mean; for example, at 00:39 and 04:39 there is no significant relationship between the

coastline and 15 km inland, the same is true between 5 km onshore and 25 km inland. A similar situation occurs at dawn and noon, showing a higher decoupling in the ocean-land variability. On the other hand, at sunset the area 20 km offshore shows significant relationships with the area 15 km inland (r = +0,44), as well the area 5 km offshore and the coastline with 25 km inland (r = +0,46 and r = +0,52, respectively), presenting a unique daytime pattern with a greater ocean-land relationship in terms of inter-annual variability in FFP.

In the case of February, inter-annual variability, despite lower FFPs, is much higher than September in sample areas. In addition, variability during February does not present a decrease offshore to onshore pattern, rather it shows even higher variability in the near offshore than in inland areas. The daily mean, present at 65 km offshore (9%; SD = 5,8), varies from minimums of 2,4, 2,6 and 2,9% in the years 2017, 1999 and 2002, respectively, to maximums of nearly 20% in 1998, 2005 and 2003 (see Fig. 38). At 20 km offshore, the average FFP is 3,6% (SD = 3,2) and minimums of around 1% occur in the years 2002, 2012, 2008, 2017 and 2011. The maximum FFP of over 11% occurs in 1998, followed by maximums over 8% in 2003, 2005 and 2010. FFP sat 5 km offshore present the highest inter-annual variability, with a mean of 2,9% (SD = 2,8). The years 2000, 2002, 2007, 2008, 2011 and 2012 present minimums values of under the 1%. Meanwhile, the maximum is repeated in 1998 (nearly 10%), as well in 2003 and 2010 with FFPs of around 8%. Over the coastline, mean FFPs were 3,2% (SD = 2,6), with an extreme minimum of nearly 0 in 2002. Maximums were repeated in 1998, 2003 and 2010, with FFPs between 9.5 and 7%. A higher mean FFP occurred at 5 km onshore than at other nearshore areas, with and FFP of 3,8% (SD = 2,8). The minimum also occurred in 2002, with an FFP of nearly 0; maximums of over 10% occurred in 1998 and 2003. At 15 km inland, the mean was 3% (SD = 2,2), and here the minimum again occurred in 2002, with less than 1%, and the maximums of over 8% occurred in 1998 and 2003. Finally, areas at 25 km inland presented a mean of 1,6% (SD = 1,4); minimums were nearly 0% during the years 2002 and 2014. As in other areas, maximums of above 5% occurred in 1998 and 2003. Inter-annual variability in February for the different daily time points, shows some slight differences compared to the daily mean. All time points present their lower variation at 65 km offshore, while higher variability varies between the near shore and inland areas (see Fig. 39). In the ocean, 20 and 5 km offshore areas, the highest inter-annual variability is produced at 04:39 and the lowest at 19:39. Over the coastline and 5 km onshore, the highest variability is at noon and the lowest is again at

sunset, a pattern that is repeated for the areas 15 and 25 km inland. The years in which maximum and minimum FFP values occurred have a high concordance for the daily time points; however, there are differences in FFP magnitudes. Although FFPs for February are low, the extreme minimums are repeated in 2002, as well as 1999, 2008, 2011 and 2012. At the same time, the maximum is repeated in 1998, 2003, 2005, 2010 and 2014.

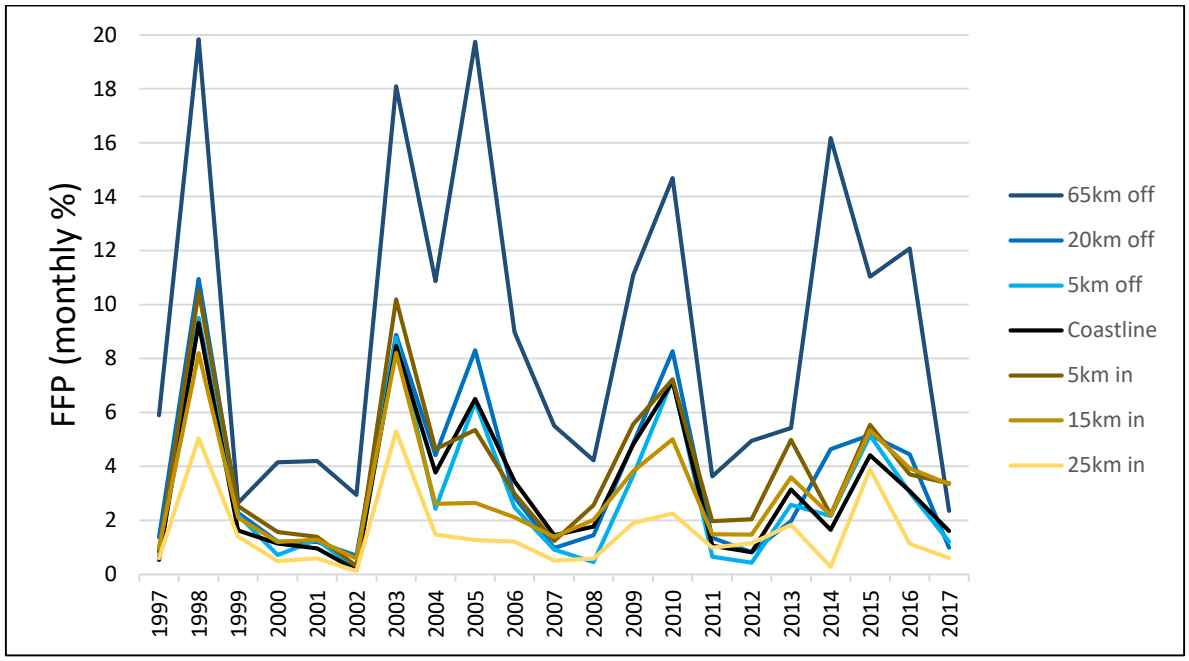

Figure 38: Daily mean fog and low cloud frequency presence and its inter-annual variability for the month of February.

Similar inter-annual variability in FFP for the different areas studied, as well for the daily time points, indicate a greater ocean-land connection than in September. Table 6 shows the daily mean correlations for February, which present significant relationships between all the areas, even 65 km offshore with 25 km inland (e.g. between 65 km and 25 km inland r = +0,62). The significant correlation between the ocean and the land is also observed for the daily time points, with significant relationships between all zones at 00:39, 04:39 and at 07:39. Exceptions occurs at 12:39, when there is no relationship between 65 km offshore and 25 km inland, and at 19:39, when there is no relationship between 65 km offshore and 15 and 25 km inland, and 20 km offshore with 25 km inland.

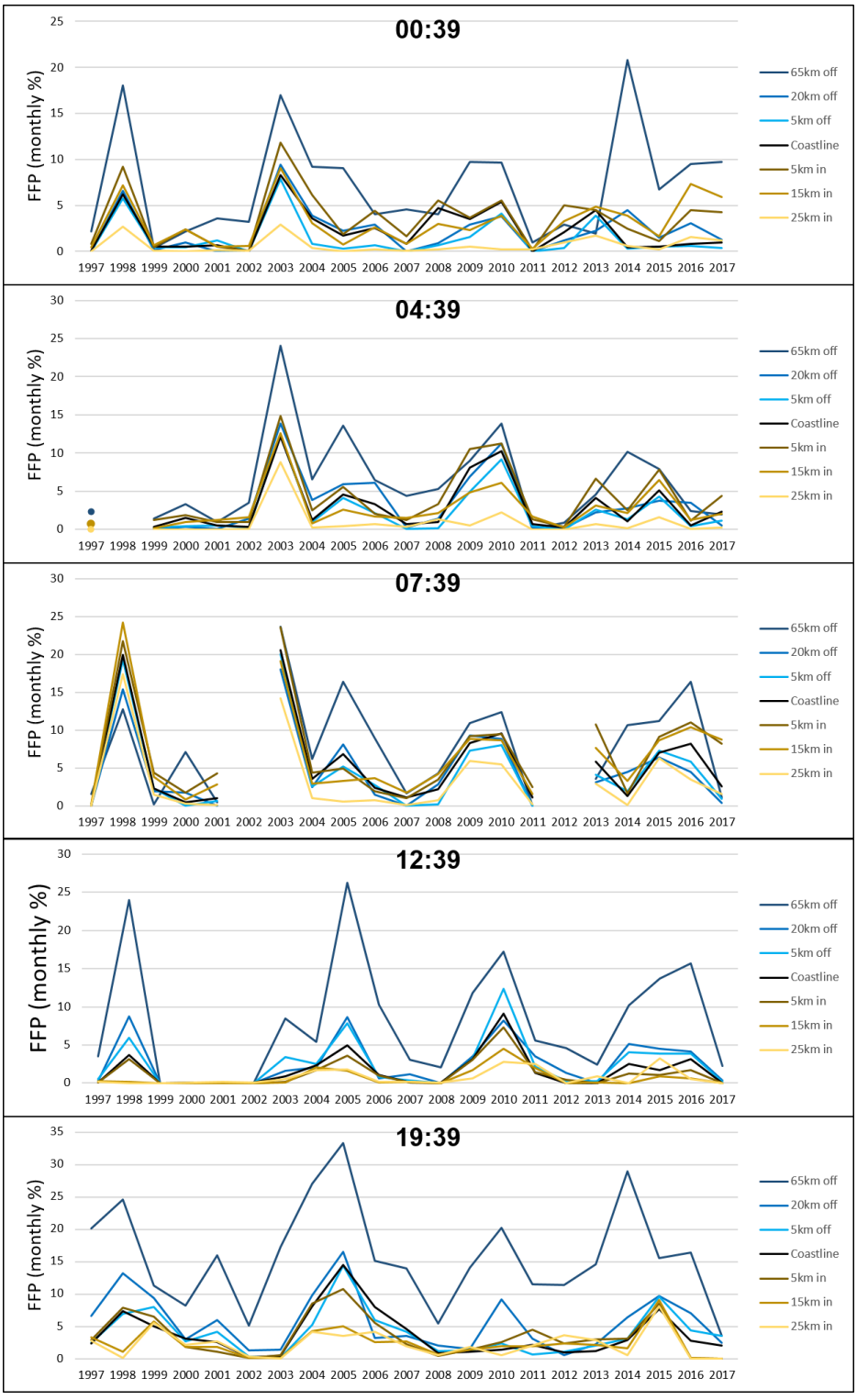

Figure 39: Mean fog and low cloud frequency presence and its inter-annual variability at analyzed daily time points for February.

		65km offshore	20km offshore	5km offshore	Coastline	5km inland	15km inland	25km inland
65km offshore	Pearson correlation	1	,942**	,863**	,854**	,769**	,703**	,629**
	Sig. (bilateral)		0	0	0	0	0	0.002
	N		21	21	21	21	21	21
20km offshore	Pearson correlation		1	,968**	,956**	,899**	,834**	,775**
	Sig. (bilateral)			0	0	0	0	0
	N			21	21	21	21	21
5km offshore	Pearson correlation			1	,977**	,947**	,904**	,869**
	Sig. (bilateral)				0	0	0	0
	N				21	21	21	21
Coastline	Pearson correlation				1	,965**	,891**	,846**
	Sig. (bilateral)					0	0	0
	N					21	21	21
5km inland	Pearson correlation					1	,960**	,911**
	Sig. (bilateral)						0	0
	N						21	21
15km inland	Pearson correlation						1	,936**
	Sig. (bilateral)							0
	N							21
25km inland	Pearson correlation							1
	Sig. (bilateral)							
	N							

**. The correlation is significant at the level 0,01 (two-sided).

Table 6: Daily means in FFP for areas sampled in the correlation analysis for the month of February.

6.3 Spatiotemporal characterization of sea surface temperature (SST) in the Coastal Atacama and its relationship with the presence of fog and low clouds

6.3.1 Sea surface temperature (SST) in the Coastal Atacama

SSTs in the Coastal Atacama present a clear seasonal cycle, with higher temperatures in February and lower temperatures in September. While September presents a mean temperature of 17,2°C for the period 2002 - 2017, February presents a mean of 20,7°C for

the same time period. Fig. 40 shows the spatial distribution of monthly mean SSTs for the time period in the first ~90 km offshore.

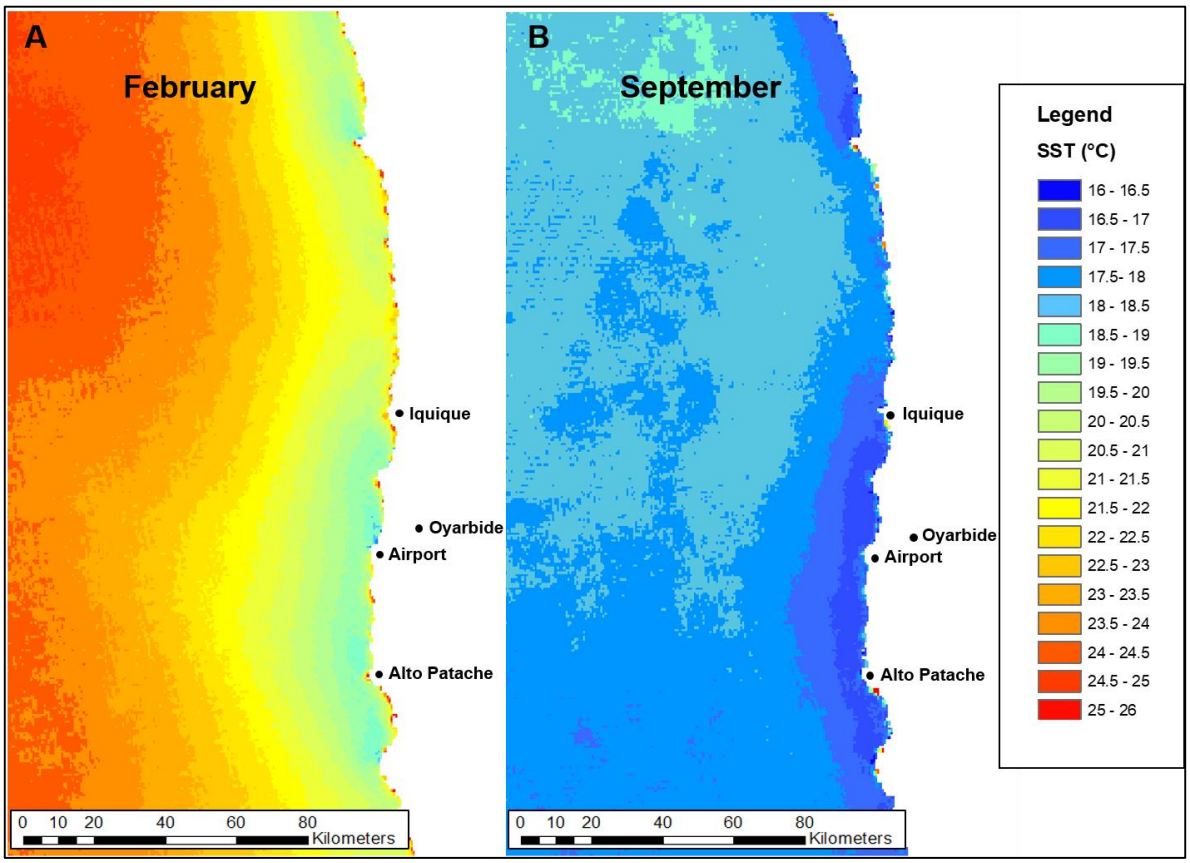

Figure 40: Spatial distribution of mean SSTs in the Coastal Atacama for the period 2002-2017.

February presents higher spatial variability (around 6°C), with SSTs that vary from >19 °C in the near shore areas to ~25°C in the areas farthest from the shoreline. The spatial distribution of SSTs shows continuously cooling ocean waters as you move closer to shore, with cooling trends occurring at a consistent distance from the shore, generating north-south temperature bands. On the other hand, in September there is lower spatial variability (around 3°C), with SSTs that range from the 16°C in near shore areas to 19°C in offshore areas in the northernmost part of the study area. Spatial distribution of SSTs in September shows a concentration of the colder waters within the first ~10 km off the coast, followed by a homogeneous distribution as you move further offshore, with an average drop in temperature of 0,5°C in the southern section as compared to the northern section of the study area.

Seasonal cycles in SST are also observed in Fig. 41, with higher SSTs in February and lower temperatures in September. At the same time, Fig. 41 shows the inter-annual variability present in SSTs for the study period. In February, SD = 0,59°C and during September SD = 0,73°C. In this sense, September presents higher inter-annual variation, with a minimum in 2007 (15,2°C) and a maximum in 2015 (18,44°C). February, on the other hand, presents a minimum in 2008 (19,71°C) and a maximum in 2016 (22,02°C), the occurrence directly following the minimum and maximum SSTs for September.

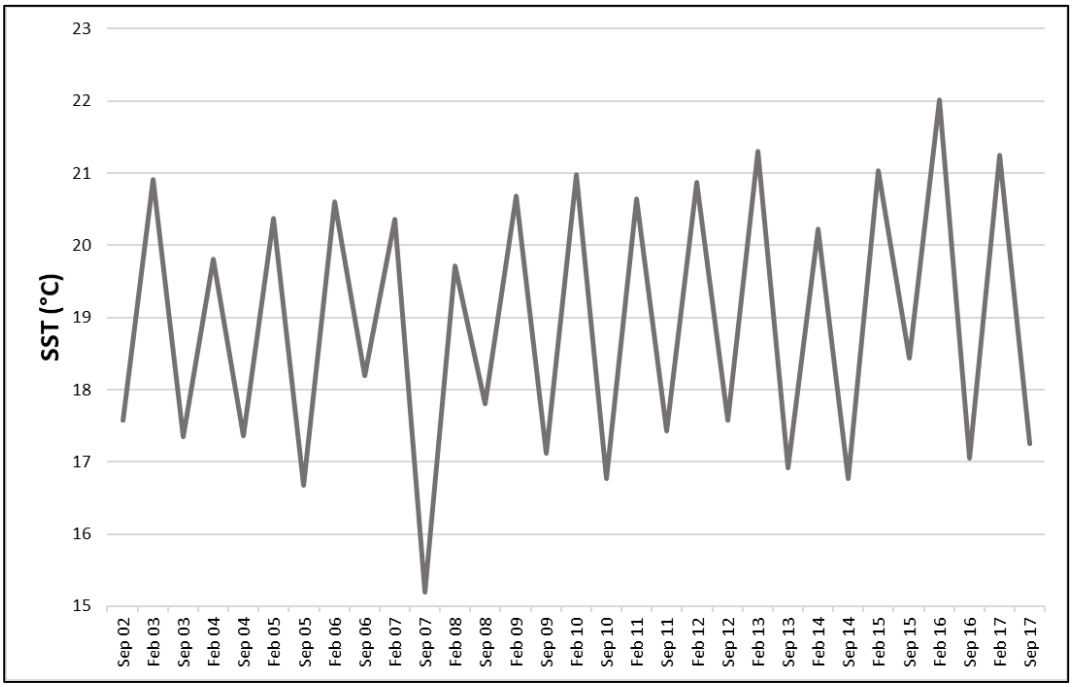

Figure 41: Inter-annual variability in SSTs in the Coastal Atacama for the period 2002-2017.

Inter-annual variability among the 3 longitudinal sample areas shows high correlation for both months, February and September (see Fig. 42). February presents an r = +0,9 between fringe 1 and 2, and between fringe 2 and 3, and an r = +0,84 between fringe 1 and 3 (all correlations are significant at 99% confidence level). The inter-annual variability of the fringes is similar, although slightly higher in fringe 2 (SST mean and SD for fringes 1,2 and 3 are 20,5°C ± 0,76, 22,7°C ± 0,89 and 24,0°C ± 0,7 respectively). September presents an r = +0,96 between fringe 1 and 2, r = +0.87 between 2 and 3, and r = +0,81 between 1 and 3 (at 99% confidence level). The inter-annual variability of the different fringes increases as you move father offshore (SST mean and SD for fringes 1,2 and 3 are 17,5°C ± 0,76, 17,9°C ± 0,86 and 18,0°C ± 1,0 respectively). Over the 16 years analyzed, September shows a weak positive trend in SSTs for the complete area (*m* = 0,034), which varies with distance

from the coast, as fringe 1 and 2, the first 60 km offshore present the same slope (*m* = 0,043), and fringe 3 (60 to 90 km offshore) presents a weaker slope (*m* = 0,014). In February, trends in SSTs over the ocean are positive and stronger than in September (*m* = 0,104), revealing an increase of over 1°C during the time period. The tendency varies slightly with distance from the coast, as fringe 1, 2 and 3 present a slope of *m* = 0,097, 1,123 and 0,091, respectively.

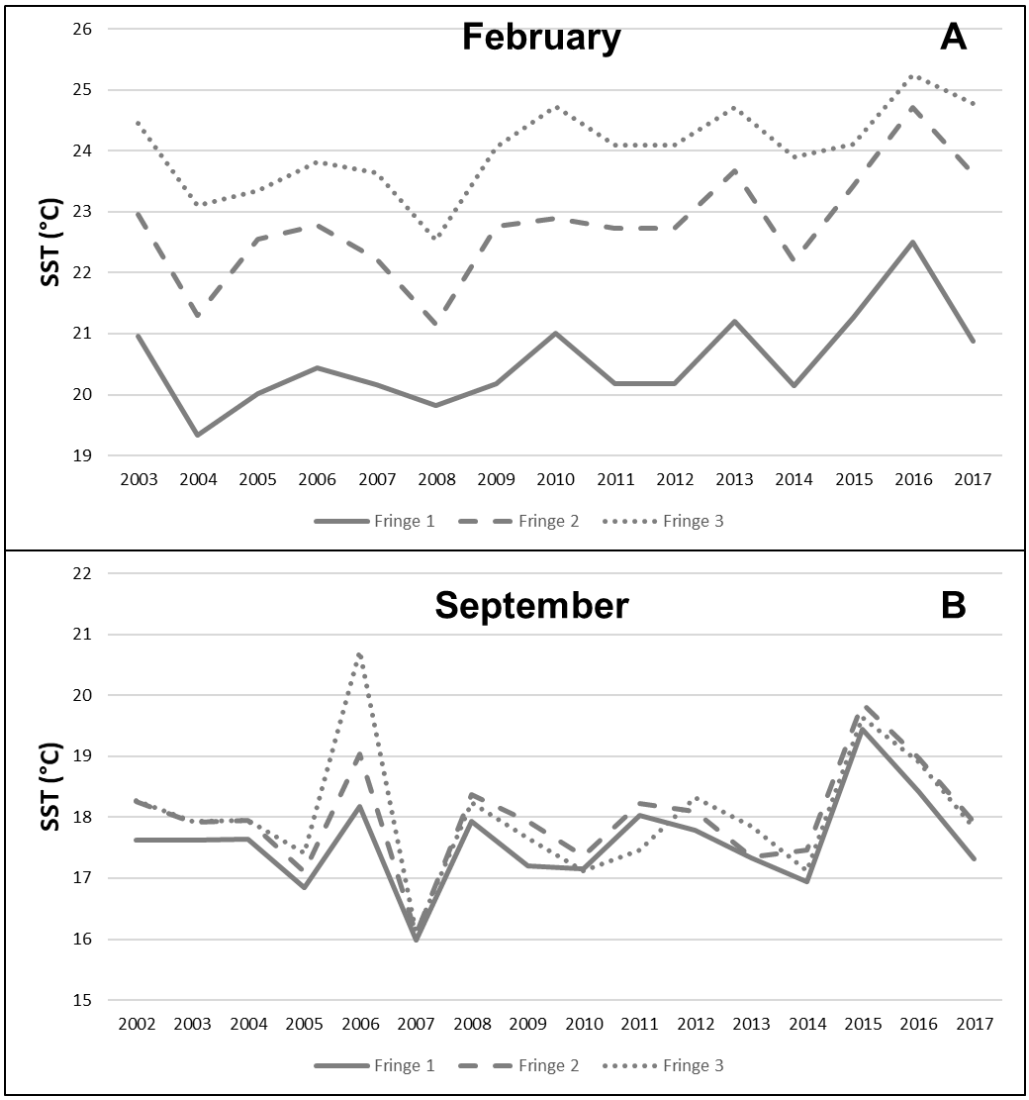

Figure 42: SST sampling fringes inter-annual variability for the period 2002-2017, for (A) February and (B) September. Fringe 1: the first 30 km offshore; Fringe 2: 30-60 km offshore; Fringe 3: 60-90 km offshore.

6.3.2 The relationship between coastal SSTs and the presence of fog and low clouds

An analysis of the relationship between SSTs in the Coastal Atacama and the estimated fog and low cloud frequency presence was performed for February and September for the period 2002-2017. There was no statistically significant relationship between FFPs and SSTs. The analysis included various SST sampling areas (total area and fringe areas) compared with the fog and low cloud sampling areas and daily time points (cluster areas for daily means, as well for individual analyzed hours). This lack of a relationship between SSTs and FFPs is discussed in the following section (Section 6.4.1).

6.4 Discussion and interpretation on a regional scale

Differences in fog and low cloud spatiotemporal distribution, trends and inter-annual variability during February and September, sustain the complex oceanic – atmospheric and geographic interactions involved in this dynamic phenomenon. Furthermore, variations are observed not only from a seasonal perspective, but also within daytime hours. The results obtained from satellite datasets lead to the identification of features involved in spatiotemporal variations in clouds and, additionally, allow to explore and determine the factors and potential causal-links implicated. In this sense, different oceanic indices (e.g. ENSO, IPO) are included in the analysis.

6.4.1 Spatiotemporal distribution of fog and low clouds

The seasonal cycle of fog and low clouds is well reflected in the differences in FFPs between February and September. As the amount of stratus cloud is closely related to the strength of the thermal inversion layer (Klein and Hartmann, 1993), it is expected that at this latitude (~20°S) February (summer) will present the minimum FLCs presence (~15% over ocean areas) and September (winter, early spring) will present the maximum (~72% over ocean areas). Several authors (e.g. Rutllant et al., 1998; Klein and Hartmann, 1993; Muñoz et al., 2011 and 2016) have established that the strength and altitude of the thermal inversion layer is due to interaction of forces above and below the inversion layer; in this sense, the seasonal and daily cycles and their corresponding spatiotemporal distribution of FLCs in the Coastal Atacama are a product of synoptic to regional and local interacting forces. In the

case of February, lower air subsidence and higher SSTs (local mean of 20,7°C) produce a higher and weaker thermal inversion layer. Therefore, the deeper MBL does not allow air particles driven by eddies within the MBL to reach saturation point, producing decoupling from the surface. The absence of clouds when the inversion layer is weaker intensifies interactions between the free troposphere and the MBL, leading to an entrance of warming air into the MBL from the free troposphere, and thus a loss of humidity (Rutllant et al., 1998). Conversely, in September, greater air subsidence and colder SSTs (local mean of 17,2°C) produce a stronger thermal inversion layer. In these conditions there is a shallower MBL, where turbulence within the MBL allows air particles to reach the condensation level and form into a cloud, which in the presence of a thermal ceiling expands horizontally. In this case, the cloud presence produces positive feedback for further cloud formation, as the cloud top is cooled by long wave emissivity, driven by relevant radiative turbulences (Duynkerke et al., 1995; Klein and Hartmann, 1993; Rutllant et al., 2003, Rozendaal et al., 1995). Low tropospheric conditions for the summer and winter are shown in Fig. 43.

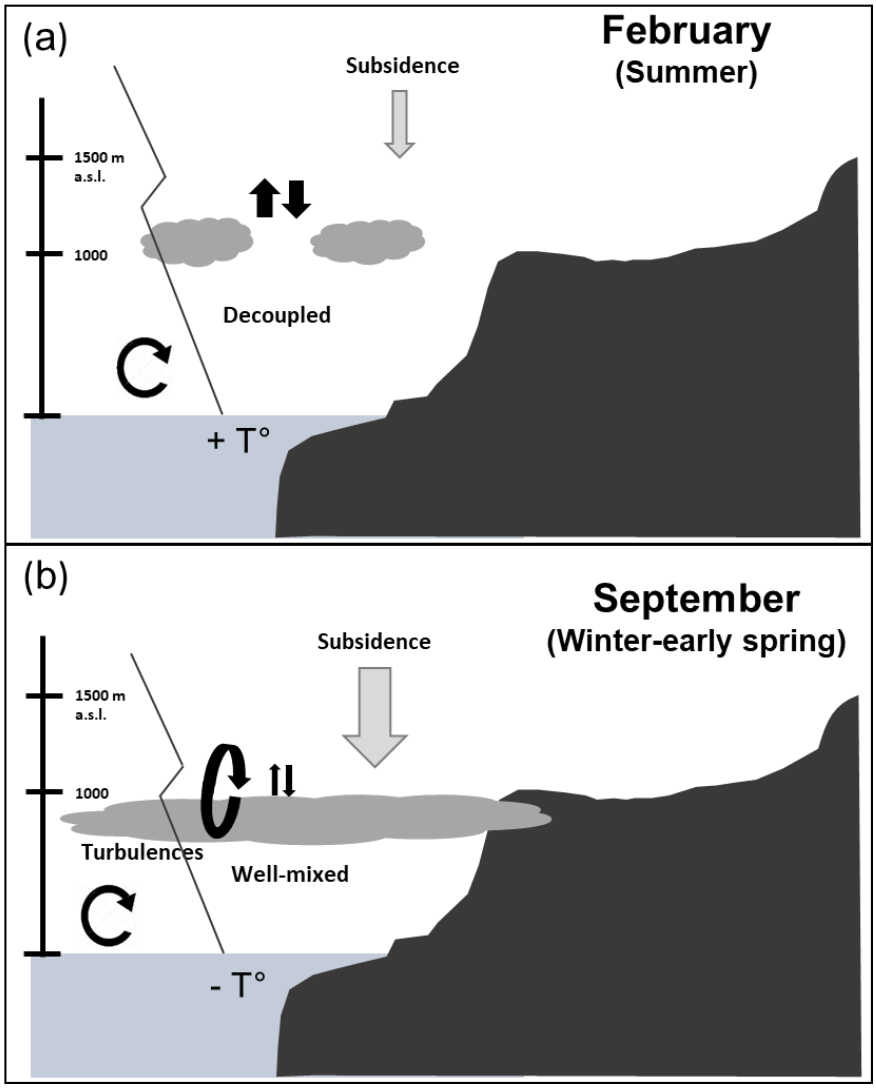

Figure 43: Schematic of the formation of fog and low clouds for (a) February, representative of summer conditions, and (b) September, representative of winter-early spring conditions (Source: Adapted from del Río et al., 2018:142).

In relation to the seasonal cycles over the near shore and inland areas, Garreaud et al., 2007, exemplified the difficulties in characterizing and interpreting the cloud cycle for latitude ~30°S, mentioning three different indicators of FLC presence at different onshore locations, and all three show differences in the maximum FLC presence. In the case of the study area, del Río et al., 2018, described the annual cycle based on fog water yields collected in the Coastal Cordillera (850 m a.s.l., about 3.5 km lineal distance from the coastline), the Iquique airport (50 m a.s.l., about 1 km from the coastline) and an indicator of low cloud presence derived from satellite images (offshore in the Atacama); all show the same maximum of FFP for September and minimum for February. Thus supporting the conclusion that the seasonal cycle in FFP is the same both offshore and onshore in the study area. In this sense, the

differences in FFPs between February and September are also observed in the near shore and inland areas. February has a mean FFP of 2 - 3% for the area between the coast and 1.000 m a.s.l. and from 1.000 to 1.200 m a.s.l.. In contrast, in September FFP means were 70 and 57% in the same areas, respectively. Here, local factors and their effects must be incorporated into the analysis (Fig 43.). One main component is topography; in the Coastal Atacama the presence of the prominent Coastal Cordillera, with altitudes that can exceed the 1.000 m a.s.l., acts as a natural barrier for fog penetration. Given that the thermal inversion layer has an altitude around 1.250 m a.s.l. in February (see section 7.2), there is little difference in FFPs in the area between the coastline and 1.200 m a.s.l. and the area between 1.200 to 1.500 m a.s.l (see Fig. 25). It is assumed that the scarce presence of fog during February is able to reach inland zones at a certain time of the day (mainly during dawn). On the other hand, September, shows high FFPs in the areas between the coastline and 1.000 m a.s.l, which gradually decrease at higher altitudes. Here, as the base of the thermal inversion layer is around 1.050 m a.s.l. (see section 7.2), a high proportion of the low advective stratus clouds get trapped by the coastal cliffs at or before 1.000 m a.s.l. Fig. 24B clearly shows how higher onshore FFPs are closely related to the 1.000 m a.s.l. contour. Observed latitudinal difference in the distribution of FFPs in the onshore areas is mainly due to the fact that in the northern section of the study area the Coastal Cordillera is on average higher and closer to the coastline. At the same time, the presence of fog corridors is associated with areas of lower altitude, through which the fog moves inland (e.g. Camarones and Loa river basins), consistent with those identified by Farias et al., 2005.

The daily cycle in FLCs is mainly determined by fluxes in ocean-land thermodynamics. The areas farthest offshore are the most stable, showing that the land's influence on FFPs only continues to 30 to 60 km offshore, observed principally at noon and sunset in September and February. In September, higher FFPs over the ocean and in the first ~15 km onshore occur at night and early morning, when cooler surface temperatures occur over both the ocean and land, generating relatively calm wind conditions. At the same time, at night and early morning the base of thermal inversion layer is at a lower altitude (see section 7.1). Here, it is assumed that the cooler conditions favor condensation of air particles and, at the same time, low cloud presence causes greater radiative turbulence. As a counterpart, there is thermal inversion strengthening, a greater air subsidence, and thus a shallower MBL (Rutllant et al., 2003; Garreaud et al., 2007). The high humidity within the MBL, the cooler surface temperatures (ocean-land) and the bounded MBL depth, increase FLC formation

and presence over the ocean and in the onshore areas, until the Coastal Cordillera intercedes, inhibiting MBL conditions inland. At 00:39, 04:39 and 07:39 (see Fig. 28), higher FFPs are limited to the 1.000 m a.s.l. contour. Inland penetration by FLCs, or eventually humidity penetration and later condensation by local radiation effects, occurs mainly at dawn, when lower surface temperatures over the desert occur, through topographic corridors. FLCs then dissipate gradually during the morning as solar radiation increases, dissipating the cloud presence and generating an almost null fog presence over the desert during daytime, with the lowest presence at noon when radiation is close to its maximum. During the afternoon, the southerly winds increase, promoting turbulences within the MBL; at the same time desert temperature increase, producing on the one hand, a deeper MBL and on the other hand, ocean to land wind circulation with a SW predominance. Despite the ocean-land wind circulation, surface heat evaporates the humidity, keeping the low fog presence inland. The southerly winds face those areas where the coastline has a southwest aspect and an elevated relief close to the coast, in this way, promoting the rise of air and consequent cooling and condensation to form orographic fog (Cereceda et al., 2002) (see in Fig. 28 the 19:39 image). On the other hand, the three zonal reductions of FFPs observed at 19:39 in the offshore areas near the coast, show similar spatial patterns to those described by Garreaud et al. (2011) for southern latitudes in Chile (~30°S). It is presumed that they are mainly related to coastline aspect and its topography, producing variations within the MBL structure. Presumably, in the presence of peninsulas, which break the predominant north-south distribution and generate coastlines exposed to the SW and NW (e.g. southern and northern Punta Patache point respectively), and for those areas facing the SW an enhancement of the southerly winds is produced, also generating enhanced upwelling and a divergence of winds northward, inhibiting wind turbulence, thus causing lower FFPs in those areas.

In February, despite the significantly lower FFPs, the daily cycle follows a similar pattern as September during the night and early morning hours, when the balance between ocean and land surface temperatures produces relatively calm winds, thus higher FFPs at this time of day, especially at dawn (07:39). Here, the base of the inversion layer is at its lowest altitude (around 1.100 m a.s.l. according to GOFOS results), permitting, on occasion, turbulence within the MBL to allow air particles to reach condensation level. At noon, inland FFPs are practically zero, due to the desert heating. At the same time, very low FFPs are observed in the offshore area near the cost, which, according to Rutllant et al. (2003), is due to enhanced

air subsidence over the coast, a result of convection created by heating of the western slopes of the Andes.

6.4.2 The connection between ENSO and inter-annual variability in fog and low clouds

The FFP results at an inter-annual level show that there are variations beyond seasonality, which can be linked to ENSO, the main driver of climate variability in the SEP. The time period analyzed in this study (1995-2017) includes some very strong El Niño (ENSO +) years (1997–1998, 2015), as well as some strong La Niña (ENSO -) years (e.g., 1999–2000 and 2010–2011). Fig. 44 shows SST anomalies in zone 3.4 estimated by the Oceanic Niño Index (ONI), a 3-month running mean based on centered 30-year base periods. It is observed that the different ENSO phases and magnitudes occur in both February and September. This allowed us to analyze FFPs under opposite ENSO oceanic-atmospheric conditions.

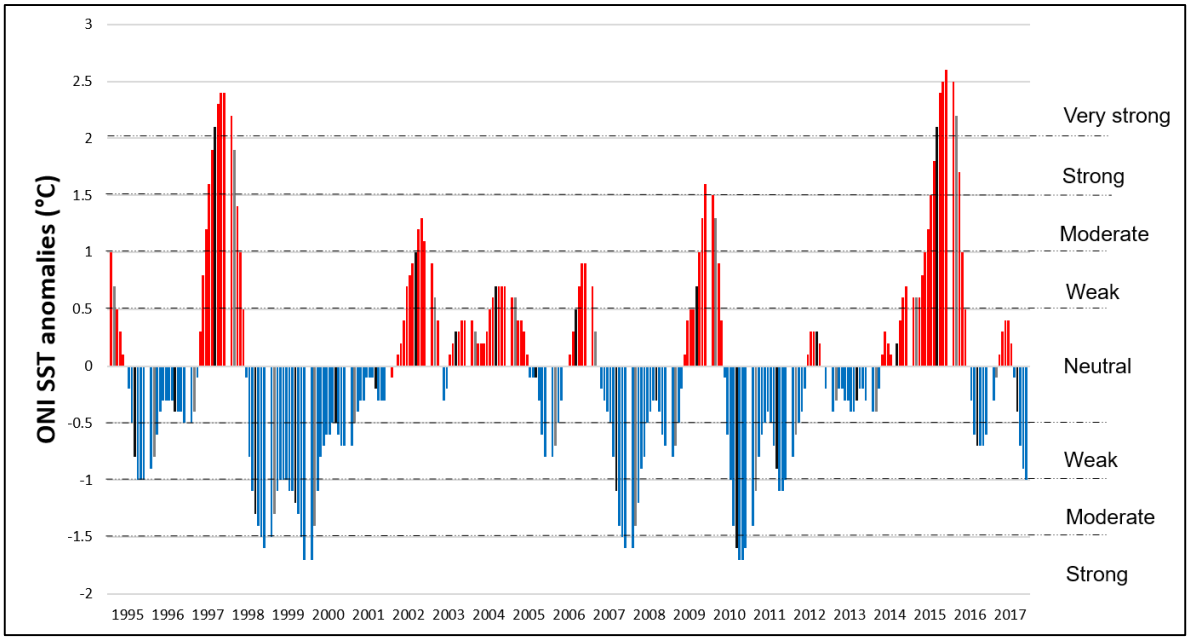

Figure 44: ONI SST anomalies in the 3.4 zone for the study time period. Grey bars correspond to February and Black bars correspond to September (Source: NOAA / Climate Prediction Center).

6.4.2.1 The connection with ENSO during summer (February)

Inter-annual variability in FFPs during February is closely linked to ENSO SST anomalies in zone 3.4, specifically in the cluster areas 1, 2 and 3, which correspond to the ocean and onshore areas near the coast. These areas show significant and strong correlations with ONI (r = + 0,60; r = +0,70 and r = +0,68, respectively, with a 99% confidence level). Cluster areas 4 and 5 do not show a significant relationship, which is expected given that these areas present a very low to null FFP. Fig. 45 shows the relationship between ENSO phases (+/-) and FFPs for the cluster areas 1, 2 and 3 during the time period. Positive correlations are observed when the ENSO (+) phase is related to higher FFPs over the ocean and coastal areas; conversely, under an ENSO (-) phase, it is observed lower FFPs. Maximum FFPs occurred in ENSO (+) phases of varying magnitudes of intensity, for example the years 1998 (strong), 2003 and 2005 (weak) and 2010 (moderate). On the other hand, minimum FFPs occurred during ENSO (-) years, also with varying magnitudes of intensity, see the years 1999-2000, 2008 and 2011 (Moderate), 2001 and 2012 (weak), and even some neutral years, such as 2002 and 2017.

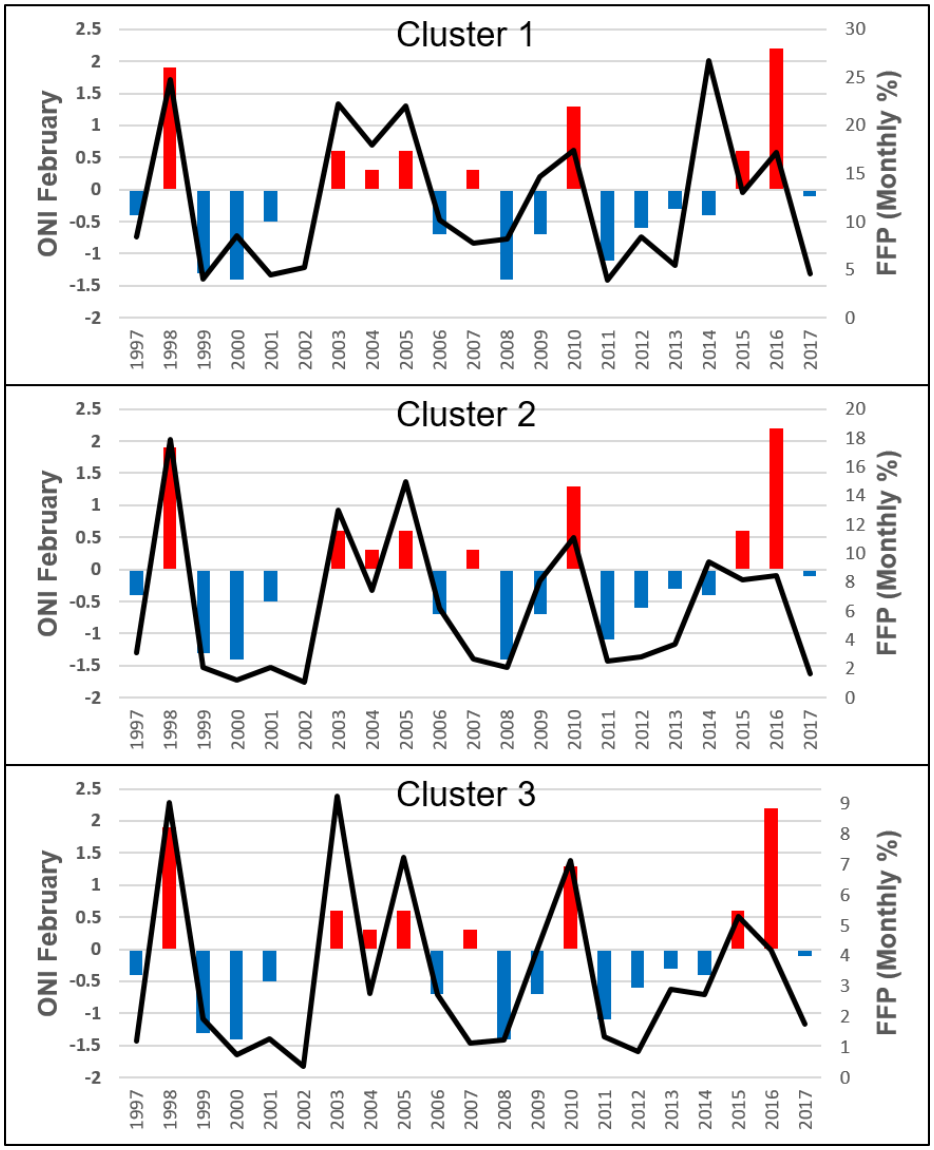

Figure 45: February ONI SST anomalies in the 3.4 zone. Red bars correspond to El Niño-like (ENSO +) phase and Blue bars correspond to La Niña-like (ENSO -) phase (Source: NOAA / Climate Prediction Center).

Fig. 46 shows the general oceanic-atmospheric interchange in the study area related to fog and low cloud formation (or not) under ENSO (-) or ENSO (+) summer conditions. During ENSO (-) years (Fig. 46a), the weak inversion layer allows interaction between the MBL and the free atmosphere; when this air enters the MBL it dries, thus hindering fog and low cloud formation (Duynkerke et al., 1995; Garreaud et al., 2007). In addition, decoupling within the MBL is even more marked when SSTs are cooler, as turbulence is not strong enough to raise the moisture level and produce condensation. Increased summer FLC cover during ENSO (+) years (Fig. 46b) in the northern Atacama can thus be explained by a significant

increase in SSTs and in air temperatures above the thermal inversion layer. These conditions are accompanied by an upward amplification of potential air temperatures together with enhanced air stability and thermal inversion, resulting in relatively extensive summer FLC formation (Garreaud et al., 2008a; del Río et al., 2018).

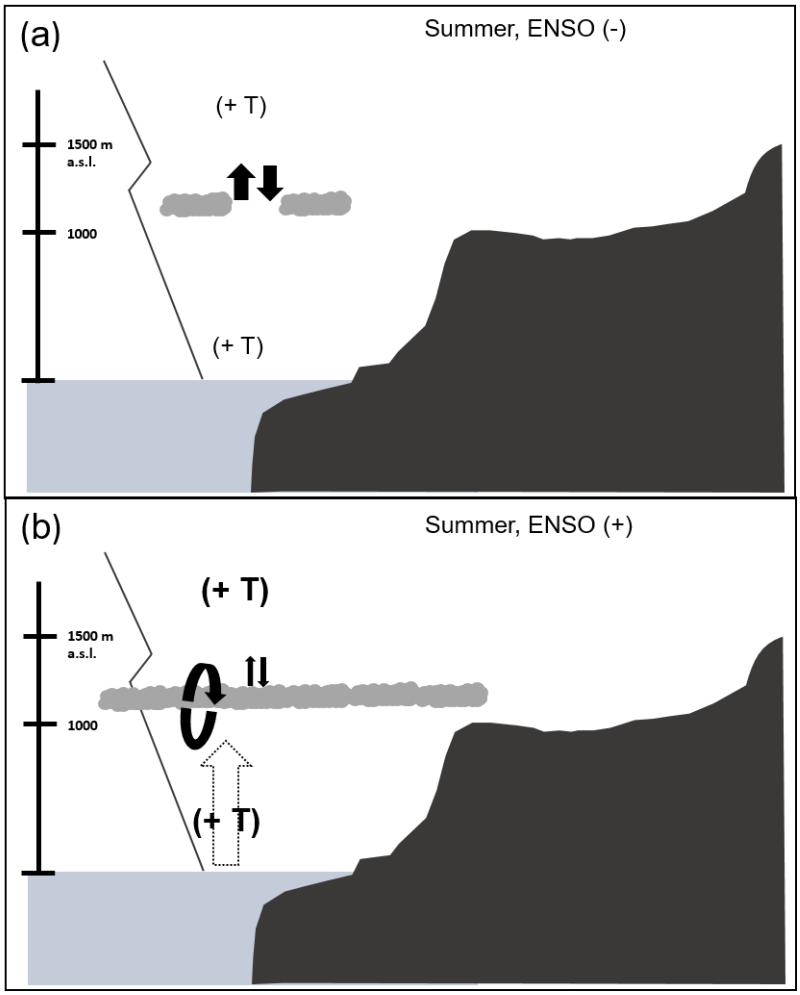

Figure 46: Schematic of fog and low cloud formation in February under different ENSO conditions, (a) ENSO (-) and (b) ENSO (+) (Source: Adapted from del Río et al., 2018:142).

Despite the high correlation between ENSO and FFPs, there are a few years when the relationship is not so evident, however this varies between cluster areas. For example, in clusters 1 and 2 have very high FFPs during 2014, but correspond to a neutral phase (with a tendency to ENSO (-)); however, FFPs decrease significantly in cluster 3 (offshore and onshore areas near the coast), with FFPs that are more in line with FLC frequencies for a neutral ENSO phase (see Table 7). Nevertheless, there are anomalies in the offshore conditions, which were not analyzed in this research. On the other hand, 2016, despite a

very strong ENSO (+) phase, does not show significantly higher FFPs as other ENSO (+) years do, despite the fact that its FFPs are higher than the averages for clusters 1 (41%), 2 (36,5%) and 3 (27,2%) (see Table 7). Presumably extreme SSTs (measured in the central Pacific 3.4 zone and in the coastal Atacama) generate intense eddies within the MBL, which occasionally break the thermal inversion layer and do not allow for the formation FLCs; this situation is more common in areas towards the open ocean (Rutllant and Garreaud 2005; Garreaud et al., 2011). In any case, as it is a special year in terms of the SST anomalies, data related to air subsidence intensity and strength of the thermal inversion would need to be reviewed to fully interpret atmospheric conditions.

	Annual FFP compared the average for the study period (%)				
Year	Cluster 1	Cluster 2	Cluster 3	ENSO (+/-)	Magnitude
1997	-30.7	-49.4	-64.0	(-)	Neutral
1998	103.9	189.8	173.5	(+)	Strong
1999	-66.9	-66.4	-41.3	(-)	Moderate
2000	-29.6	-79.7	-77.0	(-)	Moderate
2001	-62.9	-66.1	-61.4	(-)	Weak
2002	-56.8	-83.1	-88.9		Neutral
2003	82.6	109.9	180.3	(+)	Weak
2004	47.5	20.8	-16.7	(+)	Neutral
2005	80.9	141.8	118.8	(+)	Weak
2006	-16.2	0.4	-16.9	(-)	Weak
2007	-35.7	-56.7	-66.2	(+)	Neutral
2008	-33.0	-66.3	-62.2	(-)	Moderate
2009	20.3	31.1	29.2	(-)	Weak
2010	43.6	79.1	116.3	(+)	Moderate
2011	-67.5	-59.1	-59.0	(-)	Moderate
2012	-31.0	-54.1	-74.5	(-)	Weak
2013	-54.7	-39.9	-12.5	(-)	Neutral
2014	120.1	52.5	-17.9	(-)	Neutral
2015	7.3	31.8	60.3	(+)	Weak
2016	41.0	36.5	27.2	(+)	Very strong
2017	-62.3	-73.0	-47.1	(-)	Neutral

Table 7: February FFPs in relation to the cluster mean for the study period and ENSO phase

Correlation analysis between ENSO and FFPs in the coastal Atacama was also performed for the different daily time points, showing varying results. Clusters 4 and 5 only show a significant relation between ENSO and FFPs (with a 95% confidence level) at dawn, when

FFPs are higher in inland areas. On the other hand, at sunset, the only significant correlation is with cluster 1 (the area furthest from the coast), which could be explained by the greater intensity of the ocean-earth winds occurring at this time of day, revealing greater influence of the local factors on FFPs.

For the described link between the ENSO 3.4 zone and coastal Atacama FFPs in the clusters 1, 2 and 3, a linear regression was fitted for all analyzed years (see Fig. 47). The regression indicates that ENSO anomalies explain ~50% of the variance in the inter-annual FLC frequency presence during the summer. Cluster 1 has a determination coefficient (R^2) of 0,36, but if the year 2014 is not considered the coefficient increases to R^2 = 0,51. The coefficients for cluster 2 and 3 are R^2 = 0,49 and 0,47, respectively. This significant relationship suggests a potential causal link between ENSO (+/-) phases and coastal Atacama FLC presence during February (summer).

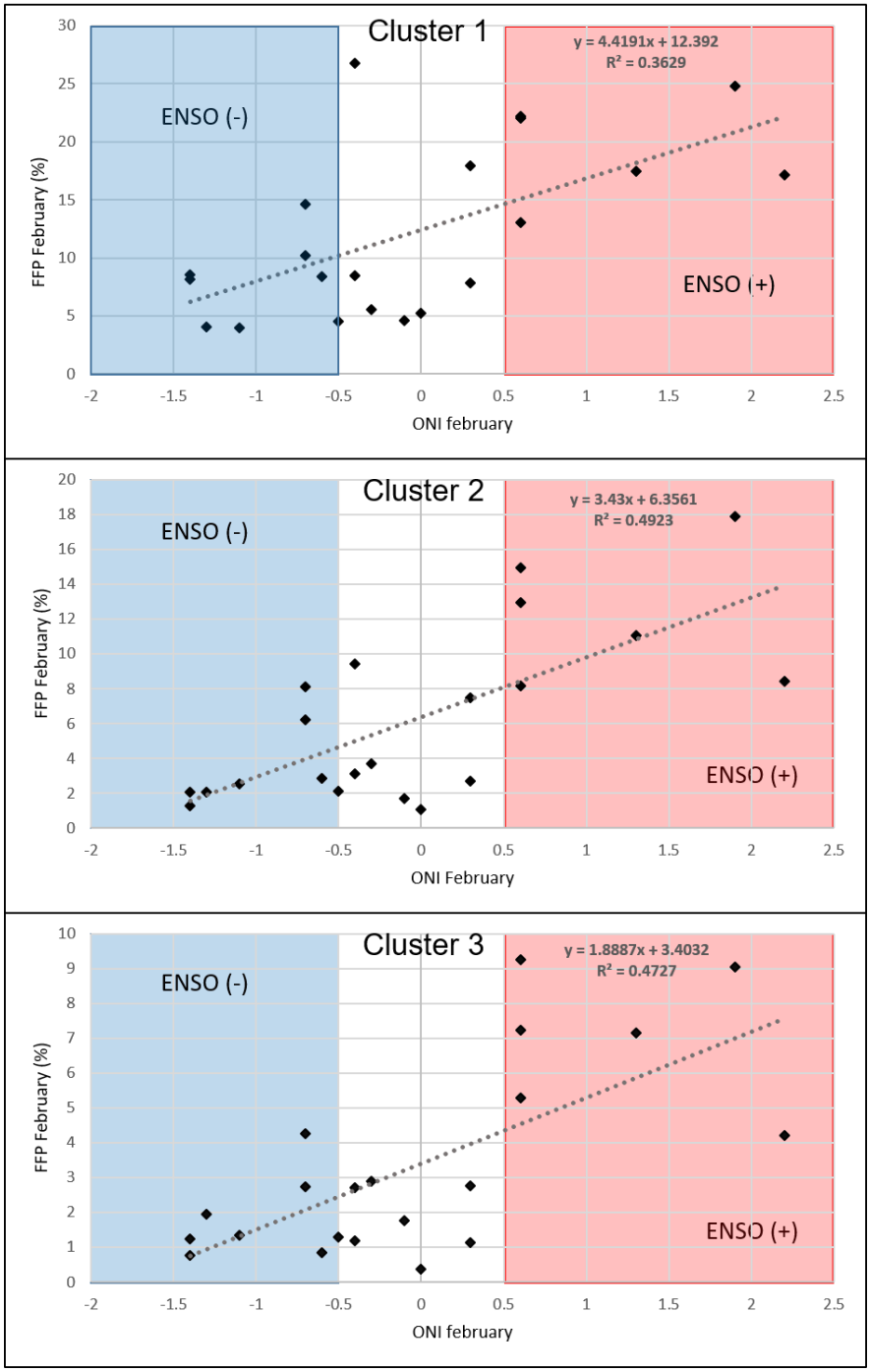

Figure 47: Scatter plot of summer (February) fog and low cloud frequency presence (FFP) versus ONI sea surface temperature anomalies (SSTAs). SSTAs < -0,5°C indicate weak to strong La Niña ENSO (-) phase; SSTAs > 0,5°C indicate weak to very strong El Niño ENSO (+) phase. The fitted lineal regression is shown with a dark dashed line.

As the analyzed ENSO zone 3.4 is located in the equatorial Pacific and is a regional indicator, statistical analyses were carried out looking for relationships between FFPs and

SST zones closer to the Atacama, such as the ENSO zone 1+2 (see Fig. 15) and the SST at the coast of Atacama (preliminarily developed in section 6.3.2), in order to find local factors involved in the inter-annual variability of FFPs. There was no significant statistical relationship between FFPs and ENSO zone 1+2. Similarly, there was no relation between FFPs and local Atacama SSTs; in this case, unlike what was done in section 6.3.2, here was searched for relationships at different times of the day. Moreover, no relationships were found between the different zones of SST anomalies (3.4, 1+2 and coastal Atacama). Therefore, local SST has no direct link with FFPs in coastal Atacama during the summer, thus emphasizing that FLC formation is largely linked to regional rather than local factors. Therefore, it can be inferred that the relationship between ENSO zone 3.4 and FFP along the Atacama coast is linked to variations in ENSO in the SEPA and its related air subsidence and strength of the thermal inversion layer, and not necessarily to related SST anomalies. Interestingly, del Río et al. (2018) found a low (r = -0,40), but significant relationship between local SST (measured in Iquique bay) and fog water yields at Alto Patache; this relationship was stronger during summer and under ENSO (+) conditions. Apparently, the relationship between coastal SSTs and fog water is mostly linked to two relationships: 1) coastal SSTs are linked to air temperatures (Vuille et al., 2015), and 2) air temperature is linked to liquid water content (LWC) of the cloud, where colder (warmer) temperatures present a lower (higher) LWC (Wallace & Hobbs, 2006), which is finally reflected in fog water yields. On the other hand, Garreaud et al. (2008a) explored direct correlations between ENSO and the presence of coastal Sc and advective fog in semiarid regions of Chile (~30°S) during spring (September, October and November). They concluded that while La Niña conditions produce an increase in the presence of fog, the opposite occurs during El Niño years. At the same time, they hypothesized that north of 25°S the effect of ENSO is the opposite, with an apparent asymmetry in fog response to ENSO between hyper-arid and semiarid regions within the Atacama. Our results confirm this hypothesis, but in this case in the period with the lowest FFPs. The relationship between ENSO and fog water yields in the study area during summer has been previously demonstrated (del Rio et al., 2018).

6.4.2.2 ENSO connections during winter-early spring (September)

Inter-annual variability in FFPs during September, do not show a significant relationship with ENSO SST anomalies in zone 3.4. Correlation and regression analyses present a null or

non-statistically significant result. Fig. 48 shows inter-annual variation in FFPs for cluster 3 (black line) and the ENSO (+/-) conditions for September within the study period.

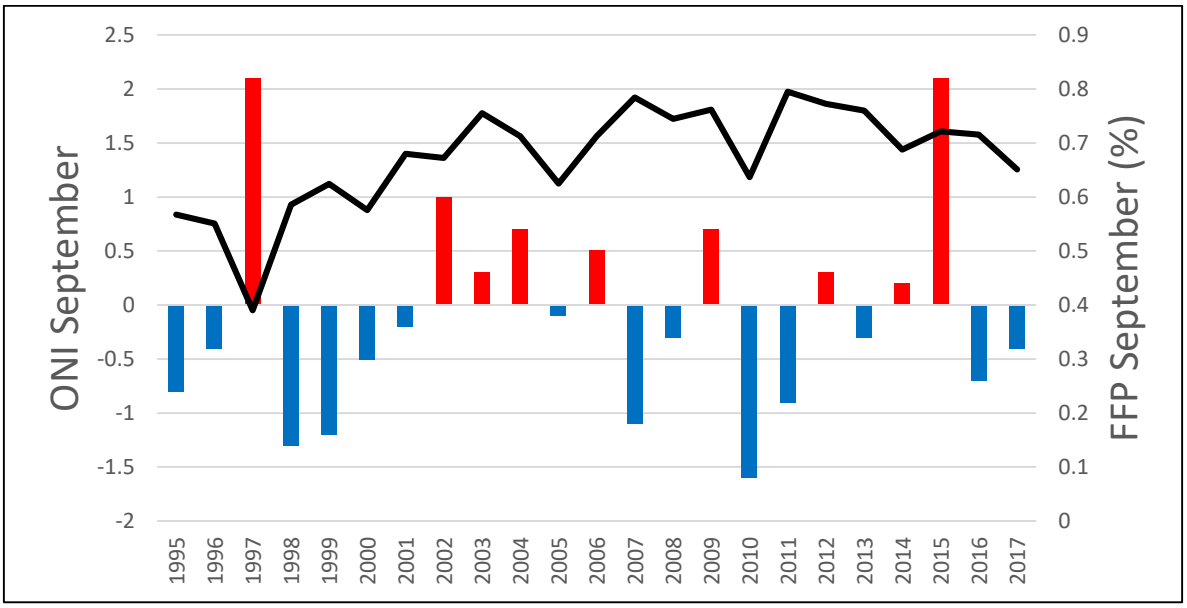

Figure 48: September ONI SST anomalies in the 3.4 zone versus fog and low cloud frequency presence in cluster 3 (black line). Red bars correspond to El Niño-like (ENSO +) phase and Blue bars correspond to La Niña-like (ENSO -) phase (Source: NOAA / Climate Prediction Center).

In terms of inter-annual variability in FFPs, at first there is a period of lower FFPs, which then increase with a peak between 2007 and 2011 approximately, followed by a final period during which FFPs decrease to the present. This tendency lead to two conclusions: 1) the trend is not linear, but polynomial; 2) at the decadal level, this trend is very similar to patterns in SST anomalies in the SEP during the study period. The inter-decadal Pacific Oscillation (IPO) is a long-term oscillation in SST, and its cycles can last from 20 to 30 years (Power et al., 1999); in recent decades, a La Niña-like tendency has predominated (Falvey and Garreaud 2009; Muñoz et al., 2016; Schultz et al., 2011a), with a peak coinciding with peaks in FFPs, and that is apparently beginning to shift towards an El Niño-like cycle (Met Office, 2017). Fig. 49) shows the polynomial (second order) curve presented for FFPs and Fig. 49b shows the same curve for the IPO index, where the same trend is observed with an inverse relationship. In this sense, and with the intention of removing the decadal signal from the inter-annual variability in FFPs during September, it was proceeded to normalize both variables (the FFP and the IPO), and then apply the difference between the two variables, thus obtaining an annual FFP dataset for September with its correspondent inter-annual variability but without the influence of the decadal signal.

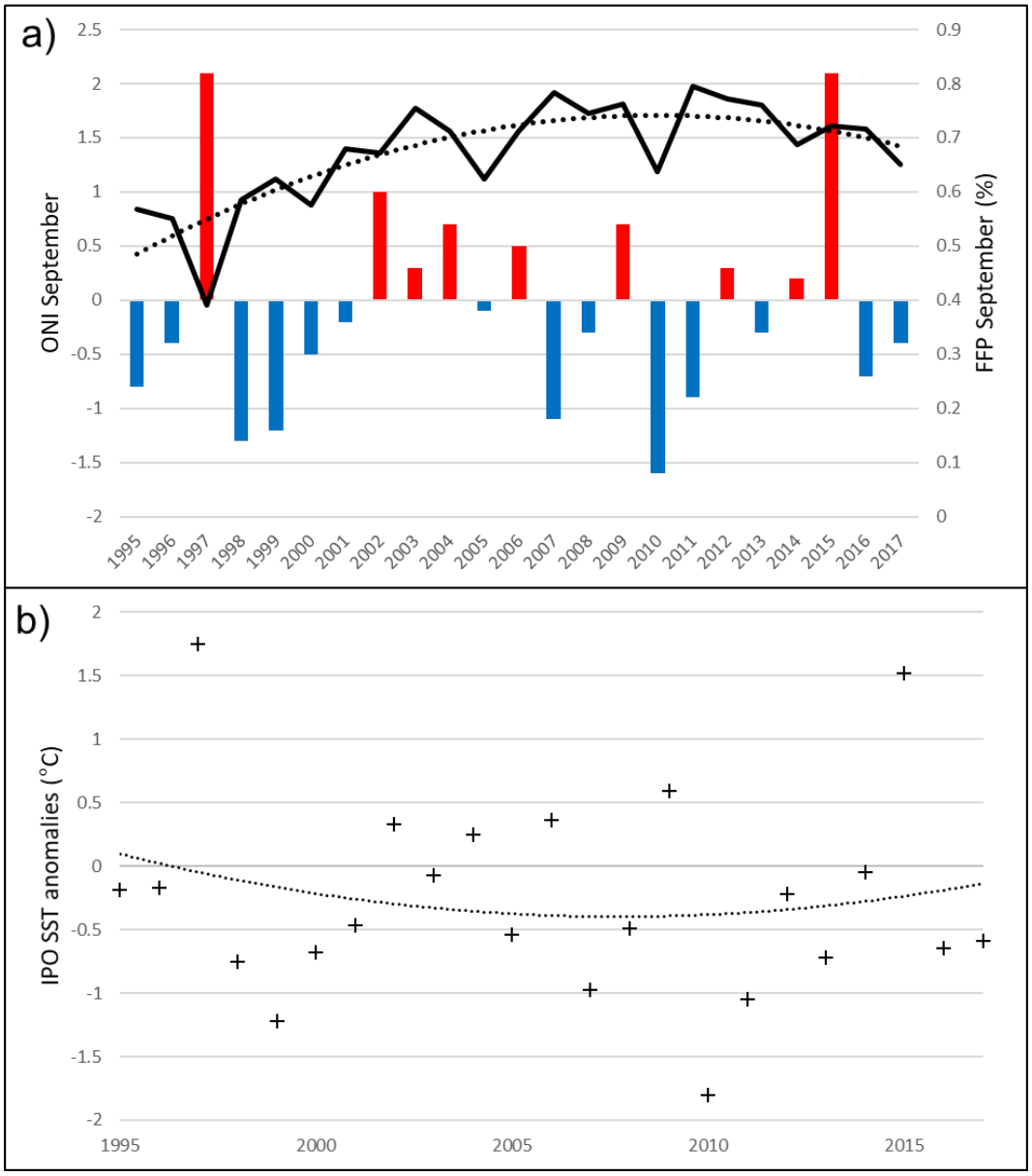

Figure 49: a) September ONI SST anomalies in the 3.4 zone and fog and low cloud frequency presence in cluster 3 (black line). The polynomial curve is shown with a dotted line. b) Inter-decadal Pacific Oscillation (IPO) SST anomalies for September. The polynomial curve is shown with a dotted line (Source: NOAA / Climate Prediction Center).

In this way, the new statistical analyses for the datasets without the decadal signal and for the different cluster areas were carried out. Correlation analyses show a strong and significant inverse relationship between FFPs and the ENSO SST anomalies in zone 3.4 presented by the ONI. Cluster 5 shows a significant and strong inverse correlation ($r = -0,69$; $r = -0,67$; $r = -0,70$; $r = -0,78$ and $r = -0,84$, for cluster 1, 2, 3, 4 and 5 respectively, with a 99% confidence level). Despite statistically significant results, cluster 5 should be interpreted

with caution given its high inter-annual variability of ~50%; this variability is due to the fact that these areas have very low to no FFP. Inter-annual variability in the other cluster areas varied between 12 and 17%. Fig. 50 (a) and (b), shows the relationship between ENSO phases (+/-) and FFPs for cluster areas 1, 2 and 3, and 4 and 5, respectively, during the study time period. Inverse correlations are observed when the ENSO (-) phase is related to higher FFPs over the ocean and coastal areas; conversely, under an ENSO (+) phase, it is observed lower FFPs, revealing an opposite response between summer and winter-early spring between FFPs and ENSO (+/-) phase anomalies. Despite high correlations, there are observable differences in the magnitude of inter-annual variations in FFPs with respect to ENSO (+/-) between areas of oceanic predominance (clusters 1, 2 and 3) and inland areas (clusters 4 and 5). Apparently, the relationship is stronger in the areas near the coast and inland. In the first 3 clusters (Fig. 50 a) maximum FFPs occurred in ENSO (-) phases with different magnitudes of intensity, highlighting the years 1995-1996 (weak-neutral), 1998-1999 (moderate), 2000 (weak) and 2010 (strong), and even the neutral years 2005 and 2016-2017. In clusters 4 and 5 Fig. 50b, maximums occurred during the same years as the first cluster areas, but in addition, there are high FFPs in 2007-2008 (Moderate to neutral). On the other hand, minimum FFPs occurred during ENSO (+) years, also with varying magnitudes of intensity; it is worth highlighting the different cluster areas for years 2002-2004, 2006 and 2009 (Moderate to weak), 2015 with the lowest FFPs (very strong), and also some neutral years, such as 2012-2013 and 2014. Fig. 51 shows the general oceanic-atmospheric interchange necessary for more or less FLC formation in the study area under ENSO (-) or ENSO (+) winter-early spring conditions. During ENSO (-) years (Fig. 51a), the stronger air subsidence, higher strength in the thermal inversion layer and the cooler temperatures within the MBL promote FLC formation, which, in turn, due to the thermal cooling at the top of the cloud enhances the radiative turbulence creating better conditions for air-mixture, thus resulting in greater than average formation of fog and low clouds. Conversely, the lower than average winter/early-spring FLC cover during ENSO (+) years (Fig. 51b) in the northern Atacama can then be explained by lower air subsidence and a weakened thermal inversion layer, with correspondingly lower FLC formation and therefore, the determinant lower radiative turbulences.

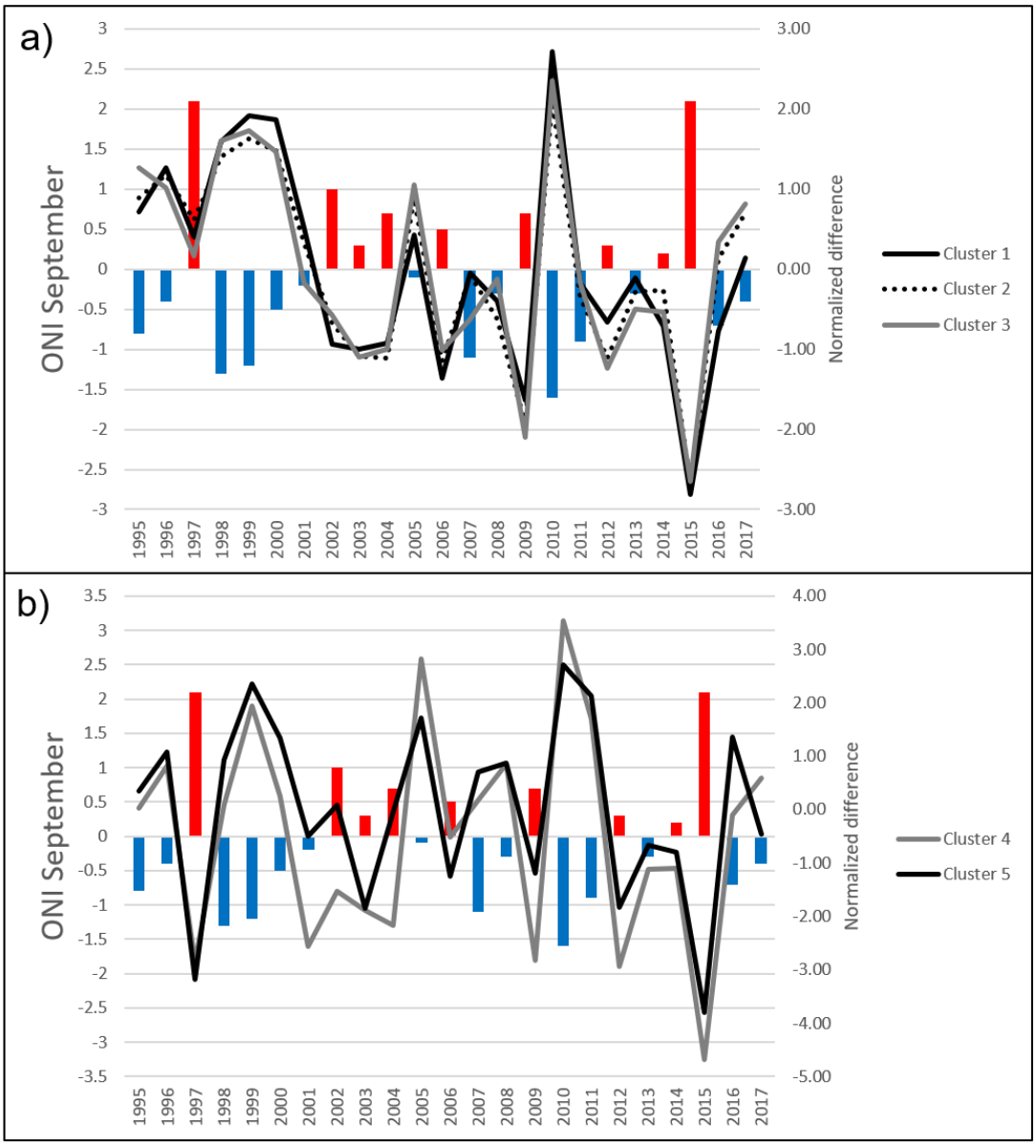

Figure 50: September ONI SST anomalies in the 3.4 zone within the time period. Red bars correspond to El Niño-like (ENSO +) phase and Blue bars correspond to La Niña-like (ENSO -) phase. a) FFP for clusters 1, 2 and 3; and b) FFP for clusters 4 and 5 (Source: NOAA / Climate Prediction Center).

The greatest difference in maximum and minimum FFP values between the cluster areas occurs in the year 1997, given that the FFP for oceanic clusters is higher than average and in the interior areas (cluster 4 and 5) the FFP is considerably below the average, demonstrating a noticeable difference between conditions over the ocean and the coast. As the very strong ENSO (+) conditions during 1997, in terms of SST anomalies, is similar to the year 2015, when all areas present their minimum FFP, the availability of air pressure and temperature data at different altitudes becomes necessary.

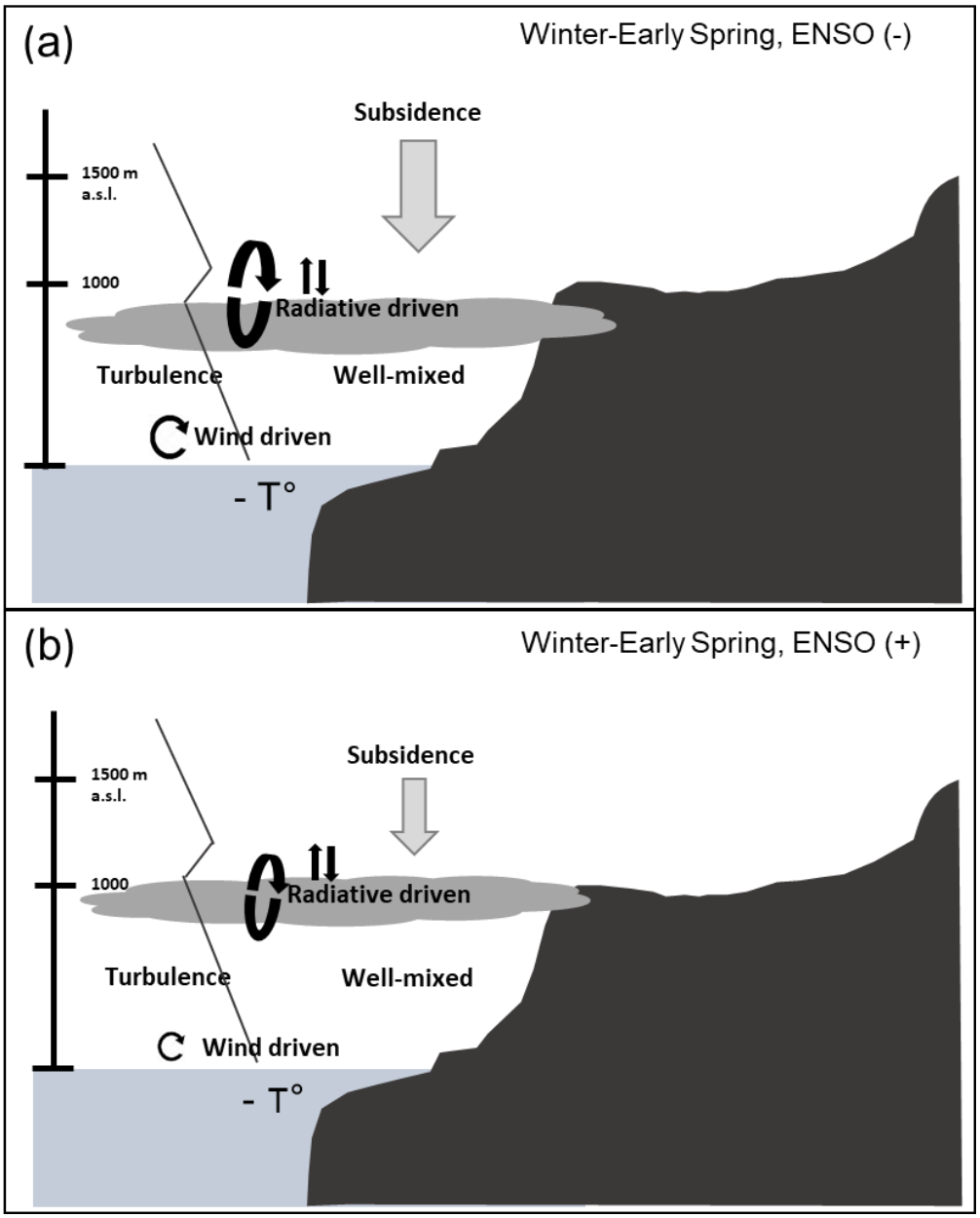

Figure 51: Schematic of fog and low cloud formation for September under different ENSO conditions, (a) ENSO (-) and (b) ENSO (+) (Source: Adapted from del Río et al., 2018:142).

In order to examine the described link between the ENSO zone 3.4 and FFPs in the coastal Atacama in the different cluster areas, linear regression was fitted for all the analyzed years (see Figs. 52 and 53). Regression indicates that ENSO anomalies explain ~47% of the variance in inter-annual FLC frequency presence during winter/early-spring in the oceanic clusters (1, 2 and 3). Clusters 1, 2 and 3 have determination coefficients (R^2) of 0,48, 0,45 and 0,49, respectively. In the case of clusters 4 and 5, the R^2 increases considerably, with coefficients of 0,61 and 0,71, respectively. As clusters 3 and 4 correspond to the areas of

highest interest in terms of fog presence and variability, the fact that ENSO phases explain 49% and 61% of inter-annual variance in FFPs, suggests a potential causal link between ENSO (+/-) phase the high season (September, winter-early spring) for FLC presence in the coastal Atacama. This is particularly relevant in terms of identifying and quantifying potentially areas for fog water collection, and at the same time, potential effects on fog-dependent ecosystems.

With the same intention of identifying relationships between inter-annual variability in FFPs and SST anomalies in zones closer to the Atacama for the month of February, statistical analyses were carried out between the FFP with SST for ENSO zone 1+2 and SSTs along the coast of the Atacama (preliminarily developed in section 6.3.2). Analysis revealed no significant relationship between FFPs (both with and without the IPO decadal sign) with ENSO zone 1+2. Similarly, no relationship was identified between FFPs and local Atacama SSTs at the different daily time points. The only exception is the daily mean FFP in cluster areas 1 and 2 (without the decadal sign), where low but significant inverse correlations were found ($r = -0,51$ and $r = -0,53$ respectively, with a 95% confidence level). However, there is no relationship between local SSTs and FFPs in clusters 3 or 4, where it was expected to find a relationship between upwelling of cooler waters and coastal fog. Therefore, just as in September, in the summer local SSTs have no direct link to FFPs in the coastal Atacama, emphasizing that FLC formation is largely linked to regional rather than local factors. Additionally, these results reinforce the hypothesis that the relationship between ENSO zone 3.4 and the FFP in the Atacama coast is linked to variations in ENSO in the SEPA and its related air subsidence and strength of the thermal inversion layer, and it is not necessarily related to SST anomalies.

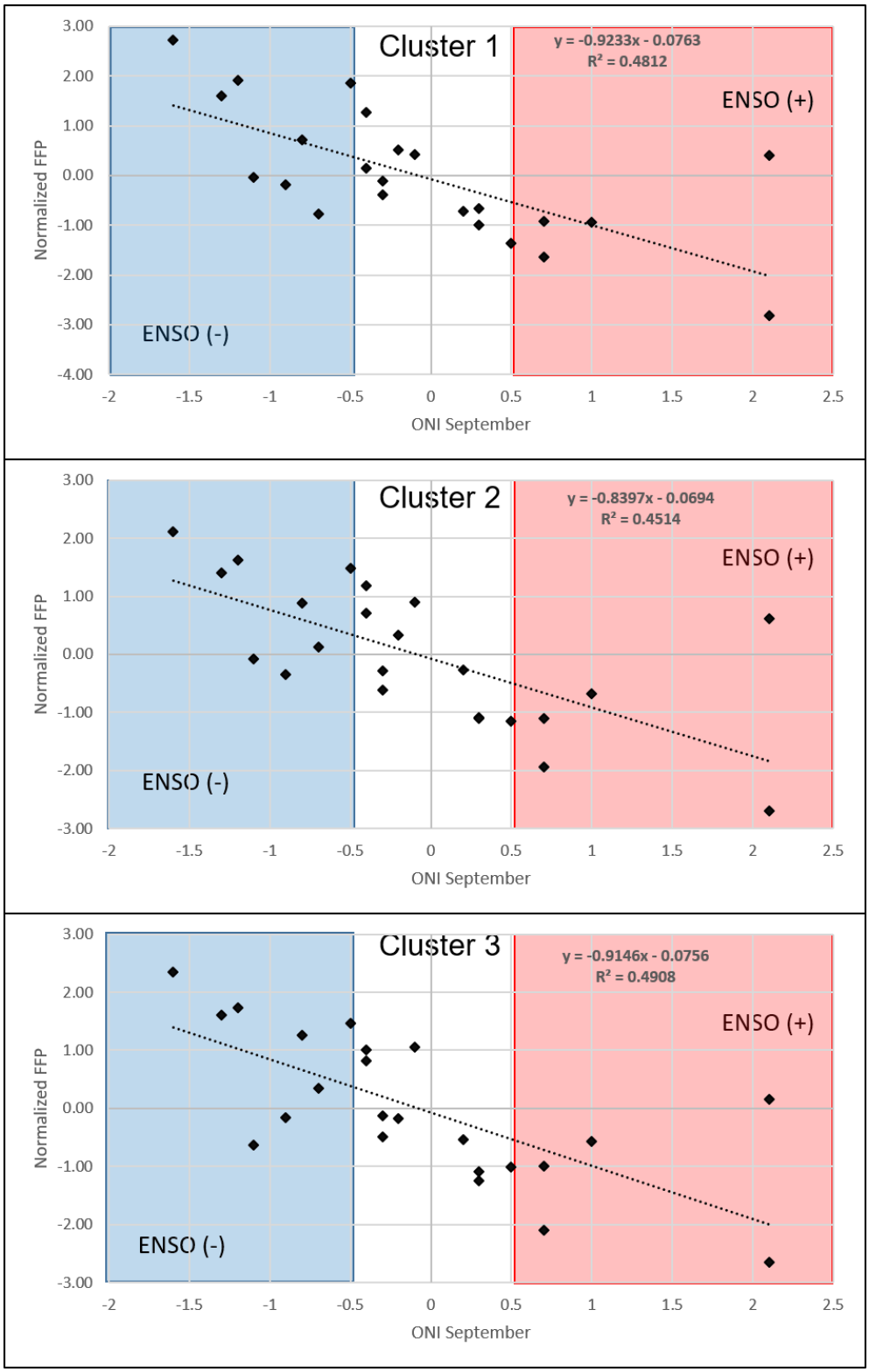

Figure 52: Scatter plot of winter-early spring (September) fog and low cloud frequency presence (normalized FFP) versus ONI sea surface temperature anomalies (SSTAs) in cluster areas 1, 2 and 3. SSTAs < -0,5°C indicate weak to strong La Niña ENSO (-) phase; SSTAs > 0,5°C indicate weak to very strong El Niño ENSO (+) phase. The fitted lineal regression is shown with a dashed line.

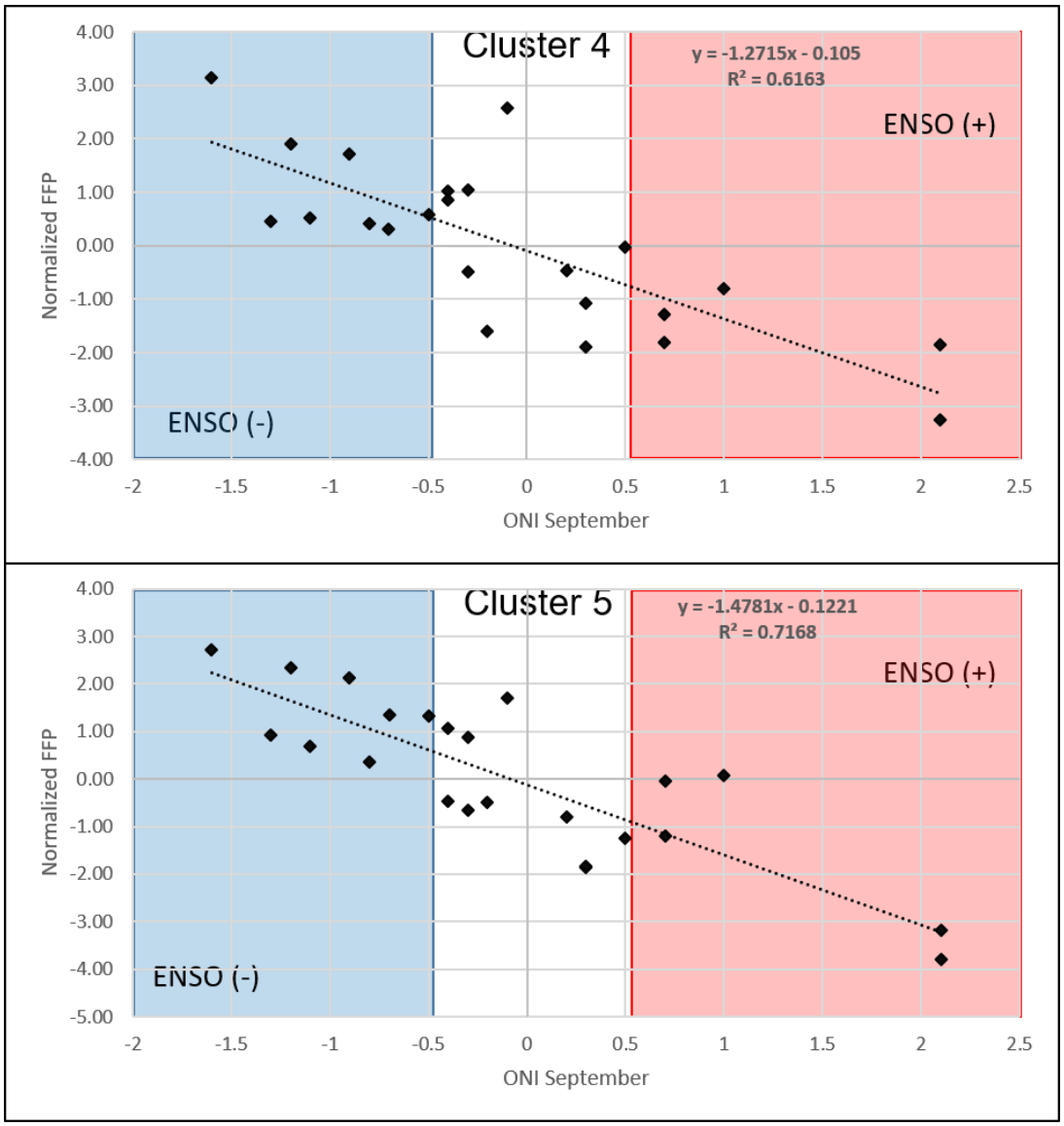

Figure 53: Scatter plot of winter-early spring (September) fog and low cloud frequency presence (normalized FFP) versus ONI sea surface temperature anomalies (SSTAs) in cluster areas 4 and 5. SSTAs < -0,5°C indicate weak to strong La Niña ENSO (-) phase; SSTAs > 0,5°C indicate weak to very strong El Niño ENSO (+) phase. The fitted lineal regression is shown with a dashed line.

Finally, returning to the hypothesis raised by Garreaud et al (2008a) that for the latitude of the study area higher FFPs are expected in ENSO (+) years and the opposite for ENSO (-) years, our results confirm this hypothesis for summer (February), but not for the winter/early-spring. Interestingly, this approach originated due to high FFPs in the semiarid springtime; in this sense, in both, in the semi-arid and the hyper-arid region, would be responding in a similar way to the ENSO signals during their high FFP season.

6.4.3 Trends in fog and low clouds and future scenarios

The null trends in FFPs during February detected in the different cluster areas are consistent with those observed by Muñoz et al (2016) at the Iquique airport, where for this particular season (summer) FFPs were equivalent to the average over the last 30 years. At the same time, a similar situation occurs during winter/early-spring, where weak positive trends over the ocean and near shore areas detected in this research are also consistent with airport observations, even as they cover a longer period of time. Also, in accordance with these results, Seethala et al (2015) showed an increase in the annual average trend of low clouds in the SEP for the period 1984-2009 using various satellite global model approximations. This latter study, despite consistent results, should be interpreted with caution, as it mainly covers low clouds over the oceans on a large scale, and does not necessarily capture the coastal-land influences. Conversely, Schulz et al (2011a) and Quintana and Berrios (2007), also based on the Iquique airport observations, show negative trends in cloud cover; however, they applied different methodological approaches, based on particular hours of the day, and with different criteria as to what is considered a low cloud. On the other hand, they analyze a longer time series that includes the decade of the 1970's, when there was a significant increase in low clouds, producing an expected decrease in the years following. In relation to the weak negative trend observed in FLC cover in areas at an altitude above ~1.000 m a.s.l. in the Coastal Cordillera during September, there were no further antecedents. The tendency in this areas is primarily related to a decrease in the thermal inversion layer altitude over the last decades, which has been estimated at about 100 m decade^{-1} for the period 1995-2010 according to Muñoz et al (2016). While on the one hand there has been an increase in the presence of FLCs (in the ocean and near shore areas), on the other hand areas that were previously covered with FLCs are no longer covered, given that a lower thermal inversion prevents the occurrence of fog at high altitudes. As the mean altitude of the thermal inversion layer in September is 1.060 m a.s.l with a mode of 1.000 m a.s.l. and variability of ±150 m (see details in section 7.1), it is expected to that FFPs decrease in these areas. However, local factors such as topography, wind speed and wind direction can have an effect on the distribution of fog that is still not well understood; furthermore, such factors could counteract a decline in the thermal inversion layer. Possible evidence of the negative trend is the observed dieback in fog dependent vegetation by Schulz et al (2011b), where less fog coverage translates into less water input, and consequently a loss in coverage of these species.

The observed trends must be interpreted in the context of a decadal time period in which the Pacific basin was undergoing cold conditions, characteristic of La Niña. Both the IPO and the PDO decadal index show cooling since the late 90's. The La Niña-like pattern is related to oceanic-atmospheric conditions during which there is an intensification of the SEP anticyclone, which is related to higher subsidence of air in the subtropical region, a strengthening of the thermal inversion layer, a shallower MBL and cooler temperatures. These conditions are conducive to FLC formation, as discussed in section 6.4.1 (see Fig. 43), and are therefore consistent with observed trends. Although inter-annual results for February show an inverse relationship (greater FFP in El Niño), these conditions have not predominated in the last few decades, yet nevertheless this relationship also occurs in the periods of lower FFP, without little impact on the annual FLC balance. Various authors have documented variations caused by this trend of La Niña-like conditions. For example, Falvey and Garreaud, (2009) and Vuille et al. (2015) documented cooling in surface temperatures along the northern Chilean coast during recent decades, which are associated with strong vertical stratification of air temperatures over the central and northern Chilean territory and which has implied reinforcement of the thermal inversion layer, producing increased temperatures above and a cooling below. However, we must also consider the influence of global warming on these trends. Seethala et al. (2015), postulates that the observed trends in FLC formation in the SEP may be due to natural variation and not necessarily to systematic responses to global warming. On the other hand, Vuille et al. (2015) postulate there is little chance that the similarity in time period and magnitude of temperature changes and trends in the Andes and the west coast of South America with the average rise in global warming is due to only natural cycles. In this sense, and despite the fact that the projections of various climate models for the coastal Atacama do not correctly capture recent cooling within the MBL (Falvey and Garreaud., 2009) or do not properly characterize the physics and dynamics within the MBL (Seethala et al., 2015), climate models agree that the temperature over the thermal inversion will continue to rise (Vuille et al., 2015), and that the SEP anticyclone will continue to strengthen (Falvey and Garreaud., 2009). Higher temperatures above the thermal inversion layer, in addition to a rugged SEP anticyclone, would imply a strengthening of the thermal inversion layer, thus an increase in stability between the layers of the atmosphere. Therefore, conditions favorable to the formation of FLCs would be maintained or increased. In any case, evidence implies that FLCs will closely follow inter-annual (ENSO) and inter-decadal (IPO, PDO) variations in the ocean-

atmosphere system in the SEP, while ENSO patterns will continue to intensify (La Niña) or counteract (El Niño) current and future global warming trends.

7 Results and discussion of local scale analysis: GOFOS

Fig. 54 presents the section of the general research concept addressed in this chapter 7. Results in this chapter include description and characterization of the spatial-temporal variations in FLCs and atmospheric variables based on GOFOS images and weather station measurements. Here in the discussion are analyzed these results and examine the factors potentially involved in the monthly and daily cycles of FLCs.

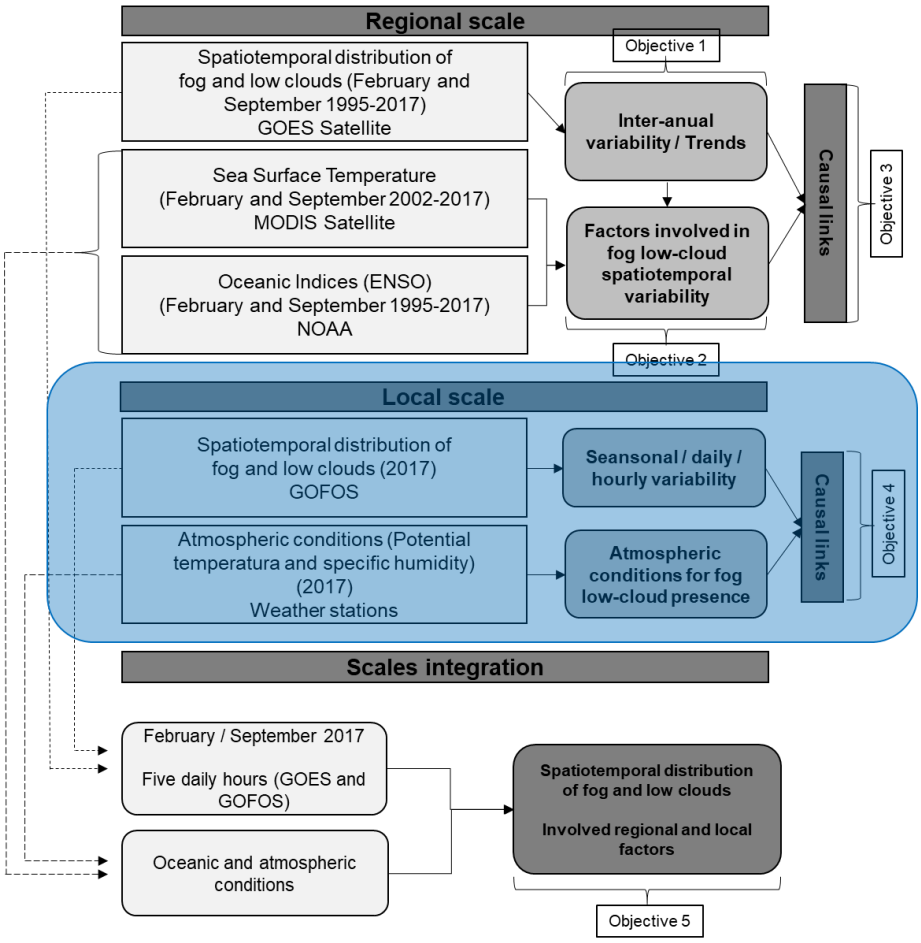

Figure 54: Local scale analysis within the overall study design for spatiotemporal characterization and analysis of fog and low clouds and atmospheric variables, based on GOFOS and weather station datasets.

The GOFOS system, installed in the coastal Atacama, allows us to describe and characterize in detail the spatiotemporal distribution and variability of fog in 2017 and part of 2016. In addition, GOFOS observations on the presence of fog and low clouds allows us to determine and characterize seasonal and hourly variability in the thermal inversion layer

altitude. The results are presented and analyzed according to the measurement of each camera (Top and bottom), and then integrated with estimations of cloud thickness.

7.1 Cloud top: Basal altitude of thermal inversion layer

The cloud top (CT) altitude, which is associated with the altitude of the base of the thermal inversion layer, shows an annual cycle with marked seasonal variations, which, in turn, are inversely related with the FFP (see Fig. 55). The highest CT altitude occurs during summer (with a seasonal mean of ~1.230 m a.s.l.), when FFP is at its minimum (seasonal mean of ~3,5 %), then the CT decreases towards autumn (~1.100 m a.s.l.), the season in which the FFP begins to increase (~20 %). The CT reaches its minimum mean altitude in winter (~1.040 m a.s.l.), the period coinciding with the maximum FFP (~50 %), then the CT begins rising slightly in spring (~1.070 m a.s.l.) when FFP is also slightly decreased (~27 %).

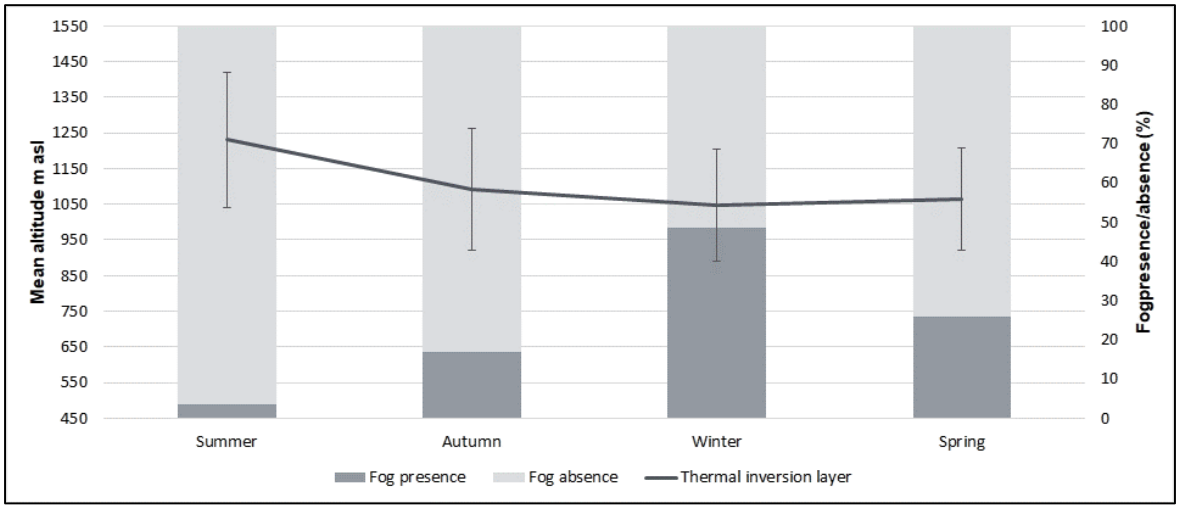

Figure 55: Altitude of the seasonal thermal inversion layer and fog and low cloud frequency presence and absence.

On a monthly scale, the CT altitude and FFP have a strong inverse correlation (r = -0, 77, with a 99 % confidence level). Fig. 56 shows that he highest average CT altitude of ~1.320 m a.s.l. occurs in January, followed by February with an average of ~1.250 m a.s.l., and continues to descend gradually until it reaches a minimum in August (1.000 m a.s.l.), after this minimum it gradually ascends again until November (1.110 m a.s.l.). The only month that breaks the trend of this annual cycle is December (1.070 m a.s.l.). In turn, the lowest FFP occurs during February (1,5 %, slightly lower than the 2 % of January) and the highest

occurs in August (50%). In relation to variability in CT altitude, the highest variability occurs in March (SD = 210) and the lowest in August (SD = 130). Despite these extremes, it is not observed an annual cycle, but rather changing variability throughout the year.

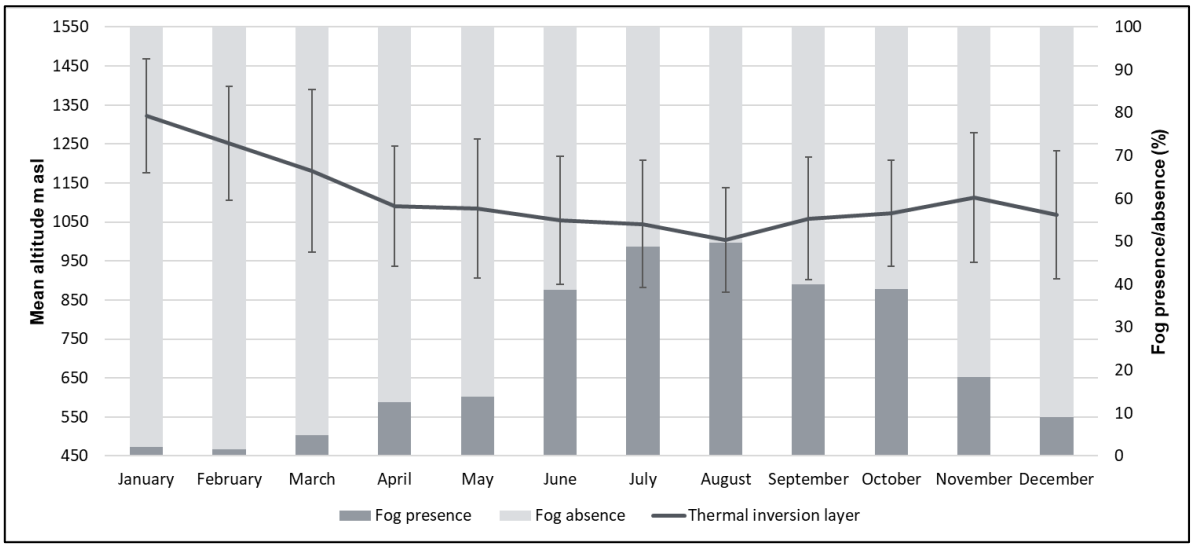

Figure 56: Monthly thermal inversion layer altitude and fog and low cloud presence.

The annual daily cycle also presents a strong inverse relation between CT altitude and FFP ($r = -0,76$ with a 95 % confidence level). Fig. 57 shows the annual mean hourly variations; variation in CT altitude presents its minimum during nighttime and dawn (~1.050 m a.s.l.), and then starts ascending during the morning until reaching its maximum during midday (~1.270 m a.s.l.), when it starts descending during sunset. Conversely, FFP presents its maximum during night and dawn (~40 %), then during the morning starts to decrease its presence until a minimum at noon (~2 %), after which it then increases again during the evening, reaching its daily maximum at 21:00 (45 %).

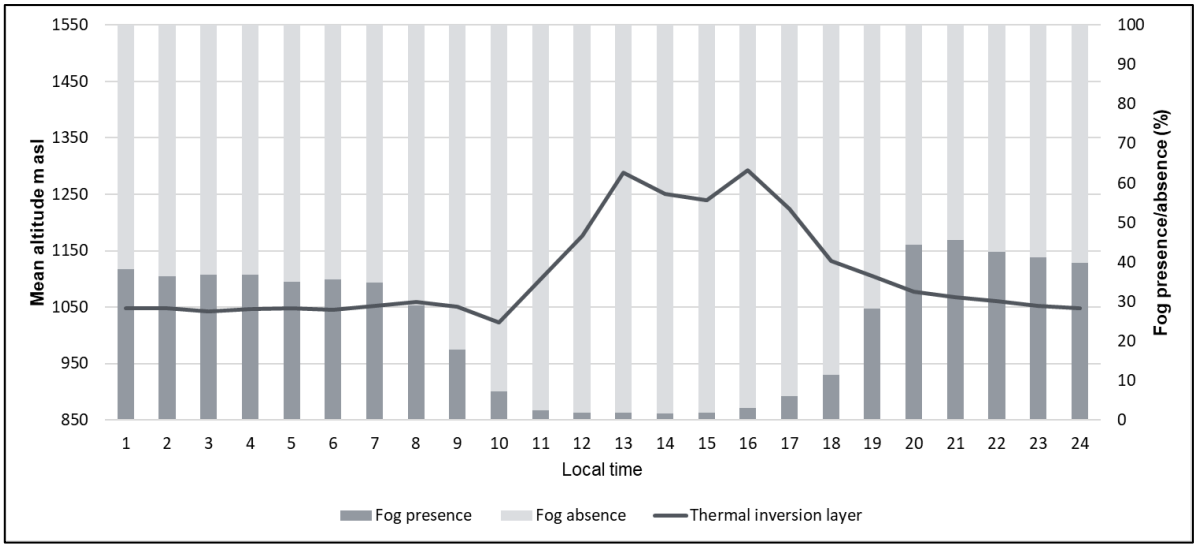

Figure 57: Annual mean daily cycle of the thermal inversion layer altitude and fog and low cloud frequency presence and absence.

At a seasonal level, daily CT altitude and FFP show variations in its inverse relation and hourly cycle. While summer does not show a statistically significant relationship, autumn shows a very strong relationship (r = -0, 93), and on the other hand, both winter and spring show a strong relationship (r = -0,64 and 0,70 respectively). Fig. 58 shows seasonal means in CT altitude and the FFP daily cycle. During summer, the CT altitude has a pronounced daily cycle, presenting on average a daily oscillation of 400 m, with a minimum at midnight (CT = 1.000 m a.s.l. with a SD = ± 100 m), then gradually increasing during the night until dawn (CT = 1.340 m a.s.l. at 09:00), it then reaches its maximum at noon (1.400 m a.s.l.; SD = 0, because the few observations have the same altitude). From afternoon to sunset, CT altitude decreases by an average of 250 m (CT = ~1.200 m a.s.l; SD = ± 140 m). The greatest variability in CT altitude occurs at dawn and sunset (SD = ± 190 and 165 m respectively), and the lowest occurs at night (e.g. at 04:00 SD = ± 50 m). Related to FFP, and considering the very low percentages of fog presence during summer, the lowest FFPs correlate with the highest CT altitudes from morning to afternoon; on the other hand, despite the fact that the lowest CT altitude is at midnight, the highest FFP occurs at sunset (~5%). During autumn, mean CT altitude varies within a daily range of about 160 meters, which is the lowest variation for any season. The lowest altitude occurs at 03:00 (CT = 1.030 m a.s.l; SD = ± 140 m), increasing slightly during the night and early morning, until reaching its highest altitude during midday-afternoon (CT = ~1.230 m a.s.l), followed by a decrease until sunset, when it reaches practically the same altitude as at midnight (CT = ~1.050 m a.s.l; SD = ± 150 m). The greatest variability in CT altitude occurs at dawn (09:00) and afternoon

(17:00) (SD = ± 190 and 180 m, respectively), but there are no significant differences compared to the other daily time points, with the exception of midday, when variability is 50 % lower. The inverse correlation between FFP and CT altitude occurs throughout the day, with the highest FFP during night and sunset (~25 %) and the minimum during the afternoon (~4 %).

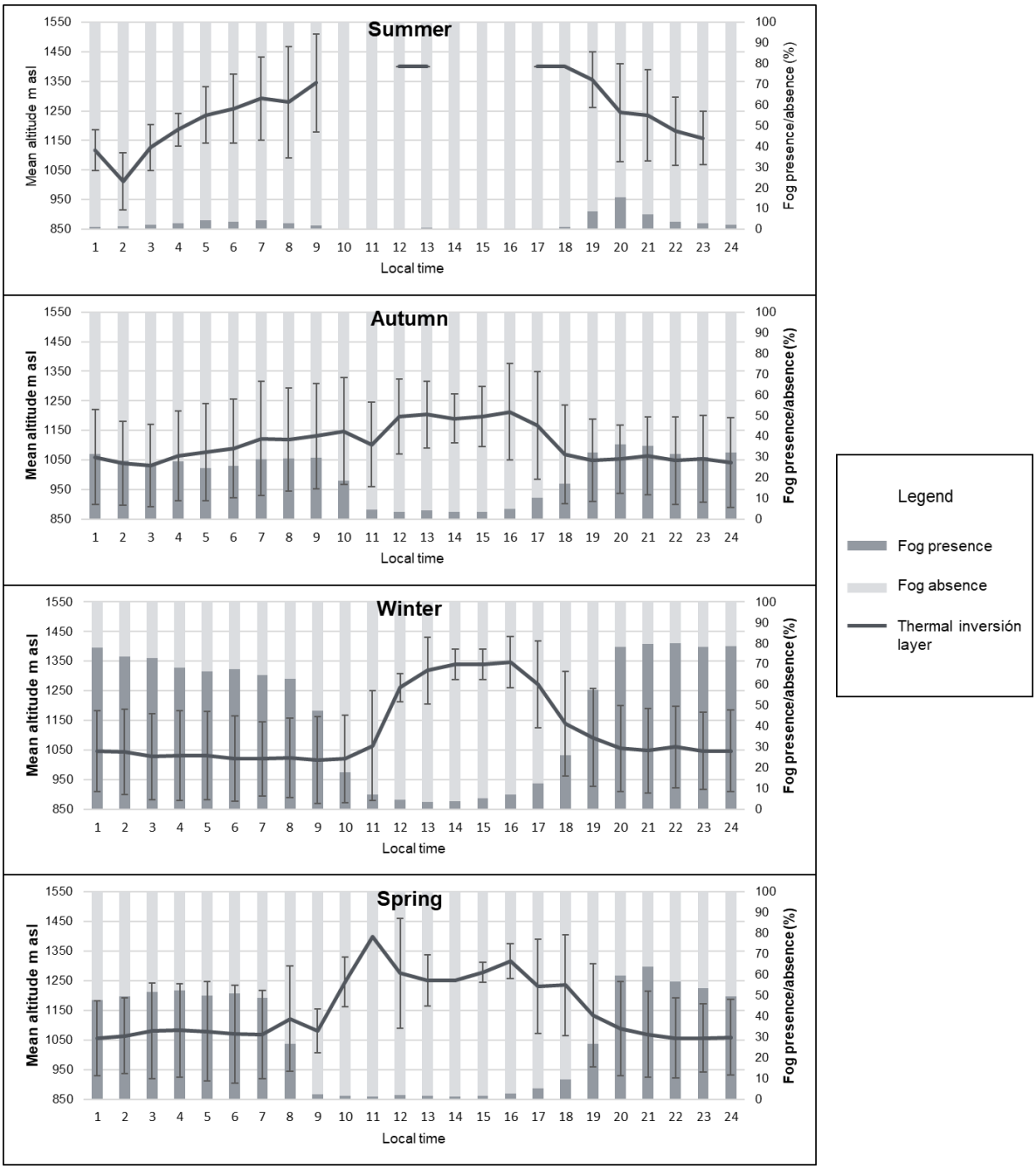

Figure 58: Daily cycles of the mean the thermal inversion layer altitude and fog low and cloud frequency presence and absence by season.

During winter, the season of maximum FFP, the daily cycle in CT altitude oscillates by about 310 meters, with a minimum and stable altitude during the night and the early morning (CT = ~1.000 m a.s.l; SD = ± 150 m); it then presents an important increase from 11:00 to 12:00, until it reaching its maximum in the afternoon (CT = 1.310 m a.s.l; SD = ± 140 m). Altitude then presents a significant decrease between 17:00 and 18:00 until reaching its minimum during sunset (CT = 1.040 m a.s.l; SD = ± 145 m). The greatest variability in CT altitude occurs during sunset (at 18:00 SD = ± 175), but just as in Autumn, there are no relevant variations in a particular daily hour, without considering the mid-afternoon. The minimum FFP (~5%) coincides with the highest CT altitude at noon-afternoon, and the maximum occurs during night and sunset (70 and 80 %, respectively), when CT altitude is significantly lower. During spring, the daily cycle in CT altitude varies 210 meters, and presents its minimum during night (CT = 1.050 m a.s.l; SD = ± 130 m), then it increases during the morning, from 09:00 to reach its maximum at 11:00 (CT = 1.400 m a.s.l), it then maintains a stable height between 12:00 and 17:00 of 1.280 m a.s.l., to gradually decrease from 17:00 to 20:00, when it reaches altitudes similar to nighttime (CT = 1.060 m a.s.l; SD = ± 130 m). The greatest variability in CT altitude occurs during early morning and sunset (SD = ± 180 and 175 m, respectively), and as with other seasons, there were no significant variations in any particular time point throughout the day, without considering the mid-afternoon. The minimum FFP (~2%) occurred along with the highest CT altitude at noon-afternoon; very low FFPs occur during the morning (09:00 to 11:00) (~3 %). The maximum FFP was at sunset (~60 %) and at night (~50%), when CT altitude is lower.

Monthly characterization of the daily cycle of CT altitude and FFP, primarily demonstrate significant inverse correlations, but with some exceptions. Fig. 59 presents the mean daily cycles for January, February and March, when annually CT altitude is higher and FFPs are lower. The null or very low FFPs at most daily time points during January and February, make a characterization of daily patterns difficult. In any case, in the case of the few observations during night (February) or at noon (January) where the FFP was between 2 to 4 %, the CT altitude was at its maximum (1.400 m a.s.l). On the other hand, both months present higher FFPs from sunset to midnight (with a peak at 20:00), the period of the day during which a gradual decrease in CT altitude is observed, until reaching its minimum altitude at 23:00 – 24:00 hours (~1.150 m a.s.l). As observations are limited, the hourly variability does not show significant patterns. In March, the FFP increases and presents a more distinct daily cycle of the CT altitude. The CT altitude reaches its lowest altitude at

03:00 (CT = 930 m a.s.l; SD = ± 80 m), then increases continuously until morning (CT = 1.350 m a.s.l; SD = ± 165 m). There is an absence of fog from 10:00 to 16:00, after which there is a decrease in CT altitude until sunset (CT = 1.150 m a.s.l; SD = ± 135 m). Higher FFPs occur during the night-early morning (~10 %) and during sunset (~16 %), which coincides with the period of the day when the CT altitude moves from and to its extremes.

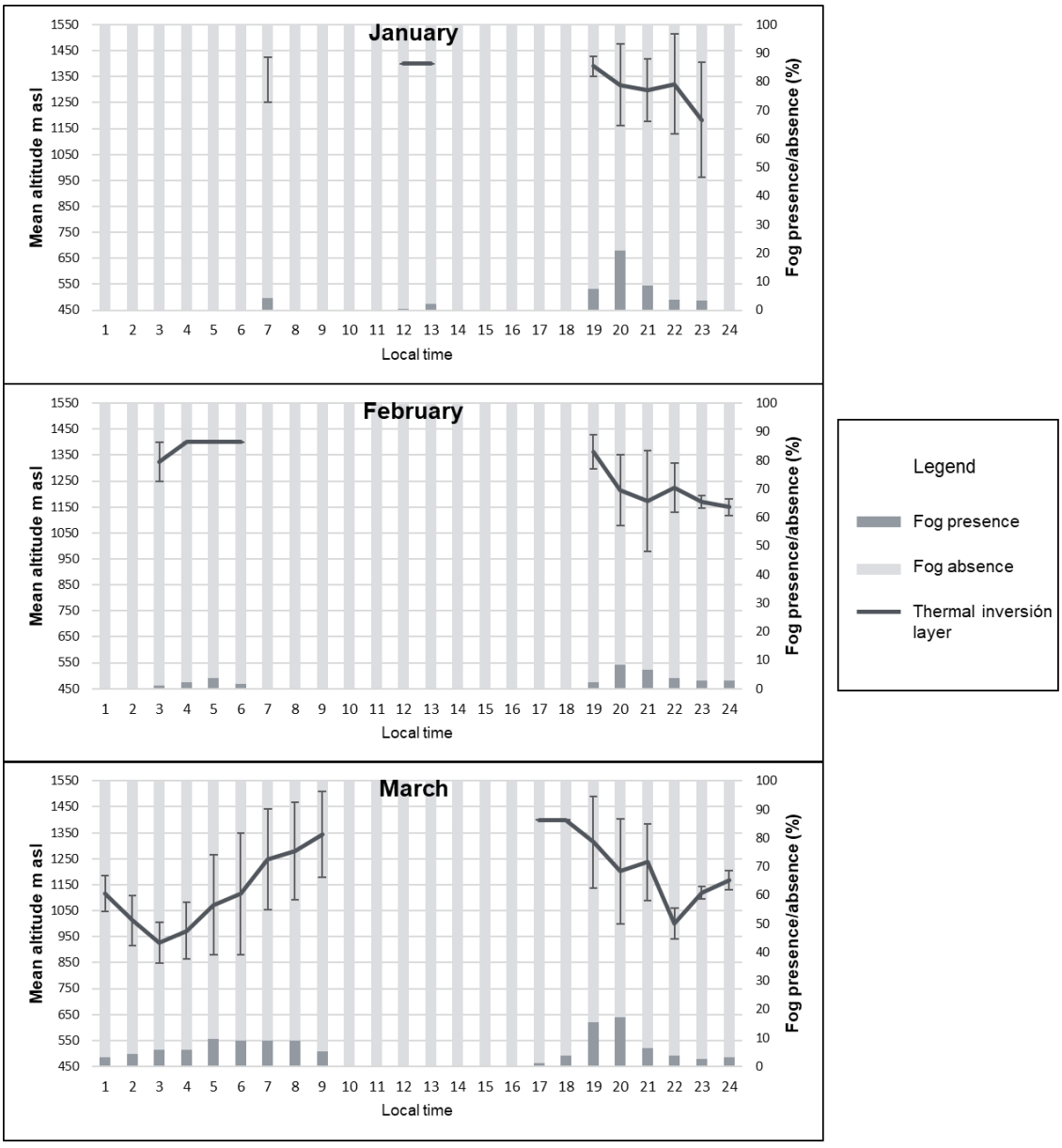

Figure 59: Monthly (January, February and March) mean daily cycles of the thermal inversion layer altitude and fog and low cloud frequency presence and absence.

Fig. 60 presents mean daily cycles for April, May and June, of which April is the only month with an absence of fog during the day (from 11:00 to 16:00). In April, there is on average

very low daily variation in the CT altitude (200 m), with minimums at night, from 23:00 to 03:00 (CT = 1.045; SD = ± 110 m), and then it gradually increases to its maximum at 10:00 and 17:00 hours (CT = 1.245 m a.s.l.; SD = ± 175 and 200 m respectively). From sunset to midnight the CT altitude decreases progressively. In April there is a correlation between CT altitude and FFP of r = -0, 61 (at a 95 % confidence level). The maximum FFP occurs at sunset (a mean of 23 %, with a peak at 20:00 of 30 %) and is a little bit higher than at nighttime (17 %), both time points coincide with lower CT altitudes. On the other hand, the minimum FFP, not considering the total absence of fog at noon-afternoon, occurred at 10:00 and 17:00 – 19:00 (~5 %), when the CT was at its highest altitude, which at the same time, coincides with the highest hourly variability. May also presents very low daily variation in the CT altitude (200 m), with minimums at night (CT = ~1.060 m a.s.l; SD = ± 175 m) and sunset (CT = ~1.045 m a.s.l; SD = ± 165 m) and a small peak during the afternoon (at 15:00 CT = 1.010; SD = ± 75 m). From 06:00, the CT altitude begins to increase slightly until it reaches its maximum at 12:00 (CT = 1.210 m a.s.l.; SD = ± 70 m). Then, between 12:00 and 15:00, the CT altitude undergoes its greatest daily decrease, stabilizing from 18:00 onwards. The highest FFPs primarily occur when the CT is at a lower altitude, but here the maximum occurs at night (a mean of 23 %, with a peak at 08:00 of 28 %), which is a little higher than at sunset (16 %). On the other hand, despite the fact that the minimum CT altitude occurs at noon, the FFP is at its minimum (~3,5 %) from morning to afternoon, a period that coincides with the lowest hourly variability. In this way, the lower altitudes of the CT and the low FFP during the noon-afternoon, make the correlation between both variables null. In June CT altitudes are very stable for most of the day, with an average of 1.045 m a.s.l from sunset (18:00) to early morning (10:00), a period of the day that also presents similar hourly variability, with an average of SD = ± 155 m. The largest increase in CT altitude occurs at 11:00, until reaching its maximum at 13:00 (CT = 1.280 m a.s.l.; SD = ± 180 m), it then remains stable until the 16:00, when it starts descending until 18:00. FFP shows a strong inverse correlation with CT altitude (r = -0, 79, with a 99 % confidence level), with FFP maximums occurring at midnight and sunset (55 and 65 % respectively) and minimums in the morning to afternoon, with an FFP mean of 10 %.

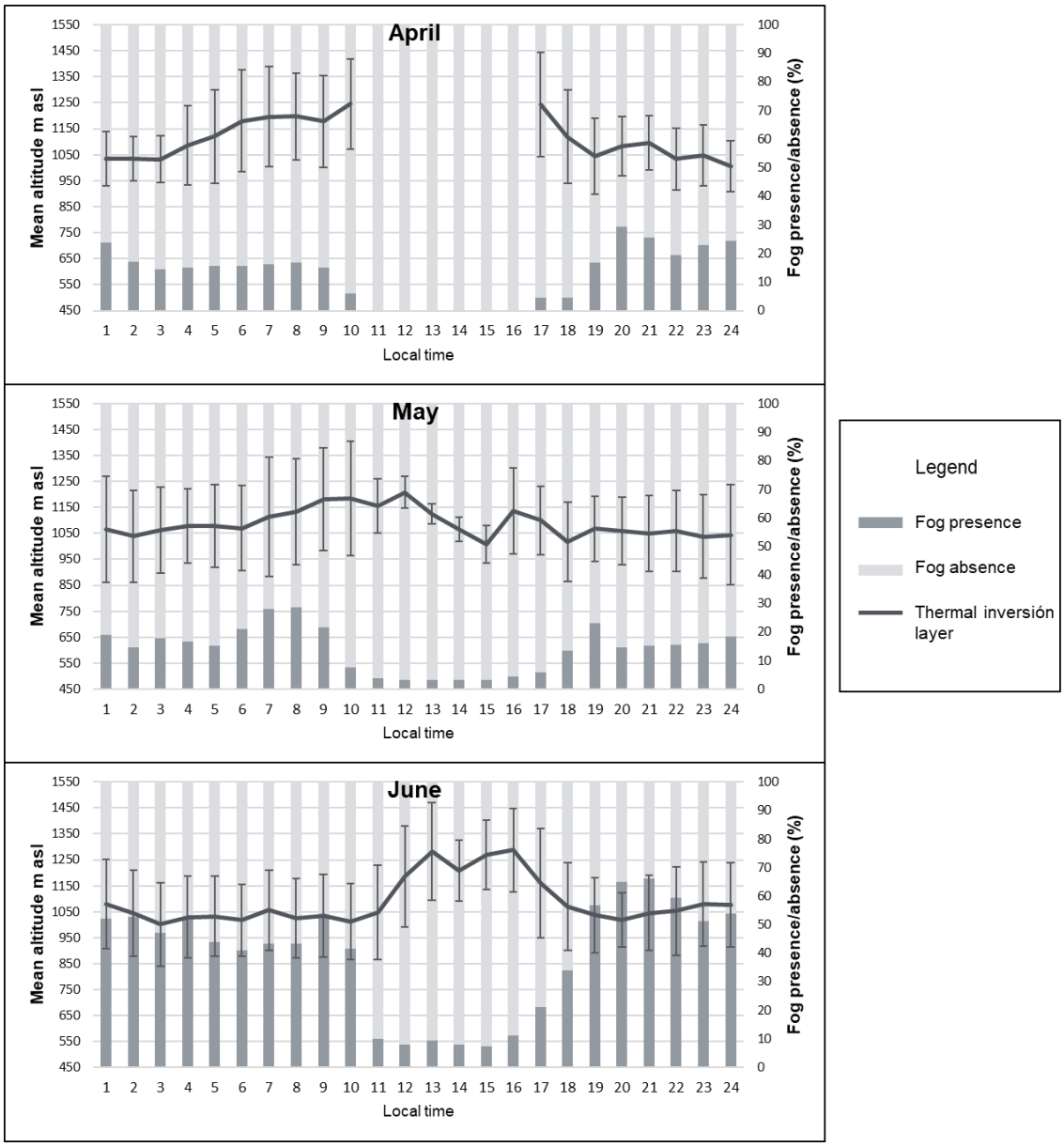

Figure 60: Monthly (April, May and June) mean daily cycles of the thermal inversion layer altitude and fog and low cloud frequency presence and absence.

During the months with the highest FFPs, July, August and September, the daily cycle of CT altitudes is well demarcated (especially in July and August), with an average similar to their minimum altitudes from sunset to early morning, and an increase in CT altitudes from morning to afternoon (see Fig. 61). The CT altitude and FFP daily cycle present a strong inverse correlation during these 3 months (r = -0,82; -0,83 and -0, 44 respectively, with a 99 % confidence level), with the correlation strongest in July and August. In this sense, July presents an average CT altitude of 1.040 m a.s.l from sunset to early morning, with a minimum of 1.000 m a.s.l., which occurs between 05:00 and 06:00. During the morning,

between 11:00 and 12:00 there is a sharp increase in CT altitude until 1.400 m a.s.l, after which it remains stable until the 16:00, when a pronounced decrease begins until 18:00 hours. Hourly variability is similar throughout the day (a SD mean of ± 150 m), but is greatest at 11:00 and 17:00 (SD = ± 220 and 180 m respectively), which coincide with the thresholds of increasing and decreasing CT altitude.

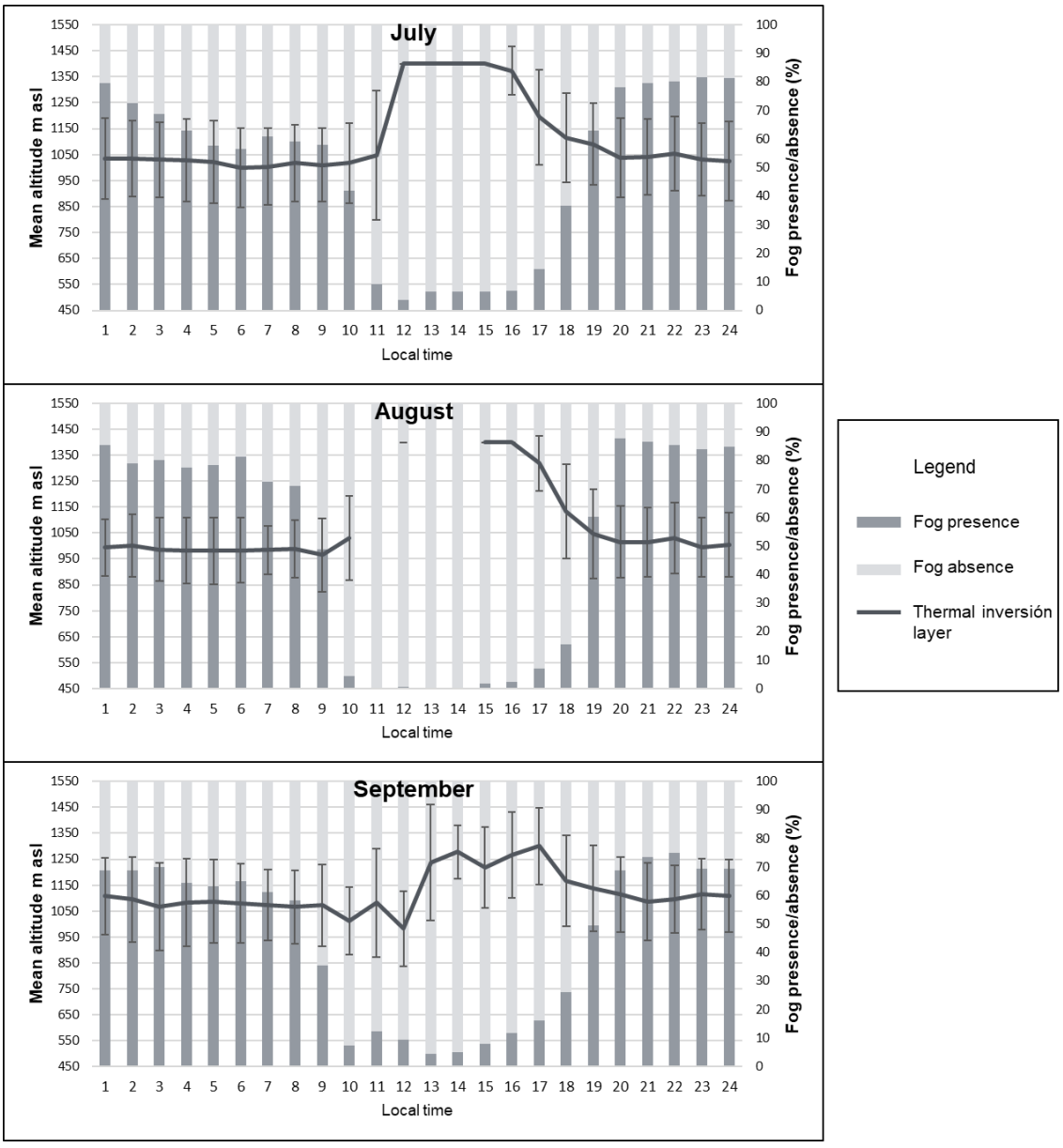

Figure 61: Monthly (July, August and September) mean daily cycles of the thermal inversion layer altitude and fog and low cloud frequency presence and absence.

The lowest average CT altitudes occur in August, not considering the daytime hours from morning to noon (1.000 m a.s.l), with minimums of 965 m a.s.l. at 09:00 and 980 m a.s.l, at

night. Despite the fact that there is no fog presence at 11:00 and 13:00 - 14:00, the high and stable CT altitude at 12:00 and 15:00 – 16:00 (1.400 m a.s.l) allow us to assume similar CT altitudes in the morning-afternoon period, which then, undergo a pronounced decrease from 17:00 until the 19:00. Just as in July, hour variability is similar throughout the day (a SD mean of ± 130 m), but its maximum occurs at 10:00 and 18:00 (SD = ± 160 and 180 m respectively), which, also coincide with the thresholds of increasing and decreasing CT altitude. September, for its part, maintains a regular CT altitude from sunset to early morning, with a mean of 1.080 m a.s.l., although the minimum occurs in the morning and at noon, specifically at 10:00 and 12:00 (CT = 1.010 and 980 m a.s.l respectively). At 13:00 the CT altitude increases, reaching an altitude of 1.250 m a.s.l,, which remains stable until 17:00 when it decreases until sunset. In relation to hourly variability, this is regular throughout the day (a SD mean of ± 150 m), and as in July and August its maximum occurs at 13:00 (SD = ± 220 m), which coincides with the threshold when CT altitude increases.

During Spring, the CT altitude presents daily differences in its cycle (see Fig. 62), and FFPs are significantly reduced towards December; nevertheless, the inverse relationship between CT altitude and FFPs is still present (r = -0,70; -0,53 and -0, 74, respectively, with a 95 % confidence level). In October, the winter daily cycle is maintained, with a very stable CT altitude from sunset to early morning (mean of 1.070 m a.s.l.), with a minimum at 07:00 (CT = 1.030 m a.s.l.). From 11:00 to 14:00 there is a total absence of fog, which reappears again in the afternoon with the highest daily altitude (CT = 1.400 m a.s.l.), then at 17:00 starts descending until 20:00. FFP has an average of 70 % from sunset to dawn, and then decreases significantly from morning to afternoon (1,5 % or no presence). The hourly variability is similar throughout the day (a SD mean of ± 120 m), and just as in winter months, the maximum occurs at 17:00 (SD = ± 210 m), which coincides with the threshold when CT altitude decreases. In the case of November, lower CT altitudes occur at night and sunset (mean of 1.080 m a.s.l.), and present an extreme minimum at 09:00 (CT = 870 m a.s.l.), which is in this case related to a very low FFP (1,6 %) that contrasts with high FFPs throughout the night and at sunset (50 and 60 %, respectively). In turn, the highest CT altitude occurs during the morning (10:00 to 12:00) with a CT = 1.400 m a.s.l., which then begins to decrease until the 19:00. Finally, in December there is a total absence of fog from morning to afternoon (09:00 to 17:00), while for the rest of the day CT altitudes are similar during night and sunset (CT = 1.070 and 1.050 m a.s.l., respectively), a period that also coincides with the greatest FFPs (25 and 38 %, respectively). The minimum CT altitude

occurs at 23:00 (CT = 1.030 m a.s.l), which in turn presents the lowest hourly variability (SD = ± 90 m). The highest CT altitudes occur at 08:00 and 18:00 (CT = 1.200 and 1.300 m a.s.l., respectively), a period of the day that coincides with the CT altitude moving from and to its extremes.

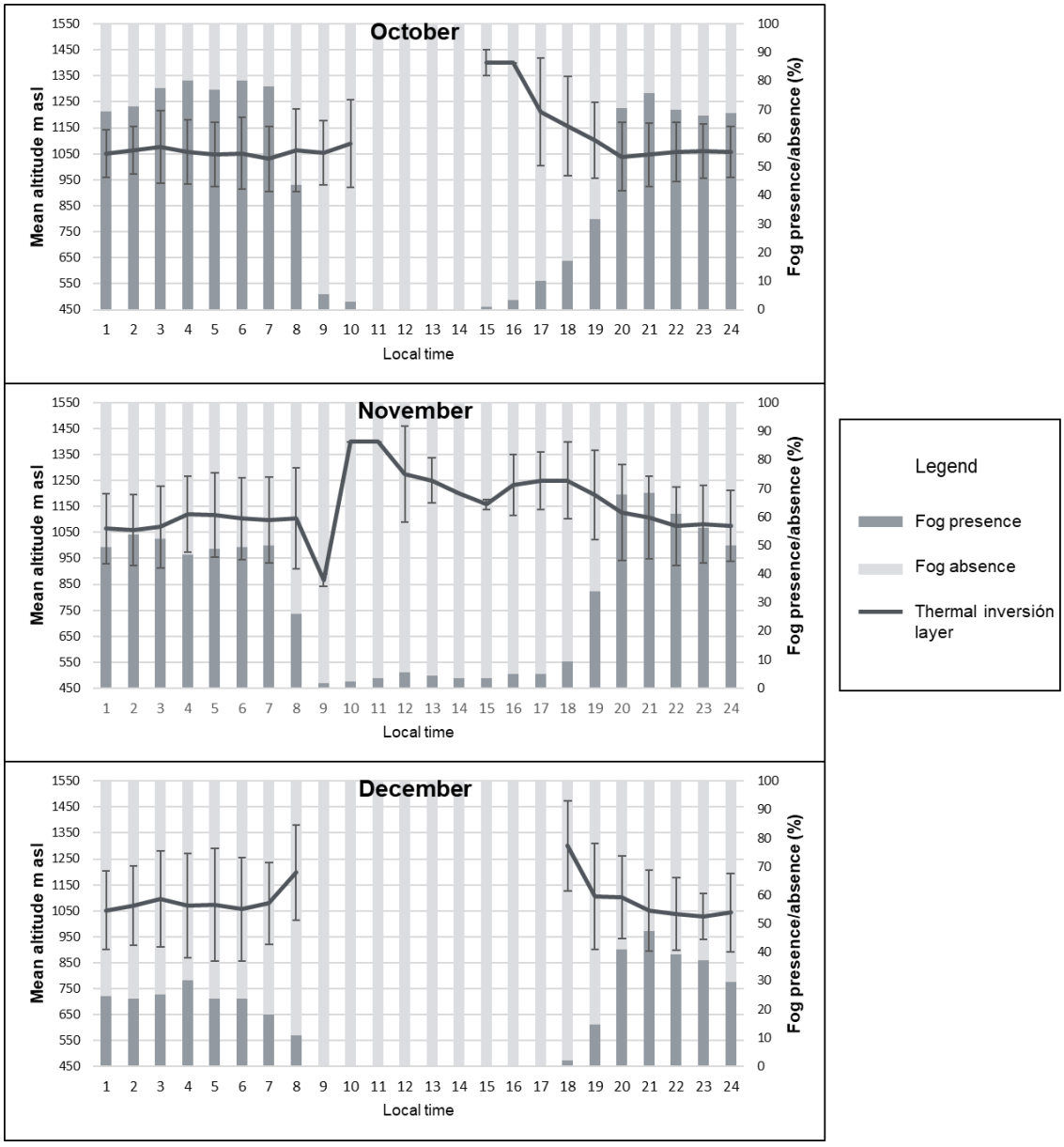

Figure 62: Monthly (October, November and December) mean daily cycles of the thermal inversion layer altitude and fog and low cloud frequency presence and absence.

7.2 Cloud base altitude

The cloud base (CB) altitude presents a well-defined annual cycle, and an inverse relationship with the FFPs (r = -0,70 with 95 % confidence level), with higher CB altitudes occurring in summer in the presence of the lowest FFPs and the opposite during winter (see Fig. 63). In this sense, the highest CB altitude during summer (with a seasonal mean at 970 m a.s.l.), occurs when the FFP is at its minimum (seasonal mean of ~3 %), then the CB decreases towards autumn (865 m a.s.l.), the season in which the FFP begins to increase (~17 %). The CB reaches its minimum mean altitude in winter (855 m a.s.l.), the period coinciding with the maximum FFP (~48 %), until finally the CB starts rising in spring (~910 m a.s.l.) and decreasing its FFP (~35 %).

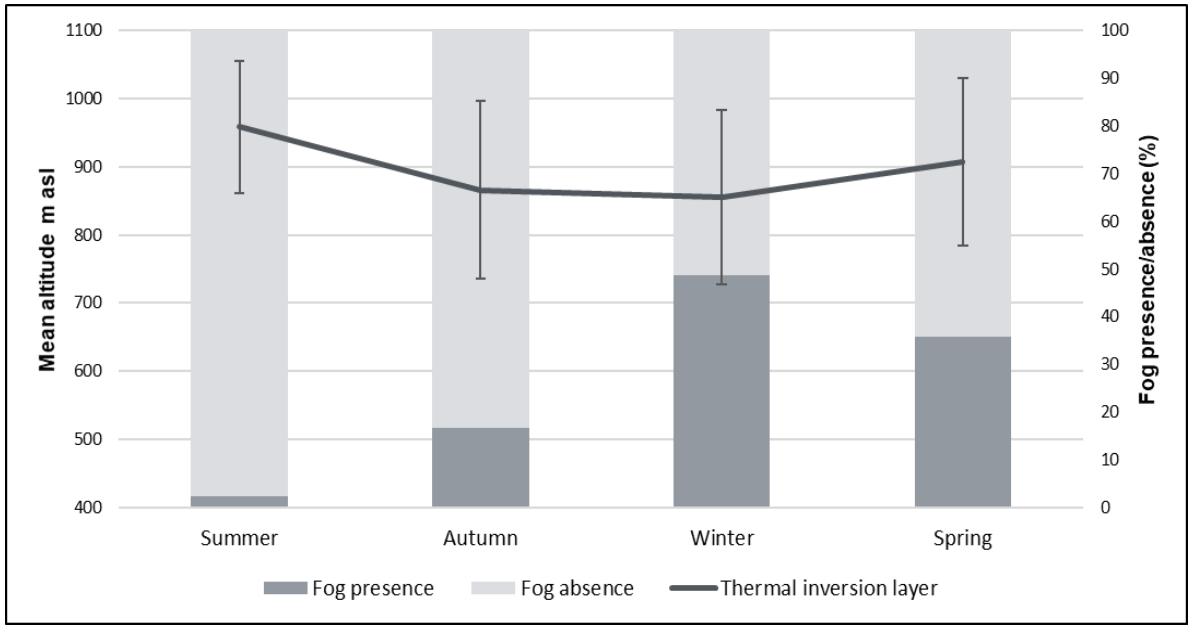

Figure 63: Seasonal cloud base altitude and fog and low cloud frequency presence and absence.

On a monthly scale, CB altitude and FFP also present a strong inverse correlation (r = -0, 72, with a 99 % confidence level). Fig. 64 shows that the highest average CB altitude occurs during January and February, at 1.000 m a.s.l., and continues to descend gradually until it reaches the minimum in July (820 m a.s.l.), and then gradually ascends again until December (955 m a.s.l.). In turn, the lowest FFP occurs during January and February (~1,5 %) and the highest in July (50 %). In relation to variability in the CB altitude, the greatest variability occurs in May and September (SD = 130), but all months from March to November present similar variability (between 120 and 130 m). The lowest variability occurs in

December (SD = 90), not considering January and February, when there is a lack of fog events at the same altitude. There is no clear annual cycle, but rather changing variability throughout the year.

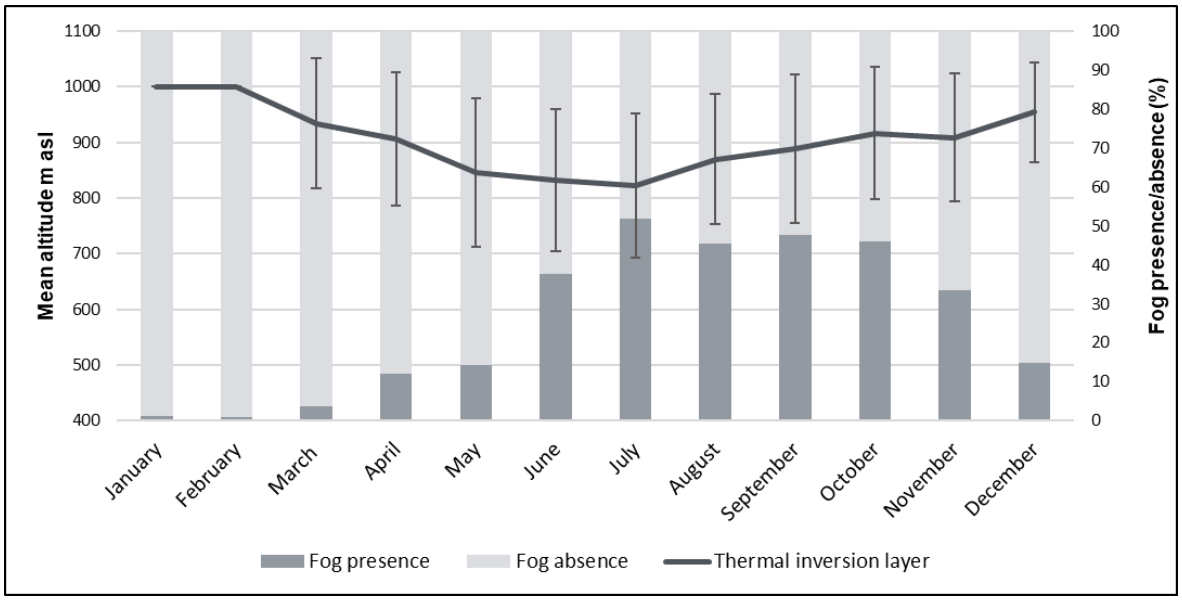

Figure 64: Monthly cloud base altitude and fog and low cloud presence.

The annual mean of the daily CB altitude cycle presents low variation, with a maximum of 115 m between nighttime and afternoon. In addition, there is no well-defined daily cycle. Conversely, FFP follows a pronounced daily cycle. Fig. 65 shows the annual mean hourly variations, with the CB altitude is at its minimum during nighttime (870 m a.s.l.), with a peak at 02:00 (CB = 840 m a.s.l.). From 09:00 the CB gradually ascends until it reaches a first maximum at 11:00 (CB = 930 m a.s.l.), then it drops slightly to increase again to its peak at 19:00 (955 m a.s.l.), after which it descends during the evening until midnight. On the other hand, FFP is high during the period between sunset and early morning (with a mean of 45 %), and very low presence during the morning-afternoon (5 %). Thus, the altitude of the CB and FFP have no relationship in the annual average of their daily cycle.

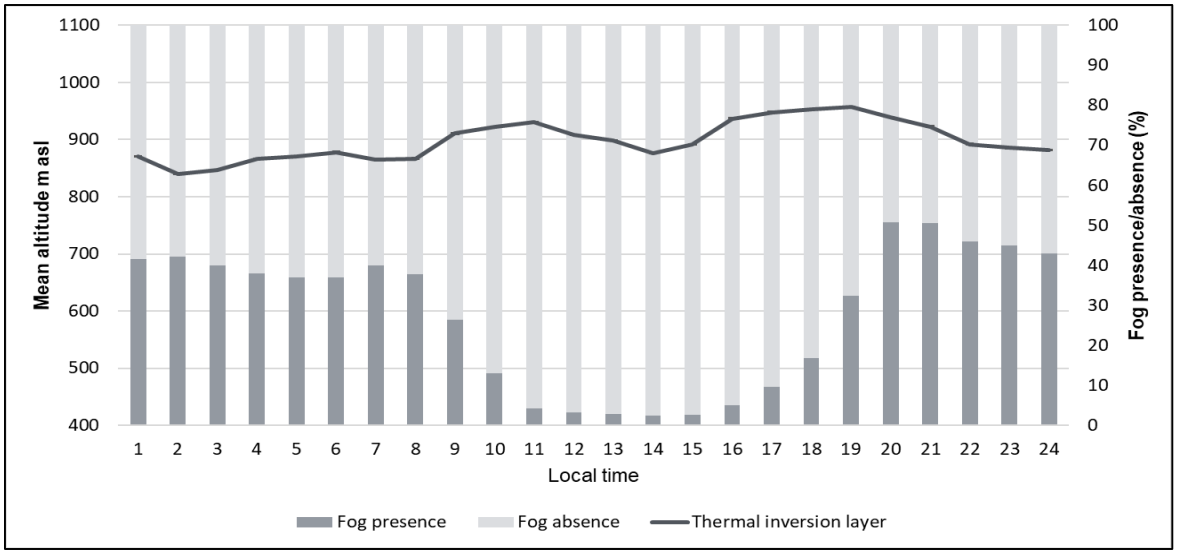

Figure 65: Average annual daily cycle of cloud base altitude and fog and low cloud frequency presence and absence.

Looking at changes in daily CB altitude from a seasonal perspective indicates there is no well-defined daily cycle, cue to little altitudinal variation. Summer, autumn, winter and spring present maximum daily differences of 160, 140, 180 and 175 m, respectively (see Fig. 66). On the other hand, FFP undergoes a daily cycle, as described, with higher fog presence from sunset to early morning, and a lower presence during the morning to afternoon. Therefore, the inverse relationship between CB altitude and FFP is not statistically significant. During summer, there is an absence of fog from 10:00 to 17:00, and for the rest of the day FFP does not exceed 5 %. The CB altitude varies from a minimum at 03:00 (CB = 840 m a.s.l; SD = ± 140 m), followed by a gradual increase into the early morning, to a maximum during the morning (09:00), which continues during sunset (18:00 to 21:00) (in both, CB = 1.000 m a.s.l). In autumn, the season with the lowest variation in CB altitude daily of 140 m, CB altitude is very stable independent of daily changes in FFP (see Fig. 66). Despite low daily variability, the minimum occurs from sunset to midnight, with a mean CB altitude of 840 m a.s.l., which coincides with higher hourly variability (SD = ± 130 m) and higher FFP (35 %). The maximum CB altitude occurs during the night (04:00 to 06:00) and in the afternoon (16:00 to 18:00), with an average CB altitude of 890 and 930 m a.s.l., respectively. At the same time, the hours with the maximum CB altitude coincide with the lowest hourly variability (SD = ± 50 and 75 m, respectively). During winter, CB altitude has a more discernible daily cycle, which begins at midnight with a CB altitude of 850 m a.s.l., and decreases gradually until it reaches its minimum altitude at dawn (06:00 - 07:00) with an average CB of 795 m a.s.l. Then the CB altitude starts to rise until it reaches its maximum

(CB = 970 m a.s.l.) at noon (11:00 to 13:00). From afternoon until sunset the CB altitude keeps varies but remains over 900 m a.s.l. until 19:00 when it begins to gradual decrease. Hourly variability shows a similar relation and distribution as in autumn, with greater variability when the CB is at lower altitudes, and conversely, lower variability when the CB is at higher altitudes.

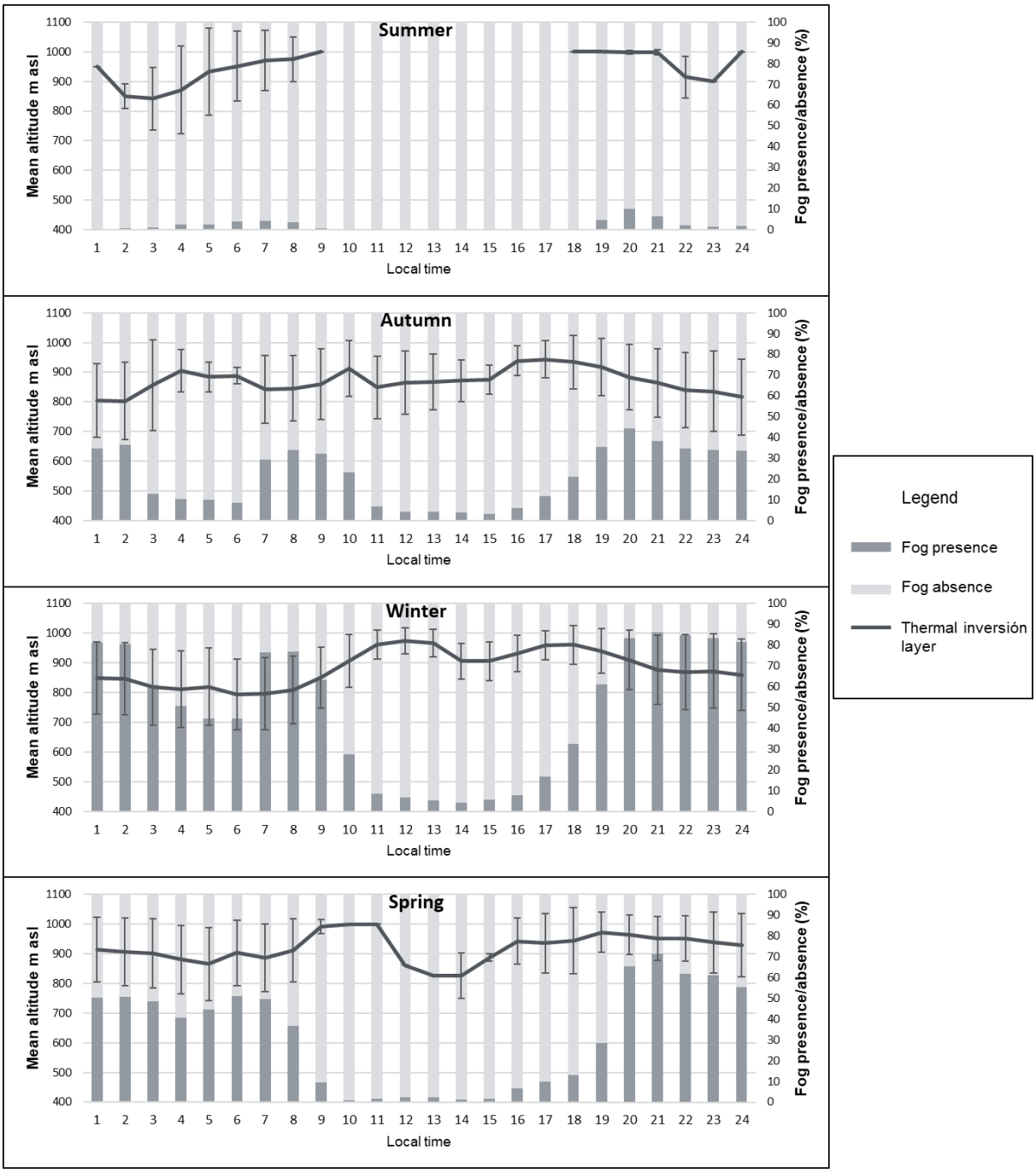

Figure 66: Seasonal mean daily cycles of cloud base altitude and fog and low cloud frequency presence and absence.

Finally, spring presents a daily cycle in CB altitude similar to winter, but with slight differences in the timing of its extremes. A gradual decrease begins at midnight until it reaches a first daily minimum at 05:00 (CB = 865 m a.s.l.), after which it increases to reach its maximum during the morning (09:00 to 11:00) with a CB altitude of 1.000 m a.s.l. At noon, the CB altitude decreases and reaches its second daily minimum at 13:00 – 14:00 (CB = 825 m a.s.l.), after which it goes up again until 19:00, when it gradually starts to descend towards nighttime. During spring, the hourly variability in CB altitude is present, but not as defined as in winter, since the higher variability is mostly found at lower CB altitudes, but there is also a presence at higher altitudes (e.g. 18:00 hours).

Monthly characterization of the daily cycle of the CB altitude and FFP, shows differences in their relationship throughout the year. Fig. 67 present the CB altitude and average FFP daily cycles for January, February and March; in January and February CB altitude is in accordance with very low FFPs. All CB altitude observations are consistent at 1.000 m a.s.l., the maximum altitude measurable by the GOFOS system, demonstrating that CB altitude during the study period did not fall below this altitude during January and February. A more distinct daily cycle is observed in March, with the lowest CB altitudes occurring at night, specifically at 02:00 (CB = 740 m a.s.l; SD = ± 100 m), then increasing continuously until the early morning, when they reach a peak (CB = 1.000 m a.s.l). The maximum altitude continues to increase between 18:00 and 21:00, and then decreases sharply until midnight. Not considering hours when there was no fog presence, when CB altitude is at its maximum FFP is, for the most part, also at the higher end of its range; at the same time, when CB altitude is at its lowest altitude the FFP is also very low. Hourly variability is higher at night (SD = ± 120 m) and lower when the CB altitude it is at its minimum (SD = ± 40 m) and maximum (SD = ± 20) m.

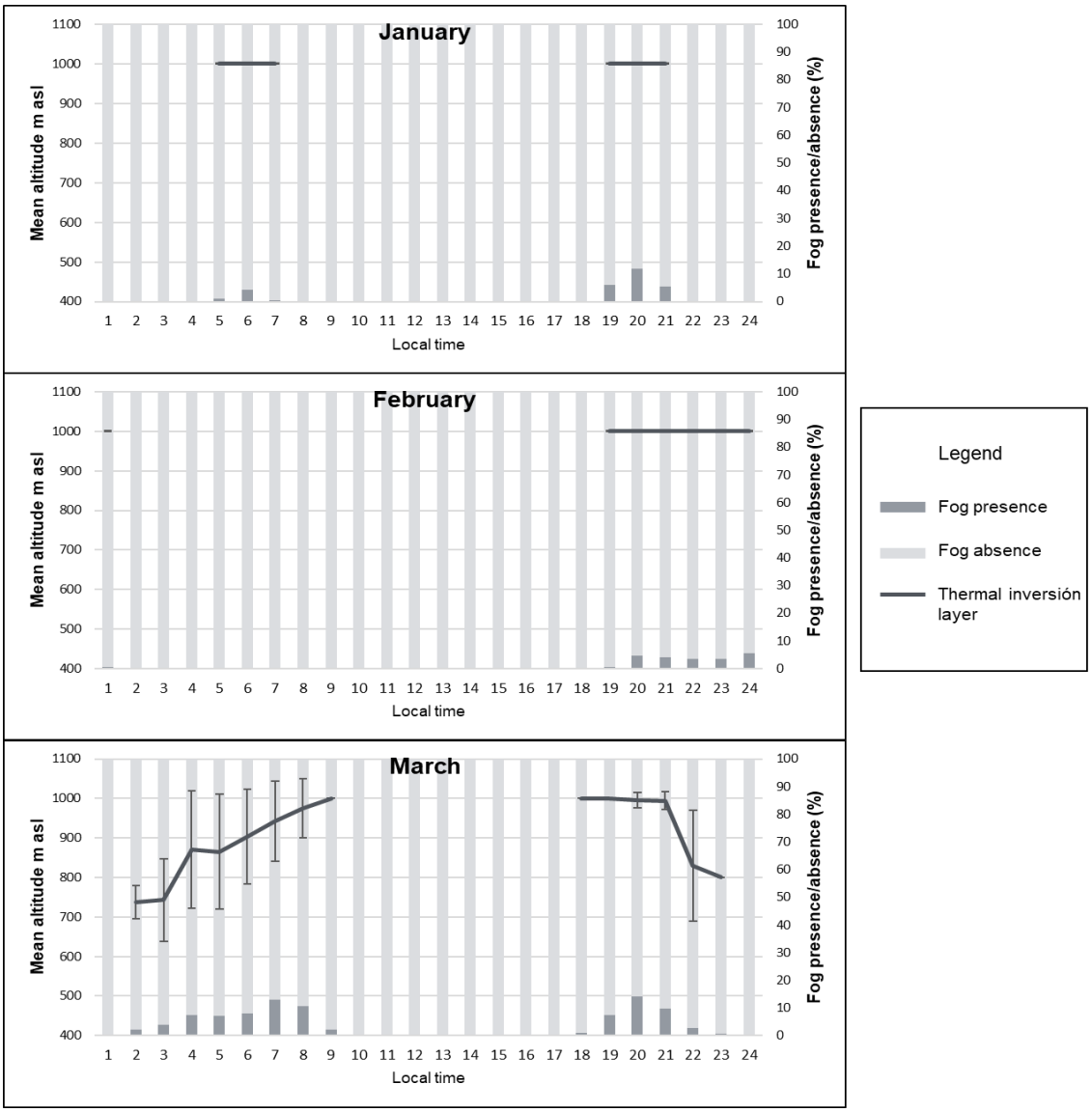

Figure 67: Monthly (January, February and March) mean daily cycles of the cloud base altitude and fog and low cloud frequency presence and absence.

Fig. 68 present the CB altitude and FFP mean daily cycles for April, May and June, with strong similarities between April and May, and limited similarities are presented between April and May with June. In the case of April, CB altitude first increases in altitude from midnight to 04:00, when it reaches its peak (CB = 1.000 m a.s.l,), it then descends until 07:00 and remains stable until 10:00. From 11:00 to 15:00 there is a complete absence of fog, and at 16:00 the fog returns at it maximum altitude, followed by a gradual decrease from 18:00 until its minimum at midnight (CB = 850 m a.s.l.). Maximum CB altitudes are correlates with times of lower FFP; the opposite occurs when the CB altitude is at lower altitudes. Hour variability does not show a clear pattern, despite the fact that lower variability tends to occur

with higher CB altitudes. The month of May shows significant similarities with April in its CB altitude daily cycle, as there is an increase from midnight to the 06:00, when it reaches its peak (CB = 1.000 m a.s.l,) followed by a decrease toward 10:00. In May fog is present from morning-noon, when the CB altitude is low and stable (CB = 800 m a.s.l.), followed by a rise in the afternoon and a descent again from 18:00 to midnight, when it reaches its minimum (CB = 795 m a.s.l.). Just as in April, there is an inverse relationship between CB altitude and FFP, but here the relationship breaks up at noon, as low CB altitudes coexist with very low FFPs.

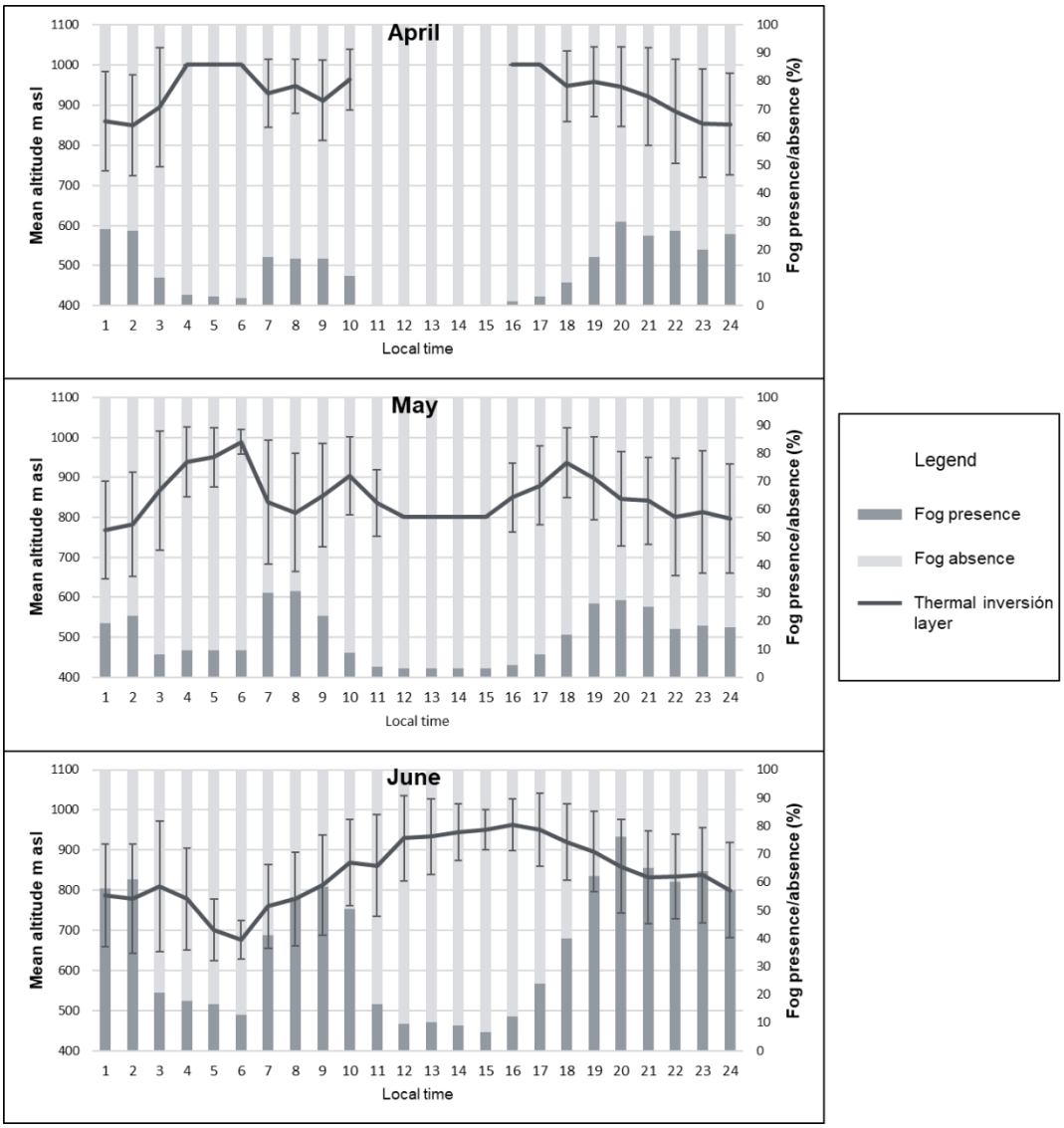

Figure 68: Monthly (April, May and June) mean daily cycles of the cloud base altitude and fog and low cloud frequency presence and absence.

On the other hand, June has a different and distinguishable daily cycle in CB altitude. Minimum altitude occurs during night-dawn, with a peak at 06:00 (CB = 675 m a.s.l; SD = ± 50 m), then increases gradually until it reaches its maximum at 16:00 (CB = 960 m a.s.l; SD = ± 65 m), finally decreasing toward midnight. There is no relationship between lower FFPs and CB altitude. There is also no relationship between hour variability and CB altitude.

During the three-month period of maximum FFPs, July and August have a CB altitude daily cycle very similar to that of June, but which differs from September in the afternoon (see Fig. 69). Minimum CB altitude in July occurs at dawn (08:00; CB = 740 m a.s.l.), coincident with a high, but not the maximum (sunset-midnight: ~85 %)., FFP of above 80 %. From early morning it starts to rise to a peak at 13:00 (CB = 1.000 m a.s.l), then from the afternoon until sunset the CB altitude varies but remains over 900 m a.s.l. until 19:00 when it begins a gradual decrease toward midnight, at which time FFP exceeds 90 %. In terms of hourly variability, at higher CB altitudes the variability is 50% less than when the CB is at lower altitudes. Minimum CB altitudes in August occur at dawn (06:00; CB = 785 m a.s.l.), after which they increase progressively until reaching their maximum at 11:00 (CB = 1.000 m a.s.l.). They then remain stable until 17:00; however, from 12:00 to 14:00 there is no fog presence. The times of day with the highest CB altitude coincide with minimum FFPs (1,5 %). From 18:00 the CB decreases until midnight, the period in which the maximum FFP occurs (nearly 90 %). Just as in July, hourly variability is around 50 % less when the CB altitude is higher than when it is lower. In the case of September, CB altitude daily cycle has low variability from sunset to early morning (less than 80 m of difference), which is similar to the daily cycle for the months of April and May. In addition, from sunset-early morning the FFP is in general stable and high. On the hand, both the maximum and minimum CB altitudes occur from noon-afternoon, with a minimum CB altitude peak at 15:00 (CB = 780 m a.s.l.), and a maximum at noon (CB = 990 m a.s.l.). Both extremes occur when the FFP is at its minimum (~10 %). In the same manner, the lower hourly variability is present when the CB altitude is higher, but not the higher variability is not necessarily coincident with lower CB altitudes, which occur at night (SD = ± 150 m).

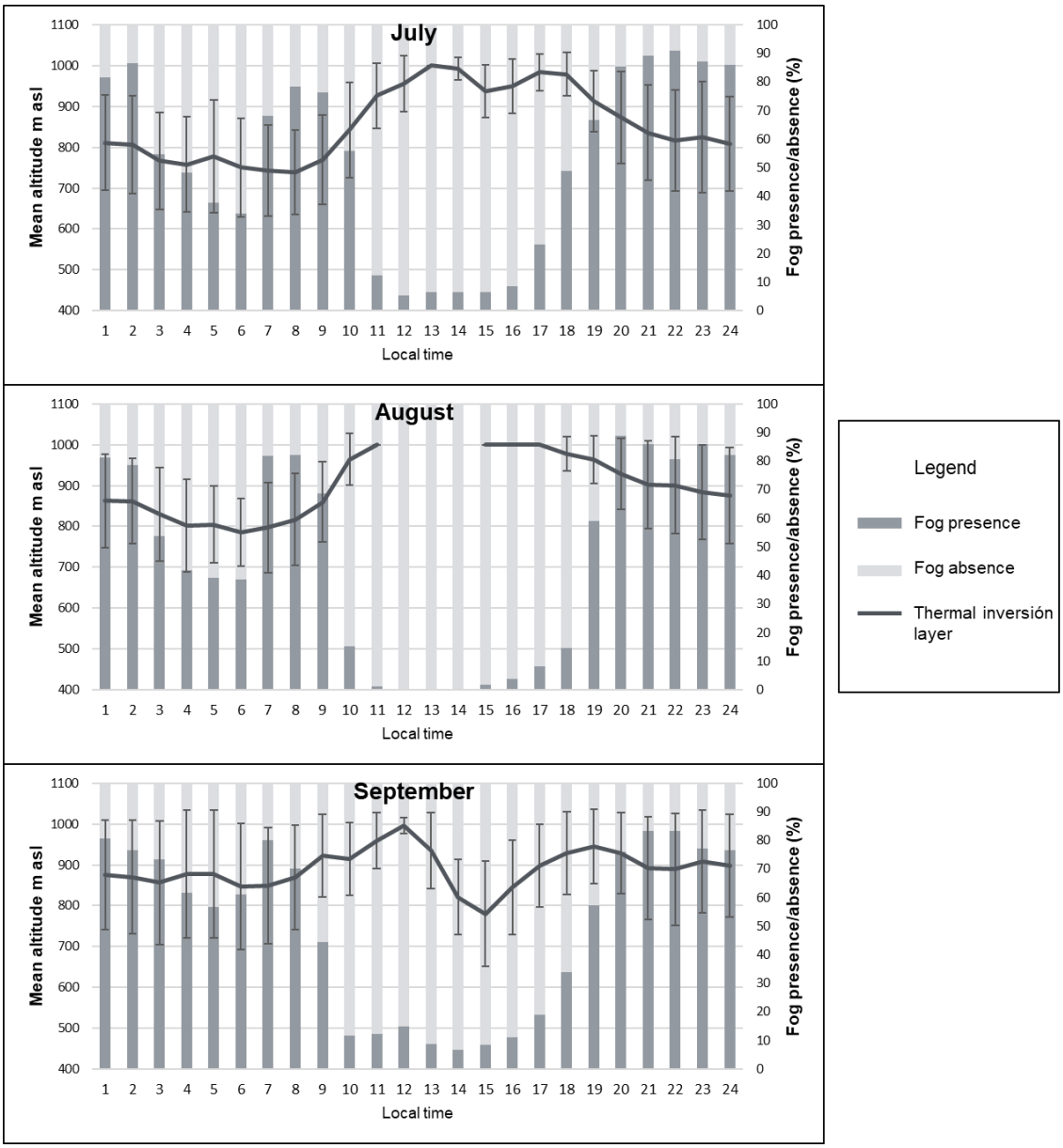

Figure 69: Monthly (July, August and September) mean daily cycles of the cloud base altitude and fog and low cloud frequency presence and absence.

For the last 3 months' period, CB altitude presents variations in its daily cycle, including changes at noon-afternoon, with significantly reduced FFPs towards December (see Fig. 70). October follows a similar daily cycle as September, with both showing a very stable CB altitude from sunset to early morning (as well high FFPs), but they differ in that, in addition to the absence of fog at some times of day (10:00 to 14:00), October has its maximum CB altitudes in the afternoon (at 15:00 the CB = 1.000 m a.s.l.), while September has its minimum. Hour variability is around 60 % less when the CB altitude is higher than when it is lower.

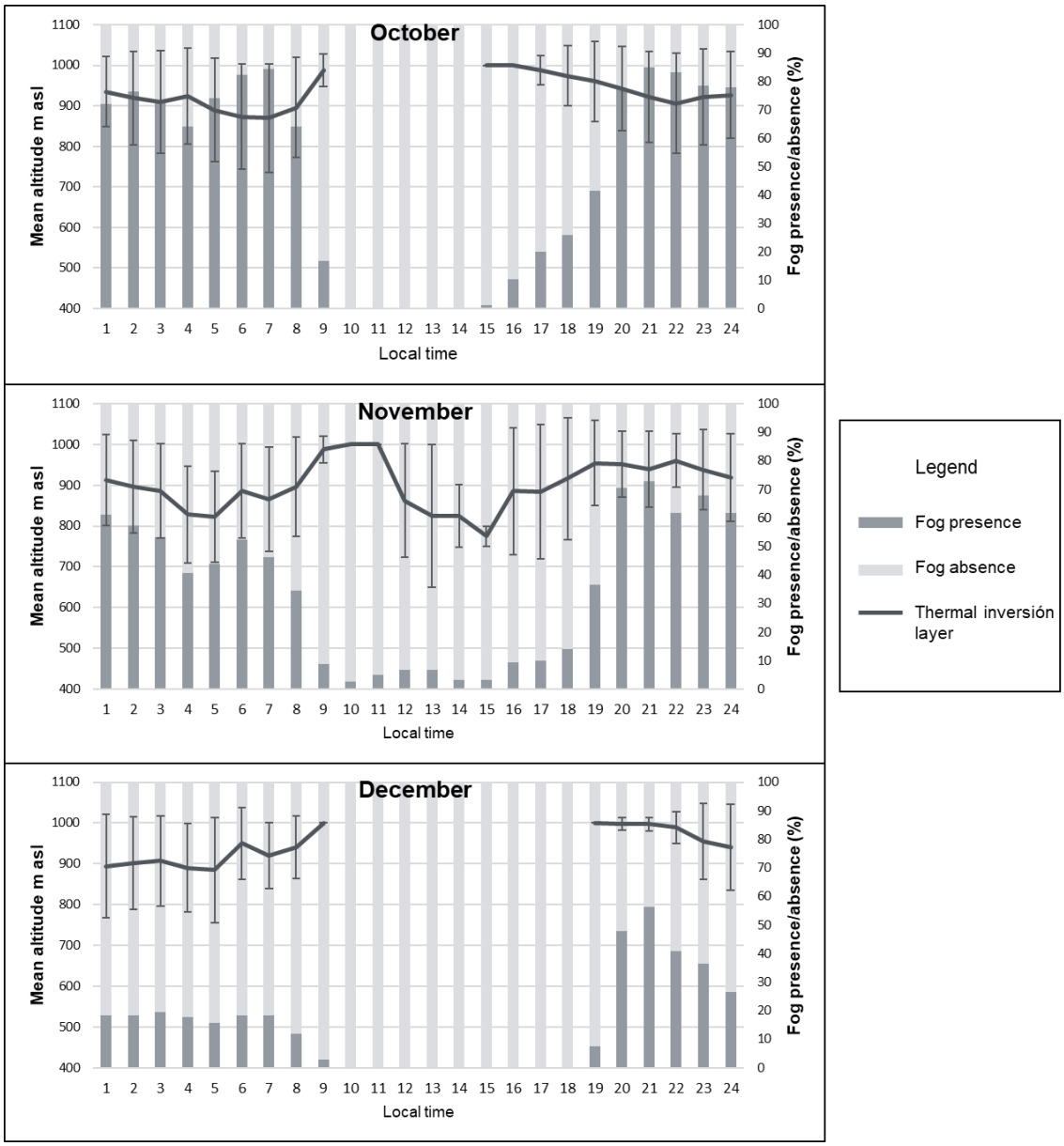

Figure 70: Monthly (October, November and December) mean daily cycles of the cloud base altitude and fog and low cloud frequency presence and absence.

November and October have similar CB altitude daily cycles as September; while the sunset-early morning is similar, there is more variability. During the night there is a first CB minimum (CB = 820 m a.s.l) at 05:00, after which altitude increases to its maximum peak at 10:00 (CB = 1.000 m a.s.l.). Then there is a sharp decrease at 12:00, until reaching the second minimum at 15:00 (CB = 780 m a.s.l.). Finally, the CB altitude increases until sunset, when it remains stable until midnight (CB = ~940 m a.s.l.). In relation to FFP, when FFP is lower (from 09:00 to 18:00) maximum and minimum peaks in the CB altitude occur. A similar situation occurs with hourly variability, as low variation occurs in both CB altitude peaks.

December follows as similar daily cycle of CB altitude as March, including the absence of fog during noon-afternoon (10:00 to 18:00). The CB altitude minimums occur throughout the night (CB = 900 m a.s.l; SD = ± 115 m), after which the CB altitude increases until the early morning when it reaches its maximum altitude, and that reappears at the same altitude at sunset (CB = 1.000 m a.s.l.), finally decreasing until sunset-midnight (CB = 975 m a.s.l). Lower CB altitudes are not necessarily related with the maximum FFP, which occurs from sunset to midnight. Hourly variability is related with CB altitude, as the lower variation occurs when the CB altitude is the higher, and the opposite occurs when the CB altitude is lower.

7.3 Cloud thickness

Cloud thickness or cloud depth (CD), is based on simultaneous measurements of the CT and CB. In order to get this measurement both systems must work together in the same sector, therefore the number of measurements differs to those available for either CT and CB altitude alone, given that the altitudinal range covered did not always allow for construction of the CD (for example, a CT at 1.350 m a.s.l. and a CB that was not observed because it was over 1.000 m a.s.l.). Thus, the results shown here correspond to the CD averages for the time periods in analyzed. Fig. 71 presents the seasonal mean, which reveals that the largest CD occurs during summer (~315 m), the period of the year when the CT and CB are at their highest altitudes. During autumn, the CD decreases to a mean of approximately 230 m, at the same time altitudes of CT and CB also decline, but CT to greater degree. The decreasing tendency in CD continues into winter, together with a low in CT and CB (CD = 220 m). Finally, the average CD in spring (220 m) is similar to that of winter, even though spring is a season in which there is a slight increase in CT and CB altitude. Thus, considering the subtle differences in altitudes between winter and spring (but the equivalent CD), there is a positive relationship between the altitude of the cloud and their thickness.

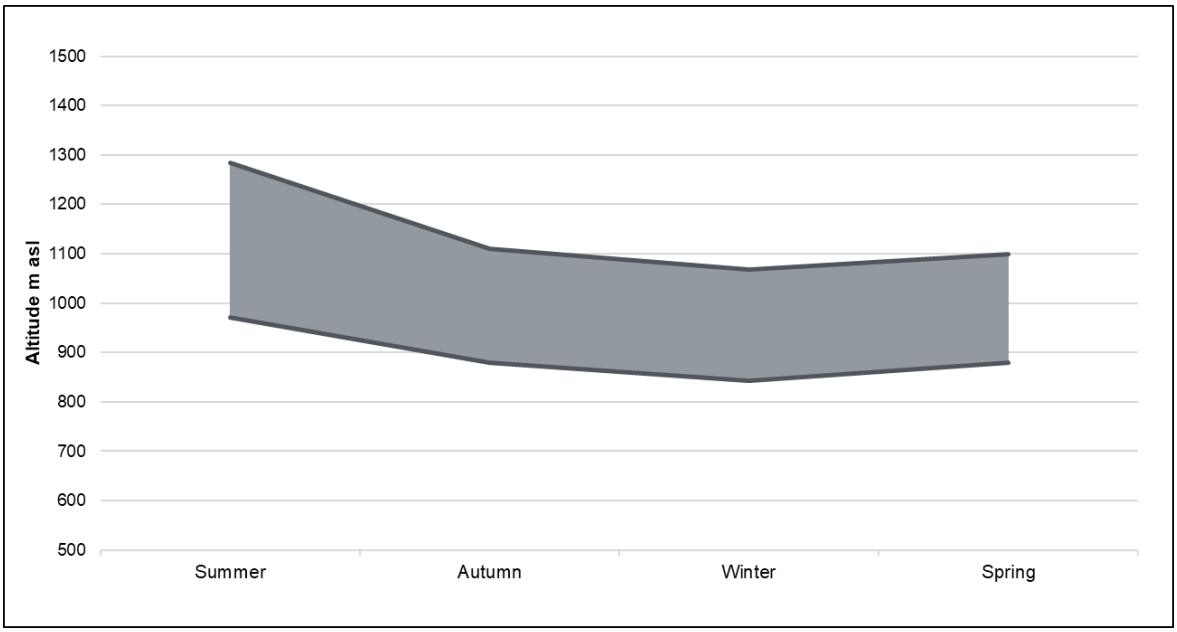

Figure 71: Seasonal cloud thickness means.

The CD monthly means show the annual cycle in 2017 with greater detail. Fig. 72 shows that while the CD maximums are observed in summer (December, January, February and March), the rest of the year is rather variable. The months with lower CD (April, August and October) are linked to specific variations in CB altitude, but not CT altitude, which is more regular in its annual cycle. In this way, January, February and March present a mean CD of 325, 300 and 275 m, respectively; this gradual decrease is primarily due to declines in the CT altitude, as CB altitude is stable (primarily in January and February). One of the lowest CDs occurs in April (175 m), when the CT altitude, but not the CB altitude (which remains stable until March), continues its descending seasonal cycle. May, June and July show a slight increase in CD (225, 235 and 240 m, respectively); over this period, the CT altitude is more stable, and it is the CB altitude that subtly falls. CD reaches a minimum in August (170 m), at which time the CT altitude goes down and the CB altitude goes up. The opposite occurs in September (240 m). Another annual minimum occurs in October (170 m), but here again, it is the CT altitude that remains stable while the CB altitude increases considerably. Finally, November and December show a gradual increase in both CT and CB altitude, therefore resulting in an increase in CD (255 and 260 m, respectively).

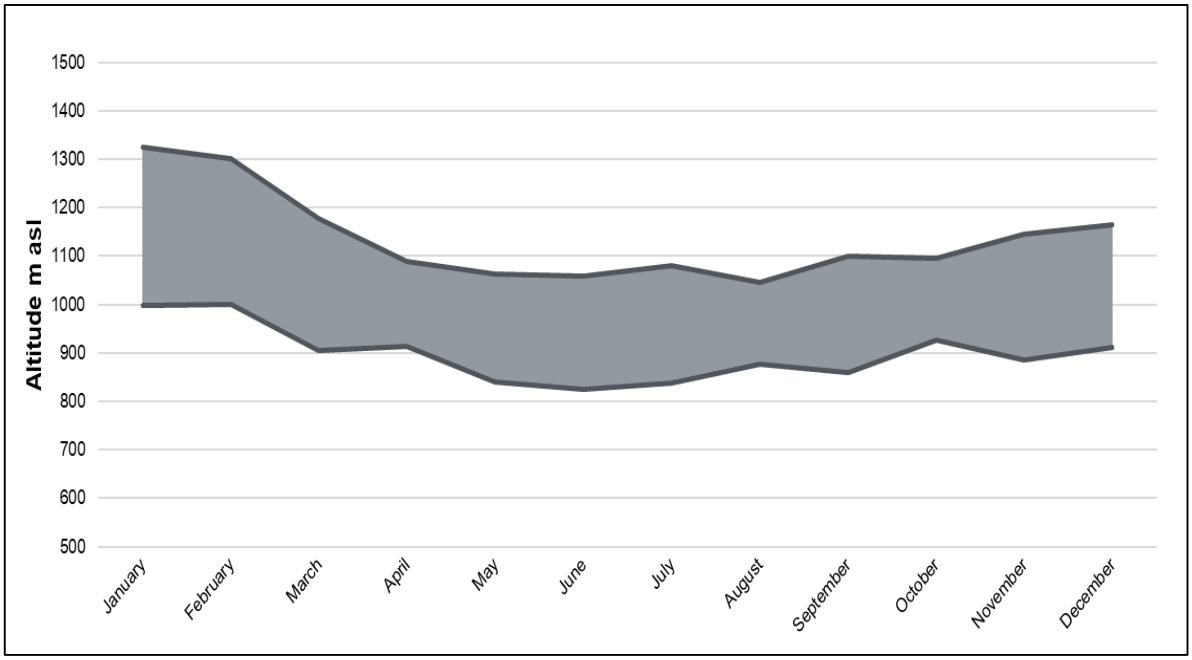

Figure 72: Monthly cloud thickness means.

Looking at the annual average of the daily cycle, a strong positive relationship between CT altitude and CD can be observed (r = 0,9 with a 99 % confidence level). Daily variations in the CT are greater than that of the CB (see Fig. 73). From midnight to dawn (01:00 - 08:00), the average CD increase from ~200 m to ~240 m, at the same time CT altitude increases from 1.060 to 1.095 m a.s.l.. In the morning (09:00 - 10:00) CD decreases again, returning to the same thickness as at midnight (CD = 200 m). At 11:00 the CT altitude rises considerably and the CB remains stable, initiating the period of the day with the greatest thicknesses, which reach its maximum by midday-afternoon (~350 m) with a peak at 15:00 - 16:00 (375 m), which coincides with a significant increase in CT altitude, but not CB altitude, to 1.300 m a.s.l. Towards sunset and midnight, the CD begins to decrease again along with the CT altitude, reaching the period with the lowest CD (180 m), with a minimum peak at 20:00 (CD = 170 m).

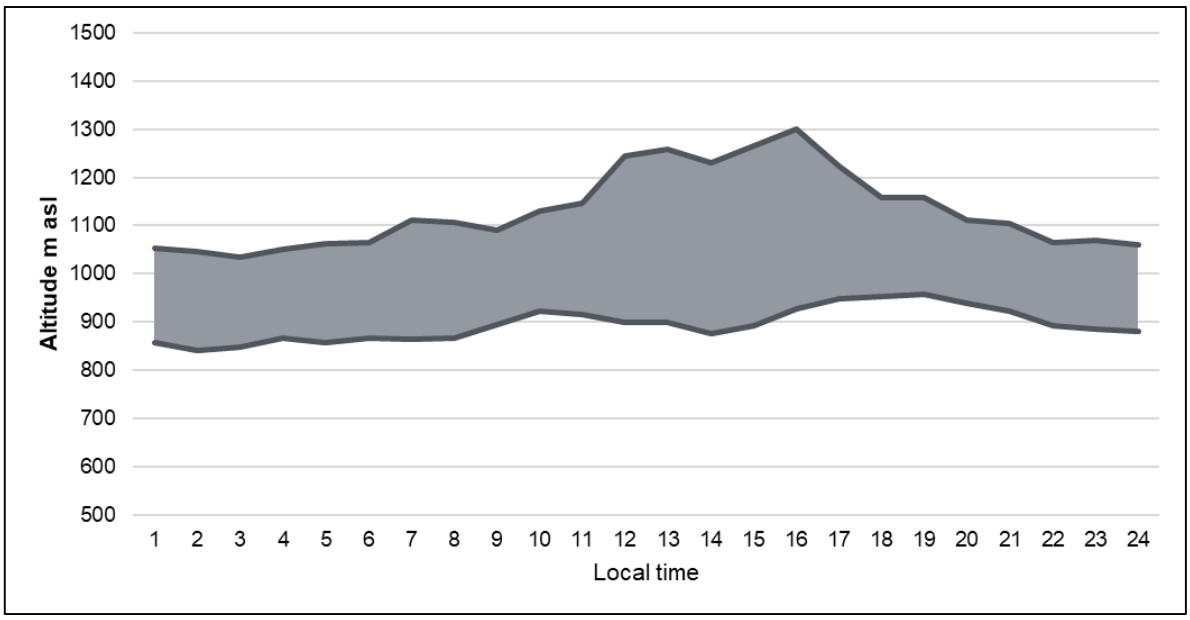

Figure 73: Annual mean daily cycle in cloud thickness.

Characterization of the daily cycle of CD for each month shows variations throughout the year, even though the summer months and some autumn months are defined by the absence of fog (or the limitations of CD construction by the GOFOS system) at some times of the day, thus making it difficult to construct the daily cycle (e.g. January has 8 observations during dawn and 66 for sunset). Fig. 74 show the mean daily cycle in CD from January to June; you can see that at noon in the first months of the year there are no CD measurements (no data - ND). During January, there is ND throughout the night; nevertheless, observations at dawn show FLCs at a high altitude and with a high CD of 340 m, the largest of the year for that time of day. The other period of the day with data is sunset, which again presents a high CD; however, in this case CD decreases by nightfall reducing from 390 m (at 19:00) to 300 m (at 21:00). February has ND from midnight to sunset; however, for the hours that have data at sunset there is a marked decrease in CD from the early hours of sunset (CD = 360 m) to midnight (CD = 200 m). This is due to a decrease in the CT altitude and a stable CB altitude. March show a more identifiable daily cycle despite the ND at noon; here the relationship between increased CD and higher CT altitudes is maintained. From midnight to early morning CD increases (from 250 m at 03:00 to 345 m at 09:00), just as CT and CB altitudes increase. Then from sunset to midnight a decreasing CD (from 400 m at 18:00 to 320 m at 23:00) is observed; at the same time the CT and CB altitude also decrease. In the case of April, there is a decrease in CT altitude at all hours (excluding the ND at noon-afternoon), which in turn is reflected in a decrease in CD. At

midnight CD is 180 m, which increases towards dawn (CD = 220 m), with a narrowing at 04:00 (CD = 100 m), after which it stabilizes in the morning (06:00 to 08:00), followed by a gradual rise until 10:00 (CD = 280 m). From sunset to midnight CD is on average reduced (CD = 160 m), coupled with a regular reduction in both the CT and CB altitude.

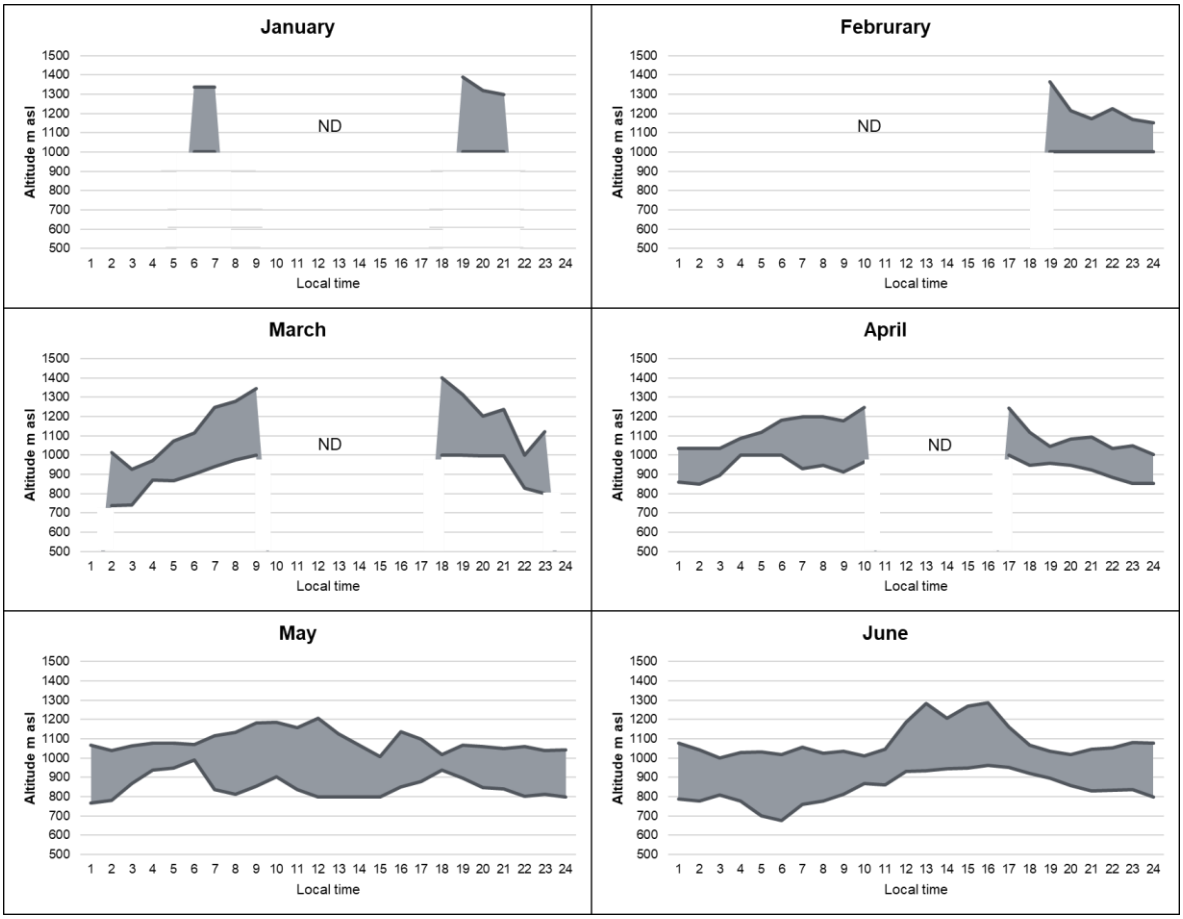

Figure 74: Monthly mean daily cycle in cloud thickness for the period from January to June. ND: no data.

May is the first month of the year with the complete daily cycle; however, this cycle is barely distinguishable. Nevertheless, it presents some observable patterns. At midnight CD is 270 m, which then increases until the daily maximum during the morning and noon (CD = 320 and 410 m, respectively). Throughout the night to morning period there is a narrowing at 06:00 (CD = 90 m), which is related with a rise in the CB altitude and a practically stable CT altitude. From the afternoon to midnight, the CT altitude decreases continuously and the CB altitude is relatively stable, but both present specific changes (e.g. 15:00 and 18:00), therefore giving less continuity to the daily cycle of CD, which results in a CD that varies from 270 to 160 m (afternoon to sunset) and finally increases again at the end of the day

(200 m). In the case of June, there is an important increase in CD at midday, produced by a significant increase in CT altitude; CB altitude also increases, but to a lesser extent. From midnight to morning there is a stable CT altitude; meanwhile the CB altitude first decreases toward dawn, and then increases continuously until the afternoon, resulting in a CD that increases from 250 to 320 m from midnight to dawn and then decreases in the morning (CD = 180 m). At noon-afternoon the CT altitude rises, leading to a CD of 350 m, followed by a sharp decrease in the CT altitude at sunset together with a smoother decrease of the CB altitude, producing a thinner CD at 19:00 (CD = 140 m) that slightly increase at midnight (CD = 260 m).

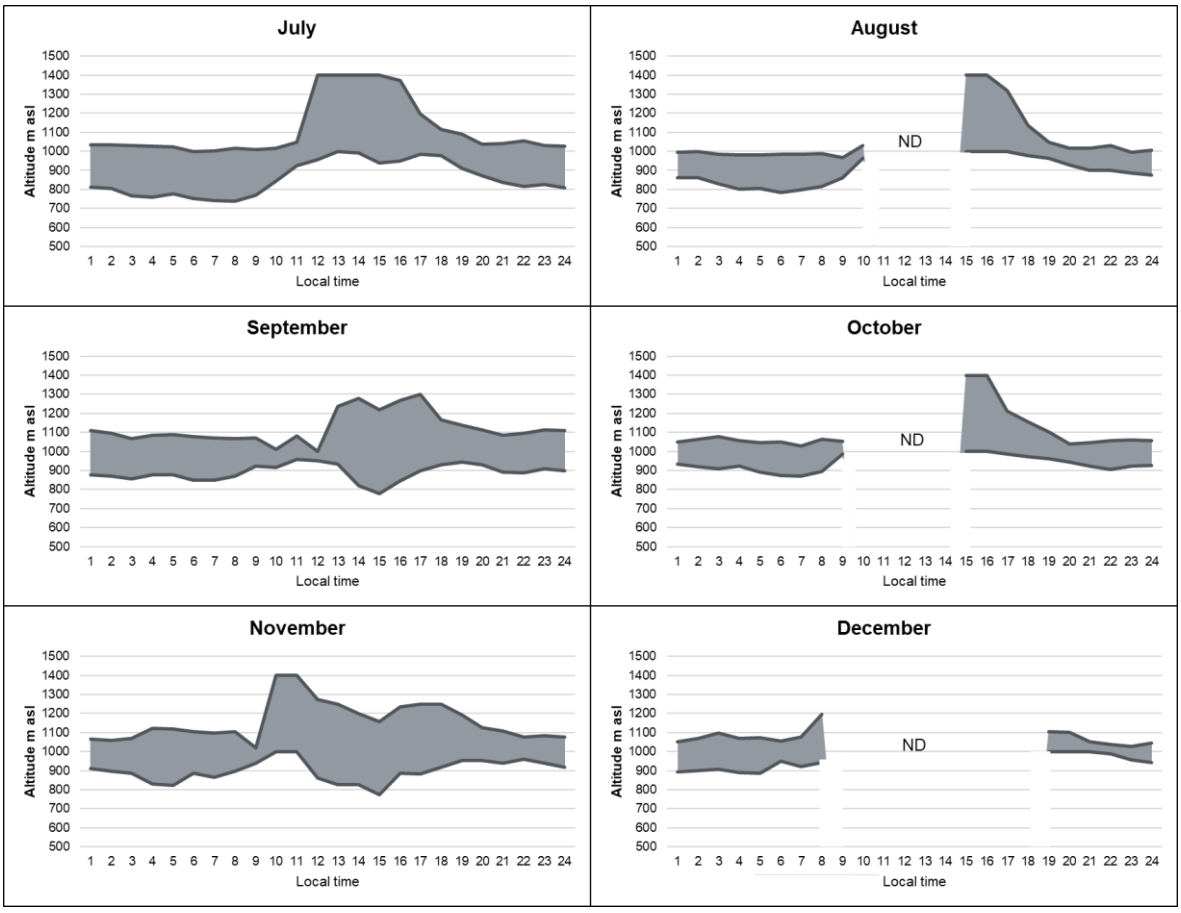

Figure 75: Monthly mean daily cycle in cloud thickness for the period from July to December. ND: no data.

Winter and early spring (July to October), seasons when fog presence is greater, show similarities in their daily CD cycle; this pattern partially breaks down as summer approaches (November and December) (see Fig. 75). July present a daily cycle in which CD is relatively similar from sunset to early morning, and then increases significantly during the middle of

the day. Nighttime shows a regular CD of around 250 m, based on very constant CT altitudes, but less regular CB altitudes, which begin to rise at 09:00, while CT altitudes begin to rise at 11:00, generating lower CDs (140 m) during the morning (10:00 – 11:00). From noon-afternoon CD reaches its maximum (CD = 430 m), then at 17:00 CD decreases considerably as the CT altitude declines sharply. From sunset to midnight the CD returns to its nighttime thicknesses (CD = 210 m). Despite the fact that there is no data at noon, August shows a similar daily CD cycle as July, however the cloud is generally thinner. During the night CD is stable around 170 m, and at 09:00, both CT and CB altitudes begin to rise, generating a reduced CD (80 m). During the afternoon, CD is at its peak (CD = 375 m), after which it decreases significantly from 18:00 to 19:00 (CD = 85 m), then maintaining a regular CD until midnight (CD = 120 m). For September, the daily CD cycle is also very similar to previous months, but with a noticeable difference in the noon-afternoon maximum, as the CD increases considerably (430 m) as a result of an increase in the CT altitude. Yet, at the same time CB altitude is decreasing in the CB, which is not observed in other winter months. For the rest of the day, (sunset to early morning) CD remains relatively stable (on average 145 m). October repeats the daily CD cycle patterns of June-August, with a thin and stable CD throughout the night and into the morning (in average CD = 130 m), which increases at noon-afternoon (not considering the ND from 10:00 to 14:00) to the daily maximum (CD = 400 m). CD then decreases until sunset-midnight (CD = 135 m). November differs from previous months, as it shows significant variability throughout the day. Even given a relatively stable CD at night (220 m), CD is very low at 09:00 (CD = 80 m), and then reaches its maximum from 10:00 to 15:00 (CD = 410). This is due to high CT and CB altitudes that then decrease and increase again, thus maintaining the CD. December returns patterns characteristic of the summer months, due to the longer period with no data, in this case from 09:00 to 18:00. Nevertheless, a stable CD it is observed from midnight to dawn (160 m), which increases at 08:00 (CD = 250 m), when CT altitude is also increasing. From sunset to midnight (19:00 to 24:00) the CD is stable and very thin (CD = 80 m).

7.4 Atmospheric variables

Here is presented a basic description of the atmospheric variables at a monthly temporal scale measured at the 3 weather stations installed in a vertical profile in coastal Atacama (see Fig. 16); the variables analyzed include: air temperature, relative humidity and air pressure. The weather station located at 750 m a.s.l. only has data from October to December, as is was installed in October of 2017. The variables are characterized from an altitudinal perspective, in order to create a vertical description of the atmospheric conditions in the lower troposphere. Table 8 summarizes air temperature at each station for the year 2017.

	Air temperature											
	50 m a.s.l.				750 m a.s.l.				1.200 m a.s.l.			
	Max	Min	Mean	SD	Max	Min	Mean	SD	Max	Min	Mean	SD
January	2,9	18,6	24,3	1,9					26,6	11,4	18,1	2,9
February	29,6	19,9	24,3	2,1					25,4	12,2	18,5	2,8
March	27,0	17,1	22,2	2,1					25,0	11,7	17,8	2,9
April	24,1	14,4	19,6	1,9					27,4	8,1	16,3	3,6
May	27,6	13,4	18,4	2,5					25,7	6,9	15,2	3,9
June	20,5	12,5	17,0	1,2					29,0	3,6	16,0	4,9
July	19,1	12,1	16,1	0,9					30,1	3,1	17,1	5,4
August	19,0	11,8	16,1	0,9					28,2	3,5	15,6	4,3
September	18,7	12,2	16,0	1,0					28,4	3,7	14,4	5,5
October	20,4	13,8	16,8	1,1	19,7	7,7	12,8	3,1	30,0	2,8	15,5	5,0
November	21,7	14,7	18,1	1,5	21,5	7,6	13,7	2,8	27,7	6,2	15,4	4,3
December	24,6	15,3	20,1	1,8	22,8	9,9	16,0	2,9	24,4	7,5	15,9	3,3

Table 8: Monthly air temperature (°C) at the 3 weather stations for the year 2017.

Annual cycles in monthly mean air temperature are distinct in at the station 50 m a.s.l., with a maximum temperature in summer, with a peaks in January and February (24,3 °C). Temperatures at this station then gradually decrease towards autumn and winter, until reaching their minimum in September (16,0 °C). In October the temperature starts to rise again moving into the summer months. Variability is greater in summer, autumn and spring months, and lower in winter, evidenced by standard deviations and differences between maximums and minimums. In the case of the station at 750 m a.s.l., there is a consistent increase in temperature from October to December. On the other hand, the station at 1.200 m a.s.l., present a different annual cycle to the station at 50 m. Although the highest

temperatures are found in the summer (also with a peak of 18,5°C in February), they begin to descend towards autumn; in May they reach their first minimum, followed by rising temperatures again in June and July, then descending once more in August, to reach a minimum of 14,4 °C that is also observed in September. Air temperatures finally rise again in October, November and December, but temperatures remain below June and July (see Table 8 and Fig. 76). The variability at 1.200 m is opposite of that at 50 m, as temperatures variability (SD) are higher in winter and early spring and lower during summer and early autumn.

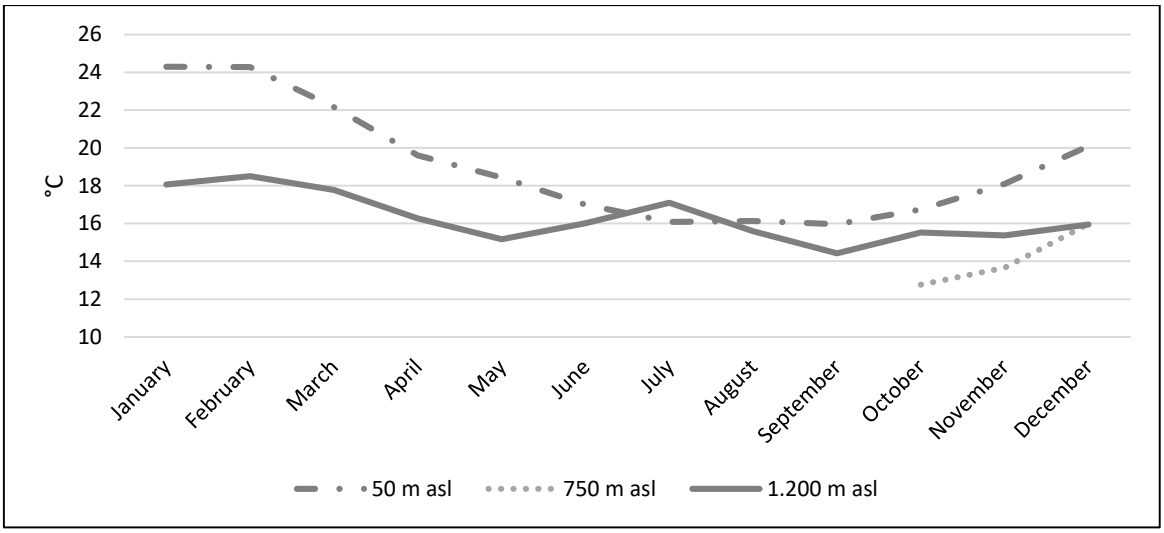

Figure 76: Monthly air temperature means at the 3 weather stations for the year 2017.

In the months that all 3 stations have recorded data (October to December), the adiabatic gradient breaks between the stations at 750 and 1.200 m a.s.l., resulting in the highest temperature over these 3 months occurring at 50 m a.s.l., Temperature then drops at 750 m a.s.l, but rises again at 1.200 (see Fig. 76). The temperature at 1.200 m is 2,8 °C, 1,7 °C and 0,1 °C warmer than at 750 m for the 3 months, respectively. Comparing the 50 m and 1.200 m stations, the lower station regularly shows a regular higher temperature than the station at 1.200 m for almost all months. The greatest differences are produced during summer and spring, with a peak in January, when the lower station records a temperature 5,9 °C higher than recorded at 1.200 m. From January to May, the difference between the two stations decreases gradually; then in June there is a turning point, where on the one hand the temperature at 50 m continues to fall, and on the other hand the temperature at 1.200 begins to rise, so that in July the temperature is higher at 1.200 than at 50 m (see Fig. 76). In August and September, the temperature at 50 m remains stable and there is a

decrease at 1.200 m, again resulting in higher temperatures at lower altitudes. From October to December, temperature increases at both stations, but at a greater rate at 50 m.

Table 9 summarizes the relative humidity for each month. At 50 m the annual differences in the monthly mean are low, with a maximum difference between February (59,4 %) and June (71 %). Even though the lowest relative humidity is found in the summer months and the highest in winter and spring, the annual cycle varies from month to month. Variability also varies throughout the year, with greater variability in summer and autumn and lesser variability in winter. At 750 m a.s.l., the monthly mean shows that October and November are nearly same, followed by a decrease in December; values for these months are and on average 10 % higher than at 50 m. Maximum relatively humidity reached 100 % humidity, minimums reached less than 30 %.

	Relative humidity											
	50 m a.s.l.				750 m a.s.l.				1.200 m a.s.l.			
	Max	Min	Mean	SD	Max	Min	Mean	SD	Max	Min	Mean	SD
January	84	47	65,04	6.6					100	34,4	75,13	13,1
February	82	41	59,4	7					100	21,7	70,22	12,6
March	89	47	66,86	7					100	11,4	71,07	14,4
April	87	47	67,6	7,6					100	5,6	67,03	21,4
May	90	44	68,19	8,2					100	2,9	65,48	24,6
June	93	55	71,57	6,1					100	2,2	48,29	29,5
July	81	55	68,94	4,3					100	1,2	35,12	30,1
August	82	49	66,03	4,4					100	0,7	34,1	26,6
September	89	51	70,03	6,3					100	1,35	51,05	32
October	83	53	68,24	6,1	100	16,1	78,32	16	100	0,7	44,11	29,5
November	93	51	68,96	6,8	100	23,1	79,29	14,9	100	6,32	54,8	27,9
December	87	43	65,26	7,9	99,2	31,1	74,88	13,3	100	3,2	63,96	19,5

Table 9: Monthly relative humidity (%) at the 3 weather stations for the year 2017.

At 1.200 m a.s.l. the annual cycle is well delineated, with higher relative humidity during summer and early autumn, with a peak in January (75 %), and lower humidity during winter and early spring, with minimum in July-August (35 %). In the same manner, minimum absolute values occur within the same cycle; in winter – early spring values can be close to 0 (e.g. 0,7 in August and October). On the other hand, the maximum absolute values were 100 % for the entire year, which is a reflection of significant variability throughout the year, which is especially significantly during the winter. In the three months when all stations

recorded data (spring to summer), the highest average relative humidity occurs at 750 m, with a 3-month average of 77 %, followed by 50 m (mean of 67 %) and the lowest occurs at 1.200 m (mean of 54 %) (see Fig. 77). Annual comparison between 50 and 1.200 m shows that during summer relative humidity is greater at higher altitudes, and during April both present almost the same value. From June onwards, relative humidity at sea level remains stable and even increases slightly, whereas at 1,200 m it falls significantly, generating a large difference between both altitudes until November.

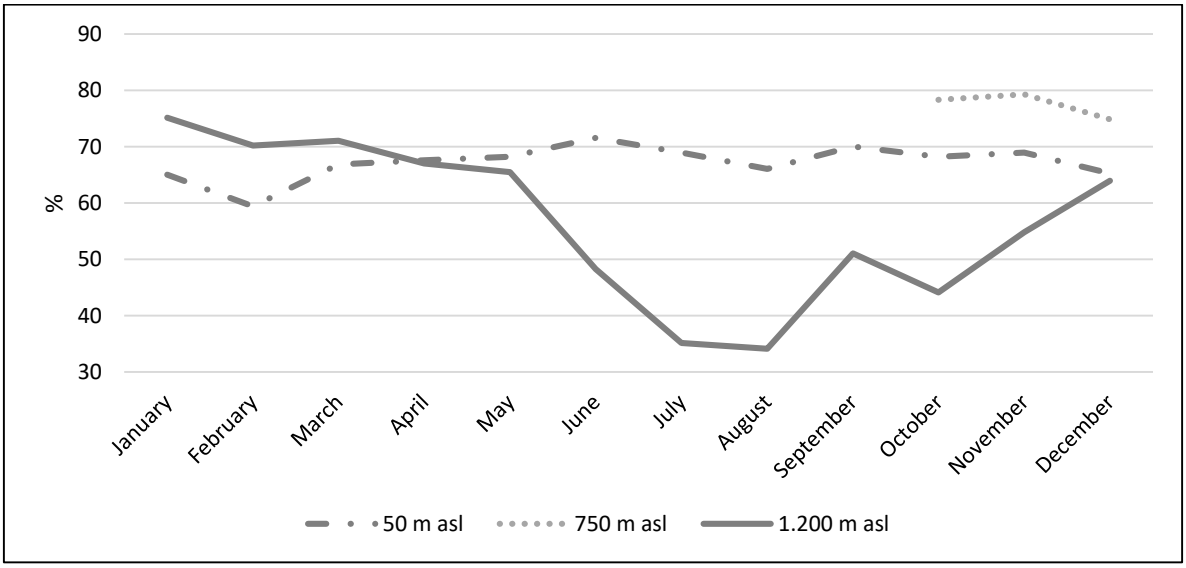

Figure 77: Monthly relative humidity means at the 3 weather stations for the year 2017.

Table 10 summarizes air pressure for each month. As expected, there are altitudinal differences altitudes in its annual cycle, with the highest atmospheric pressure occurring in winter and the lowest in summer-spring, in accordance with the annual displacement of the southeastern Pacific high-pressure center. During winter at 50 m a.s.l., air pressures reaches an average of 1.011 hPa, and with average absolute maximum and minimum of 1.017 and 1.006 hPa, respectively. This contrasts with the summer average of 1.008 hPa, with an average maximum and minimum of 1.011 and 1.004 hPa, respectively. For the 750 m a.s.l., the 3-month data shows an average of 925 hPa, with a maximum and minimum of 929 and 922 hPa, respectively. In turn, at 1.200 m a.s.l., there are few monthly differences, with an average in winter months of 881 hPa, of 879 hPa in spring-summer and 880 hPa in summer-autumn. The absolute maximum and minimum show equivalent slight monthly differences.

	Air pressure											
	50 m a.s.l.				750 m a.s.l.				1.200 m a.s.l.			
	Max	Min	Mean	SD	Max	Min	Mean	SD	Max	Min	Mean	SD
January	1011	1002	1007	1,5					884	874	880	1,5
February	1011	1004	1007	1,6					884	876	880	1,5
March	1012	1003	1008	1,7					883	876	880	1,4
April	1014	1005	1009	1,5					884	876	880	1,4
May	1015	1006	1011	1,7					884	877	881	1,5
June	1017	1006	1011	1,8					886	877	881	1,6
July	1017	1007	1012	1,9					885	877	881	1,5
August	1016	1006	1011	1,7					885	877	881	1,4
September	1017	1006	1011	2,0					885	877	880	1,5
October	1015	1005	1009	1,8	930	923	926	1,3	884	875	879	1,5
November	1013	1004	1009	1,7	928	921	925	1,5	883	875	879	1,4
December	1012	1004	1008	1,5	929	922	925	1,3	883	876	879	1,3

Table 10: Monthly air pressure (hPa) at the 3 weather stations for the year 2017.

Fig. 78 shows altitudinal differences throughout the year, which do not show annual cycle variations; however, it does show the magnitudes of difference between the three altitudes. Comparison between stations shows that the station at 50 m has greater variability in nearly every month of the year.

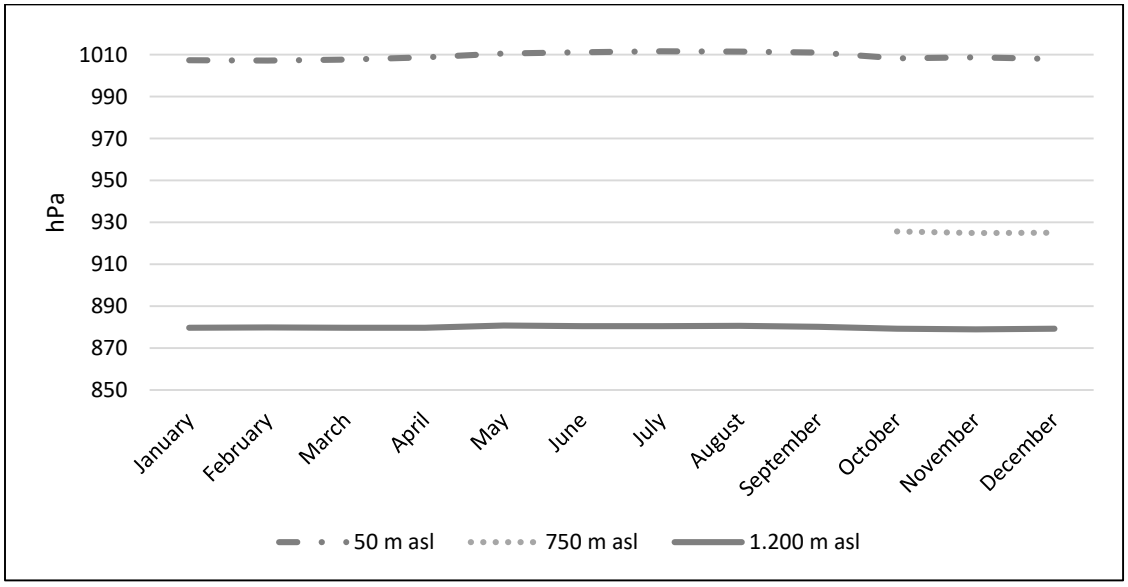

Figure 78: Monthly air pressure means at the 3 weather stations for the year 2017.

7.5 The marine boundary layer (MBL) regime

Here it is characterized the MBL regime according to atmospheric indices, potential temperature (θ) and specific humidity (*q*), by comparing GOFOS measurements with the MBL regimes conducive for fog dissipation due to a well-mixed/stratified regime. As these indices were analyzed in the presence of FLCs according to GOFOS (with a filter where CT altitude ≥ 1.200 m a.s.l., to ensure that the weather station was always within the MBL), the results are compared with monthly and hourly thresholds, and provide information on the vertical atmospheric conditions under which FLCs are present. In the presence of fog, which occurs in a well-mixed regime, a total of 467 cases were analyzed; of these, the θ and the *q* proposed thresholds showed a 79 % and 87 % match rate, respectively. Monthly, the *q* had a higher match rate in 10/12 months; the 2 months for which θ has a higher match rate were summer months (December and January). In relation to daily cycles, although there are variations throughout the year, *q* had a better match rate at dawn, morning and at sunset; on the other hand, θ had a higher match rate at night. Fig. 79 shows the distribution of the analyzed cases of both indices in relation to the proposed thresholds for January to June. Tables 11 and 12 show the number of cases and their respective match rates according to the different time points for the same months. Based on 14 observed cases in January, θ agrees in 12 instances, primarily at sunset; the 2 cases that do not match occur at noon and at sunset. On the other hand, *q* presents 50 % agreement in the evening, whereas during the rest of the day there is no concordance. For February, there is almost no concordance in θ, with only 2 of 7 cases during night-dawn matching. For *q*, 71 % of agreement occurs at night and sunset. Of 3 observations in March, 2 θ coincide and 3 *q* coincide.

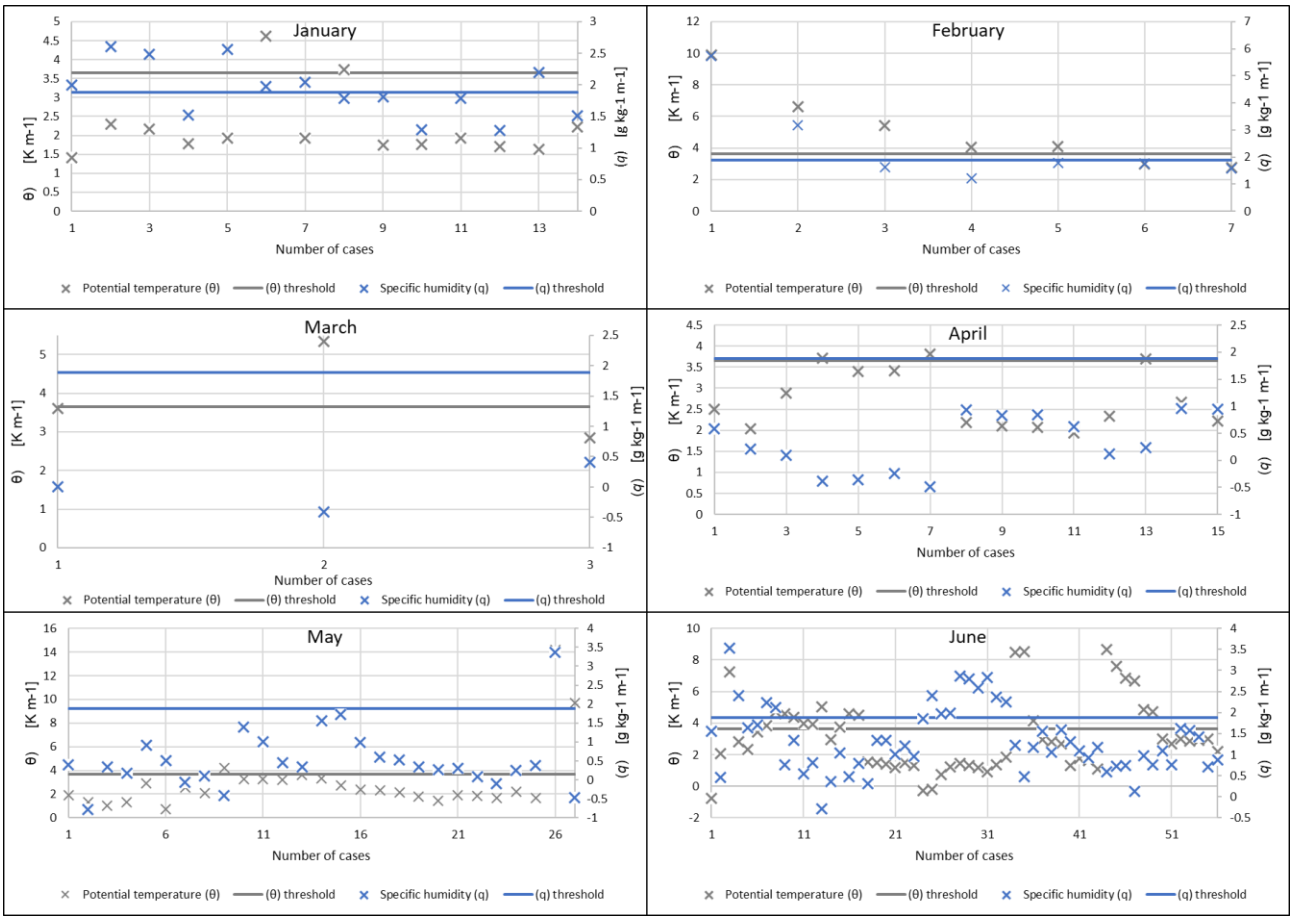

Figure 79: Observed cases of potential temperature (θ) and specific humidity (*q*) versus proposed thresholds for January to June.

In April there is a greater number of cases providing better daily coverage. Both indices show a high percentage of agreement. For θ there is 80 % agreement, with only 3 cases of non-compliance that are slightly above the proposed threshold. In turn, *q* presents 100 % concordance, with all values well below the proposed threshold. In the case of June, concordance percentage of θ decreases considerably to 64 %, while values above the threshold are mainly concentrated at noon-afternoon. For its part, *q* has 77 % concordance, and mismatches are primarily concentrated in the night.

	Match rate (%)								
	January			February			March		
Daytime	N° of cases	(θ)	(q)	N° of cases	(θ)	(q)	N° of cases	(θ)	(q)
1	0	0	0	0	0	0	0	0	0
2	0	0	0	0	0	0	0	0	0
3	0	0	0	0	0	0	0	0	0
4	0	0	0	1	0,0	100	0	0	0
5	0	0	0	1	100	100	1	0,0	100
6	0	0	0	1	100	0,0	0	0,0	0
7	1	100	0,0	0	0	0	1	100	100
8	0	0	0	0	0	0	0	0	0
9	0	0	0	0	0	0	0	0	0
10	0	0	0	0	0	0	0	0	0
11	0	0	0	0	0	0	0	0	0
12	0	0	0	0	0	0	0	0	0
13	1	0,0	0,0	0	0	0	0	0	0
14	0	0	0	0	0	0	0	0	0
15	0	0	0	0	0	0	0	0	0
16	0	0	0	0	0	0	0	0	0
17	0	0	0	0	0	0	0	0	0
18	0	0	0	0	0	0	0	0	0
19	2	50	50	1	0,0	0,0	0	0	0
20	7	100	42.9	1	0,0	100	1	100	100
21	2	100	100	1	0,0	100	0	0	0
22	1	100	100	1	0,0	100	0	0	0
23	0	0	0	0	0	0	0	0	0
24	0	0	0	0	0	0	0	0	0
Total	14	85,7	50	7	28,6	71,4	3	66,7	100

Table 11: Daily distribution and match rate for observed cases of potential temperature (θ) and the specific humidity (*q*) in January, February and March

	Match rate (%)								
	April			May			June		
Daytime	N° of cases	(θ)	(q)	N° of cases	(θ)	(q)	N° of cases	(θ)	(q)
1	0	0	0	1	100	100	4	75	50
2	0	0	0	1	100	100	4	75	50
3	0	0	0	1	100	100	1	100	0
4	1	100	100	1	100	100	3	100	66,7
5	2	100	100	1	100	100	3	100	66,7
6	2	50	100	2	100	100	2	100	50
7	2	100	100	4	100	100	2	100	50
8	2	100	100	4	100	100	1	100	0
9	2	50	100	3	66,7	100	2	50	50
10	0	0	0	1	100	100	2	50	100
11	0	0	0	0	0	0	0	0	0
12	0	0	0	1	0,0	100	1	0,0	100
13	0	0	0	0	0	0	2	0,0	100
14	0	0	0	0	0	0	1	0,0	100
15	0	0	0	0	0	0	2	0,0	100
16	0	0	0	0	0	0	2	0,0	100
17	0	0	0	1	0,0	0,0	3	66,7	100
18	0	0	0	0	0	0	3	33,3	100
19	1	0,0	100	1	100	100	3	33,3	66,7
20	2	100	100	1	100	100	1	0.0	100
21	1	100	100	1	100	100	2	50	100
22	0	0	0	1	100	100	4	75	75
23	0	0	0	1	100	100	4	100	100
24	0	0	0	1	100	100	4	100	100
Total	15	80	100	27	88,9	96,3	56	64,3	76,8

Table 12: Daily distribution and match rate of observed cases of potential temperature (θ) and specific humidity (*q*) in April, May and June.

Just as for the first 6 months of the year, Fig. 80 show the distribution of the analyzed cases of both indices in relation to the proposed thresholds for July to December and Tables 13 and 14 show, the number of cases and their respective match rates according to daily time points. July is one of the months with the highest number of cases; here θ has 82 % agreement, with 12 mismatching cases primarily occurring from afternoon to sunset. *q* shows a very high concordance (97 %), with just 2 mismatches occurring during the night, both of which were slightly above the threshold value. In August match rates drop for both indices. In July, θ goes down to 64 % and *q* to 73 %, and in both indices the distribution of discordances is spread uniformly throughout the day.

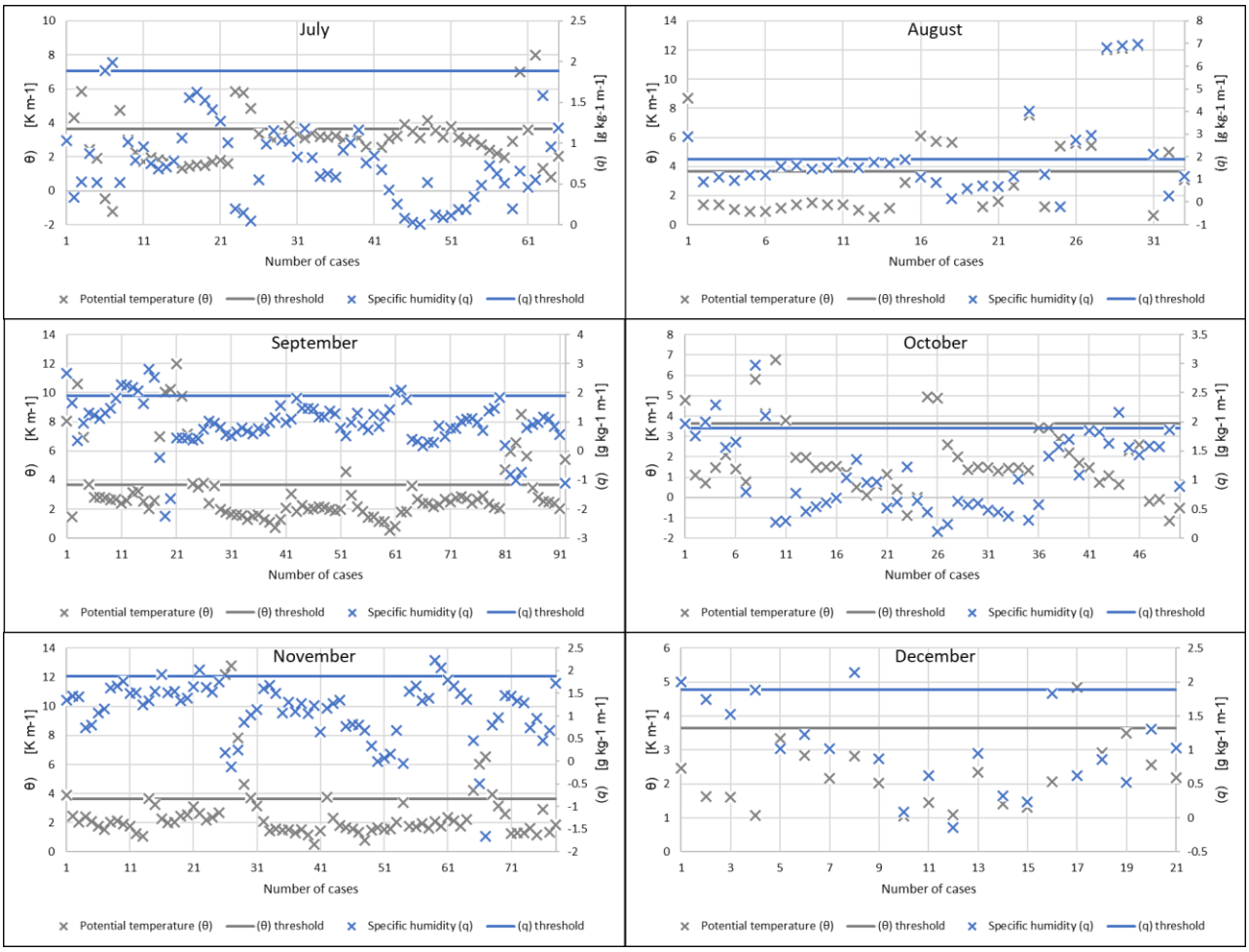

Figure 80: Potential temperature (θ) and specific humidity (*q*) of observed cases in relation to its proposed thresholds for July to December.

September is the month with the highest number of cases (92), and both indices show a high match rate. As before, disagreements in θ are concentrated in the afternoon and at

sunset, while disagreements in *q* occur during the night. In the case of October, both indices show similar percentages of agreement (86 and 88 % in θ and *q*, respectively). In this case, mismatches in θ all occur from afternoon to sunset. Mismatches in *q* all occur between 21:00 and 03:00. For November, the two indices again reach one of their highest match rates, with θ reaching 85 % and *q* reaching 95 %. In this case, mismatches in θ are concentrated in the morning to afternoon, whereas mismatches in *q* occur in the period from sunset to midnight. Finally, December, is one of the months, together with January, in which the percentage of concordance is greater in θ than in *q* (96 and 85 %, respectively). In this case, the only mismatch in θ occurs at 18:00, and in *q* between sunset and midnight.

	Match rate (%)								
	July			August			September		
Daytime	N° of cases	(θ)	(q)	N° of cases	(θ)	(q)	N° of cases	(θ)	(q)
1	3	100	100	2	50	50	6	100	100
2	3	100	100	2	50	50	6	100	83,3
3	2	100	100	3	100	66,7	5	100	80
4	4	100	75	2	50	100	6	83,3	50
5	3	100	66,7	2	50	50	5	100	60
6	2	100	100	2	50	50	5	100	100
7	2	100	100	0	0	0	2	100	50
8	2	100	100	1	100	100	3	100	66,7
9	2	100	100	1	100	0,0	3	66,7	100
10	1	100	100	0	0	0	0	0	0
11	1	0	100	0	0	0	1	0.0	100
12	1	100	100	0	0	0	0	0	0
13	2	50	100	0	0	0	1	0.0	100
14	2	0	100	0	0	0	1	0.0	100
15	2	50	100	0	0	0	2	0.0	100
16	2	100	100	1	0,0	100	2	0.0	100
17	2	50	100	1	0,0	100	3	33,3	100
18	4	50	100	2	0,0	100	4	25	100
19	6	66,7	100	4	75	75	7	42,9	100
20	6	66,7	100	2	100	100	8	87,5	100
21	3	100	100	2	100	100	7	100	100
22	3	100	100	3	66,7	66,7	4	100	100
23	3	100	100	1	100	100	5	100	100
24	4	100	100	2	50	50	6	100	100
Total	65	81,5	96,9	33	63,6	72,7	92	79,3	90,2

Table 13: Daily distribution and match rate of observed cases of potential temperature (θ) and specific humidity (*q*) for July, August and September.

	Match rate (%)								
	October			November			December		
Daytime	N° of cases	(θ)	(q)	N° of cases	(θ)	(q)	N° of cases	(θ)	(q)
1	3	100	66,7	3	100	66,7	2	100	50
2	2	100	100	4	100	100	2	100	100
3	4	100	50	5	100	100	3	100	100
4	4	100	100	6	100	100	2	100	50
5	3	100	100	7	100	100	2	100	100
6	5	100	100	6	100	100	1	100	100
7	4	100	100	5	100	100	1	100	100
8	2	100	100	2	100	100	1	100	100
9	0	0	0	0	0	0	0	0	0
10	0	0	0	1	0,0	100	0	0	0
11	0	0	0	1	0,0	100	0	0	0
12	0	0	0	1	0,0	100	0	0	0
13	0	0	0	1	0,0	100	0	0	0
14	0	0	0	1	0,0	100	0	0	0
15	0	0	0	0	0	0	0	0	0
16	1	0,0	100	0	0	0	0	0	0
17	2	0,0	100	0	0	0	0	0	0
18	2	50	100	2	0,0	100	1	0,0	100
19	1	100	100	6	50	100	2	100	100
20	3	100	100	8	75	100	5	100	80
21	5	80	80	8	100	87,5	1	100	100
22	3	66,7	66,7	4	100	100	1	100	100
23	3	66,7	66,7	4	100	75	0	0	0
24	3	100	100	3	100	66,7	3	100	66,7
Total	50	86,0	88	78	84,6	94,9	27	96,3	85,2

Table 14: Daily distribution and match rate of observed cases of potential temperature (θ) and specific humidity (*q*) for October, November and December.

7.6 Discussion of local scale factors

7.6.1 Seasonal cycles in fog and low clouds

The seasonal cycle of FLCs is well described by GOFOS observations. Although, seasonal variations in FLC cycles are mostly determined by regional scale changes in ocean-atmosphere interactions, which were discussed in the previous chapter (section 6.4), in the local analysis the various instruments used allow us to accurately quantify variations in these factors and how they are linked to the formation and to the vertical dynamics of FLCs. In this sense, considering that air subsidence and the strength of the thermal inversion layer are the main factors in FLC formation (Bretherton and Wyant, 1997; Duynkerke et al., 1995; Wood, 2012), the north-south seasonal shift in the SEPA, which is related to variations in the intensity of air subsidence and consequently in LTS, is one of the primary determinants in the greater presence of FLCs during the winter, and their lower presence during the summer in the coastal Atacama Desert. In the same way, the CT and CB altitudes and CD show a clear annual cycle that is closely related to the location of the center of the SEPA.

CT and CB altitudes are higher during summer, when the SEPA is at its southernmost position; then during autumn, both begin to decrease, as the SEPA moves northward toward the study area. In winter, CT and CB altitudes reach their minimums coupled with SEPA reaching its northernmost position, after which it restarts its seasonal southward shift during the spring, at which point CT and CB altitudes begin to increase slightly. The CT altitude has greater monthly differences compared to the CB altitude, which is much more stable throughout the year, consequently CD closely follows variations in the CT altitude, presenting the highest CD during summer and the lowest during winter. Thus, the CT altitude is related to air subsidence, and depending on the season it produces a deeper or shallower MBL, which in turn differs in its vertical structure in such a way that it generates seasonal differences in the CB altitude, and therefore in the CD. Considering that the CB altitude defines the condensation level within the MBL, it is expected that its annual variability should be lower than the CT altitude, as it depends on the vertical structure and altitude at which the mixing ratio is produced, which is determined by the thermal gradient, air pressure and relative humidity, which under well-mixed regime in the MBL should not show significant differences.

The measurements of the weather stations validate the inverse seasonal correlation between CT altitude and FFP. Both weather stations, at 50 and 1.200 m a.s.l., clearly show annual SEPA displacement in their annual air pressure cycle, as they present the highest air pressure during winter and the lowest during summer. Thus, higher FFPs are observed during winter when the air pressure is at its maximum (with a mean for the winter season of 1.011 and 881 hPa at 50 m and 1.200 m a.s.l., respectively), and mean air temperature is at its minimum (16,1 and 15,7 °C at 50 m and 1.200 m a.s.l. respectively), thus generating a strong thermal inversion layer, which strengthens the LTS and favors better conditions for FLC formation. During winter, the CT altitude (thus, the base of the thermal inversion layer) is in agreement with the seasonal higher air subsidence, and reaches its lowest altitude (1.040 m a.s.l.). At the same time, the CB altitude reaches its minimum mean altitude (855 m a.s.l.), pushing the condensation point to its lowest altitude. In relation to the CD, winter present the lowest seasonal average (220 m), which is closely related to the lowest altitude of the CT. In this sense, the shallower MBL in winter is conducive to producing turbulence within the MBL (principally through long wave cooling, Bretherton and Wyant, 1997), producing a well-mixed atmosphere structure and thus resulting in increased fog formation. Interestingly, maximum and minimum temperatures measured at 1.200 m during winter

months show high oscillation, precisely because of the lower altitude of the CT, meaning that the station at 1.200 m a.s.l. is regularly exposed to the dry conditions above the thermal inversion layer. The slight difference in mean temperature between the two stations is highly influenced by this situation, as it does not respond to the adiabatic differences expected for both altitudes. In July, temperatures at both stations are reversed, with mean temperatures higher the station 1.200 m a.s.l.. Additionally, maximum and minimum values of relative humidity registers shows an extreme difference that goes from 100 % to nearly to 0 %.

During summer the SEPA is at its southernmost position (~35 °S), therefore air subsidence is lower over the study area (with a mean for the summer season of 1.007 and 880 hPa at 50 m and 1.200 m a.s.l., respectively), and at the same time air temperature is at its maximum (23,6 and 18,1 °C at 50 m and 1.200 m a.s.l., respectively). The lower air subsidence and higher temperatures weaken the thermal inversion layer, consequently there is higher entrainment of air from the free troposphere into the MBL (Bretherton and Wyant, 1997; Wood, 2012), drying the MBL, which results in stratification of its vertical structure, and thus a significant lower FFP. On the other hand, despite lower subsidence and higher temperatures, FLC presence occurs when the CT altitude is at its highest position (mean at 1.230 m a.s.l.), with an increment of almost 200 m in relation to the winter mean. For its part, the CB altitude also reaches its highest position with a seasonal mean at 970 m a.s.l., which in this case, presents a difference of 115 m in relation to winter, and in the same manner, the CD is also at its maximum with a mean of 315 m. Here, the presence of FLCs is produced in a deeper and on average warmer MBL and where the well-mixed regime implies that within its vertical structure the condensation point occurs at higher altitudes as cooler temperatures necessary occur adiabatically at those altitudes. Therefore, at higher altitudes of the thermal inversion layer, cloud thickness increases. As the altitude of the weather station at 1.200 m a.s.l. is regularly within the MBL, temperature differences with the 50 m a.s.l. station, are in closer agreement with their altitudinal gradient. Values of relative humidity are similar between both stations with respect to winter, given that both are regularly within the MBL; although the highest station has higher values, as it is located at altitudes of cloud presence and with humidity of 100%, conditions that do not occur at sea level.

Autumn and Spring are transitional seasons between the extremes (summer – winter), given the position of the SEPA and temperatures variations. The months of May – June and

September – October show high FFPs, as they also provide optimal conditions for cloud formation. In May - June, there is high air subsidence (similar to the winter mean at both stations), but temperatures are a little bit higher; on the other hand, in September-October there is lower air pressure than winter, but even cooler temperatures (at both stations). The high air pressure during autumn does not translate into CT altitudes equal to winter (they are on average 80 m higher), presumably due the countering effect exerted by higher air and sea surface temperatures. A similar situation may occur during September-October, but the influence of the variables is reversed; air pressure is lower, as is air and sea surface temperatures. In relation to the CD, spring shows almost identical thickness as winter (in autumn the difference is more significant), in correspondence with subtle differences in CT altitude and the vertical scale of analysis. In the spring, it is interesting to observe measurements from the station at 750 m a.s.l. for the period from October to December, which show a mean air temperature 4 °C lower than at 50 m a.s.l., and 1,5 °C lower than at 1.200 m a.s.l. demonstrating a break in the adiabatic gradient, explained by the regular position of the thermal inversion between the two stations at higher altitude.

7.6.2 Daily cycles in fog and low clouds

Daily cycles in FLCs in the coastal Atacama are well described by GOFOS. Vertical variations in FLCs are primarily a product of complex daily ocean-land interactions and involved thermodynamic fluxes, along with regional factors, such as sunshine on the Andean slope and its link to air subsidence of air along the coast (Rutllant et al., 2003). GOFOS results allow us to interpret FLC variations from a meteorological and climatological perspective. Results on the mean annual daily cycle shows a strong inverse correlation between FFP and CT altitude, where a lower altitude of the thermal inversion layer is related to higher FFPs, a phenomenon that occurs from sunset to dawn, and oppositely, higher altitudes of the thermal inversion layer are related to lower FFPs, which occurs from early morning to afternoon. Therefore, considering that the altitude of the thermal inversion is a product of the interaction of daily cycle processes above and below it (Rutllant et al., 1998), the relationship between the daily cycle of the thermal inversion layer and FLC presence of clouds is based, as expected, on the daily solar cycle and its consequential thermal differences between the ocean and land. During sunshine hours, the desert begins to heat up, producing a significant thermal difference between the land and the sea, which generates significant SW-W inland winds, particularly in the afternoon, causing the base of

the thermal inversion layer to rise. Thus, evaporation of FLCs is a product of solar radiation and desert heating. In addition to a deeper MBL, which is linked to greater possibility of stratification, significantly lower FFPs are generated during this time of day.

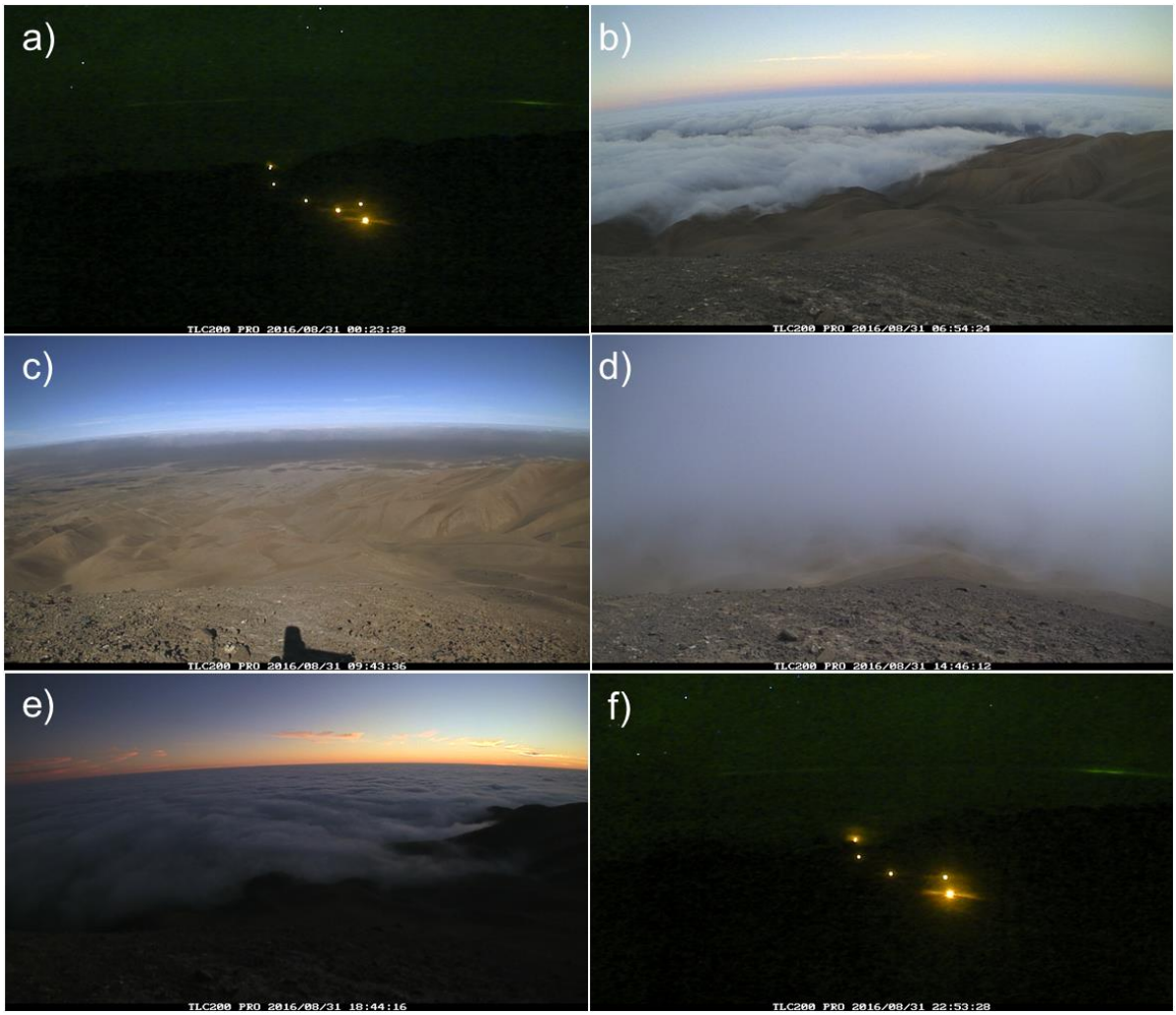

Figure 81: The daily cycle of fog for August 31, 2016, as observed from the top GOFOS camera. Photos were taken at the following local times: a) 00:33, b) 06:54, c) 09:43, d) 14:44, e) 18:44 and f) 22:53.

From sunset to dawn, the altitude of the thermal inversion layer is more stable and lower (annual mean of 1.050 m a.s.l.), as the ocean – land temperatures are lower and the difference between these temperatures is also lower. Thus, here the regional processes above the thermal inversion layer predominate and generate its lower altitude, given that the synoptic scale air subsidence is strengthened by winds coming down from the Andes (mainly during winter dawn) (Rutllant el al., 2003). The cooler conditions within the MBL, in addition to the lower altitude of the thermal inversion layer, promote the formation of FLCs, which is

enhanced by long wave cooling at the top of the cloud, generating a well-mixed vertical structure. Fig. 81 exemplifies a medium daily cycle, with low thermal inversion and high fog presence during the night and dawn (Figs. 81a and b, respectively). Then when sunshine appears in the morning, the cloud dissipates (Fig. 81c). At times there may be fog in the afternoon, but at higher altitudes, given the impulse of factors (wind) within the MBL (Fig. 81d). Towards sunset, the altitude of the thermal inversion begins to fall until it again reaches its lowest point (Figs. 81e and f, respectively).

Monthly differences in the daily cycle are determined by the number of daylight hours with FLC presence (Muñoz et al., 2016). Given the dynamism of the processes that generate fog presence, high hourly variability is observed, resulting in high altitudinal variation in fog (CT and CB altitudes) at the same time of day within any given month. In this sense, daily cycles show steep changes in some months, while others months exhibit little variation; this results in daily maximum and minimum CT and CB altitudes and CD occurring at different times of day. For example, the CT altitude (and its consequent CD) rise earlier in the day from November to May (09:00 - 10:00) than from June to October (11:00 - 12:00). Summer months have very low FFPs, primarily due to increased sun exposure throughout the day with a nearly vertical solar angle, thus causing dissipation of FLCs during most of the day. Consequently, air and the sea temperatures are also higher, pushing the thermal inversion layer to higher altitudes and a causing a stratified vertical structure within the MBL. These conditions are conducive to a weak thermal inversion layer, promoting the entry of warm air from the free troposphere, fragmenting or dissipating the formation of the cloud (see Fig. 82). As part of the same system, the low to null presence of FLC cover does not allow the process that promotes turbulence within the MLB to be activated, enhancing factors that support low fog presence throughout the day. Fog events are practically null during January and February, and when they do rarely occur, mostly at sunset, they last only a few hours. Presumably these summer fog events correspond to orographic fog, since they occur at times when the wind from the ocean is strong and daily temperatures drop (19:00 - 21:00); as the wind decreases, temperature equalizes and the fog disappears. GOFOS recordings (not shown) show the absence of low clouds on the coastline occurs prior to and after the events, discarding the possibility of advective fog. Summer fog events occur at high altitudes (CT = 1.400 m a.s.l.; SD = ± 180 m), and their thickness reaches 400 m, but they show high altitudinal variability, which can be characteristic of an orographic event, albeit this could also be influenced by the small number of measurements available. CT elevation during the

afternoon apparently contradicts local daily circulation in summer, when heating of the Andean slopes produces convection and subsequent air divergence on the coast, generating enhanced air subsidence that inhibits the FLC presence (Rutllant et al., 2003). However, this may be a regular situation that is partly explained by the absence of FLCs on the coast.

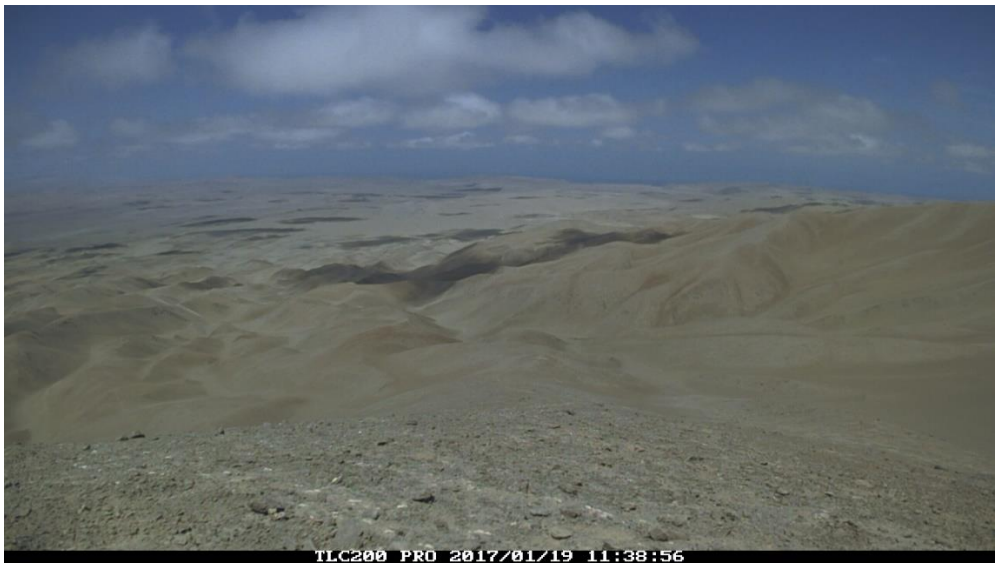

Figure 82: Fragmented low cloud, typical of summer conditions with a weak thermal inversion layer.

Winter and early spring months have less sunshine hours than summer, thus limiting the time of day when there is very low or null fog presence due to solar radiation (mainly 11:00 to 15:00). The CT and CB altitudes and mean daily CD in June to October show several similarities. CT altitude is low and stable during the night, coupled with LTS conditions, creating a strong thermal inversion layer between the warm air in the free troposphere and cooler temperatures within the MBL, favoring the formation of clouds and immediate enhancement by turbulence driven by radiative cooling. On the other hand, the CB altitude varies more at night, due to the dynamism of the turbulence process, as well as due to the fact that winds speed and soil temperature interact with the contact of the cloud with the desert, where the lowest GOFOS camera recorded its measurements. Therefore, the same variability occurs in CD, which reaches its thinnest at dawn along with the lowest daily air temperatures. The rise in CT altitude begins a few hours later than summer, because the solar radiation began to heat the desert later and therefore the SW winds are activated around 11:00. During sunset, the SW winds tend to decrease and even reverse into the night

(Muñoz et al., 2016), thus lowering the thermal inversion layer together with the temperature, thus favoring the conditions for cloud formation.

7.6.3 The role of topography in the vertical distribution of fog and low clouds

The influence of topography on the spatial distribution of fog has been considered a critical factor by various authors (e.g. Farías et al., 2005, Osses et al., 2007), but the vast majority focused on how fog is distributed over complex topographies, how topographic relief inhibits the passage of fog, or have identified corridors through which fog manages to penetrate the land and maintain a regular presence. However, the role topography plays in the vertical distribution and spatial-temporal variations in fog have rarely been quantified. Here it is presented a first approximation, by comparing observations and measurements taken at the airport on the height of the cloud base with the observations by GOFOS at the exact same moment for 2017. Along with CB altitude, it is quantified the presence of FLCs at the airport according to the following criteria: 1) oktas observations greater than 7 (low cloud fragmentation), or 2) cloud base altitude of less than 1.500 m a.s.l. (low cloud). This compares the situation at the airport when low clouds are present (Sc type by the criteria applied) that are not in contact with the surface. In the case of GOFOS measurements, the system was installed on western facing slopes in the Coastal Cordillera. Fig. 83 presents monthly comparisons, showing seasonal differences in CB altitude, with higher altitudes at the airport in December to May (summer - autumn), and higher CB altitude in the GOFOS measurements from June to November (winter - spring).

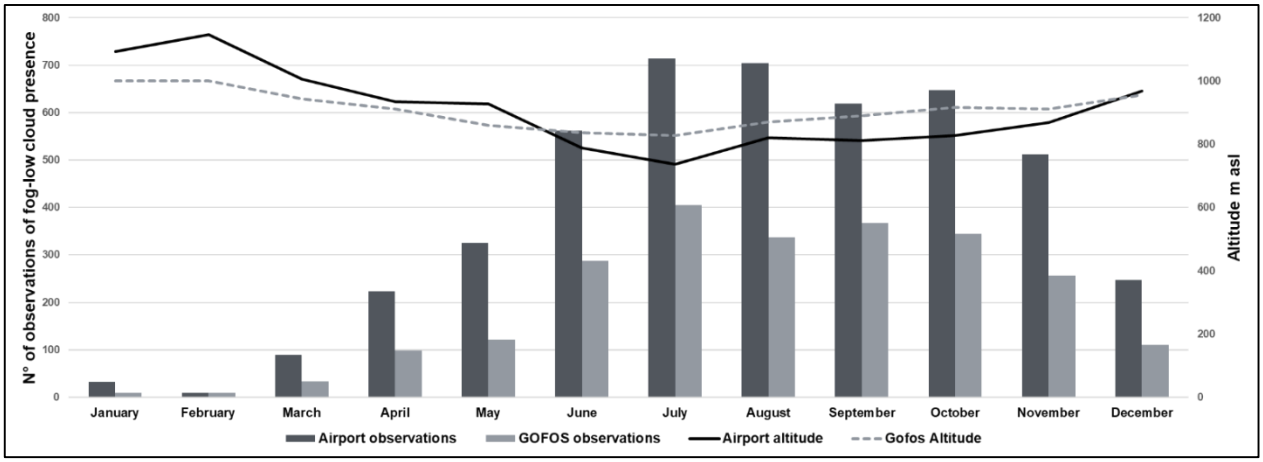

Figure 83: Comparison of the annual cloud base altitude and the presence of fog and low clouds between airport observations and GOFOS.

Altitudinal differences were higher in January and February (with a mean of 120 m), and then tended to decrease toward May (March-May: mean of 50 m). When the CB altitude is higher according to GOFOS the difference is relatively similar, with a mean of 70 m. Interestingly, the months for which GOFOS presents a higher CB coincide with the seasons with a shallower MBL; that is, the CT and CB altitude are at their lowest altitudes, and CD is at its thinnest Therefore, it is to be expected that this difference occurs due to the topographic effects, which acts as an inclined platform, and due to the support of the prevailing winds (SW - W), which lift the base of the FLC. It is important to consider that during these months (specifically from August onwards), the lowest CB altitudes measured at the airport were taken with a ceilometer, a precision instrument designed to precisely measure CB altitude. In this sense, it is possible to confirm that topography plays a role in the vertical distribution of FLCs (quantified here at monthly scale, with an increase of 70 m in the CB altitude). It is also important to contemplate that in summer-autumn, altitudes are reversed (CB altitude is higher, according to airport measurements), but in this period there are two factors that make this difference questionable. The first is technical, given that the measurement was made by visual observation by professionals at the airport of Iquique, and that according to personally communications with these professionals, the main control on the measurement of CB height is the coastal cliff next to the airport that provides an altitudinal reference, but that in this sector, does not exceed 650 m a.s.l. The second factor is the regular condition of the MBL during those months, since it is the period in which it is deepest, with a higher altitude of the CT and CB (cloud base around 1.000 m a.s.l.). Therefore, observations made when the base of the cloud is higher are less precise.

When comparing measurements of the CB altitude from an hourly perspective for the different months, differences between both sources are maintained (see Fig. 85). However, is interesting to observe that the highest differences in the winter – spring season occurs between 16:00 to 20:00, a period of the day when the ocean to land winds are the strongest, enhancing the effect of topography. In addition, ground heating contributes to cloud evaporation, making CB altitude even more variable at this time of day (see Fig. 84).

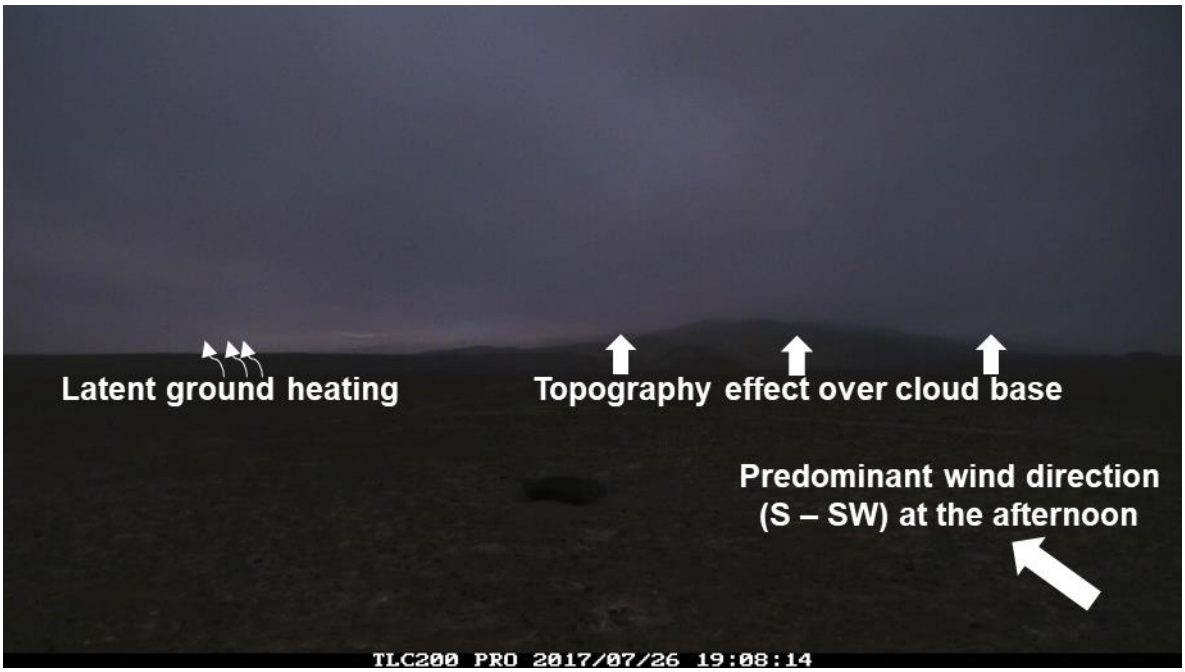

Figure 84: Influence of topography and ground heating on cloud base altitude during the afternoon.

On the other hand, the lowest differences occur when there are relatively calm winds, which from night to early morning. Thus at this time of day wind is not a determining factor on the vertical distribution of fog. Fig. 86 schematically synthesizes the differences found in regards to the cloud base due to the differing location of measurements. Despite the fact that there are no systematic local accurate measurements of CT altitude to be compared with GOFOS, it is expected that topography also influences the altitude of the thermal inversion layer, and consequently the thickness of FLCs, in such a way that the relief together with the wind will drive the fog inland to higher altitudes, producing a rise in the thermal inversion, but this rise will be lower than that of the cloud base, consequently resulting in thinning of the CD.

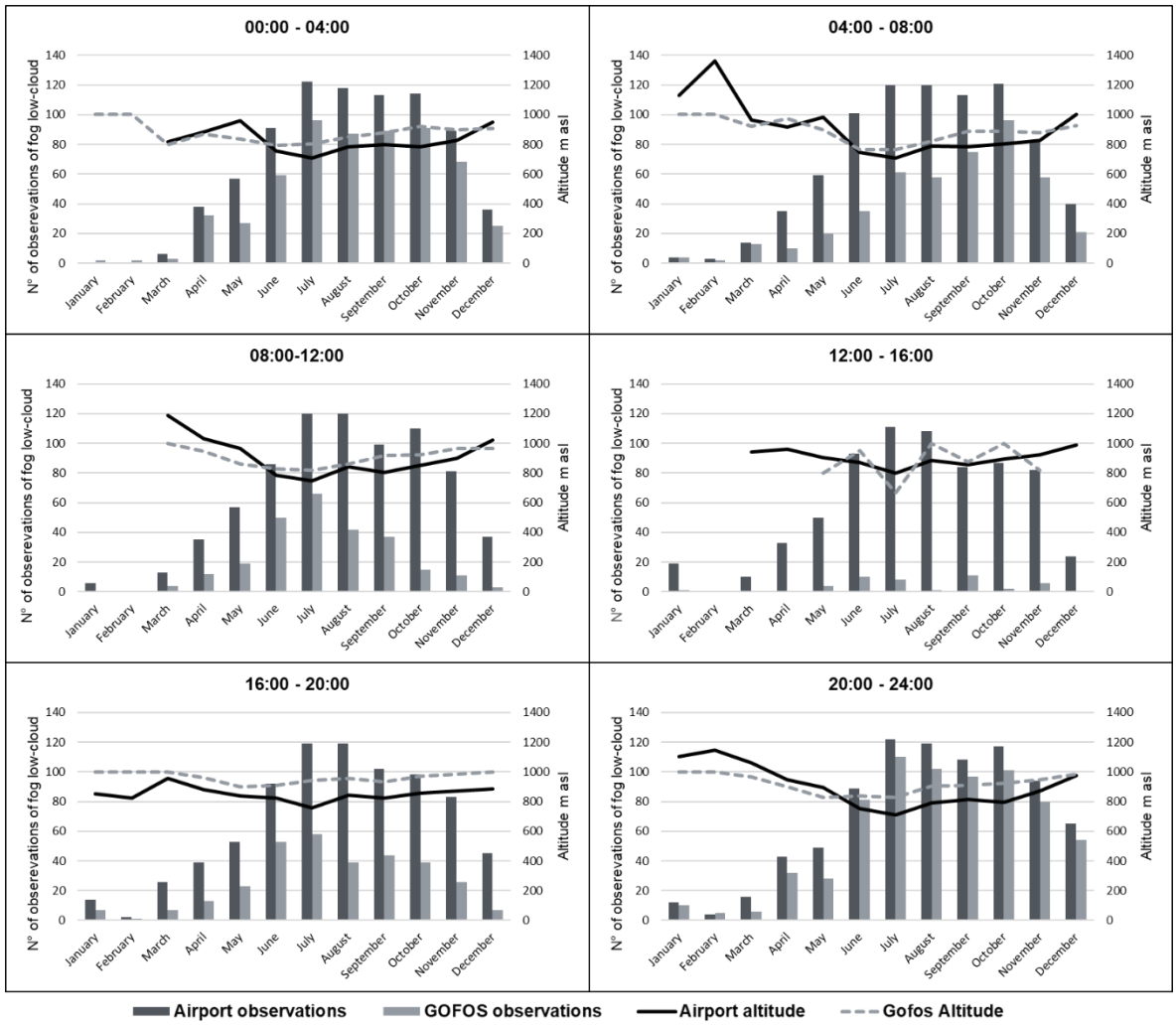

Figure 85: Hourly comparison of the daily cloud base altitude and fog and low cloud presence between airport observations and GOFOS.

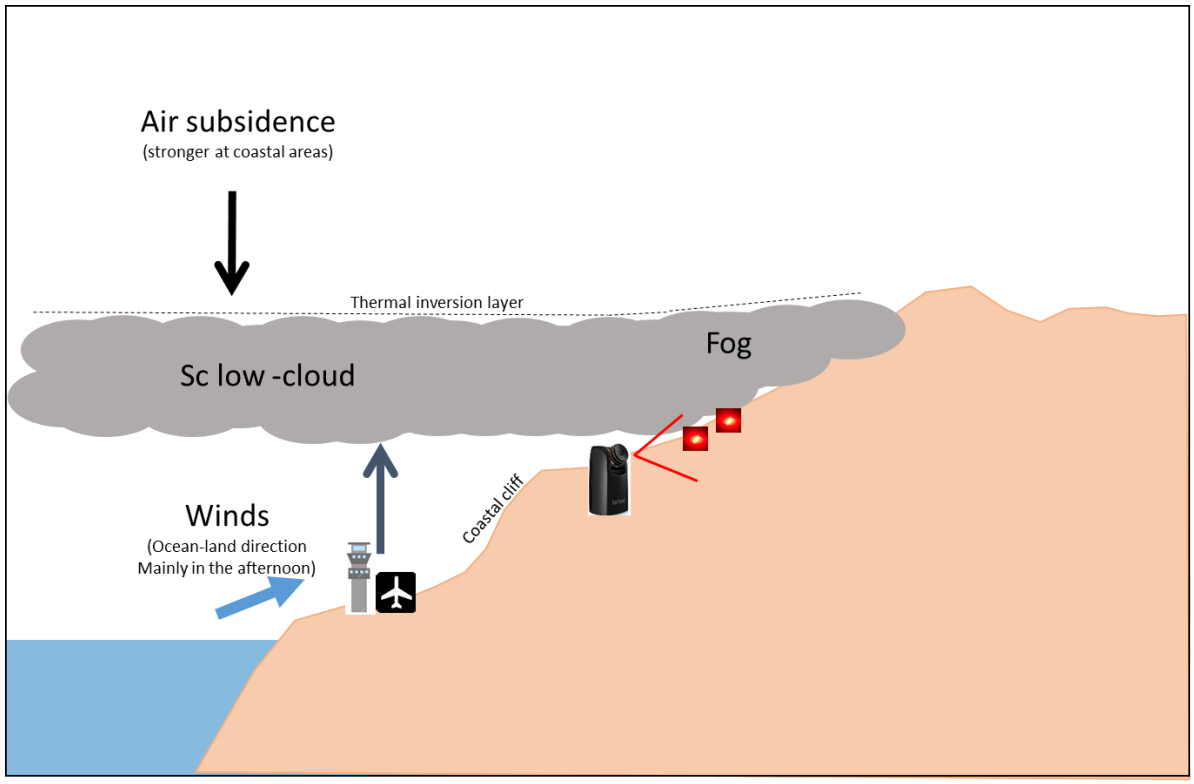

Figure 86: Scheme of topographic influences on vertical variation in fog and low clouds influenced and the location of the measurement systems (airport observations and GOFOS).

Annually, the presence of FLCs was 45 % higher at the airport than in the coastal range, a difference that is very similar throughout the year. The principal explanation for this difference is that at certain times of the day the low cloud covers the ocean and the coastline, but not the Coastal Cordillera, due to evaporation by solar radiation and desert heating (see Fig. 87a). Another less common reason, is the presence of a very low thermal inversion layer, resulting in an FLC that is under the minimum altitude observable by GOFOS (600 m a.s.l.) as it enters (backwards) into (from) the desert (see Fig. 87b). When analyzing differences in the presence of FLCs by time of day (see Fig. 85), we find the greatest differences occur during sunshine hours, mainly between 12:00 and 16:00, when the situation illustrated in Fig. 87a occurs. The smallest differences occur from sunset to nighttime (20:00 to 04:00), when FLCs have the greatest presence and cover both measurement areas. At dawn and towards sunset the situation illustrated in Fig. 87b occurs.

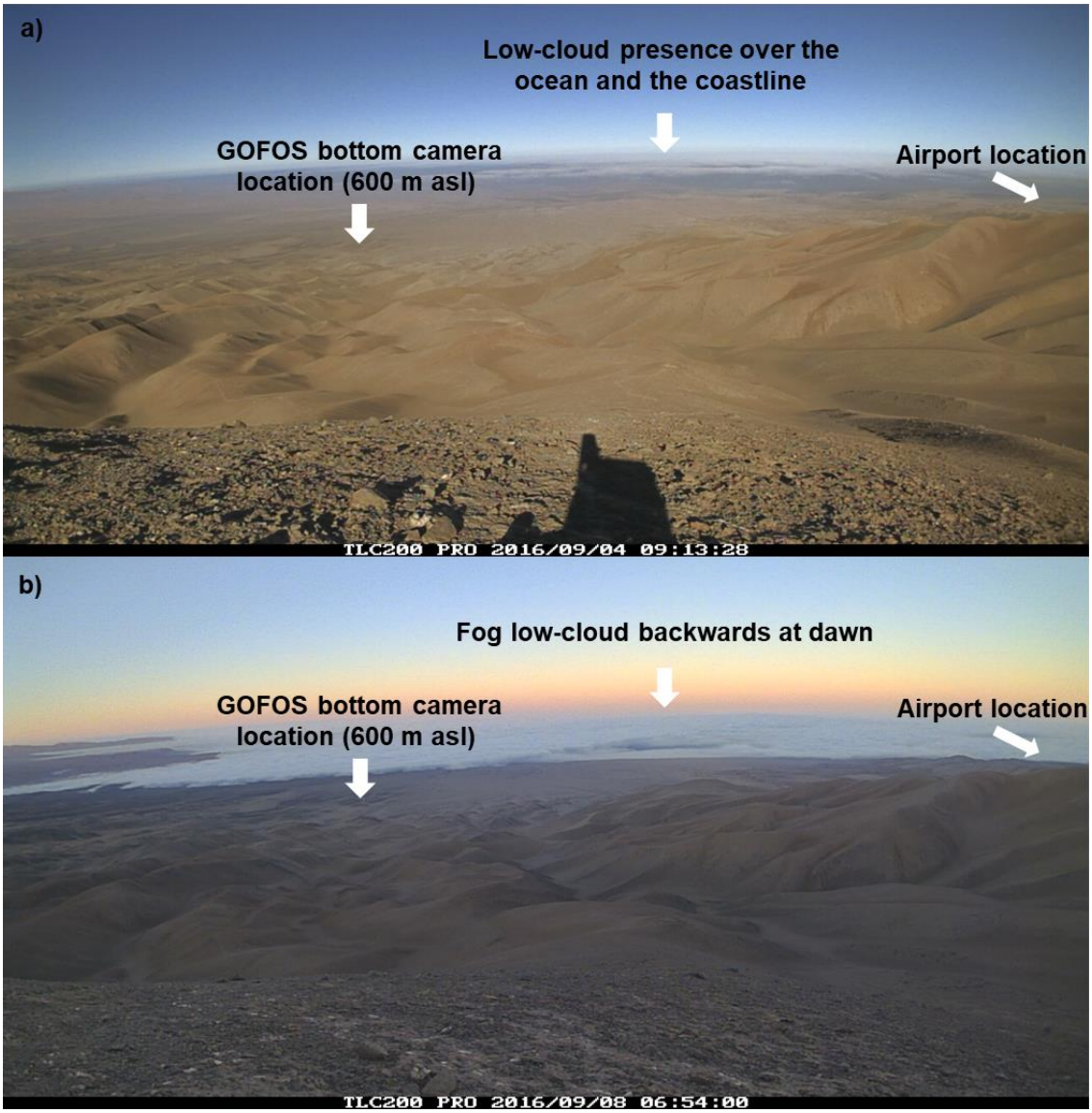

Figure 87: Examples of circumstances under which GOFOS records the absence of fog and the airport registers the presence of a low cloud.

7.6.4 The marine boundary layer regime

Assuming that the presence of FLCs occur under a well-mixed MBL regime, results show that by contrasting FFP with the proposed thresholds, concordance with specific humidity (q) is greater than 87%, while for potential temperature (θ) it reaches 79%. The greater concordance of q with fog presence can be explained given that this index precisely estimates humidity (g kg^{-1} m^{-1}), which is what is physically observed by GOFOS (fog - condensed humidity). Therefore, according to the results, it is a better indicator of a well-

mixed regime than θ for most seasons and time points. The high agreement between both indices, indicates that in the presence of FLCs there is a well-mixed regime when a very low vertical gradient of θ and moisture within the MBL predominates; that is, the FLC (with a thermal inversion layer altitude base greater than or equal to 1.200 m a.s.l.) forms when both weather stations present a θ and *q* that differs by less than 3.65 K and less than 1.88 gr kg^{-1}, respectively. Yet, there are daily and seasonal variations. The well-mixed conditions are scarce during sunshine hours (thus a lower FFP), when a vertical stratified MBL prevails, resulting in marine moisture in the lower section of the MBL and a considerably drier layer in the upper portion. This can be seen in the higher daily differences in θ and *q* between the 50 and 1.200 m a.s.l. stations during extreme seasons, summer and winter (see Figs. 88 and 89, respectively).

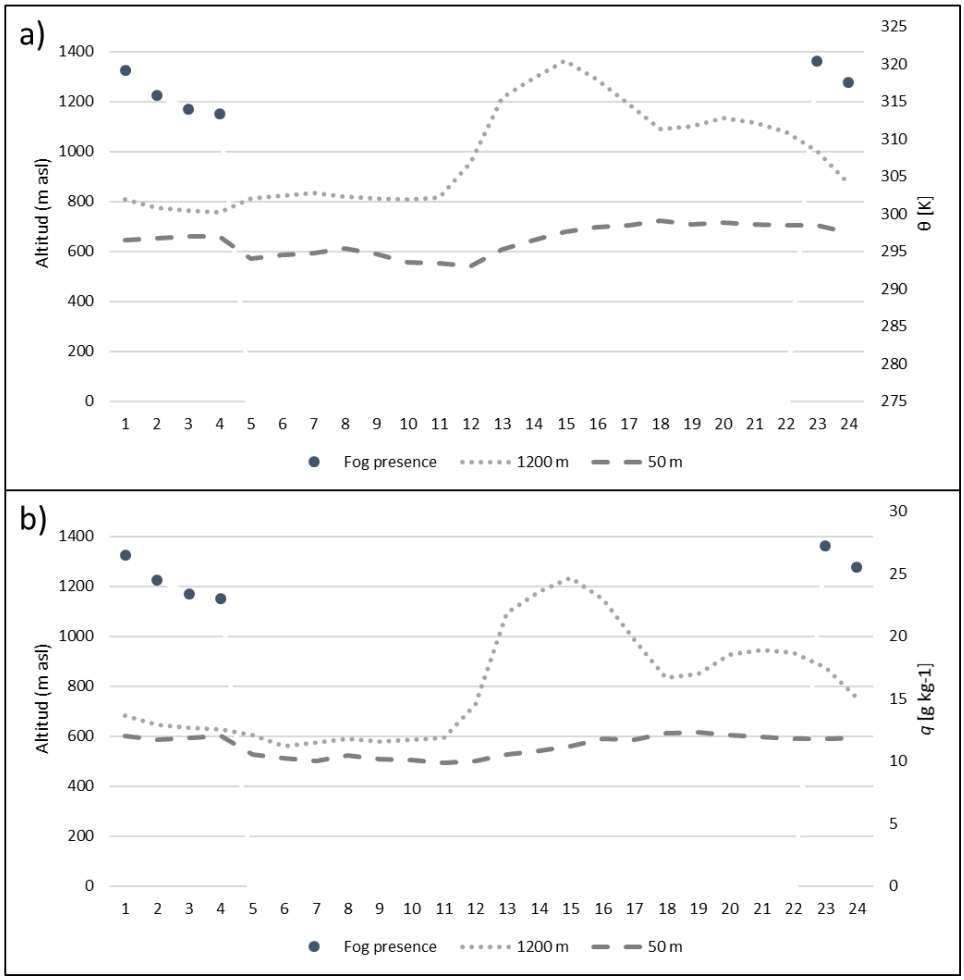

Figure 88: Hourly average for (a) θ and (b) *q* on February 6, 2017. Black dots represent fog presence and the altitude of the cloud top. Dotted and dashed lines represent observations at the 1.200 m and at the 50 m a.s.l. stations, respectively.

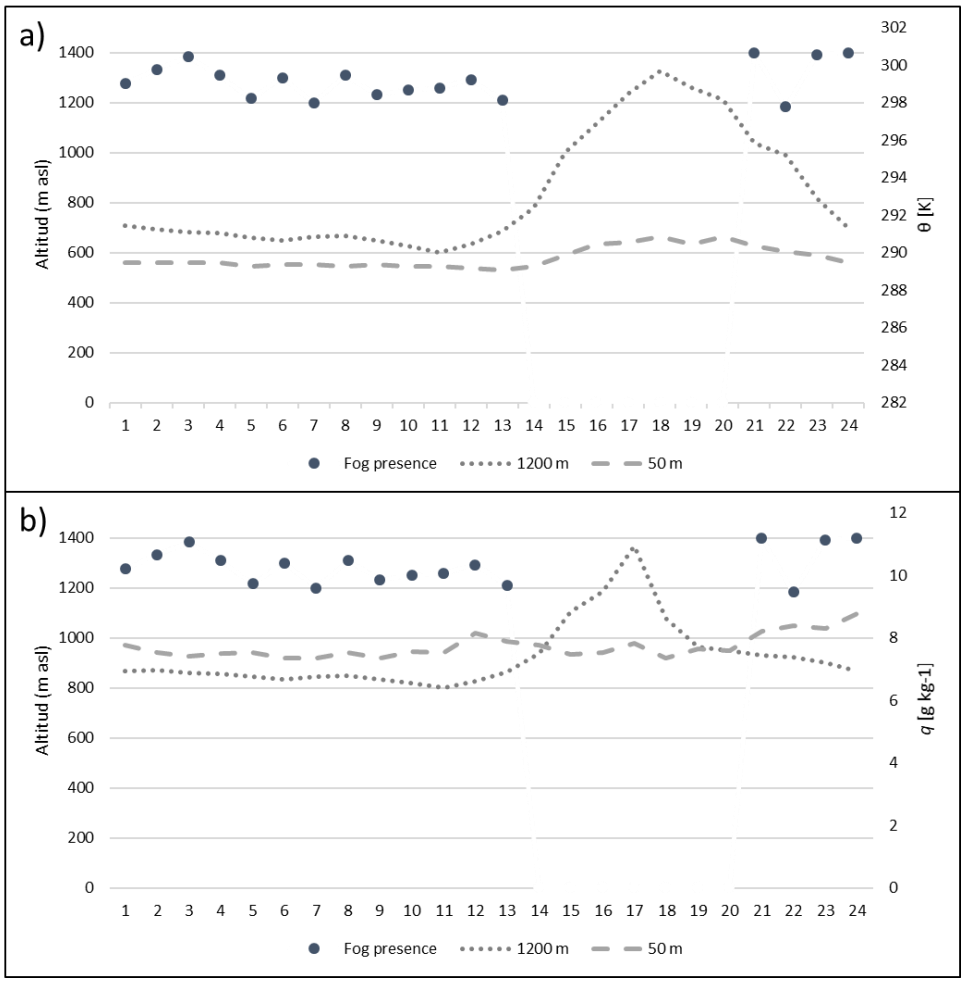

Figure 89: Hourly average for (a) θ and (b) *q* on September 9, 2017. Black dots represent fog presence and the altitude of the cloud top. Dotted and dashed lines represent observations at the 1.200 m and at the 50 m a.s.l. stations, respectively.

Fig. 88 shows the hourly average for θ and *q* on February 6, 2017. According to GOFOS, fog is present from midnight until 04:00 and from 23:00 to 24:00, when θ has its lowest difference between the two stations, indicating well-mixed conditions within the MBL. At 05:00 the difference in θ between the stations increases, with a maximum during the afternoon, resulting in the absence of fog during the day, an apparent consequence of a stratified MBL. In the case of *q*, although the presence of fog occurs when the difference is smaller, thus well-mixed conditions, from 05:00 and 11:00 the difference is equally low, yet there is no fog presence. The latter could be explained by the difference in θ, shown in Fig. 88a; in this sense, there is possibly differentiated stratification between water content and temperature along the MBL. Fog presence occurs when θ is above the proposed thresholds (between 23:00 and 02:00), indicating a lesser influence of well-mixed ocean conditions at 1.200 m a.s.l. According to Lobos et al (2018), the presence of fog under stratified regimes

is due to a residual turbulent layer that mixes with air decoupling from the surface, which refers to well-mixed conditions at the altitude that the fog is present, but that is stratified compared to the surface. On September 9, there was regular fog presence with a cloud top altitude around the 1.300 m a.s.l., with the exception of 14:00 and 20:00 when there is no fog. Fig. 89 presents the hourly average of θ and *q*, which show that in the presence of fog, both indices present lower differences between the two stations, indicating well-mixed conditions within the MBL; in the afternoon with no fog presence, the differences between the stations increase considerably for both indices, revealing a stratified regime within the MBL. The presence of fog is adjusted to the θ threshold, with values of less than 3.65 K, with the exception of 21:00 and 22:00 hours, when there is fog presence and differences at approximately 5; this, likely occurs because there is a transition between regimes at this time of day. For hours with no fog presence (14:00 to 20:00), differences are between 5.5 and 8.5 K. In the case of *q*, all values when fog is present are within the thresholds; however, interestingly for hours with no fog presence, the station at 1.200 m a.s.l. has higher values than at 50 m a.s.l., which may be due to the presence of local orographic fog present at the station at higher altitude that is not observed by GOFOS.

Finally, it should be noted, that the new fog monitoring system (GOFOS), in addition to accurately characterizing vertical fog dynamics in the coastal Atacama Desert, allows for the characterization of MBL regime, both of which are key indicators for forecasting future fog harvesting potential. The fact that estimated MBL regimes are compared with empirical GOFOS results means that in the future the thresholds can be adjusted, and in this way a better understanding of the necessary conditions for fog, at different time scales.

8 Integration of scales

This chapter presents results of scale integration of the methodological approaches used here (see Fig. 90). Then it was interpreted scale integration results, emphasizing an overview of what has been learned regarding the fog climate.

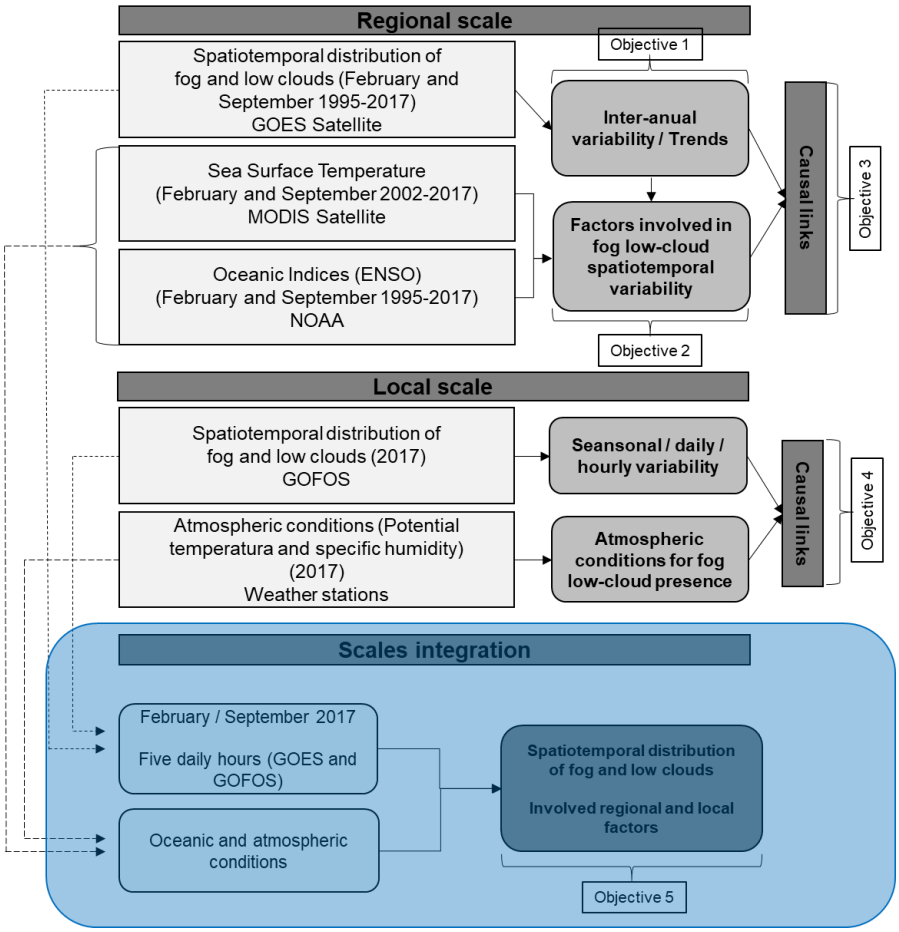

Figure 90: Scale integration scale within the study design for spatiotemporal characterization and analysis of the relationship between fog and low clouds and atmospheric variables.

Results from both scales produced complementarity datasets on the frequency of fog presence for the year 2017. This allows us to integrate and interpret the knowledge generated from both scales with respect to the ocean-atmosphere-land interactions involved in fog cycles and spatiotemporal variations in fog.

8.1 GOFOS as a ground truth system for validation of satellite results

Datasets from the two scales analyzed coincide during February and September of 2017, and in September 2016. The 2016 datasets from GOES and the top GOFOS camera were used for satellite data validation; the 2017 datasets were used to contrast and contextualize results spatially and temporally. The first scale integration is part of the methodological process of validating the results obtained from the classification criteria of FLCs using GOES satellite images. Validation was performed for all GOES images from September 2016, and consisted in the analyzing the consistence of results on the presence or absence of FLCs as well as the inversion layer altitude. Fig. 91 shows data integration of results on fog presence (light red: present; transparent: absent) using the free software *Google Earth* according to GOES on September 1, 2016 at 19:39 local time based on data from the top GOFOS camera.

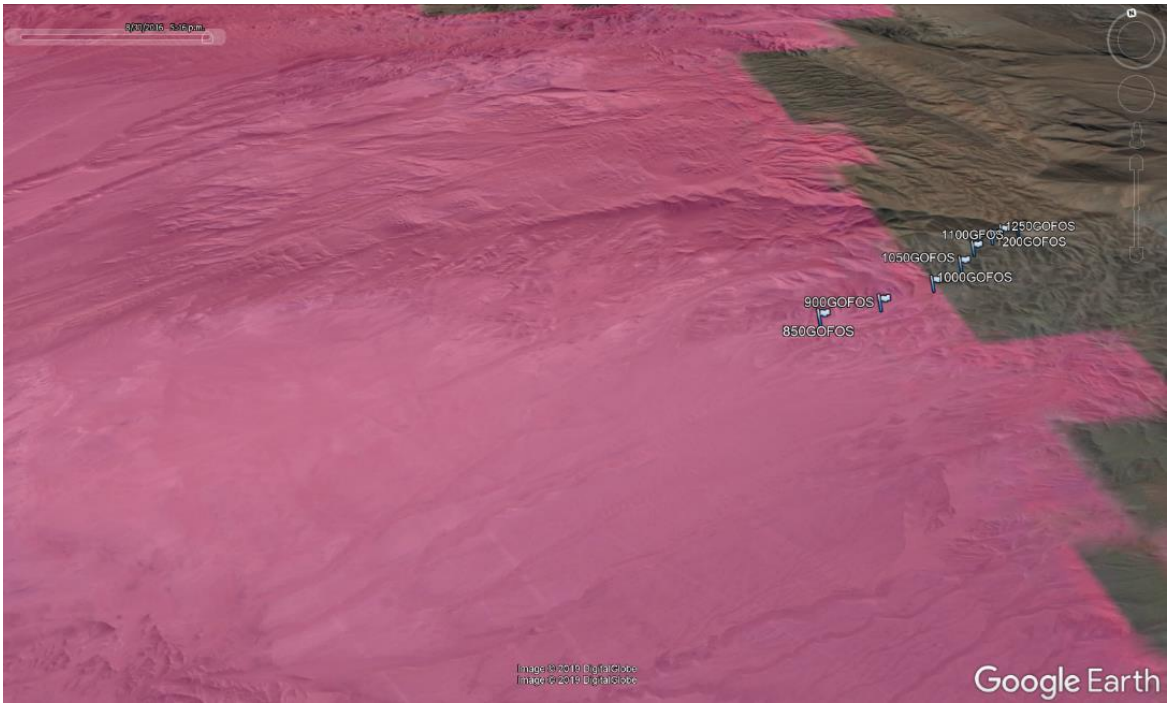

Figure 91: Integration of result on the presence (light red) or absence (transparent) of low clouds according to GOES classification and the location of the GOFOS system in the free software *Google Earth*.

GOES image classification shows extensive FLC coverage over the Coastal Cordillera, and that the thermal inversion layer is in between the 1.000 and 1.050 m a.s.l.. For the same day

at 19:36 (3 minutes before the satellite images were taken), GOFOS observations shows wide presence of FLCs and a thermal inversion layer base at 1.200 m a.s.l. (see Fig. 92).

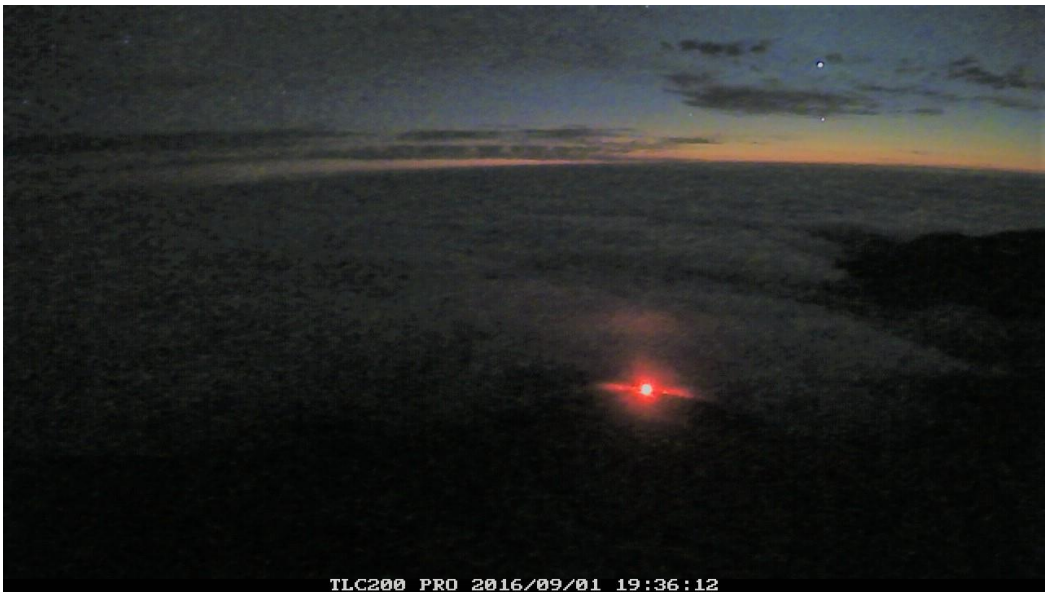

Figure 92: Image from the top GOFOS camera taken on September 1, 2016 at 19:36 local time.

In the case of the example presented, there is concordance between the observations made by both methodological approaches as to the presence of FLCs, thus validating satellite results. A synthesis of the results of all the images can be found in Table 15.

Local time GOES / GOFOS	N° of images / observations	N° of concordance GOES / GOFOS	Percentage (%)
0:39	27	26	96,2
4:39	27	25	92,5
7:39	27	27	100
12:39	27	27	100
19:39	27	21	77,7
Total	135	126	93,3

Table 15: Comparison and validation of satellite classification results from ground truth data (GOFOS) for September 2016.

Validation was performed for 135 images, 27 for each of the 5 daily images, obtaining a concordance of 93,3 %. The greatest matches were at 07:39 and 12:39 with 100 %, and the lowest at 19:39 with 77,7 %. Differentiating between the type of algorithm used, the images

taken at night (00:39, 04:39 and 07:39) and during day (12:39 and 19:39), have a concordance rates of 96,2 and 88,8 %, respectively. For estimates of the altitude of the base of the thermal inversion layer, the GOES estimate was systematically lower than the GOFOS measurement, by an average of 215 m; the GOFOS mean was 1.050 m a.s.l (SD = ± 145 m) and GOES mean was 835 m a.s.l. (SD = ± 215 m). However, this underestimation is relatively constant, showing a strong and significant correlation of r = 0,84.

8.2 Comparison of monthly and hourly fog and low cloud frequency presence

FFP results from the GOES satellite over the GOFOS area and the airport were compared with GOFOS observations and oktas results. Based on the data available, the comparison was conducted based on monthly means; for GOES, it was used data from the 5 daily images, for GOFOS it was used measurements every 10 minutes and for oktas observations every one hour. In addition, the monthly averages for each of the 5 daily GOES images were contrasted with what airport observations at the same hours by GOFOS.

Fog and low cloud frequency presence (%) for September 2017				
Mean	GOES over GOFOS area	GOFOS	GOES over airport area	Airport (oktas)
Monthly	41	44	52	56,3
0:39	58	68	71	73
4:39	56	63	68	70
7:39	56	58	68	70
12:39	7	7	29	40
19:39	28	49	23	30

Table 16: Comparison of fog and low cloud frequency results between GOES, GOFOS and Oktas (airport) data for September 2017.

The monthly mean estimated by GOES for both areas (over GOFOS and the airport) in September show slight underestimates with respect to local measurements, which is the same level of concordance (93 %) as estimated in section 8.1. (see Table 16). It is important to considered that the estimation of GOFOS and oktas monthly means is based on more significantly more data. For monthly hourly averages, also in accordance with the results presented in section 8.1, the greatest difference between GOES and GOFOS occurs at sunset, but here the underestimation is greater, reaching concordance of 57%. At the same

time, the other hours analyzed, show a very high concordance, even reaching 100% for half of the day. In the case of GOES and oktas, there is very high agreement at night (nearly 100 %), but concordance decreases at noon (73 %) and sunset (77 %). In the case of February 2017, results should be interpreted with greater caution, given the low FFP. However, monthly averages show strong coincidence between GOES and GOFOS, both with 1,5 % of FFP. In the case of GOES and oktas, there is an underestimation on the part of GOES that reaches around 50 % (see Table 17). For the monthly hourly averages, GOES and GOFOS, and GOES and oktas show similar agreement, as both present identical FFPs at night, but differ at dawn, noon and sunset.

Fog and low cloud frequency presence (%) February 2017				
Mean	GOES over GOFOS area	GOFOS	GOES over airport area	Airport (oktas)
Monthly	1,5	1,5	0,7	1,6
0:39	3	3	3	3
4:39	3	3	3	3
7:39	3	0	0	3
12:39	0	0	0	0
19:39	0	3	0	0

Table 17: Comparison of fog and low cloud frequency results between GOES, GOFOS and Oktas (airport) data for February 2017.

8.3 Discussion of scales integration

FFPs estimated by the top GOFOS camera, which is considered to be the most accurate estimation of FFP, showed that for the year 2017 maximum FFPs occurred in July and August (~50 %), followed by September and June (~43 %). Leading to a discussion as to whether September is really the month with the greatest FLC presence in the study area (~20° S). Cereceda et al., 2002 and Muñoz et al., 2016, suggest that maximums occur between July and September, based on satellite observations and at the airport (oktas), respectively. On the other hand, Cereceda et al., 2008b, Larraín et al., 2002 and del Río et al., 2018, propose that maximums occur in September, based on the amount of water collected by SFCs located in Alto Patache; furthermore, del Río et al., 2018 showed a positive correlation (r = 0.6) between fog water and the presence of low clouds (oktas from Iquique airport). The difference may be due to a particularity in the year 2017, or more probably to the location of GOFOS, about 10 km inland in the Coastal Cordillera, in relation

to Alto Patache and the airport, which are very close to the coast (less than 4 and 1 km to the coastline, respectively). Moreover, fog water measurements at the Cerro Guatalaya site, located about 12 km from the coastline and at 1.050 m a.s.l. at the latitude of iquique, have maximum yields during July and August (Cereceda et al., 2008a; del Río et al., 2018), indicating that the best conditions for the formation and inland penetration of advective fog possibly occurs in the winter months.

8.3.1 Spatiotemporal distribution

Tesults of the satellite classification and the ground observations (GOFOS and oktas) of the FLCs show, based on both the image-by-image and the comparison of monthly averages, high concordance (reaching ~93 %). This makes it possible to validate and support the regional scale results, which assert that coverage and spatiotemporal variations in FLCs slightly underestimate reality. In this sense, the location of GOFOS, as well as the airport, can be considered as representative of the large-scale situation of cloud presence along the coast of the Atacama Desert, at least in its hyper-arid section (~20° S).

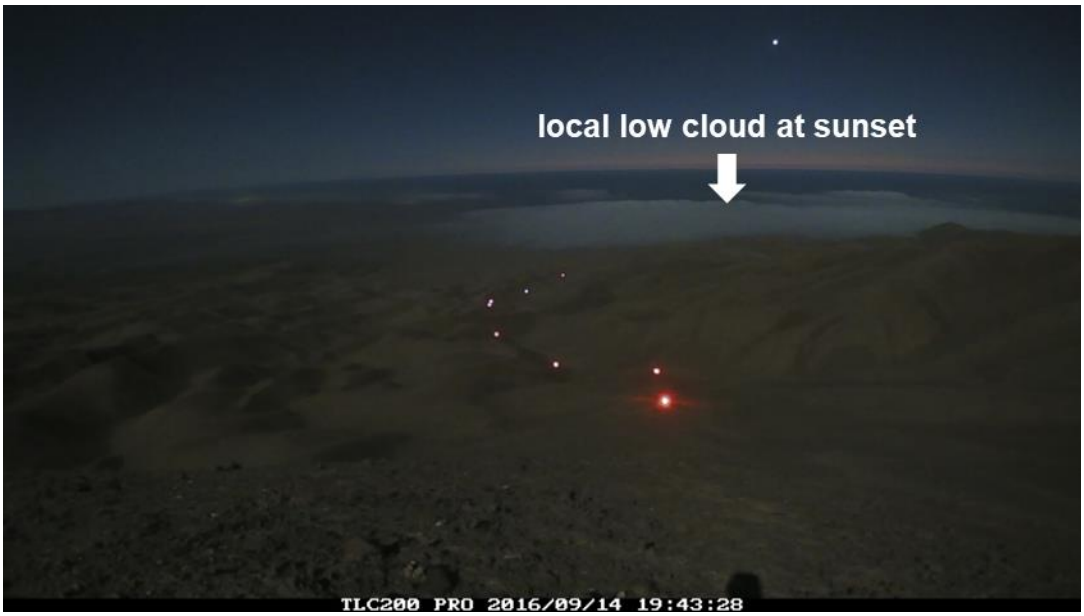

Figure 93: Local low cloud over GOFOS and the airport on September 14, 2016 at 19:43 local time.

At sunset concordance is lower; this occurs as at 19:39 there is an intensification of ocean - land winds, and the presence of the coastal mountain range means that the formation of orographic fog predominates. This type of fog has a limited and local spatial coverage, which

is captured by local sensors, but given spatial resolution it is not captured by the satellite (1-4 km). A potential case of orographic fog at sunset can be observed on September 14, 2016 (Fig. 93).

Because of the very low FFPs observed in February, of ~1,5 %, differences produced by a single non-consistent observation at different scales generate changes that appear to be relevant. It is therefore difficult to observe systematic temporal patterns in time, however cases of underestimation (yes GOFOS - no GOES) are produced by the presence of local clouds, just as described at sunset in September. The inverse situation (no GOFOS - yes GOES), occurs when there is a low cloud whose base exceeds the altitude observable by GOFOS (1.350 m a.s.l.).

Regular underestimation of the thermal inversion layer base altitude (215 m) by satellite classification compared to the accurate estimations made by GOFOS, may be due to the low spatial resolution of the satellite when interacting with a steep sloping topography, in such a way that the cells of the sensor to be classified as low cloud must have at least 50% of their area covered, otherwise they will be classified as the absence of a low cloud. We would expect there to be an absence of FLC in cells where the cloud borders the Coastal Cordillera.

8.3.2 GOFOS in the context of the last decade

According to the GOES results, February 2017 presented one of the lowest FFPs on average within the study period (1997 – 2017). But its low average is largely explained by a significant reduction in low cloud cover over the ocean (e.g. at 65 km offshore the average for the period is 9 % and in 2017 2,4 %). In the inland areas, FFPs in 2017 were still below average, but the difference decreased (e.g. 5 km inland was 3,0 %, when the period average was 3,8 %). If it is considered the validation carried out by local observation, where a very high correlation in monthly averages is demonstrated based on satellite information from both the GOFOS area and the airport area, can be state that for inland areas in February of 2017 FFP was slightly below average for the period 1997 – 2017. In this sense, considering that ENSO was in a neutral phase during February 2017 (negative anomaly of -0.1 °C), according to the potential causal-link between ENSO and FFPs presented in section 6.4.2.1., where in the summer positive (negative) ENSO phases are related to higher (lower)

FFPs and neutral phases below average FFPs, it is possible to assume that for 2017 in the inland sectors, thus where GOFOS measured information, was presented within the expected range of FFP.

When analyzing satellite results for September 2017, the various areas under study were either on average of slightly above average (e.g. at 65 km offshore and at 5 km inland averages for the period were 75 % and 31 %, and in 2017 these values were 74 % and 36 %, respectively). Considering potential coupling between FFP and the Pacific decadal cycle (discussed in section 6.4.2.2.) during September, data from 2017 are close to the average over the last 2 decades; 2017 was above FFPs in the late 1990s and below the years of maximum FFP (2009-2011). In this sense, GOFOS is representative of the average over the last 22 years, but distant from extreme FFP years (maximum and minimum), forming part of the decadal transition of the Pacific basin that apparently begins to move from a negative phase (La Niña-like) that predominated in recent decades, to a positive phase (El Niño-like). However, when the decadal influence is removed to look at inter-annual variability (see section 6.4.2.2.), the potential causal-link of the inter-annual variability of ENSO in FFP appears inverse, where in winter the positive (negative) ENSO phases are mostly related to lower (higher) FFPs. In this context, ENSO during September 2017, just as in February, was in a neutral phase (negative anomaly of -0.4 °C) and in turn FFPs were slightly above the period average at both offshore and onshore areas, which could be in concordance with the favorable conditions for FLC formation due to a debilitating La Niña phase. Finally, and in direct relation with the FFP, the thermal inversion layer altitude measured by GOFOS in 2017 must be contextualized within a period that has seen a systematic decline in its altitude over the past few decades (Muñoz et al. 2016). Nevertheless, these estimates were based on a location that was not influenced by topographic relief, as it is the case for GOFOS. Thus, especially during September when the inversion layer is at its lowest, the influence of the relief is greater, and its long-term effects have not been properly described.

8.4 An overall interpretation of new knowledge on the fog climate

In the introductory chapter various questions were raised on the characteristics and relationship between the past, present and future fog climate, and in particular its spatial-temporal distribution and variability. These questions arose due to a partial lack of understanding of the fog climate. Such questions guided this research (e.g. What are the

trends in fog low and cloud frequency presence over the last decades? Is the spatiotemporal distribution of fog and low clouds changing? Does inter-annual variability in ENSO affect the presence of fog in the Atacama? Is there any relationship between the amount of fog and low clouds and the thermal inversion layer altitude? Does Sc cloud thickness have the same variability and daily cycle as the related fog cloud? Is there a decreased presence of fog at higher altitudes? What are the basic atmospheric conditions necessary for the presence of fog?). The development of the present research, allows us to assess how the analyzed variables, spatiotemporal quantifications and relationships increased ou knowledge on the fog climate in coastal Atacama.

Trends in fog and low clouds over recent decades were neutral in the summer and neutral to positive for the winter. This information contributes to the discussion of inconsistent results found by other authors on this subject; however here it is provided a new source of information, satellite images, rather than observations at coastal airports, which has been the major data source for previous publications (e.g. Schulz et al., 2011a; Muñoz et al., 2016). Furthermore, the use of satellite images and their spatial dimension, allowed us to identify areas that as a result of the drop in altitude of the thermal inversion layer during the last decades, associated with the intensification of the SEPA, are generating a negative trend in fog presence in higher altitude areas of the Coastal Cordillera, and neutral to positive trends over the ocean and low altitude coastal areas. This finding is of great interest for our understanding of the atmosphere-biosphere relationship, given that several studies of fog-ecosystems suggest that a decrease in the altitude of the inversion layer may be related to a natural die-back of some species (e.g. Schulz et al., 2011b). The latter is interesting, because on the other hand, GOFOS results showed that topography produces a lifting of the cloud base, but its influence as a counterpart over stronger subsidence can only be assessed with a longer GOFOS dataset. In any case, the spatially differentiated trends demonstrated by satellite data indicate a change in the spatial distribution of the fog belt in coastal Atacama.

There is little information on the inter-annual variability of fog and low clouds in the hyper-arid coastal Atacama. Here, through statistical correlations and regressions, a potential causal-link was established between ENSO anomalies in the 3.4 zone and the frequency presence of fog and low clouds. Moreover, this relationship, which until now had only been established for a particular season (e.g. Garreaud et al (2008a) for spring in the Chilean

semiarid (~30°S), and del Río et al (2018) for summer in the Chilean hyper-arid (~20°S), was identified in both summer and winter. This contributes to the discussion on how the factors involved in the ocean-atmosphere-land interactions vary and generate either favorable or unfavorable conditions for fog formation. At the same time, we are able to connect dominant regional factors in the cloud formation (e.g. air subsidence, strength of the thermal inversion layer, SST) with the local atmospheric conditions, such as atmospheric variables (air temperature, relative humidity and air pressure) and indices used to establish the MBL regime (well-mixed or stratified). In this sense, interpretation of the effects produced by ENSO anomalies (e.g. presented in Figs. 46 and 51), where the conditions for the presence or absence of fog are reproduced, have an impact at a local scale, which is quantified by sensors on land, and thus provide a better understanding of the atmospheric thresholds for the fog and low cloud development.

Meteorologists, researchers interested in the relationship between fog and the biosphere, and those searching for optimal sites for fog water collection have all been interested in the spatiotemporal distribution of fog at a local scale. However, observations made by airport professionals have been used as the primary source of information; while such observations are systematic, they are not an accurate measurement and are limited to the cloud base height alone. In addition, the only existing radiosonde station is around 350 km (Antofagasta) away from the study area, and only takes measurements at two unique times of day, thus not providing proper coverage of the daily cycle. In this sense, the unique measurements produced here for the first time with GOFOS, provide greater accuracy than previous satellite approaches. GOFOS provides results on the spatiotemporal vertical dynamics of the fog cloud, including the cloud top altitude, cloud base and the cloud depth. GOFOS data are also unique in that they were obtained in the Coastal Cordillera, providing a better understanding of the influence of topography on the distribution of fog, something that is not able to be determined by airport measurements, as they are located on the coastal plain and provide information on low Sc clouds and not necessarily fog. GOFOS along with satellite image data, provides new information that allows us to compare the fog presence in the coastal areas, and at the same adds insight on the atmospheric variables that determine differences in both seasonal and daily cycles.

9 Conclusions and outlooks

In terms of the spatial-temporal characterization of coastal fog and low clouds in the Atacama Desert, fog and low cloud frequency presence (FFP) trends for the study period (1995 – 2017) shows a weak positive trend over the ocean and onshore areas below 1.000 m a.s.l. for September. However, for those areas close to the coast above 1.000 m a.s.l. there is a weak negative trend, demonstrating a decrease in the altitude of the thermal inversion layer over the years, which is consistent with observations by Muñoz et al. (2016). February does not present statistically significant trends due to very low fog presence.

ENSO apparently exerts a significant influence on inter-annual variability in the fog and low clouds in the coastal Atacama, as there is a possible causal-link between ENSO anomalies at 3.4 zone and FFP. During February, the ONI index is positively correlated with the FFP. Furthermore, linear regression indicates that ENSO anomalies explain ~50% of the variance in inter-annual FFPs during summer. In the case of September, a first approximation does not show a relationship with ENSO anomalies at the 3.4 zone. It appears that this relationship was hidden under the Pacific decadal signal (La Niña-like), but once the decadal patter was removed, the ONI index correlated inversely with FFP. Regression indicates that ENSO anomalies explain ~47 % and ~66 % of the variance in inter-annual fog and low cloud frequency presence during winter-early spring in the oceanic and onshore areas, respectively. The fact that most of the fog is concentrated in winter-early spring and the possibility that ENSO explains over 65 % of inter-annual variability in FFP, is of great importance in determining fog water collection sites, predicting potential quantities of water that might be collected, and the potential effects on fog-dependent ecosystems.

The conditions (la Niña-Like) over the last decades were favorable to the formation of fog and low clouds (higher stability in the low tropospheric), producing positive trends over the ocean and near shore areas. Additionally, greater air subsidence as a consequence of decreases in the altitude of the thermal inversion layer generated negative tendencies in fog presence at altitudes above 1.000 m a.s.l. However, ENSO phases (+/-) generate opposite seasonal fog conditions; ENSO (+) produces an increase (decrease) of FFP during summer (winter); ENSO (-) produces a decrease (increase) of FFP during summer (winter). One limitation of this study is that it was not consider the potential decadal (IPO) signal on winter FFPs, whose influence can only be confirmed with a longer dataset.

Cloud top (CT) and cloud base (CB) altitude and the cloud depth (CD) shown a distinct annual cycle that is close related to the location of the center of the SEPA. The CT and CB are at a higher altitude during summer, when the SEPA is at its southernmost position. In winter, the CT and CB reach their minimum altitudes when the SEPA reaches its northern position. The CT shows higher monthly differences in relation to the CB, which is much stable throughout the year. Consequently, the CD closely follows variations in the CT altitude, with the highest CD occurring during summer and the lowest during winter. The annual daily cycle shows a strong inverse correlation between FFP and the thermal inversion layer altitude, with a lower (higher) thermal inversion layer altitude related with higher (lower) FFPs from sunset to dawn (from early morning to afternoon). Therefore, the hypothesis at the local scale is in principle correct, given that the highest FFPs occur in the months and daily hours when the CT is at lower altitudes. At the same time that the CD is higher when the CT is at higher altitudes. However, the CB tends to be more stable in its cycles, which may be due to the fact that the temperature and humidity conditions necessary for condensation are assimilated by adiabatic effect, but also eventually due to the effect of topography and local winds, which should be studied with greater attention.

Spatiotemporal identification and characterization of fog and low clouds along the coast of the Atacama, allow us to precisely determine areas with greater or lesser fog presence, as well as fog's seasonality and daily cycles (both horizontal and vertical). Such results are vital to determine sites with greater potential for fog water collection, as well as for predicting future fog harvesting potential in a region where the growing demand for water resources will require sustainable alternative sources. In the same manner, estimates of spatial-temporal changes in fog and low clouds allows to link them with recent spatial changes in fog-dependent ecosystems, in order to better understand the existing connection between the atmosphere and biosphere, which may be key to our knowledge of past and future climatic changes.

The methodological approaches used to observation and characterize fog and low clouds, satellite remote sensing, GOFOS and weather stations, allowed us to characterize the different cycles of the low cloud in a complementary way. Specifically, GOFOS, the new fog monitoring system created for this research, on the one hand, acts as a ground truth validator for satellite classification at different time scales, (e.g. the image-by-image and the monthly averages comparison), and on the other hand, allows characterization of the local

vertical dynamics. At the same time, as it is a simple, reliable and economic system, it presents an attractive and viable alternative for systematic monitoring of fog presence and vertical dynamics, which can be adapted and improved to fit different topographic conditions. Although one of the complexities of the system is the need to precisely identify the ideal place where it can be applied, factors to consider include: accessibility for installation, the requirements of necessary altitudinal ranges, and the distance between cameras and lights so that it can clearly capture the presence/absence of fog. In this research, given the altitude of the thermal inversion layer in summer, it would have been advisable to cover an extra 150-200 altitudinal meters with the system.

Since the presence of fog and its variability in space and time are the result of several factors, it is advisable to incorporate new variables into monitoring systems in order to improve our understanding of the potential causal-links of its variability. Ideally at a regional scale satellite measurement would be complemented by, for example, radiosonde measurements to determine the strength and altitude of the thermal inversion with greater accuracy, thus achieving an enhanced understanding of the oceanic-atmosphere interactions in fog and low cloud formation. This knowledge would allow us to assess the implications of ENSO anomalies on fog climate variations and future projections with even greater certainty. The local scale datasets (GOFOS and the new weather stations) are an excellent complement to better understand the physics of cloud formation. However, it would be desirable to incorporate new sensors to measure additional atmospheric variables (e.g. temperature, relative humidity and air pressure) to the GOFOS light system, thus obtaining with high detail the vertical profile of the marine layer, which is a key element in understanding fog presence and relevant physical characteristics, such as liquid water content.

References

Albrecht, B. A., Randall, D. A. and Nicholls, S. (1988). Observations of marine stratocumulus during FIRE. Bull. Amer. Meteor.Soc., 69, 618–626.

Alonso, H. (2001). Uso competitivo del agua en minería y agricultura en el Norte de Chile. *Minería Chilena* 236: 31–37.

Anthis, A. and Cracknell, A.P. (1999). Use of satellite images for fog detection (AVHRR) and forecast of fog dissipation (METEOSAT) over lowland Thessalia, Hellas. *Int. J. Remote Sens.* 20: 1107–1124.

American Meteorology Society (AMS) (n.d.). Publication online. Retrieved 2018-09-25, from http://glossary.ametsoc.org/wiki/Stratocumulus.

Armijo, R., Lacassin, R., Coudurier-Curveur, A. and Carrizo, D. (2015). Coupled tectonic evolution of Andean orogeny and global climate. *Earth-Science Reviews* 143: 1-35.

Bendix, J. (2002). A satellite-based climatology of fog and low level stratus in Germany and adjacent areas. *J. Atmos. Res.* 64: 3–18.

Bendix, J., Thies, J., Cermark, J. and Nauss, T. (2005). Ground fog detection from space on MODIS daytime data – a feasible study. Weather and Forecasting, 20: 989-1005.

Beresford-Jones, D.G., Pullena, A.G., Whaley, O.Q., Moat, J., Chauca, G. E., Cadwallader, L., Arce, S., Orellana, A., Alarcón, C., Gorriti, M., Maita, P.K., Sturt, F.C., Dupeyron, A., Huaman, O., Lane, K.J. and French, C.I. (2015). Re-evaluating the resource potential of lomas fog oasis environments for Preceramic hunter–gatherers under past ENSO modes on the south coast of Peru. *Quat. Sci. Rev.* 129: 196–215.

Bretherton, C. S., & Wyant, M. C. (1997). Moisture transport, lower-tropospheric stability, and decoupling of cloud-topped boundary layers. J. Atmos. Sci., 54, 148–167.

Bretherton, C.S., Wood, R., George, R.C., Leon, D., Allen, G. and Zheng, X. (2010). Southeast pacific stratocumulus clouds, precipitation and boundary layer structure sampled along 20° S during VOCALS-Rex. *J. Atmos. Chem. Phys*. 10: 10639–10654.

Centro de Investigación y Desarrollo en Recursos Hídricos, CIDERH, (2013). Recursos hídricos Región de Tarapacá. Ed Universidad Arturo Prat, Iquique, Chile.

Cereceda, P. & Schemenauer, R. (1997). Agua en el Aire. In: Revista Universitaria PUC Chile 56: 45-49.

Cereceda, P., Larrain, H., Lázaro, P., Osses, P., Schemenauer, R.S. and Fuentes, L. (1999). Campos de tillandsias y niebla en el desierto de Tarapacá. *Rev. Geogr. Norte Gd.* 26: 3–13.

Cereceda, P., Osses, P., Larrain, H., Farías, M., Pinto, R. & Schemenauer, R.S. (2002).

Advective orographic and radiation fog in the Tarapacá region, Chile. *J. Atmos. Res*. 64: 261–271.

Cereceda, P., Larraín, H., Osses. P., Farías, M. & Egaña, I. (2008a). The spatial and temporal variability of fog and its relation to fog oases in the Atacama Desert, Chile. *J. Atmos. Res*. 87: 312–323.

Cereceda, P., Larraín, H., Osses, P., Farías, M. & Egaña, I. (2008b). The climate of the coast and fog zone in the Tarapacá Region, Atacama Desert, Chile. *J. Atmos. Res*. 87: 301–311.

Cereceda, P. & Errázuriz, A. M. (2015). Geografía, Chile y el Mundo. Ed. Vicens Vives, Santiago, Chile.

Cermark, J. (2007). SOFOS – A new Sattelite-based Operational Fog Observation Scheme. Marburg/Lahn : Marburger Geographische Ges.XIX, 132 S graph. Darst., Kt.

Clarke, J. (2006). Antiquity of aridity in the Chilean Atacama Desert. *Geomorphology* 73: 101-114.

del Río, C., Garcia, J.-L., Osses, P., Zanetta, N., Lambert, F.,Rivera, D., Siegmund, A., Wolf, N., Cereceda, P., Larraín H. & Lobos, F. (2018). ENSO influence on coastal fog-water yield in the Atacama Desert, Chile. *Aerosol Air Qual. Res*. 18 (1), 127–144.

Dirección General de Aguas, DGA (2017). Estimación de la demanda actual, proyecciones futuras y caracterización de la calidad de los recursos hídricos en Chile. Ministerio de Obras Públicas, Santiago, Chile.

Dirección Meteorológica de Chile, DMC (2017). Climatología, Informe de Precipitaciones. Publication online. Retrieved 2017-09-30, from: http://www.meteochile.gob.cl/inf_precipitacion.php.

Duynkerke, P.G., Zhang, H.Q. & Jonker, P.J., (1995). Microphysical and turbulent structure of nocturnal stratocumulus as observed during ASTEX. J. Atmos. Sci. 52 (16), 2763–2777.

Ellrod, G. (1995). Advances in the Detection and Analysis of Fog at Night Using GOES Multiespectral Infrared Imagery. *Weather Forecasting* 10: 606–619.

Escobar, M. & García, M. (2017). Camanchaca. Flujos etnonímicos y neblineros en la costa norte de Chile. *Revista de Geografía Norte Grande*, 68: 11-32.

Eyre, J.R. (1984). Detection of fog at night using Advanced Resolution Radiometer (AVHRR) imagery. *Meteorol. Mag.* 113: 266–271.

Falvey, M. & Garreaud, R. (2009). Regional cooling in a warming world: Recent temperature trends in the SE Pacific and along the west coast of subtropical South America (1979-2006). *J. Geophys. Res.* 114: D04102.

Farías, M., Cereceda, P., Osses, P. & Larraín, H. (2005). Comportamiento espacio temporal de la nube estratocúmulo, productora de niebla en la costa del desierto de Atacama (21° lat. S., 70° long W.) durante un mes de invierno y otro de verano. *Invest. Geog.* 56: 43–61.

Farías, M. (2006). Estudio Biogeográfico de Tillandsiales de la Región de Tarapacá, Chile y sus Relaciones con el Comportamiento de la Niebla. Scientific report proyect FONDECYT 1051035. DOI:10.13140/RG.2.1.4975.9201.

Garreaud, R. & Munoz, R. (2004). The diurnal cycle of circulation and cloudiness over the subtropical southeast Pacific: A modelling study. *J. Clim.* 17: 1699–1710.

Garreaud, R., Christie, D., Barichivih, J. & Maldonado, A. (2007). Climate, Weather and Fog along the west coast of Subtropical South America. 4th International Conference on Fog, Fog Collection and Dew, Proc., La Serena, Chile, 2007, pp. 22–27.

Garreaud, R., Barichivich, J., Christie, D. & Maldonado, A. (2008a), Interannual variability of the coastal fog at Fray Jorge relicts forests in semiarid Chile. *J. Geophys. Res.* 113: G04011.

Garreaud, R., Vuille, M., Compagnucci, R. & Marengo, J. (2008b). Present-day South American climate. *Palaeogeogr. Palaeoclimatol. Palaeoecol.* 281: 180–195.

Garreaud, R. D., Rutllant, J. A., Muñoz, R. C., Rahn, D. A., Ramos, M., & Figueroa, D. (2011). VOCALS-CUpEx: The Chilean Upwelling Experiment. Atmos. Chem. Phys., 11, 2015–2029.

Hartley, A. J. Chong, G., Houston, J. & Mather, A.E. (2005). 150 million years of climatic stability: evidence from the Atacama Desert, northern Chile. *J. of the Geological Society*, 162, 421-424.

Hartman, M., Ockert-Bell, E. & Michelsen, M.L. (1992). The effect of cloud type on earth´s energy balance-global analysis. *J Climate*, 5:1281-1304.

Hesse, R. (2012). Spatial distribution of and topographic controls on Tillandsia fog vegetation in coastal southern Peru: Remote sensing and modelling. *J. of Arid Environments*, 78: 33–40.

Hoaglin D.C., Frederick, M. & Tukey, J. W. (2000) Understanding Robust and Exploratory Data Analysis. New York: John Wiley & Sons, Inc.

Instituto Nacional de Estadísticas, INE (2017). Estimaciones y Proyecciones de la Población de Chile 1992-2050 (Total País), CENSO 2017.

Jedlovec, G. J., & Laws, K. (2003), GOES cloud detection at the Global Hydrology and Climate Center, paper P1 presented at 12th conference on satellite meteorology and oceanography, Am. Meteorol. Soc., Long Beach, Canada, Feb.

Jensen, J. R. (2005). Introductory Digital Image Processing, Upper Saddle River, NJ: Pearson Prentice Hall.

Jordan, T.E., Kirk-Lawlor, N.E., Blanco, N., Rech, J.A. & Cosentino, N. (2014). Landscape modification in response to repeated onset of hyperarid paleoclimate states since 14 Ma, Atacama Desert, Chile. *Geological Society of America Bulletin* 126(7-8):1016-1046.

Klein, S. A., & Hartmann, D. L. (1993). The seasonal cycle of low stratiform clouds. *J. Climate*, 6, 1587–1606.

Klein, S. A., Hartmann, D. L. & Norris, J. R. (1995). On the relationships among low-cloud structure, sea surface temperature, and atmospheric circulation in the summertime northeast Pacific. J. Climate, 8, 1140–1155.

Larraín, H., Velásquez, F., Cereceda, P., Espejo, R., Pinto, R., Osses P. & Schemenauer R.S. (2002). Fog measurements at the site "Falda Verde" north of Chañaral compared with other fog stations of Chile. *J. Atmos. Res*. 64: 273–284.

LaDochy, S. & Witiw, M. (2012). The Continued Reduction in Dense Fog in the Southern California Region: Possible Causes. *Pure and Applied Geophysics*, 169 (5-6):1157-1163.

Latorre, C., González, A.L., Quade, J., Fariña, J.M., Pinto, R. & Marquet, P.A. (2011). Establishment and formation of fog-dependent Tillandsia landbeckii dunes in the Atacama Desert: Evidence from radiocarbon and stable isotopes. *J. Geophys. Res.* 116: G03033.

Latorre, C., Santoro, C., Ugalde, P., Gayo, E., Osorio, Salas-Egaña, C., De Pol-Holz, R., Joly, D. & Rech, J.A. (2013). Late Pleistocene human occupation of the hyperarid core in the Atacama Desert, northern Chile. Quaternary Science Reviews, 77:19-30.

Lee, T., Turk, J. & Richardson, K. (1997). Stratus and fog products using GOES-8-9 3.9 µm Data. *Weather Forecasting* 12: 664–677.

Lobos, F., Vilà-Guerau J. & Pedruzo-Bagazgoitia, X. (2018). Characterizing the influence of the marine stratocumulus cloud on the land fog at the Atacama Desert. *J. Atmos. Res*. 214: 109–120.

Manrique, R., Ferrari, C. & Pezzi, G. (2010). The influence of El Niño Southern Oscillation (ENSO) on fog oases along the Peruvian and Chilean coastal deserts. 5th International Conference of Fog and Fog Collection Proc., Munster, Germany, 148–150.

Mantua, N.J., Hare, S.R., Zhang, Y., Wallace, J.M. & Francis, R.C. (1997). A Pacific interdecadal climate oscillation with impacts on salmon production. *Bull. Am. Meteorol. Soc.* 78: 1069–1079.

Marzol, M.V. (2002). Fog water collection in a rural park in the Canary Islands (Spain). *J. Atmos. Res*. 64: 239–250.

Marzol, M.V. & Sánchez, J. (2008). Fog water harvesting in Ifni, Morocco. An assessment

of potential and demand. *Die Erde* 139: 97–126.

Masuzawa, T. (1985). Structure of Tillandsia Lomas Community in Peru. Grant-in-aid for Scientific Research Reports for Overseas Scientific Survey. Tokyo Metropolitan University 93.

Met Office, Press office (2017). A Pacific flip triggers the end of the recent slowdown. Publication online. Retrieved 2017-06-15, from: https://www.metoffice.gov.uk/about-us/press-office/news/weather-and-climate/2017/a-pacific-flip-triggers-the-end-of-the-recent-slowdown.

McRostie, V., Gayo, E.M., Santoro, C.M., De Pol-Holz, R. & Latorre, C. (2017) The pre-Columbian introduction and dispersal of Algarrobo (Prosopis, Section Algarobia) in the Atacama Desert of northern Chile. PLoS ONE 12(7): 1-15.

Montecinos, A., Diaz, A. & Aceituno, P. (2000). Seasonal diagnostic and predictability of rainfall in subtropical South America based on tropical Pacific SST, *J. of Climate*, 13(4): 746-758.

Montecinos, A. & Aceituno, P. (2003). Seasonality of the ENSO-related rainfall variability in central Chile and associated circulation anomalies, *J. of Climate*, 16(2): 281-296.

Muñoz, R., Zamora, R. & Rutllant, J. (2011). The coastal boundary layer at the eastern Margin of the southeast Pacific (23.4 degrees S, 70.4 degrees W): Cloudiness-conditioned climatology. *J. Clim.* 24: 1013–1033.

Muñoz, R., Quintana, J., Falvey, M., Rutllant, J. & Garreaud, R. (2016). Coastal clouds at the eastern Margin of the southeast Pacific: Climatology and trends. *J. Clim.* 29: 4525–4542.

Muñoz-Schick, M., Pinto, R. & Mesa, A. (2001). Oasis de neblina en los cerros costeros del sur de Iquique, región de Tarapacá, Chile, durante el evento El Niño 1997-1998. *Rev. Chil. Hist. Nat.* 74: 389–405.

NASA Goddard Space Flight Center, Ocean Biology Processing Group; (2014): Sea-viewing Wide Field-of-view Sensor (SeaWiFS) Ocean Color Data, NASA OB.DAAC, Greenbelt, MD, USA. http://doi.org/10.5067/ORBVIEW-2/SEAWIFS_OC.2014.0. Retrieved 2017-03-15. Maintained by NASA Ocean Biology Distibuted Active Archive Center (OB.DAAC), Goddard Space Flight Center, Greenbelt MD.

Norris, J. R., & Leovy, C. B. (1994). Interannual variability in stratiform cloudiness and sea surface temperature. J. Climate, 7, 1915–1925.

Observatorio Social, (2014). Alto Hospicio, Región de Tarapacá. Ministerio de Desarrollo Social, Gobierno de Chile. Publication Online, Retrieved 2017-07-20 from http://observatorio.ministeriodesarrollosocial.gob.cl/indicadores/reportes_com1_2.php.

Ortlieb, L. (1995). Eventos El Niño y episodios lluviosos en el desierto de Atacama: el

registro de los últimos dos siglos. *Bull. Inst. Français d'Etudes Andines* 24: 191–212.

Osses, P., Cereceda, P., Larraín, H. & Schemenauer, R.S. (1998). Influence of relief on the origin and behaviour of fog at Tarapaca, Chile, 1st International Conference of Fog and Fog Collection Proc., Vancouver, Canada, 1998, pp. 245–247.

Osses, P., Cereceda, P., Larrain, H. & Astaburuaga, J. P. (2007). Distribution and geographical factors of the Tillandsia fields in the coastal mountain range of the Tarapacá Region, Chile. 4th International Conference on Fog, Fog Collection and Dew, Proc., La Serena, Chile, 2007, pp. 93–96.

Oyarzún, J. & Oyarzún, R. (2011). Sustainable development threats, inter-sector conflicts and environmental policy requirements in the arid, mining rich, northern Chile territory. *Sust. Dev.* 19: 263–274.

Painemal D. & Zuidema, P. (2009). Microphysical variability in southeast Pacific Stratocumulus clouds: synoptic conditions and radiative response. *Atmos. Chem. Phys*., 10: 6255-6269.

Park, S. & Leovy, C.B. (2004). Marine low cloud anomalies associated with ENSO. *J. Clim*. 17: 3448–3469.

Parker, D., Folland, C., Scaife, A., Knight, J., Colman, A., Baines, P. & Dong, B. (2007) Decadal to multidecadal variability and the climate change background. *J Geophys Res*., 112(D18): D18115.

Pauchard, A. & Villarroel, P. (2002). Protected areas in Chile: History, current status, and challenges. *Natural Areas Journal*, 22:318-330.

Pinto, R., Barria, I. & Marquet, P. A. (2006). Geographical distribution of Tillandsia lomas in the Atacama Desert, northern Chile. *J. Arid Environ*. 65: 543–552.

Power, S., Casey, T., Folland, C., Colman, A. & Mehta, V. (1999). Inter-decadal modulation of the impact of ENSO on Australia. *Climate Dynamics* 15: 319–324.

Quintana, J. & Berríos, P. (2007). Study of the coastal low cloud in the northern coast of Chile: Variability and tendency. Proc. Fourth Int. Conf. on Fog, Fog Collection and Dew, La Serena, Chile, FogQuest, 189–192.

Randall, J.A., Coakley, C.W., Fairall, R., Knopfli, A. & Lenschow, D.H. (1984). Outlook for research on marine subtropical stratocumulus clouds. *Bull. Amer. Meteor. Soc*., 65:1290-1301.

Richter, I. & C. Mechoso, R. (2006). Orographic Influences on Subtropical Stratocumulus. *J Atmos Sci*, 63:2585-2601.

Roach, W. T., Brown, R., Caughey, S. J., Crease, B. A. & Slingo, A. (1982). A field-study of nocturnal stratocumulus: 1. Mean structure and budgets. Quart. J. Roy. Meteor. Soc., 108,

103–123.

Roach, W. T. (1994). Back to basics: Fog: Part 1 – Definition and basic physics. Weather, 49: 411-415.

Rojas, R. & Dassargues, A. (2007). Groundwater flow modelling of the regional aquifer of the Pampa del Tamarugal, northern Chile. *Hydrogeol. J.,* 15, 537-551.

Romero, H., Méndez, M., Smith, P. & Mendoça, M. (2012). Enfoque ecológico-social de la variabilidad climática, extracciones de agua y demandas territoriales en las cuencas del desierto de Atacama. *Revista Geonorte*, [S.l.], v. 3, n. 7:252-278.

Rozendaal, M. A., Leovy, C. B. & Klein, S. A. (1995). An observational study of the diurnal cycle of marine stratiform cloud. J. Climate, 8, 1795–1809.

Rundel, P.W. and Dillon, M.O. (1998). Ecological patterns in the Bromeliaceae of the lomas formation of Coastal Chile and Peru. *Plant Syst. Evol.* 212: 261–278.

Rutllant, J., Fuenzalida, H., Torres, R. & Figueroa, D. (1998). Interacción océano-atmósfera-tierra en la Región de Antofagasta (Chile, 23 o S): Experimento DICLIMA. *Rev. Chilena de Historia Natural*, 71:405-427.

Rutllant, J., Fuenzalida, H. & Aceituno, P. (2003). Climate dynamics along the arid northern coast of Chile: The 1997–1998 Dinámica del Clima de la Región de Antofagasta (DICLIMA) experiment. *J. Geophys. Res.* 108: 4538.

Rutllant, J. & Garreaud, R. (2005). Capa límite marina en el Pacífico suroriental subtropical durante el Crucero CIMAR-5. Revista Chilena de Ciencia y Tecnología del Mar, 28(1): 25-33.

Santoro, C., Capriles, J., Gayo, E., de Porras, M.E., Maldonado, A., Standen, V., Latorre, C., Castro, V., Angelo, D., McRostie, V., Uribe, M., Valenzuela, D., Ugalde, P.C. & Pablo Marquet, P. (2017). Continuities and discontinuities in the socio-environmental systems of the Atacama Desert during the last 13,000 years. Journal of Anthropological Archaeology. Volume 46: 28-39.

Schemenauer, R. S. & Cereceda, P. (1994). A proposed standard fog collector for use in high elevation regions. In: *Journal of Applied Meteorology*, Vol 33, No. 11: 1113-1322.

Schulz, N., Boisier, J.P. & Aceituno, P. (2011a). Climate change along the arid coast of northern Chile. *J. Clim*. 32: 1803–1814.

Schulz, N., Aceituno, P. & Richter, M. (2011b). Phytogeographic divisions, climate change and plant dieback along the coastal desert of northern Chile. *Erdkunde* 65:169-197.

Seethala, C., Norris, J. R. & Myers, T. A. (2015). How has subtropical stratocumulus and associated meteorology changed since the 1980s? *J. Climate*, 28, 8396–8410.

Serpetzoglou, E., Albrecht, B.A., Kollias, P. & Fairall, C. (2008). Boundary layer, cloud, and

drizzle variability in the southeast Pacific stratocumulus regime. *J. Climate*. 21: 6191–6214.

Stull, R. (1988). An Introduction to Boundary Layer Meteorology. Kluwer Academic Publishers, The Netherlands. 670 pp.

Torregrosa, A., Combs, C. & Peters, J. (2015). GOES-derived fog and low cloud indices for coastal north and central California ecological analyses. *Earth and Space Science*, 3:46-67.

Underwood, J., Ellrod, G. & Kuhnert, A. (2004). A multiple-case analysis of nocturnal radiation-fog development in the central valley of California utilizing the GOES nighttime fog product. *J. Appl. Meteorol.* 43: 297–311.

Vuille, M., Franquist, E., Garreaud, R., Lavado, W. & Bolivar Cáceres, C. (2015). Impact of the global warming hiatus on Andean temperature. *J. Geophys. Res.* 120: 3745–3757.

Wallace, J.M. & Hobbs, P.V. (2006). Atmospheric science: An introductory survey, 2nd Ed., Elsevier Inc. U.K.

Weischet (1975). Las condiciones climáticas del desierto de Atacama como desierto extremo de la tierra, *Rev. Geogr. Norte Gd.* Nº 4-5.

Westbeld, A., Klemm, O., Grießbaum, F., Sträter, E., Larrain, H., Osses, P. & Cereceda, P. (2009). Fog deposition to a Tillandsia carpet in the Atacama Desert. *Ann. Geophys*. 27: 3571–3576.

Witiw, M. & LaDochy, S. (2008). Trends in fog frequencies in the Los Angeles Basin, *J. Atmos. Res.* 87: 293-300.

Wood, R. (2012). Stratocumulus Clouds, Mon. Weather Rev., 140, 2373–2423.